UNIVERSITAT POLITÈCNICA DE CATALUNYA BARCELONATECH

Efficient simulation tools for real-time monitoring and control using model order reduction and data-driven techniques

Giacomo Quaranta

École Centrale de Nantes
Nantes, France

Universitat Politècnica de Catalunya
Barcelona, Spain

PHD THESIS

Efficient simulation tools for real-time monitoring and control using model order reduction and data-driven techniques

Dissertation presented in partial fulfilment of the requirements for the degree of

PhD of the Ecole Centrale de Nantes
Docteur de l'Ecole Centrale de Nantes

PhD of the Universitat Politècnica de Catalunya
Doctor de la Universitat Politècnica de Catalunya

by
Giacomo Quaranta

September 2019

President:	Michel Visonneau	-	Ecole Centrale de Nantes
Jury members:	Antonio Gil	-	Swansea University
	David González	-	Universidad de Zaragoza
	Benjamin Klusemann	-	Leuphana Universität Lüneburg
	Pedro Diez	-	Universitat Politècnica de Catalunya
	Rubén Sevilla	-	Swansea University
Advisors:	Francisco Chinesta	-	ENSAM ParisTech Paris
	Antonio Huerta	-	Universitat Politècnica de Catalunya
Co-Advisors:	Emmanuelle Abisset-Chavanne	-	ENSAM ParisTech Bordeaux
	Jean-Louis Duval	-	ESI Group
	Elías Cueto	-	Universidad de Zaragoza

Abstract

Numerical simulation, the use of computers to run a program which implements a mathematical model for a physical system, is an important part of today technological world. It is required in many scientific and engineering fields to study the behavior of systems whose mathematical models are too complex to provide analytical solutions and it makes virtual evaluation of systems responses possible (*virtual twins*). This drastically reduces the number of experimental tests for accurate designs of the real system that the numerical model represents.

However these virtual twins, based on classical methods which make use of a rich representations of the system (e.g. finite element method), rarely allows real-time feedback, even when considering high performance computing, operating on powerful platforms. In these circumstances, the real-time performance required in some applications are compromised. Indeed the virtual twins are static, that is, they are used in the design of complex systems and their components, but they are not expected to accommodate or assimilate data so as to define dynamic data-driven application systems. Moreover significant deviations between the observed response and the one predicted by the model are usually noticed due to inaccuracy in the employed models, in the determination of the model parameters or in their time evolution.

In this thesis we propose different methods to solve these handicaps in order to perform real-time monitoring and control. In the first part Model Order Reduction (MOR) techniques are used to accommodate real-time constraints; they compute a good approximation of the solution by simplifying the solution procedure instead of the model. The accuracy of the predicted solution is not compromised and efficient simulations can be performed (*digital twins*). In the second part data-driven modeling are employed to fill the gap between the parametric solution, computed by using non-intrusive MOR techniques, and the measured fields, in order to make dynamic data-driven application systems, DDDAS, possible (*hybrid twins*).

Résumé

La simulation numérique, c'est-à-dire l'utilisation des ordinateurs pour exécuter un programme qui met en œuvre un modèle mathématique d'un système physique, est une partie importante du monde technologique actuel. Elle est nécessaire dans de nombreux domaines scientifiques et techniques pour étudier le comportement de systèmes dont les modèles mathématiques sont trop complexes pour fournir des solutions analytiques et elle rend possible l'évaluation virtuelle des réponses des systèmes (*jumeaux virtuels*). Cela réduit considérablement le nombre de tests expérimentaux nécessaires à la conception précise du système réel que le modèle numérique représente.

Cependant, ces jumeaux virtuels, basés sur des méthodes classiques qui utilisent une représentation fine du système (ex. méthode des éléments finis), permettent rarement une rétroaction en temps réel, même dans un contexte de calcul haute performance, fonctionnant sur des plates-formes puissantes. Dans ces circonstances, les performances en temps réel requises dans certaines applications sont compromises. En effet, les jumeaux virtuels sont statiques, c'est-à-dire qu'ils sont utilisés dans la conception de systèmes complexes et de leurs composants, mais on ne s'attend pas à ce qu'ils prennent en compte ou assimilent des données afin de définir des systèmes d'application dynamiques pilotés par les données. De plus, des écarts significatifs entre la réponse observée et celle prévue par le modèle sont généralement constatés en raison de l'imprécision des modèles employés, de la détermination des paramètres du modèle ou de leur évolution dans le temps.

Dans cette thèse, nous proposons différentes méthodes pour résoudre ces handicaps afin d'effectuer une surveillance et un contrôle en temps réel. Dans la première partie, les techniques de Réduction de Modèles sont utilisées pour tenir compte des contraintes en temps réel ; elles calculent une bonne approximation de la solution en simplifiant la procédure de résolution plutôt que le modèle. La précision de la solution n'est pas compromise et des simulations efficaces peuvent être réalisées (*jumeaux numériquex*). Dans la deuxième partie, la modélisation pilotée par les données est utilisée pour combler l'écart entre la solution paramétrique calculée, en utilisant des techniques de réduction de modèles non intrusives, et les champs mesurés, afin de rendre possibles des systèmes d'application dynamiques basés sur les données (*jumeaux hybrides*).

Resumen

La simulación numérica, el uso de ordenadores para ejecutar un programa que implementa un modelo matemático de un sistema físico, es una parte importante del mundo tecnológico actual. En muchos campos de la ciencia y la ingeniería es necesario estudiar el comportamiento de sistemas cuyos modelos matemáticos son demasiado complejos para proporcionar soluciones analíticas, haciendo posible la evaluación virtual de las respuestas de los sistemas (*gemelos virtuales*). Esto reduce drásticamente el número de pruebas experimentales para los diseños precisos del sistema real que el modelo numérico representa.

Sin embargo, estos gemelos virtuales, basados en métodos clásicos que hacen uso de una rica representación del sistema (por ejemplo, el método de elementos finitos), rara vez permiten la retroalimentación en tiempo real, incluso cuando se considera la computación en plataformas de alto rendimiento. En estas circunstancias, el rendimiento en tiempo real requerido en algunas aplicaciones se ve comprometido. En efecto, los gemelos virtuales son estáticos, es decir, se utilizan en el diseño de sistemas complejos y sus componentes, pero no se espera que acomoden o asimilen los datos para definir sistemas de aplicación dinámicos basados en datos. Además, se suelen apreciar desviaciones significativas entre la respuesta observada y la predicha por el modelo, debido a inexactitudes en los modelos empleados, en la determinación de los parámetros del modelo o en su evolución temporal.

En esta tesis se proponen diferentes métodos para resolver estas limitaciones con el fin de realizar un seguimiento y un control en tiempo real. En la primera parte se utilizan técnicas de Reducción de Modelos para satisfacer las restricciones en tiempo real; estas técnicas calculan una buena aproximación de la solución simplificando el procedimiento de resolución en lugar del modelo. La precisión de la solución no se ve comprometida y se pueden realizar simulaciones eficientes (*gemelos digitales*). En la segunda parte se emplea la modelización basada en datos para llenar el vacío entre la solución paramétrica, calculada utilizando técnicas de reducción de modelos no intrusivas, y los campos medidos, con el fin de hacer posibles los sistemas de aplicación dinámicos basados en datos (*gemelos híbridos*).

Résumé étendu

Depuis la précédente (troisième) révolution industrielle, la simulation numérique a été largement utilisée dans de nombreux domaines scientifiques et techniques et elle est aujourd'hui l'un des acteurs majeurs du monde technologique. En fait, elle permet d'étudier virtuellement les comportements et les réponses des systèmes (i) sans avoir besoin de résoudre analytiquement les modèles mathématiques (généralement complexes) associés aux systèmes, (ii) en réduisant le nombre d'expériences (généralement coûteuses et longues) réalisées sur le système lors de sa phase de conception. Au cours du XXe siècle, de nombreuses méthodes ont été mises au point pour réaliser des simulations numériques capables d'émuler un système physique en résolvant les modèles mathématiques décrivant son comportement complexe (différences finies, éléments finis, volumes finis, méthodes spectrales, technique sans maillage, ...) définissant les *jumeaux virtuels* qui, avec la modélisation et les expériences (pour la calibration et la validation des modèles) ont joué un rôle prépondérant en ingénierie.

Cependant, les jumeaux virtuels ont un inconvénient majeur. Avant de résoudre un problème donné, l'utilisateur doit introduire les différents paramètres impliqués (par exemple les paramètres des matériaux et les charges appliquées) et définir le domaine dans lequel le problème est posé. Dès que le problème est résolu (en utilisant des ordinateurs de plus en plus puissants et des algorithmes rapides, robustes et précis), différentes quantités d'intérêt peuvent être calculées. Cela signifie que les jumeaux virtuels sont statiques : ils sont utilisés dans la conception de systèmes complexes et de leurs composants, mais ils ne peuvent pas accueillir ou assimiler des données afin de définir des systèmes d'application dynamiques pilotés par le données (DDAS, *Dynamic Data-Driven Application Systems* en anglais). En raison du temps caractéristique des stratégies de simulation standard, ils permettent rarement le retour d'information en temps réel requis dans certaines applications (par exemple le retour d'information haptique dans la simulation chirurgicale ou le contrôle basé sur la simulation impliqué dans la robotique, l'internet des objets ou les robots autonomes), même si on considère le calcul haute performance, fonctionnant sur des plateformes puissantes. De plus, l'optimisation et les analyses inverses impliquées dans les procédures d'étalonnage nécessitent respectivement de nombreux calculs directs pour trouver les paramètres optimaux ou les paramètres recherchés. Enfin, la quantification et la propagation de l'incertitude nécessitent également d'améliorer l'efficacité des stratégies habituelles.

Le contrôle en temps réel pourrait être obtenu au moyen de techniques basées sur l'utilisation de représentations adaptées du système, reliant certaines entrées à certaines sorties par une fonction de transfert. Même si ces méthodes assurent une représentation en temps réel, leur représentation du système est

trop grossière par rapport aux représentations fines des systèmes, comme celles réalisées par exemple par éléments finis (transitoires 3D dans la plupart des cas), qui permettent des simulations haute fidélité. Cependant, comm déjà mentionné, ces représentations trop riches, excellentes du point de vue de la compréhension du système et de la contrôlabilité à petite échelle, ne permettent pas de procéder en temps réel sur les plates-formes de calcul habituelles ou sur les systèmes déployés.

Même si l'utilisation d'ordinateurs plus puissants pouvait résoudre ces problèmes, cela en entraînerait deux autres. Premièrement, il ne permettrait pas aux petites et moyennes entreprises d'avoir accès aux ressources de simulation appropriées (nécessaires pour assurer l'innovation) et, deuxièmement, il ne serait pas facilement intégré aux systèmes déployés. Ce besoin d'outils de simulation en temps réel et en même temps accessibles a donné naissance, au début de XXIe siècle, à de nouvelles solutions en matière de modélisation et de procédures de simulation. C'est là que les techniques de Réduction de Modèles (MOR, *Model Order Reduction* en anglais) ont ouvert de nouvelles possibilités pour des simulations plus efficaces. Une alternative possible dans le cadre de la méthode MOR consiste à extraire "hors ligne" les modes les plus significatifs impliqués dans la solution du modèle, qui constitueront la base dite d'approximation réduite, puis à projeter la solution des problèmes "assez similaires" dans cette base réduite. Comme le nombre de fonctions impliquées dans la base réduite est assez faible, seuls quelques coefficients doivent être calculés pour déterminer la solution du problème et un problème discret de très petite taille doit être résolu à chaque itération ou pas de temps. Ainsi, les techniques de discrétisation basées sur les MOR permettent d'importantes économies de temps de calcul, de plusieurs ordres de grandeur dans certains cas, ce qui permet de tenir compte des contraintes en temps réel. Une autre possibilité consiste à calculer hors ligne en utilisant toutes les ressources de calcul nécessaires, par exemple le calcul haute performance (HPC, *High Performance Computing* en anglais), et tout le temps de calcul nécessaire, une solution paramétrique contenant la solution de tous les scénarios possibles. Cette solution paramétrique est ensuite particularisée en ligne à l'aide d'installations de calcul légères, comme des dispositifs déployés, des tablettes ou des smartphones pour effectuer en temps réel une simulation efficace, une optimisation, une analyse inverse, une propagation de l'incertitude ou un contrôle par simulation. C'est la philosophie adoptée par la *Proper Generalized Decomposition* (PGD) qui a été utilisée dans de nombreuses applications pour calculer des solutions paramétriques de modèles représentant des processus, structures et systèmes complexes. Ainsi, quelques heures de calcul intensif hors ligne permettent de construire des solutions paramétriques très générales capables d'assurer des réponses quasi instantanées aux requêtes, tout en conservant le niveau de précision des discrétisations habituelles. De plus, les techniques de réduction de modèles permettent également d'assimiler les données collectées par les capteurs dans les modèles physiques. Des données collectées qui peuvent être analysées, classées et visualisées grâce à de nombreuses techniques développées à partir de la fin du XXe siècle dans les domaines de l'intelligence artificielle et de l'apprentissage machine

comme les techniques de réduction de dimensionnalité linéaire et non linéaire basées sur l'analyse de variétés et des *model learners* basés sur l'utilisation de régression linéaire et non linéaire, arbres décisionnels, forêts aléatoires, réseaux de neurones et techniques d'apprentissage profond. L'intégration des techniques de réduction de modèles avec l'intelligence artificielle a donné naissance à ce qu'on appelle les *jumeaux numériquex* dans le but principal d'identifier les paramètres impliqués dans le modèle ainsi que leur évolution en temps réel, anticipant les actions de leurs capacités prédictives. Grâce à l'utilisation des jumeaux numériquex, le contrôle par simulation a été envisagé et réalisé avec succès dans de nombreuses applications, dans de nombreux cas en utilisant des dispositifs informatiques déployés.

En raison de la grande importance que les jumeaux numériquex basés sur la réduction de modèles ont sur le monde technologique, la partie principale de cette thèse concerne le développement de nouvelles techniques qui peuvent être utilisées pour améliorer ces jumeaux numériquex. Cette thèse concerne en particulier l'utilisation de la réduction de modèles et des techniques pilotés par les données afin de développer de nouveaux outils de simulation pour la surveillance et le contrôle en temps réel à deux échelles différentes :

1. Echelle du *composant mécanique* : on propose des méthodes pour évaluer efficacement la réponse dynamique des plaques métalliques et composites dans des cas linéaires et non linéaires, avec un accent particulier sur sa dépendance vis-à-vis des paramètres et sur les méthodes non-intrusives. L'intérêt de l'étude de la réponse dynamique est donné par l'importance qu'elle a dans l'identification de l'existence d'un dommage et de sa localisation dans le composant mécanique, c'est-à-dire dans les techniques de surveillance de la santé structurelle pour lesquelles une méthode est également présentée dans ce travail.

2.1. Echelle du *processus mécanique* : on développe des outils de simulation des processus permettant le calcul (et le recalcul) en temps réel des prédictions, l'optimisation, l'identification des paramètres, le contrôle et l'analyse inverse pendant le processus et on les applique à un procédé de fabrication additive.

Cependant, même si l'utilisation de jumeaux numériquex permet d'examiner les modèles haute fidélité à toutes leurs échelles presque en temps réel en utilisant des plateformes informatiques raisonnables (dès que les efforts hors ligne sont accomplis), lorsque ces installations informatiques sont intégrées dans des systèmes d'applications pilotés par les données, des difficultés imprévues apparaissent immédiatement. Dans la pratique, on constate des écarts importants entre les réponses prévues et observées, ce qui limite leur utilisation dans de nombreuses applications. Ces écarts peuvent être dus à : (i) des inexactitudes dans les modèles employés qui parfois ne sont pas suffisamment précis pour décrire les systèmes réels ; (ii) une évolution temporelle *a priori* presque imprévisible de certains modèles et (iii) des inexactitudes dans la détermination des paramètres des modèles ou dans leur évolution temporelle, qui peuvent présenter des fluctuations stochastiques dans

le temps et l'espace. Une certaine partie de l'écart (sa composante non biaisée au sens statistique) peut être considérée comme un bruit, mais la partie biaisée restante prouve l'existence d'un modèle caché qui fonctionne mais qui échappe à notre compréhension. Afin de résoudre ce problème et d'obtenir un contrôle efficace du système, une possibilité consiste à construire "à la volée" un modèle piloté par les données capable de combler l'écart entre la prédiction du modèle et les mesures. En fait, dès que le modèle piloté par les données permet de faire des prévisions précises, les stratégies de contrôle peuvent être appliquées en toute sécurité. Une alternative importante pour alléger la construction de telles corrections pilotées par les données, mais qui n'est pas développée dans ce travail de thèse, consiste à extraire les connaissances des modèles phénoménologiques guidés par les données en utilisant à nouveau des stratégies d'apprentissage machine (arbres de décision et ses variantes et améliorations). De plus, afin d'améliorer le dialogue entre les prédictions (modèle et modèle piloté par les données) et les utilisateurs, la réalité augmentée pourrait également être utilisée.

La dernière partie de la thèse est donc consacrée au développement d'un nouveau concept : le concept de *jumeaux hybrides* (HT, *Hybrid Twins* en anglais). Les jumeaux hybrides combinent des solutions de modèles paramétriques basées sur le HPC avec des modèles de déviation construits "à la volée" et pilotés par les données, rendant possibles des systèmes d'application dynamiques pilotés par les données. En particulier, on applique le concept des jumeaux hybrides à l'

2.2. Echelle du *processus mécanique* : on développe DDDAS pour deux processuss différents, un processus de Moulage par Transfert de Résine (RTM, *Resin Transfer Molding* en anglais) et un processus de démantèlement d'une centrale nucléaire, composé de trois ingrédients principaux : (i) un noyau de simulation capable de résoudre des problèmes mathématiques complexes représentant des modèles physiques sous contraintes en temps réel (en utilisant les méthodes MOR présentées dans la partie précédente de la thèse) ; (ii) des stratégies avancées capables de procéder à l'assimilation et au traitement des données, ainsi qu'à la modélisation pilotés par les données ; (iii) un mécanisme permettant d'adapter le modèle en ligne à des environnements en évolution (contrôle).

On propose ici un bref aperçu de chaque chapitre.

Echelle du composant mécanique

La première partie de la thèse est consacrée à l'échelle du composant mécanique. En particulier, le **Chapitre 2** traite de la surveillance non destructive de la santé structurale et présente une nouvelle technique efficace pour l'évaluation en temps réel des dommages dans les structures. Ce travail a été motivé par le fait que la détérioration et la dégradation des structures sont très préoccupantes dans le monde entier, car elles sont la principale cause des défaillances structurelles. Une attention

particulière doit alors être portée afin d'éviter la défaillance soudaine des composants structurels. Les améliorations dans les domaines des capteurs de déplacement et d'accélération à faible coût, du matériel de conditionnement et d'échantillonnage des signaux, des systèmes électroniques d'acquisition de données, ont poussé la communauté scientifique à utiliser la réponse dynamique des systèmes structurels comme outil d'évaluation des dommages et de la sécurité. Récemment, diverses techniques non destructives basées sur l'évolution des vibrations structurelles ont fait l'objet de nombreuses publications, non seulement pour détecter la présence de dommages, mais aussi pour en déterminer l'emplacement et la gravité. Les méthodes de Contrôle Non Destructifs (NDT, *Non-destructive Testing* en anglais) sont l'un des sujets les plus importants dans le domaine de la Surveillance de la Santé Structurale (SHM, *Structural Health Monitoring* en anglais). Ces méthodes doivent être capables d'identifier les dommages lorsqu'ils apparaissent et de capturer et localiser la zone endommagée.

Il existe plusieurs techniques d'identification du système pour obtenir des paramètres structurels inconnus comme le rapport d'amortissement, les fréquences propres ou la forme des modes. La base de ces méthodes est d'extraire des informations de certaines mesures sur la structure, comme, par exemple, les accélérations ou les déplacements. Une première classification divise les méthodes du domaine fréquentiel et du domaine temporel.

Les réponses dans le domaine fréquentiel peuvent être obtenues à partir de réponses de séries temporelles par des techniques d'estimation non paramétriques et de traitement du signal qui utilisent la transformée de Fourier. En ce qui concerne les méthodes d'analyse modale, elles reposent sur l'utilisation d'informations modales extraites de mesures d'entrées-sorties au moyen des méthodes d'analyse modale ou uniquement de données de sortie mesurées sous excitation ambiante (vent, charges de trafic, etc.) sans utiliser de forces artificielles.

Les méthodes dans le domaine temporel évitent les problèmes de fuite ou de proximité des fréquences naturelles. Les paramètres modaux peuvent être identifiés à partir de mesures dans le domaine temporel et les caractéristiques de vibration et les propriétés modales extraites peuvent être utilisées pour détecter l'occurrence et/ou la localisation des dommages en comparant les propriétés modales identifiées avec les valeurs initiales. Ces méthodes permettent également de détecter directement les dommages sur la base des données mesurées. Une autre approche de ce groupe fait appel à de nombreuses techniques de traitement du signal et à l'intelligence artificielle comme outils d'analyse pour étudier les signaux de vibration et en extraire des caractéristiques pour représenter les caractéristiques du signal.

Une autre classification pourrait être faite en fonction de la nature de la force d'excitation : certaines méthodes fonctionnent avec une force d'impulsion connue, d'autres avec des excitations naturelles inconnues, et un troisième groupe travaille avec une combinaison des méthodes précédentes.

L'analyse par ondelettes est également une technique attrayante largement utilisée pour le contrôle non destructif, dans laquelle une transformation ondelettes est appliquée sur les formes modales de vibration. Comme cette analyse est capable

d'identifier les changements dans les formes modales, les dommages peuvent être facilement identifiés ainsi que leur emplacement spatial.

Les techniques de réduction de modèles ont été largement utilisées afin de localiser les dommages sous contraintes en temps réel. L'apprentissage automatique permet également d'extraire la multiplicité dans laquelle vivent les solutions de problèmes d'ingénierie complexes et couplés. Ainsi, des paramètres non corrélés peuvent être efficacement extraits des données collectées à partir de simulations numériques, d'expériences ou même de données collectées à partir d'appareils de mesure adéquats. La *Proper Orthogonal Decomposition* (POD), qui est équivalente à l'Analyse en Composantes Principales (PCA, *Principal Components Analysis* en anglais), peut être considérée comme un extracteur d'information d'un ensemble de données qui tente de trouver un sous-espace linéaire de dimensionnalité inférieure à l'espace original. De plus, les transformations basées sur le PCA préservent les distances, là où d'autres stratégies de réduction de la dimensionnalité non linéaire n'y parviennent pas. Il est également habituel voir dans ce contexte des approches qui combinent les techniques d'apprentissage automatique et techniques de réduction de modèles ; de plus, les techniques d'exploration de données sont également utilisées dans le cadre du SHM.

Ce chapitre propose une nouvelle stratégie basée sur la combinaison de la réduction de modèles, qui extrait une base réduite des instantanés non endommagées, qui servira à projeter n'importe quelle solution mesurée sur celle-ci, avec des techniques d'exploration de données. Lors de la projection du champ mesuré dans cette base réduite, on s'attend à ce que les régions non endommagées soient mieux approximés que celles dans lesquels les dommages sont présents. Ainsi, des stratégies d'exploration de données peuvent être utilisées pour différencier les deux régions (non endommagées et endommagées). Enfin, afin de limiter le nombre de points de collecte des données, la méthodologie décrite ci-dessus est combinée à une stratégie de complétion de données basée sur l'utilisation de l'apprentissage par dictionnaire.

Pour calculer la réponse dynamique d'un système, le **Chapitre 3** se concentre sur des techniques numériques efficaces basées sur une représentation séparée.

La première partie du chapitre se concentre sur les problèmes dynamiques 3D définis dans les domaines de type plaque. De nombreux systèmes mécaniques et structures complexes impliquent des pièces en plaque et en coque dont la principale particularité est d'avoir une dimension caractéristique (celle liée à l'épaisseur) beaucoup plus petite que les autres (dimensions du plan). L'introduction d'hypothèses cinématiques et mécaniques appropriées permet de réduire le problème mécanique général 3D à un problème 2D impliquant les coordonnées en plan. C'était la voie utilisée pour dériver les théories des poutres, des plaques et des coques en mécanique des solides, qui ont été étendues plus tard à beaucoup d'autres domaines de la physique, comme les écoulements dans des espaces étroits, les problèmes thermiques ou électromagnétiques des stratifiés, parmi tant d'autres. Cependant, dans de nombreux cas, lorsque l'on aborde des physiques complexes couplées, la validité

des hypothèses capables de réduire les modèles de la 3D à la 2D devient douteuse et par conséquent, afin d'assurer des résultats précis, des discrétisations 3D semblent obligatoires. Cependant, ces dernières impliquent des mailles trop fines lorsqu'on considère des procédures éprouvées de discrétisation basées sur des maillages, où la taille des mailles est presque déterminée par l'épaisseur du domaine et par les détails du matériau et/ou de la solution à représenter. Afin d'alléger la complexité de calcul associée, une solution entièrement en 3D peut être calculée à l'aide d'une représentation séparée plan/hors-plan dont la complexité de calcul reste celle qui caractérise les simulations 2D en plaque ou en coque.

Dans de nombreuses analyses structurelles et simulations des processus de formage les aspects dynamiques ne peuvent pas être négligés et les modèles élastiques sont alors remplacés par leurs homologues élastodynamiques. Différentes techniques de discrétisation et procédures d'intégration temporelle peuvent être utilisées dans ce cas.

Lorsqu'on considère une analyse implicite, la solution à chaque pas de temps nécessite quelques itérations pour faire respecter l'équilibre. Au contraire, les schémas explicites ne nécessitent pas d'itération car les accélérations nodales sont résolues directement, et à partir desquelles les vitesses et les déplacements sont calculés par simple intégration. A son tour, les déplacements permettent de calculer les déformations et les contraintes. Le principal inconvénient des simulations explicites est que le pas de temps doit vérifier la condition de stabilité, qui diminue avec la taille de l'élément.

Au contraire, les intégrations élastodynamiques implicites deviennent inconditionnellement stables, c'est-à-dire qu'il n'y a pas de limite dans le pas de temps à considérer en matière de stabilité. Ainsi, les pas de temps implicites sont généralement de plusieurs ordres de grandeur plus grands que ceux considérés dans les intégrations temporelles explicites. Cependant, l'intégration implicite nécessite la solution de systèmes linéaires plusieurs fois à chaque étape de chargement lorsqu'il s'agit de modèles non linéaires. Les techniques explicites n'exigent pas cette inversion de matrice et, par conséquent, abordent facilement les non-linéarités (non-linéarités de contact ou de matériaux).

Lorsque la dynamique s'applique à des domaines dégénérés, comme les plaques ou les coques, et qu'aucune hypothèse de simplification acceptable n'est disponible pour réduire leur complexité à 2D, des solutions entièrement 3D semblent obligatoires. C'est par exemple le cas lorsque on considère l'endommagement dynamique progressif des stratifiés composites, où une description riche à travers l'épaisseur pourrait être extrêmement utile.

Les représentations séparées plan/hors-plan permettent de réduire la solution 3D à une séquence de problèmes 2D (dans le plan) et 1D (le long de l'épaisseur), comme il a été prouvé dans des travaux antérieurs par l'étude des élastostatiques dans les domaines des plaques et des coques.

Même si la mise en œuvre de schémas d'intégration implicites dans une représentation séparée 3D plan/hors-plan n'implique pas de difficultés majeures, l'utilisation d'une intégration explicite, préférable dans de nombreuses applications, par exemple

les simulations de crash, devient une question délicate. En fait, le maillage utilisé pour discrétiser la dimension hors plan (épaisseur) détermine le pas de temps limite assurant la stabilité, et par conséquent il pourrait devenir rapidement inabordable lors du raffinage de la discrétisation hors-plan.

Ainsi, dans cette première partie du chapitre, nous introduisons une nouvelle représentation hybride explicite/implicite plan/hors-plan pour les problèmes dynamiques définis dans des domaines en forme de plaques qui calculent efficacement des solutions 3D et où les contraintes de stabilité sont exclusivement déterminées par les discrétisations plus grossières dans le plan.

La deuxième partie du chapitre analyse différents schémas d'intégration de la dynamique des solides dans le domaine fréquentiel, avec la *Proper Generalized Decomposition*. Comme déjà mentionné, les équations qui régissent la dynamique des solides sont généralement formulées soit dans le domaine temporel, soit dans le domaine fréquentiel. La première est préférée pour le calcul des réponses transitoires, alors que l'approche en fréquence est un choix intéressant pour le calcul des réponses forcées.

Les descriptions temporelles sont utilisées à la fois dans les cas linéaires et non linéaires, étant particulièrement efficaces lorsqu'elles sont combinées avec l'analyse modale. Cette dernière permet d'exprimer la solution sur une série d'équations différentielles ordinaires découplées.

Les problèmes deviennent un peu plus complexes dans le cas de la dynamique paramétrée, et plus concrètement lorsque ces paramètres dépendent de la fréquence. Dans ce cas, la modélisation basée sur la fréquence semble plus appropriée que sa contrepartie temporelle, dès lors que les formes fonctionnelles exprimant la dépendance paramétrique de la fréquence sont compatibles avec l'utilisation d'une représentation séparée espace-fréquence-paramètres.

Nous revenons dans cette deuxième partie du chapitre, par souci d'exhaustivité, sur le cas de la dynamique linéaire et de l'approche hybride harmonique-modale développée dans des travaux antérieurs et on l'étend au traitement de la dynamique paramétrique non linéaire.

Cependant, la solution entièrement 3D calculée à l'aide de la représentation séparée plan/hors-plan et dont la complexité de calcul reste celle caractéristique des simulations 2D de plaques ou de coques, semble trop intrusive pour être mise en œuvre dans les logiciels commerciaux de mécanique structurelle qui proposent généralement différents éléments finis de plaques et de coques, même dans le cas des plaques ou coques composites multicouches. C'est pourquoi dans le **Chapitre 4** nous proposons des méthodes qui permettent d'intégrer des descriptions 3D dans des modèles de plaques ou de coques implémentés dans tous les logiciels, sans affecter sa complexité informatique qui reste celle liée aux analyses 2D standard.

Comme l'expérience a montré que ces descriptions enrichies ne sont souvent obligatoires que localement, dans certaines régions ou composants de structure, la première partie du chapitre est consacrée à proposer une procédure d'enrichissement capable de traiter les comportements locaux en 3D, en préservant le couplage direct

minimalement invasif avec les discrétisations existantes des plaques et coques. Pourfaire ça, deux voies d'enrichissement différentes sont envisagées, la première basée sur l'utilisation de la représentation séparée et la deuxième sur une simple condensation. La première méthodologie permet d'obtenir des descriptions très fines enrichies en 3D tandis que la dernière est particulièrement bien adaptée aux comportements inélastiques et dynamiques.

Afin de traiter les problèmes pour lesquels les descriptions enrichies sont obligatoires dans tous le domaine, la deuxième partie du chapitre propose une méthode plus générale qui permet une intégration efficace des descriptions entièrement en 3D dans les logiciels de plaques existants.

Echelle du processus mécanique

La deuxième partie de la thèse concerne l'échelle du processus mécanique. Elle commence dans le **Chapitre 5** en utilisant les concepts de réduction de modèles développés dans les chapitres précédents afin de traiter de l'évaluation de la distorsion des pièces dans les processuss de Fabrication Additive (AM, *Additive Manufacturing* en anglais). La motivation de ce travail a été donnée par le fait que l'adoption des technologies de fabrication additive au niveau industriel a posé plusieurs défis à la communauté scientifique, allant de l'étude des interactions à l'échelle de la particule à la prévision de l'état mécanique de la pièce finale.

Les processuss de fabrication additive ont été largement simulés à l'aide de la méthode des éléments finis. D'autres techniques ont également été prises en compte, telles que les méthodes lattice Boltzmann, les différences finies, les volumes finis et les modèles discrets.

Une modélisation globale des processus et la solution efficace qui lui est associée restent aujourd'hui hors de portée car de nombreux défis subsistent, concernant la physique et les échelles multiples nécessitant des modèles fins et riches, bien calibrés dans des conditions extrêmes (dans l'espace, le temps et les conditions du processus). Ces circonstances et la longueur extrêmement longue de la trajectoire du processus compromettent l'efficacité d'outils de simulation numérique bien éprouvés. Ces difficultés peuvent être regroupées en trois catégories :

- Complexité géométrique. La flexibilité des technologies de fabrication additive permet l'utilisation de l'optimisation de la topologie au stade de la conception. Il en résulte généralement des pièces minces, très sensibles aux déformations. Les géométries complexes nécessitent également des maillages plus fins et donc des modèles numériques de grande taille.

- Forte dépendance à la stratégie de fabrication. Ceci est principalement dû aux modèles non linéaires et couplés impliqués dans les transformations de phase et les comportements inélastiques.

- La nature progressive du processus. Une partie est composée de milliers de couches déposées constituées chacune d'une succession de rubans de moins de $1mm$ d'épaisseur.

Ces difficultés justifient le fait que les approches standard conduisent à des temps de simulation prohibitifs. Ainsi, les technologies de simulation bien éprouvées ne peuvent pas être utilisées pour effectuer des analyses paramétriques et explorer efficacement l'espace de conception paramétrique pour optimiser les processus ou pour effectuer des contrôles en temps réel basés sur la simulation.

Des efforts importants ont été déployés afin de proposer de nouvelles stratégies informatiques. Parmi celles-ci, les approches d'adaptabilité de maillage, qui consistent à effectuer un raffinage/grossissement, sont largement considérées comme permettant de résoudre la région dans laquelle le spot s'applique. Cependant, et malgré les progrès significatifs dans l'adaptation du maillage, le remaillage entraîne ses propres difficultés et a motivé au cours de la dernière décennie la proposition et le développement de méthodes sans mailles, qui ont résolu certains problèmes et en ont créé de nombreux autres. Dans tous les cas, le grossissement est limité par la localisation du champ ainsi que par la nécessité de décrire avec précision des géométries extrêmement complexes. Cependant, l'un des principaux obstacles à une simulation efficace des processus AM de prédiction des distorsions des pièces, indépendamment de la richesse du modèle, est lié au modèle numérique lui-même, par le fait d'assembler et de résoudre de très grands systèmes d'équations à chaque pas de temps et dans une géométrie qui évolue avec le temps. Ainsi, la réduction de modèles a été envisagée comme un remède possible pour atteindre des simulations plus rapides sans compromettre la précision.

Ce chapitre présente une modélisation paramétrique simplifiée et sa solution paramétrique ultérieure pour évaluer les distorsions paramétriques survenant dans les pièces fabriquées par fabrication additive. Les paramètres pris en compte sont ceux qui paramétrent les trajectoires du processus (qui dépendent de plusieurs paramètres de matériau et de processus), l'intensité et l'anisotropie de retrait thermique (qui dépendent directement de la trajectoire du processus) et les couches déposées (qui décrivent la progression du processus). L'outil de simulation proposé permet d'évaluer en temps réel l'impact des paramètres qui viennent de se référer sur la distorsion de la pièce, de procéder à la compensation géométrique requise et d'effectuer l'optimisation, l'analyse de sensibilité et la propagation des incertitudes.

Alors que le chapitre 5 traite d'un problème mis en place dans un contexte de simulation standard (jumeaux numériquex), où les techniques MOR sont utilisées pour accélérer le processus de simulation, le **Chapitre 6** présente un concept complètement nouveau : le concept de jumeaux hybrides. La modélisation pilotée par les données est utilisée pour combler l'écart entre la solution déterministe paramétrique calculée en utilisant le constructeur PGD non intrusif (et dont les paramètres sont déterminés par assimilation des données) et les champs mesurés. Dès que le modèle piloté par les données permet de faire des prédictions précises, les stratégies de contrôle peuvent être appliquées en toute sécurité.

Ce concept est d'abord appliqué aux pièces composites fabriquées à partir du processus RTM. Le RTM est une famille de processuss connexes dans la fabrication de composites, dans laquelle des fibres continues, utilisées comme renfort (milieu

poreux), sont d'abord placées dans la partie inférieure d'un moule et ensuite une matrice polymère est injectée sous forme de résine liquide dans la cavité. Après durcissement, la pièce est démoulée. L'imprégnation de la préforme avec la résine est régie par la loi de Darcy, mais le tenseur de perméabilité est généralement difficile à déterminer. Ensuite, pendant le processus de formage, le jumeau hybride est utilisé pour assurer une prédiction numérique correcte à des fins de contrôle et pour introduire les informations précises du processus de formage dans la prédiction du cycle de vie de la pièce afin de permettre la maintenance prédictive.

Ensuite, nous appliquons le jumeau hybride à un processus de démantèlement d'une centrale nucléaire. Le jumeau hybride est utilisé pour aider l'opérateur à se déplacer dans une salle avec différentes sources d'émission (points de travail) situées à différents endroits pour choisir la trajectoire la plus sûre grâce aux capteurs dont il est équipé.

Enfin, le chapitre de conclusion résume les principales contributions de la thèse et discute de certaines possibilités de développements futurs.

Contents

Chapter 1

Introduction

1.1 Motivations and objectives of the thesis

Since the previous (third) industrial revolution numerical simulation has been widely used in many scientific and engineering fields and is now one of the mayor players in the technological world. In fact it allows to virtually study the behaviors and the responses of systems (i) without the need to analytically solve the (usually complex) mathematical models associated to the systems, (ii) reducing the number of (usually expensive and long) experiments performed on the system to get accurate designs. During the 20th century many methods have been developed to carry out numerical simulations able to emulate a physical system by solving the mathematical models describing its complex behavior (finite differences, finite elements, finite volumes, spectral methods, meshless technique, ...) defining the so called *virtual twins*, which together with modeling and experiments (for model calibration and validation purposes) played a major role in engineering [Hey *et al.* 2009].

However the virtual twins have a main drawback. Prior to solve a given problem, the user must introduce the different involved parameters (e.g. material parameters and applied loads) and define the domain in which the problem is posed. As soon as the problem is solved (by using more and more powerful computers and fast, robust and accurate algorithms) different quantities of interest can be then calculated. That means that the virtual twins are static: they are used in the design of complex systems and their components, but they can not accommodate or assimilate data in order to define Dynamic Data-Driven Application Systems (DDAS) [Darema 2015]. Due to the characteristic time of standard simulation strategies they rarely allows real-time feedback required in some applications (e.g. haptic feedback in surgical simulation or simulation-based control involved in robotics, internet of things or autonomous robots), even when considering high performance computing, operating on powerful platforms. Moreover, optimization and inverse analyses involved in calibration procedures require respectively many direct calculations to find the optimal or the searched parameters. Finally, uncertainty quantification and propagation also require enhancing the efficiency of usual strategies.

Real-time control could be gotten by means of techniques based on the use of adapted representations of the system, relating some inputs to some outputs through a transfer function. Even if these methods ensure real-time, their representation of the system is too coarse compared to rich representations of systems,

as the ones performed using for example finite elements (3D transient in the most of cases), which allow for high fidelity simulations. However, as previously said, these too rich representations, excellent from the point of view of the system understanding and fine-scale controllability, do not allow proceeding in real-time in usual computational platforms or deployed systems.

Even if the use of more powerful computers could overcome these issues, in fact it would bring other two problems. First it would not allow small and medium industries to access to the appropriate simulation resources (required for ensuring innovation) and second it would not be easily integrated in deployed systems. This need of real-time and, at the same time, accessible simulation tools brought to the birth, at the beginning of the 21st century, of new solutions in what concerned modeling and simulation procedures. It's here when Model Order Reduction (MOR) techniques opened new possibilities for more efficient simulations. A possible alternative within the MOR framework consists in extracting "offline" the most significant modes involved in the model solution, that will constitute the so-called reduced approximation basis, and then project the solution of "quite similar" problems in that reduced basis. As the number of functions involved in the reduced basis is quite low, only a few coefficients must be calculated for determining the problem solution and a discrete problem of very small size must be solved at each iteration or time step. Thus, MOR-based discretization techniques allow important computing-time savings, of several orders of magnitude in some cases, making possible accommodating to real-time constraints [Chinesta *et al.* 2015, Chinesta & Ladeveze 2014]. Another possibility consists of calculating offline using all the needed computational resources, e.g. High Performance Computing (HPC), and computing time, a parametric solution containing the solution of all possible scenarios. This parametric solution is then particularized online using light computational facilities, as deployed devices, tablets or smartphones for performing in real-time efficient simulation, optimization, inverse analysis, uncertainty propagation and simulation-based control. This was the philosophy adopted by the so-called Proper Generalized Decomposition (PGD) which was used in many applications in order to compute parametric solutions of models representing complex processes, structures and systems [Bur *et al.* 2016, Chinesta *et al.* 2011, Chinesta *et al.* 2013b, Chinesta *et al.* 2014a, Chinesta *et al.* 2014b, Chinesta *et al.* 2015]. Thus, few hours of intensive offline computation allow the construction of very general parametric solutions able to ensure almost instantaneous responses to queries, while keeping the level of accuracy of usual discretizations. Moreover model order reduction techniques also allow to assimilate data collected from sensors into the physically-models. Collected data which can be analyzed, classified and visualized thanks to many techniques developed, starting from the end of the 20th century, in the areas of artificial intelligence and machine learning as linear and nonlinear dimensionality reduction techniques based on manifold learning [Lee & Verleysen 2007, Kambhatla & Leen 1997, Schölkopf *et al.* 1998,

Schölkopf *et al.* 1999, Zhang & Zha 2003, T. Roweis & K. Saul 2000] and model learners based on the use of linear and nonlinear regressions, decision tress, random forests, neural networks and deep-learning techniques [Parsa *et al.* 2018, Ibáñez Pinillo *et al.* 2018, Criminisi *et al.* 2011, Criminisi *et al.* 2012, Goodfellow *et al.* 2016, Raissi *et al.* 2017a, Raissi *et al.* 2017b, Moitra 2018, Anandkumar *et al.* 2014]. The integration of MOR techniques with artificial intelligence gave arise to the so-called *digital twins* with the main aim of identifying parameters involved in the model as well as their time evolution in real time, anticipating actions from their predictive capabilities. By using digital twins simulation-based control was envisaged and successfully accomplished in many applications, in many cases using deployed computing devices [Alfaro *et al.* 2014].

Because of the great importance that digital twins based on MOR have on the technological world, the main part of this thesis concerns the development of new techniques that can be used to improve these digital twins. In particular this thesis concerns the use of model order reduction and data-driven techniques in order to develop new simulation tools for real-time monitoring and control at two different scales:

1. Scale of the *mechanical component*: we propose methods to efficiently evaluate the dynamical response of metal and composite plates in both linear and nonlinear case, with a focus in particular on its dependence on parameters and on non-intrusive methods. The interest in the study of the dynamical response is given by the importance that it has in the identification of the existence of damage and of its location in the mechanical component, i.e. in the structural health monitoring techniques for which a method is presented in this work too.

2.1. Scale of the *mechanical process*: we developed processes simulation tools allowing real time calculation (and re-calculation) of the predictions, optimization, parameters identification, control and inverse analysis during the process and we apply them to an additive manufacturing process.

However, even if by using digital twins high-fidelity models can be examined at all their scales in almost real-time by using reasonable computing platforms (as soon as the offline efforts is accomplished), when these computing facilities are integrated into data-driven applications systems unexpected difficulties appear immediately. In practice significant deviations between the predicted and observed responses are noticed, limiting their use in many applications. These deviations can be due to: (i) inaccuracies in the employed models that sometimes are not accurate enough descriptions of the real systems; (ii) an *a priori* almost unpredictable time evolution of certain models and (iii) inaccuracies in the determination of the model parameters or in their time-evolution, that can present space and time stochastic fluctuations. A certain part of the deviation (its unbiased component in a statistical sense) can be viewed as a noise, but the remaining biased part proves the existence

of an hidden model that operates but escapes to our understanding. In order to address this problem and efficiently attained system control, one possibility consists in constructing "on-the-fly" a data-driven model able to fill the gap between model prediction and measurement. In fact, as soon as the data-driven model allows making accurate predictions, control strategies can be safely applied. An important alternative alleviating the construction of such data-driven corrections, but which is not developed in this thesis work, consists of extracting knowledge from the phenomenological data-driven models by using again machine-learning strategies (decision trees and its variants and improvements). Moreover in order to improve the dialogue between predictions (model and data-driven) and users, augmented reality could also be employed.

Thus the last party of the thesis is devoted to the development of a new concept: the *Hybrid Twin* (HT) concept. The hybrid twins combine HPC-based parametric model solutions with "on-the- fly" data-driven constructed deviation-model, making DDDAS possible [Chinesta *et al.* 2018]. In particular we apply the HT concept to the

2.2. Scale of the *mechanical process*: we developed DDDAS for two different processes, a Resin Transfer Molding (RTM) process and a dismantling process of a nuclear central, consisting of three main ingredients: (i) a simulation core able to solve complex mathematical problems, representing physical models, under real-time constraints (by using the MOR methods presented in the previous part of the thesis); (ii) advanced strategies able to proceed with data-assimilation, data-curation and data-driven modeling; and (iii) a mechanism to adapt the model online to evolving environments (control).

1.2 Contributions and structure of the thesis

This thesis is actually a compilation of results published (or submitted for publication) in articles and conference proceedings of scientific journals. Chapters 2, 3 and 4 address the scale of the mechanical component, while chapters 5 and 6 address the scale of the mechanical process. In particular chapter 6 develops the new concept of the Hybrid Twin.

1.2.1 Scale of the mechanical component

The first part of the thesis is devoted to the scale of the mechanical component. In particular the thesis begins in **Chapter 2** dealing with non-destructive structural health monitoring and presenting a new efficient technique for real-time evaluation of damage in structures. The motivation for this work came up from the fact that structural deterioration and degradation are of great concern worldwide, being damage the main cause of structural failure. A special attention must then be paid in

order to avoid the sudden failure of structural components. The improvements in the fields of low-cost displacement and acceleration transducers, signal conditioning and sampling hardware, electronic data acquisition systems, pushed the interest of the scientific community in the use of the dynamic response of structural systems as a tool to evaluate damage and safety. Recently, various non-destructive techniques based on changes in the structural vibrations patterns have been extensively published not only to detect the presence of damage but also to identify the location and the severity of it. Non-destructive Testing (NDT) methods are one of the most important topics in the Structural Health Monitoring (SHM) field. These methods have to be able to identify damage when it appears and capture and locate the damaged area.

Several system identification techniques exist to obtain unknown structural parameters as damping ratio, natural frequencies or mode shapes [Ljung 1999, Peeters & De Roeck 2001]. The basis of these methods is to extract information from some measurements on the structure, as, for example, accelerations or displacements. A first classification divides the methods in frequency domain and time domain methods.

Frequency domain techniques have the advantage of modal analysis methods, where the analysis can be done in some range of frequencies of interest or with some structural modes. In [Maia *et al.* 1997, Liu *et al.* 2009, Mohan *et al.* 2013, Canales *et al.* 2009, Brincker *et al.* 2001] frequency domain responses are obtained from time series responses by non-parametric estimation and signal processing techniques which make use of the Fourier transform. Concerning modal analysis methods [Cawley & Adams 1979, West 1986, Salehi *et al.* 2010, Pandey *et al.* 1991, Yam *et al.* 1996, Zhang & Aktan 1995, Xu *et al.* 2015] they are based on the use of modal information extracted from input-output measurements by means of the modal analysis methods or from only output data measured under the ambient excitation (wind, traffic loads, etc.) without making use of artificial forces.

Time domain methods avoid problems as leakage or closeness to natural frequencies. In [Ibrahim & Mikulcik 1977, Vandiver *et al.* 1982, Ibrahim 1986, Juang & Pappa 1985, Cattarius & Inman 1997, Peeters & De Roeck 2001, Ruocci *et al.* 2011] authors identified modal parameters from time domain measurements and used the extracted vibration features and modal properties for detecting damage occurrence and/or location by comparing the identified modal properties with the original values. It is also possible with these methods [Park *et al.* 2008, Todorovska & Trifunac 2010, Todorovska & Rahmani 2013] to directly detect damage based on the measured data. Another approach in this group [Lu & Hsu 2002, Law *et al.* 2005, Xu & Chen 2004] makes use of many signal processing techniques and artificial intelligence as analysis tools to investigate the vibration signals and extract features to represent the signal characteristics.

Another classification could be done depending on the nature of the excitation force: some methods work with a known impulse force [Ibrahim & Mikulcik 1976], others work with unknown natural excitations [James *et al.* 1992], and a third group works with a combination of the previous ones [Reynders *et al.* 2010].

Wavelet analysis is also an appealing technique widely used for the non-destructive testing, in which a wavelet transform is applied on modal shapes of vibration. Since this analysis is capable to identify changes in the modal shapes, damage can be easily identified as well as its spatial location. There is a vast literature on the extensive use of wavelets [Huang *et al.* 2009, Rucka & Wilde 2006, Chang & Chen 2004, Wang & Deng 1999, Huang *et al.* 2009, Loutridis *et al.* 2004, Loutridis *et al.* 2005, Fan & Qiao 2009, Kim & Melhem 2004].

Reduced order modeling techniques have been widely used in order to locate damage under real-time constraints. In [Capellari *et al.* 2015] authors applied the Proper Orthogonal Decomposition (POD) to track the structural behavior followed by an improved particle filtering strategy (extended Kalman updating). Machine learning is also helping for extracting the manifold in which the solutions of complex and coupled engineering problems are living. Thus, uncorrelated parameters can be efficiently extracted from the collected data coming from numerical simulations, experiments or even from the data collected from adequate measurement devices. The Proper Orthogonal Decomposition (POD), that is equivalent to Principal Components Analysis (PCA), can be viewed as an information extractor from a data set that attempts to find a linear subspace of lower dimensionality than the original space. Moreover, PCA-based transformations preserve distances, where other non-linear dimensionality reduction strategies fail to accomplish it. In [Vitola *et al.* 2016] authors proposed a data-driven methodology for the detection and classification of damages by using multivariate data-driven approaches and PCA. Support Vector Machine (SVM) was used for damage detection in [Gui *et al.* 2017].

It is also usual in this context approaches that combine machine learning techniques and reduced order modeling, like in [Taddei *et al.* 2016] where authors used machine-learning algorithms to generate a classifier that monitors the damage state of the system and a Reduced Basis method to reduce the computational burden associated with model evaluations. Proper Orthogonal Decomposition approximations and Self-Organizing Maps (SOM) are combined to realize a fast mapping from measured quantities in order to propose a data-driven strategy to assist online rapid decision-making for an unmanned aerial vehicle that uses sensed data to estimate its structural state [Mainini & Willcox 2015].

Data mining techniques are also used in the context of the SHM. In [Muthuraman *et al.* 2016] authors propose an approach for damage identification and optimal sensor placement in Structural Health Monitoring by using a Genetic Algorithm technique (GA) whereas in [Gordan *et al.* 2017] authors combined data mining (GA), machine learning (PCA) and deep learning (neural networks) techniques in the damage identification context. Concerning deep learning techniques, it is interesting the work developed in [Selva *et al.* 2013] in which a smart monitoring of aeronautical composites plates based on electromechanical impedance measurements and artificial neural networks is presented. At its turn [Lin 2012] proposes the same technique in the monitoring of a frame structure model for damage identification.

This chapter proposes a new strategy based on the combination of model order

reduction, that extracts a reduced basis from undamaged snapshots, that will serve for projecting any measured solution on it, with data-mining techniques. When projecting into this reduced basis the measured field, undamaged regions are expected being better approximated than the ones in which damage occurs. Thus, data-mining strategies can be then used to differentiate both regions (undamaged and damaged). Finally, in order to limit the number of points at which data is collected, the just described methodology is combined with a data-completion strategy based on the use of dictionary learning.

In order to compute the dynamical response of a system, **Chapter 3** focuses on efficient numerical techniques based on separated representation.

The first part of the chapter focuses on 3D dynamical problems defined in plate-like domains. Many mechanical systems and complex structures involve plate and shell parts whose main particularity is having a characteristic dimension (the one related to the thickness) much lower than the other ones (in-plane dimensions). The introduction of appropriate kinematic and mechanic hypotheses allow the reduction of the general 3D mechanical problem to a 2D involving the in-plane coordinates. This was the route employed for deriving beam, plate and shell theories in solid mechanics [Oñate 2010, Ahmad *et al.* 1970], that were extended later to many other physics, like flows in narrow gaps, thermal or electromagnetic problems in laminates, among many others. However, in many cases, when addressing complex coupled physics the validity of hypotheses able to reduce models from 3D to 2D becomes doubtful and consequently, in order to ensure accurate results, 3D discretizations seem compulsory. However the last imply too fine meshes when considering well-experienced mesh-based discretization procedures, where the mesh size is almost determined by the domain thickness and the material and/or solution details to be represented. In order to alleviate the associate computational complexity in [Bognet *et al.* 2012, Bognet *et al.* 2014] authors proposed computing the fully 3D solution employing an in-plane-out-of-plane separated representation whose computational complexity remains the one characteristic of 2D plate or shell simulations.

In many structural analysis and simulations of forming processes dynamical aspects cannot be neglected and then elastic models are replaced by their elastodynamics counterparts. It exists a vast literature on structural dynamics, covering different discretization techniques and time integration procedures [Sun *et al.* 2000, Gravouil & Combescure 2001, Prior 1994, Taylor *et al.* 1995, Pinho *et al.* 2006].

When considering an implicit analysis, solution at each time step needs some iterations to enforce equilibrium. On the contrary explicit schemes do not require iteration as the nodal accelerations are solved directly, and from which velocities and displacements are calculated by simple integration. At its turn displacements allow the calculation of strains and stresses. The main handicap of explicit simulations is that the time step must verify the stability condition, decreasing with the element size.

On the contrary implicit elastodynamics integrations become unconditionally stable, that is, there is not a limit in the time step to be considered in what con-

cerns stability. Thus, implicit time steps are generally several orders of magnitude larger than the ones considered in explicit time integrations. However, implicit integration requires the solution of linear systems several times at each loading step when addressing nonlinear models. Explicit techniques do not require that matrix inversion and consequently address nonlinearities (contact or material nonlinearities) easily. In [Hughes & Liu 1978] a hybrid schema was proposed that considers the domain composed of two parts in which explicit and implicit time integrations apply.

When dynamics applies on degenerated domains, like plates or shells, and no acceptable simplifying hypotheses are available for reducing their complexity to 2D, fully 3D solutions seem compulsory. This is for example the case when considering the progressive dynamic damage of composite laminates, where a rich through-the-thickness description could be extremely valuable, among many other scenarios in which a fully 3D formulation is retained.

In plane-out-of-plane separated representations allow reducing the 3D solution to a sequence of 2D (in-plane) and 1D (along the thickness) problems, as proved when considering elastostatics in plate and shell domains [Bognet *et al.* 2012, Bognet *et al.* 2014].

Even if the implementation of implicit integration schemes into a 3D in-plane-out-of-plane separated representation does not imply major difficulties, the use of explicit integration, preferable in many applications, e.g. crash simulations, becomes a tricky issue. In fact the mesh employed for discretizing the out-of-plane dimension (thickness) determines the limit time-step ensuring stability, and consequently it could become quickly unaffordable when refining the out-of-plane discretization.

Thus, in this first part of the chapter, we introduce a new hybrid explicit/implicit in-plane-out-of-plane separated representation for dynamic problems defined in plate-like domains that computes efficiently 3D solutions and where the stability constraints are exclusively determined by the coarser in-plane discretizations.

The second part of the chapter analyses different integration schemes of solid dynamics in the frequency domain involving the Proper Generalized Decomposition. As previously said, governing equations in solid dynamics are usually formulated either in the time or in the frequency domains. The former is preferred when calculating transient responses, whereas the frequency approach is an appealing choice for calculating forced responses. Both approaches have been extensively used and described in many classical books as, for instance [Warburton 1995].

Time descriptions are used in both the linear and the nonlinear cases, being specially efficient when combined with modal analysis. The last allows expressing the solution on a series of decoupled ordinary differential equations. Other works considered advanced space-time separated representations [Ladeveze 1989, Ladeveze 1999, Ladevèze & Chamoin 2011], for addressing transient dynamics [Barbarulo *et al.* 2015, Boucinha *et al.* 2014, Gregori *et al.* 2017]. Medium frequencies were efficiently attained within the Variational Theory of Complex Rays –VTCR– proposed by P. Ladeveze and intensively and successfully used (the interested reader can refer to [Barbarulo *et al.* 2015] and the numerous refer-

ences therein). Recently, a PGD-based dynamical integrator that takes as parameter the field of initial conditions—conveniently expressed in a reduced basis—has also been developed [González *et al.* 2014, Cueto *et al.* 2016].

As discussed in [Crandall 1970, Germoso *et al.* 2016, Malik *et al.* 2018a], problems become a bit more complex in the case of parameterized dynamics, and more concretely when those parameters depend on frequency. In this case, frequency-based modeling seems more appropriate than its time counterpart, as soon as the functional forms expressing the parametric dependence on frequency are compatible with the use of a space-frequency-parameters separated representation [Chinesta *et al.* 2013b, Chinesta *et al.* 2014a, Aguado *et al.* 2014].

We revisit in this second part of the chapter, for a sake of completeness, the case of linear dynamics and the harmonic-modal hybrid approach developed in [Malik *et al.* 2018b] and we extend it for treating nonlinear parametric dynamics.

However, the fully 3D solution computed employing the in-plane-out-of-plane separated representation and whose computational complexity remains the one characteristic of 2D plate or shell simulations presented in [Bognet *et al.* 2012, Bognet *et al.* 2014] and extended in Chapter 3, appears to be too intrusive to be implemented in structural mechanics commercial software that generally propose different plate and shell finite elements, even in the case of multilayered composites plates or shells. For this reason in **Chapter 4** we propose methods which allows integrating 3D descriptions in plate or shell models implemented in any software, without affecting its computational complexity, that remains the one related to standard 2D analyses.

As experience indicated that many times such enriched descriptions are only compulsory locally, in some regions or structure components, the first part of the chapter is devoted to propose an enrichment procedure able to address 3D local behaviors, preserving the direct minimally-invasive coupling with existing plate and shell discretizations. For that purpose, two different enrichment routes are considered, the first based on the use of the separated representation and the second on a simple condensation. The former methodology allows for very fine 3D enriched descriptions while the last is particularly well adapted to address inelastic and dynamical behaviors.

In order to deal with problems in which enriched descriptions are compulsory in all the domain, the second part of the chapter proposes a more general method which allows efficient integration of fully 3D descriptions into existing plate software.

1.2.2 Scale of the mechanical process

The second part of the thesis concerns the scale of the mechanical process. It begins in **Chapter 5** by using the model order reduction concepts developed in the previous chapters in order to deal with the evaluation of part distortion in additive manufacturing processes. The motivation for this work was given by the fact that adoption of Additive Manufacturing (AM) technologies at the industrial level has

set out several challenges for the scientific community, ranging from the study of the interactions at the scale of the particle to the prediction of the mechanical state of the final part [Khairallah *et al.* 2016, Chiumenti *et al.* 2017].

Additive manufacturing processes have been extensively simulated by using the Finite Element Method (FEM). In [Labudovic *et al.* 2003] a model for direct laser metal powder deposition process and rapid prototyping was developed and simulated. In [Kolossov *et al.* 2004] and [Dong *et al.* 2009] 3D FEM simulations of a thermal model of selective laser sintering were performed for evaluating the temperature evolution. In [Zekovic *et al.* 2005] a thermo-structural finite element analysis of direct laser metal deposited was proposed for evaluating residual stresses in thin-walled structures. In [Chiumenti *et al.* 2010] the FEM was considered for simulating shaped metal deposition processes. In [Marimuthu *et al.* 2013] a finite element analysis was carried out to compute the temperature induced in aero-engine component by the direct laser deposition process and the corresponding distortion and in [Li & Gu 2014] and [Loh *et al.* 2015] the effects of laser power and scan speed on the thermal behavior were investigated. FEM was also used in many other works, as for example in [Heigel *et al.* 2015] to develop a thermo-mechanical model of additive manufacturing of Ti-6Al-4V.

Other techniques have also been considered as for instance lattice Boltzmann [Körner *et al.* 2011] [Körner *et al.* 2013], finite differences [Foteinopoulos *et al.* 2018], finite volumes [Chen & Zhang 2004] [Dai & Gu 2014] or discrete models [Kovaleva *et al.* 2014] for the processes involving selective laser melting of powders.

A global process modeling and its associated efficient solution remain nowadays out of reach because many challenges persist, concerning the multiple physics and scales requiring fine and rich models, well calibrated in extreme conditions (in space, time and process conditions). These circumstances and the extremely long process trajectory length compromise the efficiency of well experienced numerical simulations tools. These difficulties can be grouped in three categories:

- Geometric complexity. The flexibility of AM technologies allows for the use of topology optimization in the design stage. This results typically in thin parts, very sensitive to distortions. Complex geometries also require finer meshes and hence, large size numerical models.

- Strong dependence on the fabrication strategy. This is mainly due to the non-linear and coupled models involved in phase transformations and inelastic behaviors.

- The incremental nature of the process. A part is composed of thousands of deposited layers each of them constituted of a succession of tapes less than 1mm thick.

These difficulties justify the fact that standard approaches (e.g. finite elements combined with the so-called born-dead-elements technique [Ding *et al.* 2011]) lead to

prohibitive simulation times. Thus, well experienced simulation technologies cannot be used for performing parametric analysis and efficiently exploring the parametric design space for optimizing processes or for performing simulation-based real-time control.

Important efforts are being deployed in order to propose new computational strategies. Among them, mesh adaptivity approaches [Zeng *et al.* 2013], performing refining/coarsening, are widely considered to resolve the region in which the spot applies. However, and despite the significant progresses in mesh adaptation, remeshing entails its own difficulties and motivated in the last decade the proposal and development of meshless methods, that solved some issues and created many others. In any case, coarsening is limited by field localization as well as by the necessity to accurately describe extremely complex geometries. However, one of the main obstacles to an efficient simulation of AM processes for predicting part distortions, independently of the model richness, is related to the numerical model itself, by the fact of assembling and solving very large systems of equations at each time step and in a geometry that is evolving in time. Thus, reduced order modeling [Chinesta & Ladeveze 2014, Chinesta *et al.* 2015] was envisaged as a possible remedy for attaining faster simulations without compromising the accuracy. Simplified models were proposed by observing that in many cases two regions can be differentiated [Aguado *et al.* 2017a]. The first, near the spot and involving the most recent deposited layers involves rich nonlinear behaviors, however outside, plastic deformation becomes frozen and does not evolve anymore. These regions were called respectively process and structure regions. This partition makes possible the use of static condensation, such that all the degrees of freedom in the structure region are condensed on the interface between both regions. However, such a condensation requires, even in the linear case, the inversion of a sub-matrix (the one related to the structure region) whose size is increasing with the number of deposited layers, and consequently with the growing of the structure region. In [Aguado *et al.* 2017a] authors proposed solving the process by assuming in the structure region a linear elastic behavior with the residual stresses installed when each point now in the structure region was located in the process zone (during its deposition). Thus, after evaluating the residual stress everywhere in the part at the end of the process, a final calculation is performed in the finite transformation framework (assuming that larger deformations / displacements do not alter the installed residual stresses). However, such a calculation allows only evaluating the part distortion but not the distortion evolution during the process.

This chapter presents a simplified parametric modeling and its subsequent parametric solution for evaluating parametrically distortions occurring in parts manufactured by additive manufacturing. The parameters taken into consideration are the ones parametrizing the process trajectories (which depend on several material and process parameters), the thermal shrinkage intensity and anisotropy (which directly depend on the process trajectory) and the deposited layers (which describe the process progression). The proposed simulation tool allows evaluating in real-time the impact of the parameters just referred to the part distortion,

to proceed to the required geometry compensation and to perform optimization, sensitivity analysis and uncertainty propagation.

While chapter 5 deals with a problem set up in a standard simulation context (digital twin), where MOR techniques are used to speed up the simulation process, as previously anticipated, **Chapter 6** presents a completely new concept: the hybrid twin concept. Data-driven modeling are employed to fill the gap between the parametric deterministic solution computed by using the non-intrusive PGD constructor (and whose parameters are determined by assimilating data) and the measured fields. The data-driven model allows making accurate predictions and control strategies can thus be applied.

This concept is first applied to composite parts manufactured from RTM process. RTM is a family of related processes in composite manufacturing, in which continuous fibers, used as reinforcement (porous medium), are first placed in the bottom part of a mold and then a polymer matrix is injected as liquid resin into the cavity. After curing, the part is demolded [Kendall *et al.* 1992]. The resin impregnation of the preform is governed by the Darcy's law [Darcy 1856], but the permeability tensor is usually difficult to determine. Then during the forming process, the hybrid twin is used to insure correct numerical prediction for control purpose and for introducing the accurate forming process information in the part life cycle prediction in order to allow the predictive maintenance.

Then we apply the hybrid twin to a dismantling process of a nuclear central [Laraia 2012]. The hybrid twin is used in order to help an operator moving in a room with different sources of emission (working points) located in different places to choose the safest trajectory thanks to the sensors he is doted with.

Finally, the conclusion chapter summarizes the main contributions of the thesis and discusses some possibilities for future development.

1.3 List of publications

These thesis works have generated the following publications:

- G. Quaranta, B. Bognet, R. Ibañez, A. Tramecon, E. Haug, F. Chinesta, *A new hybrid explicit/implicit in-plane-out-of-plane separated representation for the solution of dynamic problems defined in plate-like domains*, Computers and Structures, **210**, 135-144, 2018.

- G. Quaranta, E. Lopez, E. Abisset-Chavanne, J.L. Duval, A. Huerta, F. Chinesta, *Structural health monitoring by combining machine learning and dimensionality reduction techniques*, RIMNI, **35**:1, 2019.

- G. Quaranta, E. Haug, J.L. Duval, F. Chinesta, *Parametric evaluation of part distortion in additive manufacturing processes*, International Journal of Material Forming, **12**:1, 2019.

- G. Quaranta, M. Ziane, F. Daim, E. Abisset-Chavanne, J.L. Duval, F. Chinesta, *On the coupling of local 3D solutions and global 2D shell theory in structural mechanics*, Advanced Modeling and Simulation in Engineering Sciences, **6**:1, 2019.
- G. Quaranta, C. Argerich Martin, R. Ibañez, J.L. Duval, E. Cueto, F. Chinesta, *From linear to nonlinear parametric structural dynamics*, Comptes rendus Mecanique, **347**:5, 2019.
- G. Quaranta, M. Ziane, E. Haug, J.L. Duval, F. Chinesta, *A minimally-intrusive fully 3D separated plate formulation in computational structural mechanics*, Advanced Modeling and Simulation in Engineering Sciences, (submitted).

They also generated the following conference proceedings papers:

- G. Quaranta, E. Abisset-Chavanne, F. Chinesta, J.L. Duval, *A cyber physical system approach for composite part: From smart manufacturing to predictive maintenance*, ESAFORM2018 Conference, AIP Conference Proceedings, **1960**(1), 020025, 2018.
- G. Quaranta, E. Haug, J.L. Duval, E. Cueto, F. Chinesta, *Parametric Numerical Solutions of Additive Manufacturing Processes*, ESAFORM2019 Conference, AIP Conference Proceedings, 2019 (in press).

Chapter 2

Structural health monitoring by combining machine learning and dimensionality reduction techniques

Contents

Introduction Structural Health Monitoring of mechanical components is of major interest in many areas of structural mechanics. This chapter presents a new approach based on the combination of dimensionality reduction and data-mining techniques able to differentiate damaged and undamaged regions in a given structure. Indeed, existence, severity (size) and location of damage can be efficiently estimated from collected data at some locations from which the fields of interest are completed before the analysis, based on machine learning and dimensionality reduction techniques, proceeds.

The first section of the chapter addresses the data generator based on the solution of an elastodynamic model in a plate. Then, next section applies different techniques on the generated data in order to clusterize damaged and undamaged zones. Finally the same procedure is repeated but on the completed data obtained from data sparsely collected.

This chapter and all the results presented in it correspond to the following paper:

- G. Quaranta, E. Lopez, E. Abisset-Chavanne, J.L. Duval, A. Huerta, F. Chinesta, *Structural health monitoring by combining machine learning and dimensionality reduction techniques*, RIMNI, **35**:1, 2018.

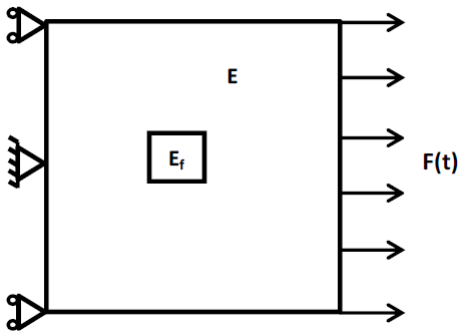

Figure 2.1 – *The 2D model.*

2.1 Elastodynamic model

The problem taken into consideration is depicted in Fig. 2.1 and it's defined in a rectangular domain $\Omega = [0, L_x] \times [0, L_y]$ where an area is damaged. A linear elastic behavior is assumed in the undamaged area, so that the relation between the stress $\boldsymbol{\sigma}$ and the strain $\boldsymbol{\varepsilon}$ reads

$$\boldsymbol{\sigma} = \mathbb{C}\,\boldsymbol{\varepsilon}, \tag{2.1}$$

where $\mathbb{C}$ is the Hooke's fourth order tensor. The relation between strain $\boldsymbol{\varepsilon}$ and displacement $\mathbf{u}$ writes

$$\boldsymbol{\varepsilon} = \nabla_s \mathbf{u}, \tag{2.2}$$

where $\nabla_s \bullet = \frac{1}{2}(\nabla \bullet + \nabla^T \bullet)$ is the symmetric gradient operator.

On the right boundary of the domain an horizontal traction is enforced, $F(t) = A\sin(\omega t)$. Considering an isotropic material, plane stress conditions and using the Voigt notation, the Hooke's tensor can be written as

$$\mathbf{C} = \frac{E}{1-\nu^2}\begin{bmatrix} 1 & \nu & 0 \\ \nu & 1 & 0 \\ 0 & 0 & (1-\nu)/2 \end{bmatrix} \tag{2.3}$$

and the relation (2.1) as

$$\begin{bmatrix} \sigma_{xx} \\ \sigma_{yy} \\ \sigma_{xy} \end{bmatrix} = \frac{E}{1-\nu^2}\begin{bmatrix} 1 & \nu & 0 \\ \nu & 1 & 0 \\ 0 & 0 & (1-\nu)/2 \end{bmatrix}\begin{bmatrix} \varepsilon_{xx} \\ \varepsilon_{yy} \\ \gamma_{xy} \end{bmatrix}. \tag{2.4}$$

The material is assumed homogeneous and isotropic everywhere, with degraded mechanical properties in the damaged region, with the Young modulus reduced by one order of magnitude, i.e. $E_f = E/10$. Moreover a nonlinear behavior is prescribed in the damaged area. The particular choice of this nonlinear dependency is irrelevant, the important point being the fact that nonlinearities generate frequen-

cies different to the one(s) involved in the loading of major relevance for identifying damage. For this reason in the sequel we consider the simplest nonlinear behavior in the damaged zones

$$\boldsymbol{\sigma} = \mathbf{C}(\boldsymbol{\varepsilon})\,\boldsymbol{\varepsilon}. \tag{2.5}$$

The displacement field evolution $\mathbf{u}(\mathbf{x}, t)$ for $\mathbf{x} \in \Omega$ and $t \in I = [0, T]$ is described by the linear momentum balance equation

$$\rho\ddot{\mathbf{u}}(\mathbf{x}, t) = \nabla \cdot \boldsymbol{\sigma}, \tag{2.6}$$

where ρ is the density.

The boundary $\partial\Omega$ is partitioned into Dirichlet, Γ_D, and Neumann, Γ_N, boundaries, where displacement and tractions are enforced respectively, as sketched in Fig. 2.1. Without loss of generality homogeneous initial conditions $\mathbf{u}(\mathbf{x}, t = 0) = 0$ and $\dot{\mathbf{u}}(\mathbf{x}, t = 0) = 0$ are assumed.

The problem weak form associated with the strong form (2.6) lies in looking for the displacement field $\mathbf{u}$ verifying the initial and Dirichlet boundary conditions such that the weak form

$$\rho \int_\Omega \ddot{\mathbf{u}} \cdot \mathbf{v}\, d\mathbf{x} + \int_\Omega \boldsymbol{\varepsilon}(\mathbf{v}) \cdot (\mathbf{C}(\boldsymbol{\varepsilon})\,\boldsymbol{\varepsilon}(\mathbf{u}))\, d\mathbf{x} = \int_{\Gamma_N} \mathbf{F}(t) \cdot \mathbf{v}\, d\mathbf{x} \tag{2.7}$$

applies for any test function $\mathbf{v}$, with the trial and test fields defined in appropriate functional spaces.

For discretizing the weak form, we introduce a standard explicit time-marching method in the time interval defined by T and a time step Δt, with $t_{k+1} = (k+1)\Delta t$

$$\rho \int_\Omega \frac{\mathbf{u}^{k+1} - 2\mathbf{u}^k + \mathbf{u}^{k-1}}{\Delta t^2} \cdot \mathbf{v}\, d\mathbf{x} + \int_\Omega \boldsymbol{\varepsilon}(\mathbf{v}) \cdot \left(\mathbf{C}(\boldsymbol{\varepsilon}^k)\,\boldsymbol{\varepsilon}(\mathbf{u}^k)\right) d\mathbf{x} = \int_{\Gamma_N} \mathbf{F}^k \cdot \mathbf{v}\, d\mathbf{x}, \tag{2.8}$$

where the notation $\mathbf{u}(\mathbf{x}, t_k) = \mathbf{u}^k$ has been used.

The displacement field $\mathbf{u}$ is then computed using a FEM space discretization with linear element over a uniform triangular mesh composed of $N_x \times N_y$ nodes such that the damaged area contains D_e elements. Using (2.2), (2.4) and (2.8), we obtain the discrete system [Fish & Belytschko 2007]

$$\mathbf{M}\frac{\mathbf{u}^{k+1} - 2\mathbf{u}^k + \mathbf{u}^{k-1}}{\Delta t^2} + \mathbf{K}(\mathbf{u}^k)\mathbf{u}^k = \mathbf{f}^k, \tag{2.9}$$

where $\mathbf{M}$ is the mass matrix, $\mathbf{K}$ the stiffness matrix and $\mathbf{f}(t)$ the force vector.

The parameters taken into consideration in the simulations of this chapter are defined in Table 2.1

Table 2.1 – *Model parameters.*

L_x: Length in the x direction (m)	1
L_y: Length in the y direction (m)	1
E: Young modulus (N/m^2)	$2\ 10^{11}$
ν: Poisson coefficient	0.25
A: Traction's amplitude	10^6
ω: Traction's angular frequency	$2\pi 10^3$
ρ: Density (kg/m^3)	8000
T: Time interval (s)	0.005
Δt: Time step (s)	10^{-6}
N_x: Number of nodes in the x direction	51
N_y: Number of nodes in the y direction	51
D_e: Number of damaged elements	128

2.2 Damage location via Machine Learning techniques

As discussed in the introduction, the main aim of this chapter is proposing a strategy through the combination of model order reduction based on the Principal Component Analysis (PCA), that extracts a reduced basis from undamaged snapshots (that will serve for projecting any measured solution on it), with data-mining techniques.

Principal Components Analysis can be viewed as an information extractor from a data set that attempts to find a linear subspace of lower dimensionality than the original space. If the data have more complicated structures which cannot be well represented in a linear subspace, standard PCA fails for performing dimensionality reduction. In that case its nonlinear counterparts (kernel-based PCA or local-PCA) could be valuable alternatives for defining reduced bases.

When projecting into this reduced basis the measured field, undamaged regions are expected being better approximated than the ones in which damage occurs. Thus, data-mining strategies could be then used to differentiate both regions (undamaged and damaged depicted in Fig. 2.1).

For that purpose, problem (2.7) is solved with the same geometrical and mechanical properties defined in Table 2.1 but without any damaged zone.

By solving the discrete equation (2.9) we obtain the undamaged displacement field $\mathbf{u}(\mathbf{x}, t)$ and from it the displacement field norm $w(\mathbf{x}, t)$ at the nodes $\mathbf{x}_i$ of the spatial mesh at times $t_m = m \cdot \Delta t$, with $i \in [1, \ldots, N]$ and $m \in [0, \ldots, M]$. In the sequel we use the notation $w(\mathbf{x}_i, t_m) \equiv w_i^m$, and $\mathbf{w}^m$ represents the vector of nodal values w_i^m at time t_m.

Then we apply the POD (equivalent to the PCA) to identify the most typical structure $\phi(\mathbf{x})$ among these $\mathbf{w}^m$, $\forall m$.

For that purpose we first define the matrix $\mathbf{Q}_{ud}$ (where the subscript $\bullet_{ud}$ makes

reference to its undamaged nature) from

$$\mathbf{Q}_{ud} = \begin{pmatrix} w_1^1 & w_1^2 & \dots & w_1^M \\ w_2^1 & w_2^2 & \dots & w_2^M \\ \vdots & \vdots & \ddots & \vdots \\ w_N^1 & w_N^2 & \dots & w_N^M \end{pmatrix} \tag{2.10}$$

and the two point correlation matrix $\mathbf{C}$

$$C_{ij} = \sum_{m=1}^{M} w^m(\mathbf{x}_i) w^m(\mathbf{x}_j), \tag{2.11}$$

or

$$\mathbf{C} = \sum_{m=1}^{M} \mathbf{w}^m \cdot (\mathbf{w}^m)^T = \mathbf{Q}_{ud} \cdot \mathbf{Q}_{ud}^T, \tag{2.12}$$

and then, within the usual POD framework, solve the resulting eigenvalue problem for obtaining the searched modes,

$$\mathbf{C}\boldsymbol{\phi} = \alpha\boldsymbol{\phi}, \tag{2.13}$$

where the i-entry of vector $\boldsymbol{\phi}$ corresponds to $\phi(x_i)$.

In order to obtain a reduced-order model we select the P eigenvectors associated with the P largest eigenvalues, for example the ones greater than $\alpha_1 10^{-6}$ (where α_1 is the highest eigenvalue). In many applications, the magnitude of the eigenvalues decreases very fast, fact that reveals that the solution $\mathbf{w}^m$ can be approximated $\forall m$ from a reduced number P ($P \ll N$) of modes (eigenvectors).

In what follows we consider only the first two eigenvectors, because, as explained later, our goal is not to reconstruct the undamaged displacement but only differentiate between damaged and undamaged solutions. Our feeling is that the undamaged displacement is better represented in the reduced basis composed of the two modes extracted from the undamaged structure than the displacement associated with damaged zones.

For this purpose, we first select the firsts eigenmodes that are expected better representing solutions at the undamaged than at the damaged regions. Note that the more eigenmodes are considered the less contrasted will be solutions in undamaged and damaged zones. In our numerical experiments we select the first two modes and we define matrix $\mathbf{B} = [\boldsymbol{\phi_1}, \boldsymbol{\phi_2}]$

$$\mathbf{B} = \begin{pmatrix} \phi_1(\mathbf{x}_1) & \phi_2(\mathbf{x}_1) \\ \phi_1(\mathbf{x}_2) & \phi_2(\mathbf{x}_2) \\ \vdots & \vdots \\ \phi_1(\mathbf{x}_N) & \phi_2(\mathbf{x}_N) \end{pmatrix}. \tag{2.14}$$

Now we repeat simulations, but including the damaged zone obtaining, as before,

the matrix of displacement norms $\mathbf{Q}_d$ as

$$\mathbf{Q}_d = \begin{pmatrix} w_1^1 & w_1^2 & \dots & w_1^M \\ w_2^1 & w_2^2 & \dots & w_2^M \\ \vdots & \vdots & \ddots & \vdots \\ w_N^1 & w_N^2 & \dots & w_N^M \end{pmatrix}. \tag{2.15}$$

Now, the damaged solutions are projected onto the two-modes basis $\mathbf{B}$ related to the undamaged structure, that results in

$$\boldsymbol{\beta} = \mathbf{B}^T \mathbf{Q}_d, \tag{2.16}$$

from which the reconstructed damaged displacement norms result from

$$\mathbf{Q}_d^{rec} = \mathbf{B}\,\boldsymbol{\beta}. \tag{2.17}$$

The residual between the real and reconstructed damaged displacement norms reads

$$\mathbf{R} = \mathbf{Q}_d - \mathbf{Q}_d^{rec}. \tag{2.18}$$

At this point a clustering technique is applied on the absolute value of the residual field $\mathbf{R}$. In this work the k-means strategy has been used. It proceeds in three steps:

1. an initial partition is done with two populations, i.e. $k = 2$. Many different methods could be used to choose initial centers of mass and a comparison of them is described in [Peña *et al.* 1999];

2. each point is assigned to the cluster whose center of mass is closer;

3. centers of mass are updated.

The second and third steps repeat until reaching a stable position of both centers of mass.

In order to reduce the dimensionality before applying the clustering, PCA is applied on the absolute value of the residual vectors.

The results of the damaged zone predicted by the proposed method for different positions of the damage are presented in Figs. 2.2 and 2.3. We can see how it detects quite precisely the position of damaged regions. Moreover in Fig. 2.4 one can see how even if the reduction of dimension performed by the PCA is extreme (only the three first principal components are taken) the zones (damaged and undamaged) are perfectly differentiated.

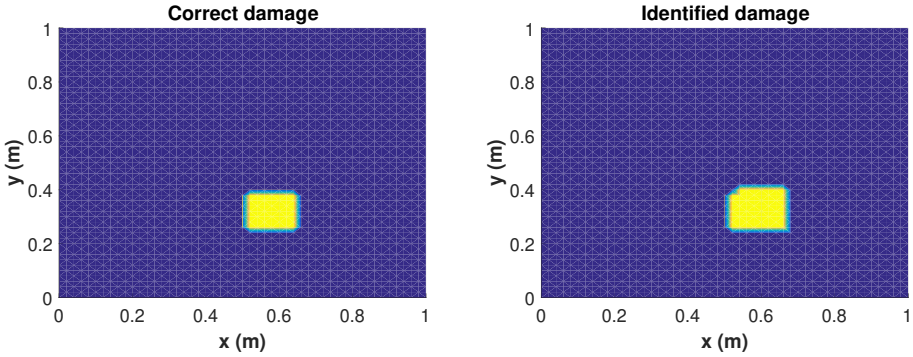

(a)

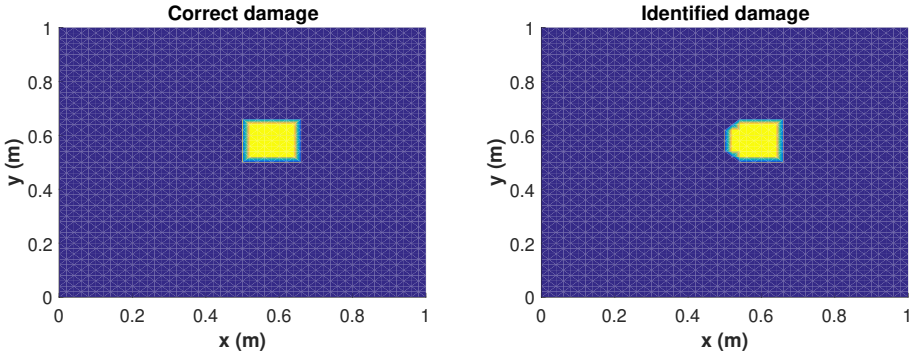

(b)

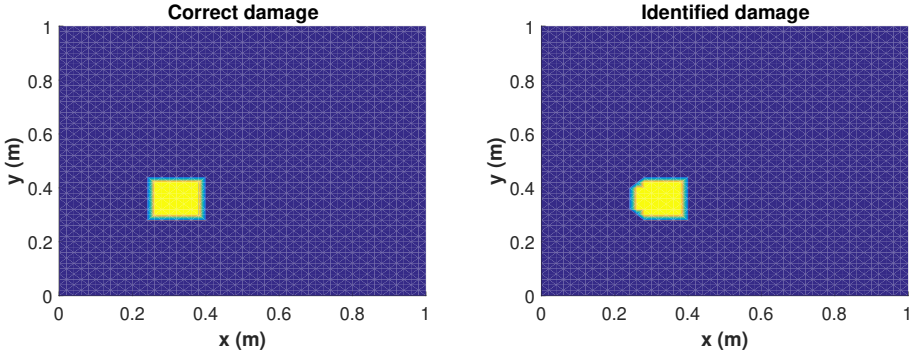

(c)

Figure 2.2 – *Prediction versus reference damage location for the first three different positions of the damaged zone.*

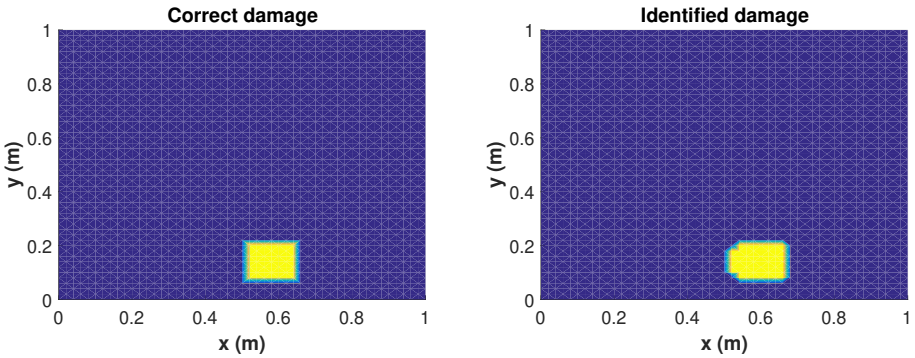

(d)

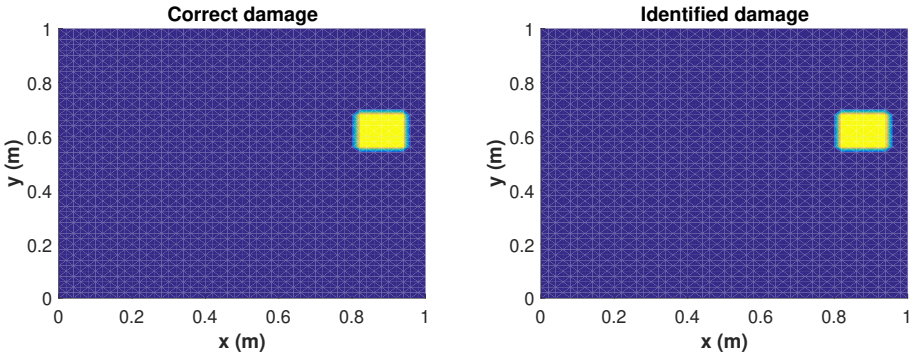

(e)

Figure 2.3 – *Prediction versus reference damage location for the last two different positions of the damaged zone.*

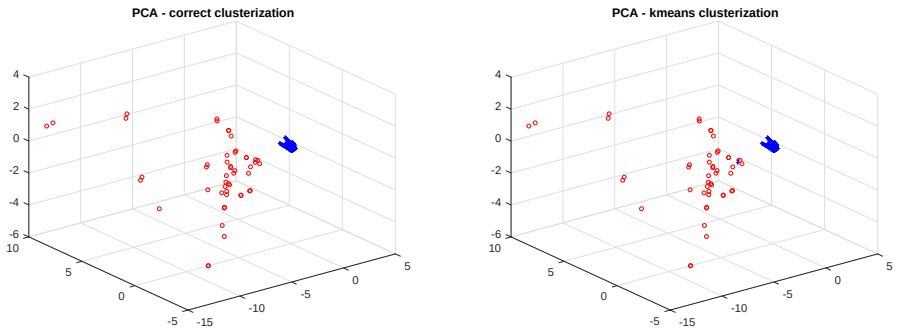

Figure 2.4 – *First three principal components of the absolute value of the residual field for case (b) of Figure 2.2. Red points belong to the damaged zone.*

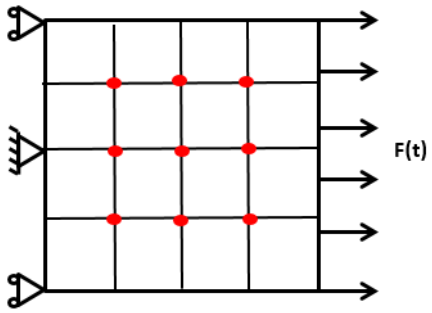

Figure 2.5 – *Domain division for the dictionary learning.*

2.3 Data completion

The main difficulty when considering the approach discussed above is that the displacement field is needed in as many locations as possible (e.g. the nodes considered in the finite element mesh). Having access to all this local information could become prohibitive in practical applications. Thus, in this section, we consider data acquisition in few locations, from which fields are completed before applying the rationale previously discussed.

For this purpose a dictionary of simulations is performed, that contains the displacements and residuals fields everywhere for the damage located in different zones and taking different sizes (both perfectly known). In what follows we consider a subdivision of the domain like the one depicted in Fig. 2.5.

We consider 102 scenarios to create our dictionary: the first 48 are given by choosing as damaged zone one of the 16 areas depicted in Fig. 2.5 and assigning to each area 3 different sizes of the damaged zone. The others 54 scenarios are given by choosing as damaged area the 9 intersections of the previous areas (the red points in Fig. 2.5) and assigning to each point 6 possible different sizes of the damaged zone centered on it.

Obviously the dictionary can be enriched with many other locations and sizes of the damaged zone, but the goal in this work is to show how the dictionary learning technique can be used to perform data completion and, for this reason, the scenarios previously described seem sufficient.

Once the dictionary has been created we suppose that a displacement field related to an unknown damaged scenario is known at few locations, that is, at the positions where sensors are placed. In this work we suppose displacements accessible at the nodes of a 9×9 uniform grid. It is important to note that coarser dictionaries require much less sensors, whereas rich dictionaries require many measurements in order to identify the closest scenario. In practice we could proceed with coarser representations for online monitoring and richer representations for maintenance operations.

The displacement norms at those locations allow defining matrix $\tilde{\mathbf{Q}}_d$, where $\tilde{\mathbf{Q}}_d$ comes from $\mathbf{Q}_d$ defined in Eq. (2.15) by taking the rows corresponding to the sensor

points. Then we compute the residual at the sensor points using the same rationale that was considered in Eqs. (2.16) and (2.18), but with the difference that now coefficients $\boldsymbol{\beta}$ are obtained in a least-squares sense from

$$\boldsymbol{\beta} = \arg\min_{\boldsymbol{\beta}} ||\tilde{\mathbf{B}}\,\boldsymbol{\beta} - \tilde{\mathbf{Q}}_d||_2, \tag{2.19}$$

where $\tilde{\mathbf{B}}$ has been obtained from $\mathbf{B}$ defined in Eq. (2.14) by taking the rows corresponding to the sensor points. Let's note that Eq. (2.19) can be solved because the number of sensor points is greater than the number of functions in the basis $\mathbf{B}$ (two in the present analysis). Then we reconstruct the damaged displacement norm field at the sensor points by computing

$$\tilde{\mathbf{Q}}_d^{rec} = \tilde{\mathbf{B}}\,\boldsymbol{\beta}. \tag{2.20}$$

The residual between the reference and the reconstructed damaged displacement norm at the sensor points reads

$$\tilde{\mathbf{R}} = \tilde{\mathbf{Q}}_d - \tilde{\mathbf{Q}}_d^{rec}. \tag{2.21}$$

Then, we compute the gaps between $\tilde{\mathbf{R}}$ and the residual field at the sensor points of all the simulations in the dictionary, and we select as reference simulation the one that minimizes the norm of this error.

The complete residual field related to the reference simulation is noted by $\mathbf{R_{ref}}$. The reduced base $\mathbf{G}$ used for data completion is then computed performing a POD on $\mathbf{R_{ref}}$ that results in

$$\mathbf{G} = \begin{pmatrix} \psi_1(\mathbf{x}_1) & \psi_2(\mathbf{x}_1) & \dots & \psi_F(\mathbf{x}_1) \\ \psi_1(\mathbf{x}_2) & \psi_2(\mathbf{x}_2) & \dots & \psi_F(\mathbf{x}_2) \\ \vdots & \vdots & \ddots & \vdots \\ \psi_1(\mathbf{x}_N) & \psi_2(\mathbf{x}_N) & \dots & \psi_F(\mathbf{x}_N) \end{pmatrix}, \tag{2.22}$$

where F is the number of functions selected to compose the reduced base used for the completion.

In order to compute the complete residual field $\mathbf{R}_{com}$ we compute first

$$\boldsymbol{\gamma} = \arg\min_{\boldsymbol{\gamma}} ||\tilde{\mathbf{G}}\,\boldsymbol{\gamma} - \tilde{\mathbf{R}}||_2, \tag{2.23}$$

where $\tilde{\mathbf{G}}$ has been obtained from $\mathbf{G}$ defined in Eq. (2.22) by taking the rows corresponding to the sensor points and where F is smaller than the number of sensors. Thus, it results

$$\mathbf{R}_{com} = \mathbf{G}\,\boldsymbol{\gamma}. \tag{2.24}$$

As in the previous section the k-means technique is then applied on the absolute value of the completed residual field $\mathbf{R}_{com}$. Again, in order to reduce the dimen-

sionality of the problem, the PCA is applied on the absolute value of the completed residual field before performing clusterization.

Results on the damaged zone detection by using the proposed methodology for the different positions of the damage considered in the previous section are presented in Figs. 2.6 and 2.7. We can notice that results are in good agreement to the ones presented in the previous section, with a quite good identification of the damaged zone.

2.4 Conclusions

In this chapter we proposed a new efficient technique for real-time evaluation of damage in structures based on their dynamical response. For that purpose few POD modes associated with the undamaged structure were used for reconstructing the fields of interest. As expected, as soon as damage occurs, the projection onto the undamaged modes allows differentiating, by using standard clustering techniques, damaged and undamaged regions. Moreover, to avoid data collection on the whole structure, a procedure for collecting data at few specified locations was proposed. Then from the collected data at these points, the fields of interest where completed everywhere, allowing for an accurate damage location.

The numerical test performed proved the validity and potential of the proposed approach that should be now validated experimentally.

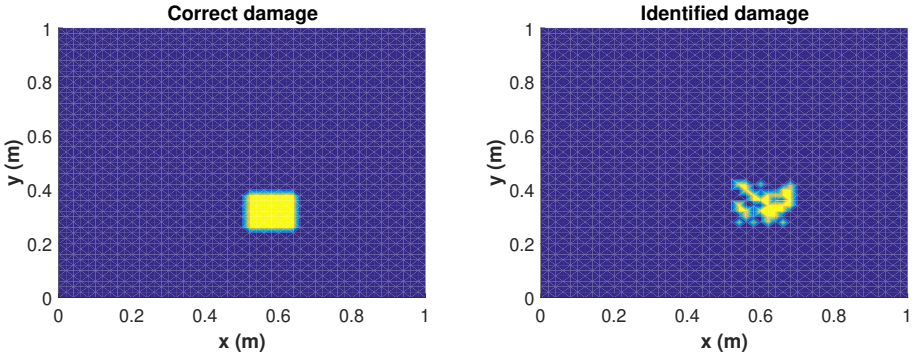

(a)

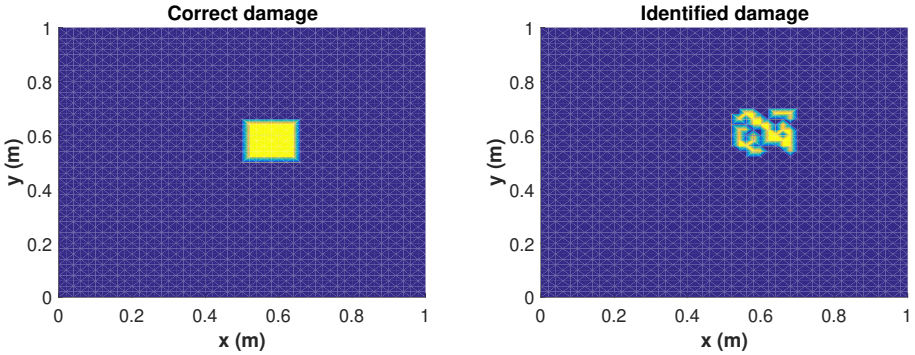

(b)

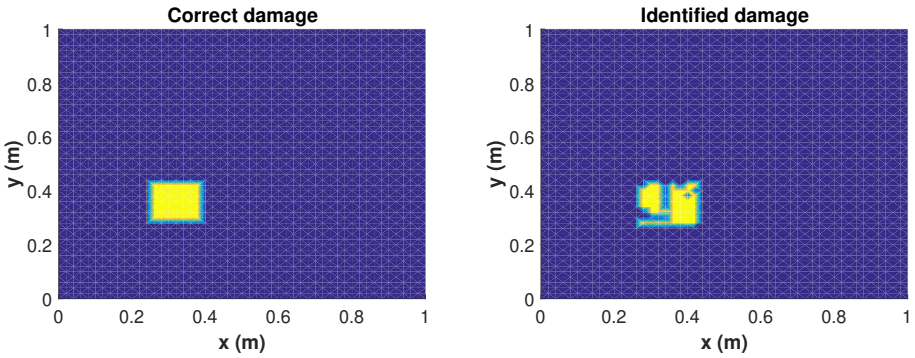

(c)

Figure 2.6 – *Results when using data completion for the first three different positions of the damaged zone.*

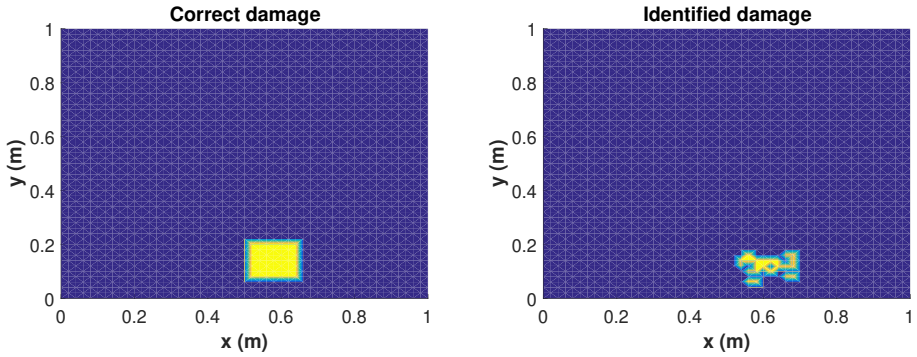

(d)

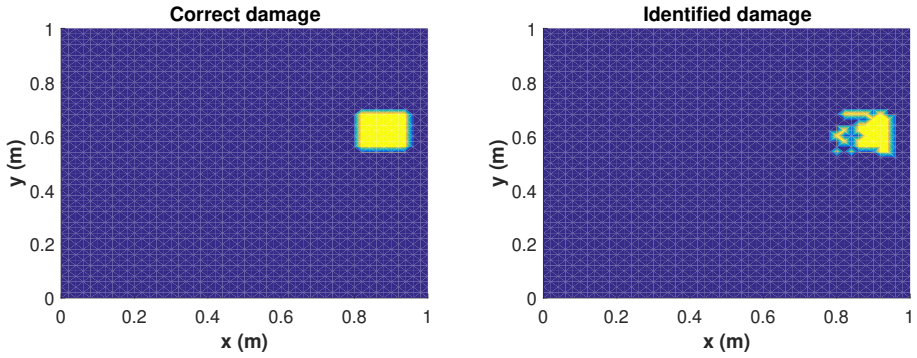

(e)

Figure 2.7 – *Results when using data completion for the last two different positions of the damaged zone.*

Chapter 3

Structural dynamics by using Model Order Reduction

Contents

In many applications, as the structural health monitoring presented in the previous chapter, it is needed to compute the dynamical response of a system. This chapter presents different techniques based on Model Order Reduction methods, in particular on the Proper Generalized Decomposition, in order to treat dynamical problems in structural mechanics in an efficient way.

3.1 A new hybrid explicit/implicit in-plane-out-of-plane separated representation for the solution of dynamic problems defined in plate-like domains

Introduction The first part of the chapter extends in-plane-out-of-plane separated representations, successfully used for addressing fully 3D model solutions de-

fined in plate-like domain, to dynamics. Common time integration are performed using explicit or implicit strategies. Even if the implementation of implicit integration schemes into a 3D in-plane-out-of-plane separated representation does not imply major difficulties, the use of explicit integration, preferable in many applications, becomes a tricky issue. In fact the mesh employed for discretizing the out-of-plane dimension (thickness) determines the maximum time-step ensuring stability. In this section we introduce a new efficient hybrid explicit/implicit in-plane-out-of-plane separated representation for dynamic problems defined in plate-like domains, that allows computing 3D solutions with the stability constraint exclusively determined by the coarser in-plane discretization.

Next subsection revisits the main concepts related to the separated representations. Then, next subsection defines the elastodynamics problem and its in-plane-out-of-plane separated representation, the next one addresses time integration within the separated representation framework and proposes an efficient hybrid explicit/implicit formulation. Finally the last subsection validates the proposed methodology from some case studies.

This first part of the chapter and all the results presented in it correspond to the following paper:

- G. Quaranta, B. Bognet, R. Ibañez, A. Tramecon, E. Haug, F. Chinesta, *A new hybrid explicit/implicit in-plane-out-of-plane separated representation for the solution of dynamic problems defined in plate-like domains*, Computers and Structures, **210**, 135-144, 2018.

3.1.1 An overview on separated representations

Separated representations, at the heart of the so-called Proper Generalized Decomposition – PGD – [Chinesta *et al.* 2011, Chinesta *et al.* 2015, Bur *et al.* 2016], consists of expressing the unknown field depending on many coordinates (space, time, parameters, ...) as a finite sum decomposition in which each term involved in the sum consists, at its turn, in the product of a series of unknown functions, each one depending on one coordinate. Thus, when addressing a transient model involving the unknown field $u(\mathbf{x}, t)$, its separated representation reads [Ladeveze 1985, Ladeveze 1989, Ladeveze 1996]

$$u(\mathbf{x}, t) \approx \sum_{i=1}^{N} X_i(\mathbf{x}) \cdot T_i(t), \tag{3.1}$$

where neither the time-dependent functions $T_i(t)$ nor the space functions $X_i(\mathbf{x})$ are "a priori" known. Both will be computed on-the-flight when solving the problem.

This rationale can be extended to the solution of any problem whose solution involves d generic coordinates $u(x_1, \cdots, x_d)$ according to [Ammar *et al.* 2006,

Ammar *et al.* 2007, Ammar *et al.* 2008]

$$u(x_1, x_2, \cdots, x_d) \approx \sum_{i=1}^{N} X_i^1(x_1) \cdot X_i^2(x_1) \cdots X_i^d(x_d), \tag{3.2}$$

where the set of coordinates can include a series of parameters $u(\mathbf{x}, t, p_1, \cdots, p_{\mathtt{p}})$ according to [Chinesta *et al.* 2013b]

$$u(\mathbf{x}, t, p_1, \cdots, p_{\mathtt{p}}) \approx \sum_{i=1}^{N} X_i(\mathbf{x}) \cdot T_i(t) \cdot \prod_{k=1}^{\mathtt{p}} P_i^k(p_k). \tag{3.3}$$

In the present section we are mainly concerned by the space separation to address the solution of mechanical problems defined in degenerated domain. Sometimes the spatial domain Ω, assumed three-dimensional, can be fully or partially separated, and consequently it can be expressed as $\Omega = \Omega_x \times \Omega_y \times \Omega_z$ or $\Omega = \Omega_{xy} \times \Omega_z$ respectively. The first decomposition is related to hexahedral domains whereas the second one is related to plate, beams or extruded domains. We consider below both scenarios:

- The spatial domain Ω is partially separable. In this case the separated representation writes:

$$u(\mathbf{x}, z) \approx \sum_{i=1}^{N} X_i(\mathbf{x}) \cdot Z_i(z), \tag{3.4}$$

  where $\mathbf{x} = (x, y) \in \Omega_{xy}$ and $z \in \Omega_z$. This decomposition implies:

  1. the solution in Ω_{xy} of two-dimensional BVP's to obtain functions X_i,
  2. the solution in Ω_z of one-dimensional BVP's to obtain functions Z_i.

  The complexity of the PGD simulation scales with the two-dimensional mesh used to solve the BVP's in Ω_{xy}, regardless of the mesh used in the solution of the BVP defined in Ω_z for calculating $Z_i(z)$.

- The spatial domain Ω is fully separable. In this case the separated representation writes:

$$u(x, y, z) = \sum_{i=1}^{N} X_i(x) \cdot Y_i(y) \cdot Z_i(z), \tag{3.5}$$

  implying:

  1. the solution in Ω_x of one-dimensional BVP's to obtain functions X_i,
  2. the solution in Ω_y of one-dimensional BVP's to obtain functions Y_i,
  3. the solution in Ω_z of one-dimensional BVP's to obtain functions Z_i.

> The cost savings provided by the PGD are potentially phenomenal when the spatial domain is fully separable. Indeed, the complexity of the PGD simulation now scales with the one-dimensional meshes used to solve the BVP's in Ω_x, Ω_y and Ω_z.

Even when the domain is not fully separable, a fully separated representation could be considered by using appropriate geometrical mappings or by immersing the non-separable domain into a fully separable one. The interested reader can refer to [González *et al.* 2010, Ghnatios *et al.* 2016b].

In-plane-out-of-plane separated representations are particularly useful for addressing the solution of problems defined in plate [Bognet *et al.* 2012], shell [Bognet *et al.* 2014], beams [Bordeu *et al.* 2015] or extruded domains [Chinesta *et al.* 2013a]. The same approach was extensively considered in structural plate and shell models in [Laurent *et al.* 2013, Vidal *et al.* 2012, Vidal *et al.* 2013, Vidal *et al.* 2014a, Vidal *et al.* 2014b, Vidal *et al.* 2015, Prulière 2014]. Space separated representations where enriched with discontinuous functions for representing cracks in [Giner *et al.* 2013], delamination in [Metoui *et al.* 2014] and thermal contact resistances in [Chinesta *et al.* 2014b]. Domain decomposition within the separated space representation was accomplished in [Nazeer *et al.* 2014]. The in-plane-out-of-plane decomposition was then extended to many other physics. Thermal models were considered in [Chinesta *et al.* 2014b] and squeeze flows of Newtonian and non Newtonian fluids in laminates in [Ghnatios *et al.* 2015, Ghnatios *et al.* 2016a, Ibáñez *et al.* 2017].

As soon as separated representations are considered, the solution of a multi-dimensional problem reduces to the solution of a sequence of lower dimensional problems with the consequent computing time savings. The solution procedure has been extensively used, described and analyzed in many former works, many of them referred in the present work. The interested reader can refer to the primer [Chinesta *et al.* 2014a] and the numerous references therein.

3.1.2 Elastodynamics: Problem definition

We consider a physical domain Ω for which a linear elastic behavior is assumed, according to

$$\boldsymbol{\sigma} = \mathbb{C}\,\boldsymbol{\varepsilon}, \tag{3.6}$$

where $\mathbb{C}$ is the fourth order stiffness tensor, and the strain tensor $\boldsymbol{\varepsilon}$ derives from the symmetric component of the gradient of displacements i.e. $\boldsymbol{\varepsilon} = \nabla_s \mathbf{u}$, where ∇_s refers to the symmetric component.

From now on we consider Voigt notation, and for the sake of notational simplicity we consider the same notation, $\boldsymbol{\sigma}$, $\boldsymbol{\varepsilon}$ and $\mathbf{C}$ for expressing the stress and strain vectors and the stiffness matrix respectively.

Thus, with

$$\boldsymbol{\varepsilon} = \begin{pmatrix} \varepsilon_{xx} \\ \varepsilon_{yy} \\ \varepsilon_{zz} \\ \gamma_{yz} \\ \gamma_{xz} \\ \gamma_{xy} \end{pmatrix} \tag{3.7}$$

and

$$\boldsymbol{\sigma} = \begin{pmatrix} \sigma_{xx} \\ \sigma_{yy} \\ \sigma_{zz} \\ \sigma_{yz} \\ \sigma_{xz} \\ \sigma_{xy} \end{pmatrix}, \tag{3.8}$$

the stiffness matrix becomes

$$\mathbf{C} = \frac{E}{(1+\nu)(1-2\nu)} \begin{bmatrix} (1-\nu) & \nu & \nu & 0 & 0 & 0 \\ \nu & (1-\nu) & \nu & 0 & 0 & 0 \\ \nu & \nu & (1-\nu) & 0 & 0 & 0 \\ 0 & 0 & 0 & \frac{(1-2\nu)}{2} & 0 & 0 \\ 0 & 0 & 0 & 0 & \frac{(1-2\nu)}{2} & 0 \\ 0 & 0 & 0 & 0 & 0 & \frac{(1-2\nu)}{2} \end{bmatrix}. \tag{3.9}$$

The dynamic problem, in absence of damping and external forces, with the displacement field $\mathbf{u}(\mathbf{x}, t)$ for $\mathbf{x} \in \Omega$ and $t \in I = [0, T]$, reads

$$\rho \ddot{\mathbf{u}}(\mathbf{x}, t) = \nabla \cdot \boldsymbol{\sigma}, \tag{3.10}$$

with ρ the material density and $\ddot{\mathbf{u}}$ the second time derivative of the displacement field, i.e. the acceleration.

The domain boundary $\Gamma = \partial\Omega$ is partitioned in Dirichlet and Neumann regions, Γ_D and Γ_N, where respectively displacements and tractions are enforced, with $\Gamma_D \cup \Gamma_N = \Gamma$ and $\Gamma_D \cap \Gamma_N = \emptyset$. Dynamic problems require specifying the initial displacement and velocity that without loss of generality in what follows are assumed null, i.e. $\dot{\mathbf{u}}(\mathbf{x}, t = 0) = \mathbf{0}$ and $\mathbf{u}(\mathbf{x}, t = 0) = \mathbf{0}$.

Assuming again the trial and test displacements belonging to appropriate functional spaces, and considering an elastic constitutive equation, the weak form associated with (3.10) reads

$$\rho \int_\Omega \mathbf{u}^* \cdot \ddot{\mathbf{u}} \, d\mathbf{x} + \int_\Omega \boldsymbol{\varepsilon}(\mathbf{u}^*) \cdot (\mathbf{C}\, \boldsymbol{\varepsilon}(\mathbf{u})) \, d\mathbf{x} = \int_{\Gamma_N} \mathbf{u}^* \cdot \mathbf{F} \, d\mathbf{x}, \tag{3.11}$$

where the applied traction depends on time, i.e. $\mathbf{F} = \mathbf{F}(t)$.

3.1.2.1 In-plane-out-of-plane separated representation

As discussed in the previous section, with Ω having one dimension (the one related to the thickness) much smaller than the others involving the in-plane coordinates, an in-plane-out-of-plane separated representation seems again the most appealing route for addressing 3D discretizations while keeping the computational complexity the one characteristic of 2D discretizations. The domain is expressed from $\Omega = \Omega_{xy} \times \Omega_z$.

Even if, as also indicated, space-time separated discretizations were considered many times in the past [Ladeveze 1985, Ammar *et al.* 2007], in the present work time derivatives are discretized using standard schemes.

By considering the notation $\mathbf{u}(x, y, z, t = k\Delta t) = \mathbf{u}^k(x, y, z)$, with Δt the time step, the in-plane-out-of-plane separated representation of the displacement field at time $t_k = k\Delta t$, $\mathbf{u}^k(x, y, z)$, reads

$$\mathbf{u}^k(x,y,z) = \begin{pmatrix} u^k(x,y,z) \\ v^k(x,y,z) \\ w^k(x,y,z) \end{pmatrix} \approx \mathbf{u}_N^k(x,y,z) = \sum_{i=1}^{N} \begin{pmatrix} u_{xy}^{i,k}(x,y) \cdot u_z^{i,k}(z) \\ v_{xy}^{i,k}(x,y) \cdot v_z^{i,k}(z) \\ w_{xy}^{i,k}(x,y) \cdot w_z^{i,k}(z) \end{pmatrix} =$$

$$\sum_{i=1}^{N} \mathbf{U}_{xy}^{i,k}(x,y) \circ \mathbf{U}_z^{i,k}(z) \tag{3.12}$$

where " $\circ$ " refers to the Hadamard product, and with

$$\mathbf{U}_{xy}^{i,k}(x,y) = \begin{pmatrix} u_{xy}^{i,k}(x,y) \\ v_{xy}^{i,k}(x,y) \\ w_{xy}^{i,k}(x,y) \end{pmatrix} = \begin{pmatrix} u_{xy}^{i,k} \\ v_{xy}^{i,k} \\ w_{xy}^{i,k} \end{pmatrix}, \tag{3.13}$$

$$\mathbf{U}_{z}^{i,k}(z) = \begin{pmatrix} u_{z}^{i,k}(z) \\ v_{z}^{i,k}(z) \\ w_{z}^{i,k}(z) \end{pmatrix} = \begin{pmatrix} u_{z}^{i,k} \\ v_{z}^{i,k} \\ w_{z}^{i,k} \end{pmatrix}, \tag{3.14}$$

where for alleviating the notation the coordinate dependences will be omitted.

From all them we can obtain the separated vector form of the strain tensor at time t_k, $\boldsymbol{\varepsilon}^k \equiv \boldsymbol{\varepsilon}(\mathbf{u}^k)$:

$$\boldsymbol{\varepsilon}(\mathbf{u}^k) \approx \sum_{i=1}^{N} \begin{pmatrix} \frac{\partial u_{xy}^{i,k}}{\partial x} \cdot u_z^{i,k} \\ \frac{\partial v_{xy}^{i,k}}{\partial y} \cdot v_z^{i,k} \\ w_{xy}^{i,k} \cdot \frac{\partial w_z^{i,k}}{\partial z} \\ \frac{\partial w_{xy}^{i,k}}{\partial y} \cdot w_z^{i,k} + v_{xy}^{i,k} \cdot \frac{\partial v_z^{i,k}}{\partial z} \\ \frac{\partial w_{xy}^{i,k}}{\partial x} \cdot w_z^{i,k} + u_{xy}^{i,k} \cdot \frac{\partial u_z^{i,k}}{\partial z} \\ \frac{\partial u_{xy}^{i,k}}{\partial y} \cdot u_z^{i,k} + \frac{\partial v_{xy}^{i,k}}{\partial x} \cdot v_z^{i,k} \end{pmatrix}. \tag{3.15}$$

The separated representation constructor proceeds by computing a term of the sum at each iteration. Assuming that the first $n-1$ modes (terms of the finite

sum) of the solution were already computed, $\mathbf{u}^k_{n-1}(x,y,z)$ with $n \geq 1$, the solution enrichment reads:

$$\mathbf{u}^k_n(x,y,z) = \mathbf{u}^k_{n-1}(x,y,z) + \mathbf{U}^{n,k}_{xy}(x,y) \circ \mathbf{U}^{n,k}_z(z) \tag{3.16}$$

where both vectors $\mathbf{U}^{n,k}_{xy}$ and $\mathbf{U}^{n,k}_z$ are unknown at the present iteration defining a nonlinear problem. The test function $\mathbf{u}^*$ reads $\mathbf{u}^* = \mathbf{U}^*_{xy} \circ \mathbf{U}^{n,k}_z + \mathbf{U}^{n,k}_{xy} \circ \mathbf{U}^*_z$.

With both $\mathbf{U}^{n,k}_{xy}$ and $\mathbf{U}^{n,k}_z$ unknown the resulting problem becomes nonlinear. We proceed by considering the simplest linearization strategy, an alternated directions fixed point algorithm widely considered and described in the previously mentioned works.

When $\mathbf{U}^{n,k}_z$ is assumed known, we consider the test function $\mathbf{u}^\star$ given by $\mathbf{U}^\star_{xy} \circ \mathbf{U}^{n,k}_z$. By introducing the trial and test functions into the weak form and then integrating in Ω_z, because all the functions depending on the thickness coordinate are known, we obtain a 2D weak formulation defined in Ω_{xy} whose discretization (by using a standard discretization strategy, e.g. finite elements) allows computing $\mathbf{U}^{n,k}_{xy}$.

Analogously, when $\mathbf{U}^{n,k}_{xy}$ is assumed known, the test function $\mathbf{u}^\star$ is given by $\mathbf{U}^{n,k}_{xy} \circ \mathbf{U}^\star_z$. By introducing the trial and test functions into the weak form and then integrating in Ω_{xy}, because all the functions depending on the in-plane coordinates (x,y) are at present known, we obtain a 1D weak formulation defined in Ω_z whose discretization (using any technique for solving standard ODE equations) allows computing $\mathbf{U}^{n,k}_z$.

Thus, the 3D computational cost is transformed into a sequence of 2D and 1D solutions, with the associated computing time savings [Bognet *et al.* 2012].

3.1.3 Time discretization

Before introducing the hybrid strategy we consider at time t_{k+1} the standard implicit and explicit formulations (two common time integration schemas among other possibilities [Bathe 2006]), given respectively by

$$\rho \int_\Omega \mathbf{u}^* \cdot \frac{\mathbf{u}^{k+1} - 2\mathbf{u}^k + \mathbf{u}^{k-1}}{\Delta t^2} d\mathbf{x} + \int_\Omega \boldsymbol{\varepsilon}(\mathbf{u}^*) \cdot \left(\mathbf{C}\, \boldsymbol{\varepsilon}\left(\frac{\mathbf{u}^{k+1} + \mathbf{u}^{k-1}}{2} \right) \right) d\mathbf{x} = \int_{\Gamma_N} \mathbf{u}^* \cdot \frac{\mathbf{F}^{k+1} + \mathbf{F}^{k-1}}{2} d\mathbf{x}, \tag{3.17}$$

that as previously indicated is unconditionally stable, and the explicit one

$$\rho \int_\Omega \mathbf{u}^* \cdot \frac{\mathbf{u}^{k+1} - 2\mathbf{u}^k + \mathbf{u}^{k-1}}{\Delta t^2} d\mathbf{x} + \int_\Omega \boldsymbol{\varepsilon}(\mathbf{u}^*) \cdot \left(\mathbf{C}\, \boldsymbol{\epsilon}(\mathbf{u}^k) \right) d\mathbf{x} = \int_{\Gamma_N} \mathbf{u}^* \cdot \mathbf{F}^k d\mathbf{x}, \tag{3.18}$$

that is conditionally stable, with the stability limit Δt_{max}, defining the stability domain $\Delta t < \Delta t_{max}$, given by

$$\Delta t_{max} = \frac{L}{c}, \tag{3.19}$$

where L is the characteristic length of the spatial discretization and the dilatational wave speed c is given by

$$c = \sqrt{\frac{E(1-\nu)}{(1+\nu)(1-2\nu)\rho}}. \tag{3.20}$$

As previously commented explicit strategies are employed in many commercial codes. However, when applied to discretize 3D problems defined in degenerated domains, like plates or shells, the extremely fine meshes considered along the thickness direction have an unfavorable impact on the time step that becomes extremely small to ensure stability. The in-plane-out-of-plane separated representation cannot escape to this important issue, being the mesh size along the out-of-plane coordinate (much finer than the one used in the plane) the one that determines the time step.

It is important emphasizing the main aim of the present work and the proposed methodology for performing it. First, it is important to note that we are interested in performing fully 3D simulations in degenerated geometries (e.g. plate domains) while considering explicit time integrations.

In this context the following remarks can be addressed:

- When using 2D discrete models (considering for example plate elements), the stability criterion related to explicit time integrations involves the size of the elements, but as the mesh is the one related to the middle plane, the critical time step remains reasonable in most of cases;
- However, as soon as 3D discretizations are considered, the characteristic size of the finite elements along the plate thickness becomes much smaller than the in-plane characteristic length, and then when considering explicit time integrations the time step needed for ensuring stability decreases with the through-of-thickness characteristic element length;
- Increasing the resolution in the thickness direction implies the increase of the number of elements involved in the discretization as well as the decrease of the time step for ensuring stability, both having unfavorable consequences on the computational cost;
- In previous works [Bognet *et al.* 2012, Bognet *et al.* 2014] authors considered, in the framework of elastostatics, in-plane-out-of-plane separated representations that allowed reducing the computational complexity of solving a fully 3D problem to the one characteristic of 2D solutions;
- However, as just indicated, such a decomposition when combined with explicit time integrations fails, because again the stability is associated to the smallest discretization characteristic length, the one related to the through-of-thickness discretization;

- It is in that impasse that one is tempted of using, in the case of explicit time integration, the in-plane-out-of-plane separated representation (that reduces the computational complexity to the one characteristic of 2D models) combined with an hybrid time integration, explicit in the plane (conditionally stable but with the critical time-step scaling with the characteristic in-plane discretization length) and implicit along the thickness (unconditionally stable), that allows reducing the computational complexity while keeping as stability constraint the one associated to the in-plane explicit time integration;

- Obviously fully implicit in-plane-out-of-plane decompositions are possible, where the implicit time integration ensures unconditional stability while the space separated representation reduces the computational complexity. Despite of its intrinsic interest, it is not considered in the present work, and in all cases, the associated solutions are the same as the ones obtained by using a fully 3D finite element discretization but reducing the solution computational complexity. As previously commented fully explicit integrations fail because the too stringent stability conditions induced by the too fine through-of-thickness discretization;

- Thus, in this work we analyze the intermediate procedure, the one in which the fine through-of-thickness representation is alleviated thanks to the use of the in-plane-out-of-plane space separated representation and its associated implicit unconditionally stable time integration. Thus, the stability of the resulting discretization is expected being induced by the in-plane mesh in which an explicit time integration is retained. The present work is intended analyzing this hybrid methodology and proving that in the case of fully explicit separated representations (as in the case of fully explicit 3D finite elements) the stability is dictated by the smallest characteristic discretization length (the one along the domain thickness). On the contrary when considering the hybrid scheme described in the next subsection, we expect the stability being dictated by the characteristic in-plane discretization length (being the trough-of-thinness discretization implicit).

In summary, the main goal is enriching explicit 2D plate and shell formulations widely employed in industry and commercial codes, with a fine through-of-thickness description (3D) without affecting unfavorably the integration stability.

3.1.3.1 Explicit-in-plane / implicit-out-of-plane hybrid scheme

As just indicated, in order to circumvent the just referred stability issues, we propose an out-of-plane implicit discretization (unconditionally stable) while the in-plane discretization (implying coarser meshes) makes use of an explicit schema. Thus, the stability is prescribed by the in-plane size mesh, several order of magnitude higher than the one associated to the thickness.

For that purpose we propose considering at time t_k the strain defined by

$$\boldsymbol{\varepsilon}^h(\mathbf{u}^k) = \begin{pmatrix} u^k_{,x} \\ v^k_{,y} \\ \frac{w^{k+1}_{,z}+w^{k-1}_{,z}}{2} \\ \frac{v^{k+1}_{,z}+v^{k-1}_{,z}}{2} + w^k_{,y} \\ \frac{u^{k+1}_{,z}+u^{k-1}_{,z}}{2} + w^k_{,x} \\ u^k_{,y} + v^k_{,x} \end{pmatrix} \approx$$

$$\begin{pmatrix} \sum_{i=1}^{N_k} u^{i,k}_{xy,x} \cdot u^{i,k}_z \\ \sum_{i=1}^{N_k} v^{i,k}_{xy,y} \cdot v^{i,k}_z \\ \frac{\sum_{i=1}^{N_{k+1}} w^{i,k+1}_{xy} \cdot w^{i,k+1}_{z,z} + \sum_{i=1}^{N_{k-1}} w^{i,k-1}_{xy} \cdot w^{i,k-1}_{z,z}}{2} \\ \frac{\sum_{i=1}^{N_{k+1}} v^{i,k+1}_{xy} \cdot v^{i,k+1}_{z,z} + \sum_{i=1}^{N_{k-1}} v^{i,k-1}_{xy} \cdot v^{i,k-1}_{z,z}}{2} + \sum_{i=1}^{N_k} w^{i,k}_{xy,y} \cdot w^{i,k}_z \\ \frac{\sum_{i=1}^{N_{k+1}} u^{i,k+1}_{xy} \cdot u^{i,k+1}_{z,z} + \sum_{i=1}^{N_{k-1}} u^{i,k-1}_{xy} \cdot u^{i,k-1}_{z,z}}{2} + \sum_{i=1}^{N_k} w^{i,k}_{xy,x} \cdot w^{i,k}_z \\ \sum_{i=1}^{N_k} u^{i,k}_{xy,y} \cdot u^{i,k}_z + \sum_{i=1}^{N_k} v^{i,k}_{xy,x} \cdot v^{i,k}_z \end{pmatrix} \tag{3.21}$$

where for the sake of notational simplicity the derivatives of function $u_\bullet$ with respect the coordinate x is noted by $u_{\bullet,x}$ (and similarly for the other functions involved in the displacement components with respect to any coordinate). Moreover, the superscript $\bullet^h$ refers to its hybrid nature and N_{k+1}, N_k, N_{k-1} are the number of products involved in the separated representation of the displacement at times steps $k+1, k$ and $k-1$ respectively.

It can be noticed that the derivatives involving the out-of-plane (thickness) coordinate are treated using an implicit schema whereas an explicit one is retained for the in-plane derivatives. Thus, the hybrid schema is some place in between standard implicit and explicit techniques, taking profit of the advantages of both them.

When using the hybrid schema the weak form at time t_{k+1}, consists of finding $\mathbf{u}^{k+1}$, verifying

$$\int_\Omega \rho \mathbf{u}^* \cdot \frac{\mathbf{u}^{k+1} - 2\mathbf{u}^k + \mathbf{u}^{k-1}}{\Delta t^2} d\mathbf{x} + \int_\Omega \boldsymbol{\varepsilon}(\mathbf{u}^*) \cdot \Big(\mathbf{C}\, \boldsymbol{\varepsilon}^h(\mathbf{u}) \Big)\, d\mathbf{x} = \int_{\Gamma_N} \mathbf{u}^* \cdot \mathbf{F}^k \, d\mathbf{x}. \tag{3.22}$$

To construct the separated representation of the solution at time t_{k+1} we consider the standard procedure, assuming that $n-1$ terms have been already computed and that at the present iteration looks for the term n, according to

$$\mathbf{u}^{k+1}_{n-1}(x,y,z) = \begin{pmatrix} u^{k+1}_{n-1}(x,y,z) \\ v^{k+1}_{n-1}(x,y,z) \\ w^{k+1}_{n-1}(x,y,z) \end{pmatrix} = \sum_{i=1}^{n-1} \mathbf{U}^{i,k+1}_{xy}(x,y) \circ \mathbf{U}^{i,k+1}_z(z), \tag{3.23}$$

with

$$\mathbf{u}^{k+1}_n(x,y,z) = \mathbf{u}^{k+1}_{n-1}(x,y,z) + \mathbf{P}^{k+1}(x,y) \circ \mathbf{T}^{k+1}(z). \tag{3.24}$$

where for the sake of notational simplicity the unknown fields $\mathbf{U}^{n,k+1}_{xy}$ and $\mathbf{U}^{n,k+1}_z$

are referred by $\mathbf{P}^{k+1}(x,y)$ and $\mathbf{T}^{k+1}(z)$, with components

$$\mathbf{P}^{k+1}(x,y) = \begin{pmatrix} p_u^{k+1}(x,y) \\ p_v^{k+1}(x,y) \\ p_w^{k+1}(x,y) \end{pmatrix}, \tag{3.25}$$

and

$$\mathbf{T}^{k+1}(z) = \begin{pmatrix} t_u^{k+1}(z) \\ t_v^{k+1}(z) \\ t_w^{k+1}(z) \end{pmatrix}. \tag{3.26}$$

The linearity allows writing

$$\boldsymbol{\varepsilon}_n^h(x,y,z) = \boldsymbol{\varepsilon}_{n-1}^h(x,y,z) + \boldsymbol{\varepsilon}_{PT}^{\boldsymbol{h}}(x,y,z) \tag{3.27}$$

where

$$\boldsymbol{\varepsilon}_{n-1}^h(x,y,z) = \begin{pmatrix} u_{,x}^k \\ v_{,y}^k \\ \frac{w_{n-1,z}^{k+1} + w_{,z}^{k-1}}{2} \\ \frac{v_{n-1,z}^{k+1} + v_{,z}^{k-1}}{2} + w_{,y}^k \\ \frac{u_{n-1,z}^{k+1} + u_{,z}^{k-1}}{2} + w_{,x}^k \\ u_{,y}^k + v_{,x}^k \end{pmatrix} =$$

$$\begin{pmatrix} \sum_{i=1}^{N_k} u_{xy,x}^{i,k} \cdot u_z^{i,k} \\ \sum_{i=1}^{N_k} v_{xy,y}^{i,k} \cdot v_z^{i,k} \\ \frac{\sum_{i=1}^{n-1} w_{xy}^{i,k+1} \cdot w_{z,z}^{i,k+1} + \sum_{i=1}^{N_{k-1}} w_{xy}^{i,k-1} \cdot w_{z,z}^{i,k-1}}{2} \\ \frac{\sum_{i=1}^{n-1} v_{xy}^{i,k+1} \cdot v_{z,z}^{i,k+1} + \sum_{i=1}^{N_{k-1}} v_{xy}^{i,k-1} \cdot v_{z,z}^{i,k-1}}{2} + \sum_{i=1}^{N_k} w_{xy,y}^{i,k} \cdot w_z^{i,k} \\ \frac{\sum_{i=1}^{n-1} u_{xy}^{i,k+1} \cdot u_{z,z}^{i,k+1} + \sum_{i=1}^{N_{k-1}} u_{xy}^{i,k-1} \cdot u_{z,z}^{i,k-1}}{2} + \sum_{i=1}^{N_k} w_{xy,x}^{i,k} \cdot w_z^{i,k} \\ \sum_{i=1}^{N_k} u_{xy,y}^{i,k} \cdot u_z^{i,k} + \sum_{i=1}^{N_k} v_{xy,x}^{i,k} \cdot v_z^{i,k} \end{pmatrix}, \tag{3.28}$$

and

$$\boldsymbol{\varepsilon}_{PT}^h(x,y,z) = \begin{pmatrix} 0 \\ 0 \\ \frac{p_w^{k+1} \cdot t_{w,z}^{k+1}}{2} \\ \frac{p_v^{k+1} \cdot t_{v,z}^{k+1}}{2} \\ \frac{p_u^{k+1} \cdot t_{u,z}^{k+1}}{2} \\ 0 \end{pmatrix}.$$

The test displacement reads

$$\mathbf{u}^*(x,y,z) = \begin{pmatrix} p_u^*(x,y) \cdot t_u^{k+1}(z) + p_u^{k+1}(x,y) \cdot t_u^*(z) \\ p_v^*(x,y) \cdot t_v^{k+1}(z) + p_v^{k+1}(x,y) \cdot t_v^*(z) \\ p_w^*(x,y) \cdot t_w^{k+1}(z) + p_w^{k+1}(x,y) \cdot t_w^*(z) \end{pmatrix} =$$

$$\mathbf{P}^* \circ \mathbf{T}^{k+1} + \mathbf{P}^{k+1} \circ \mathbf{T}^*, \tag{3.29}$$

and the associated strain

$$\boldsymbol{\varepsilon}(\mathbf{u}^*(x,y,z)) = \begin{pmatrix} p^*_{u,x}\cdot t^{k+1}_u + p^{k+1}_{u,x}\cdot t^*_u \\ p^*_{v,y}\cdot t^{k+1}_v + p^{k+1}_{v,y}\cdot t^*_v \\ p^*_{w}\cdot t^{k+1}_{w,z} + p^{k+1}_{w}\cdot t^*_{w,z} \\ p^*_{w,y}\cdot t^{k+1}_w + p^{k+1}_{w,y}\cdot t^*_w + p^*_v\cdot t^{k+1}_{v,z} + p^{k+1}_v\cdot t^*_{v,z} \\ p^*_{w,x}\cdot t^{k+1}_w + p^{k+1}_{w,x}\cdot t^*_w + p^*_u\cdot t^{k+1}_{u,z} + p^{k+1}_u\cdot t^*_{u,z} \\ p^*_{v,x}\cdot t^{k+1}_v + p^{k+1}_{v,x}\cdot t^*_v + p^*_{u,y}\cdot t^{k+1}_u + p^{k+1}_{u,y}\cdot t^*_u \end{pmatrix}. \tag{3.30}$$

For the sake of simplicity, and without loss of generality, we assume that the applied traction $\mathbf{F}$ on Γ_N, can be expressed from the single term separated representation, i.e.

$$\mathbf{F}^k(x,y,z) = \mathbf{F}^k_{x,y}(x,y)\circ\mathbf{F}^k_z(z). \tag{3.31}$$

Using the previous expressions, Eq. (3.22) reads

$$\int_\Omega \rho\mathbf{u}^*\cdot\frac{\mathbf{P}^{k+1}\circ\mathbf{T}^{k+1}}{\Delta t^2}\,d\mathbf{x} + \int_\Omega \boldsymbol{\varepsilon}(\mathbf{u}^*)\cdot\left(\mathbf{C}\,\boldsymbol{\varepsilon}^h_{PT}\right)\,d\mathbf{x} =$$

$$-\int_\Omega \rho\mathbf{u}^*\cdot\frac{\mathbf{u}^{k+1}_{n-1}-2\mathbf{u}^k+\mathbf{u}^{k-1}}{\Delta t^2}\,d\mathbf{x} - \int_\Omega \boldsymbol{\varepsilon}(\mathbf{u}^*)\cdot\left(\mathbf{C}\,\boldsymbol{\varepsilon}^h_{n-1}\right)\,d\mathbf{x} + \int_{\Gamma_N}\mathbf{u}^*\cdot\mathbf{F}^k\,d\mathbf{x}. \tag{3.32}$$

As both $\mathbf{P}^{k+1}$ and $\mathbf{T}^{k+1}$ are unknown, problem (3.32) becomes nonlinear and consequently requires an appropriate linearization strategy. An alternated directions fixed point strategy is considered that by assuming $\mathbf{T}^{k+1}$ known calculates $\mathbf{P}^{k+1}$ and from the last updates $\mathbf{T}^{k+1}$. The process continues until reaching convergence (the fixed point).

When assuming $\mathbf{T}^{k+1}$ known the test displacement reads

$$\mathbf{u}^*(x,y,z) = \begin{pmatrix} p^*_u(x,y)\cdot t^{k+1}_u(z) \\ p^*_v(x,y)\cdot t^{k+1}_v(z) \\ p^*_w(x,y)\cdot t^{k+1}_w(z) \end{pmatrix} = \mathbf{P}^*\circ\mathbf{T}^{k+1}, \tag{3.33}$$

that introduced into the weak form (3.32) results in a 2D problem involving the in-plane coordinates that allows calculating $\mathbf{P}^{k+1}$. Now, assuming that last known, the test displacement becomes

$$\mathbf{u}^*(x,y,z) = \begin{pmatrix} p^{k+1}_u(x,y)\cdot t^*_u(z) \\ p^{k+1}_v(x,y)\cdot t^*_v(z) \\ p^{k+1}_w(x,y)\cdot t^*_w(z) \end{pmatrix} = \mathbf{P}^{k+1}\circ\mathbf{T}^*, \tag{3.34}$$

that introduced at its turn into the weak form (3.32) results in a 1D problem involving the thickness, whose solution results in $\mathbf{T}^{k+1}$. As previously indicated the

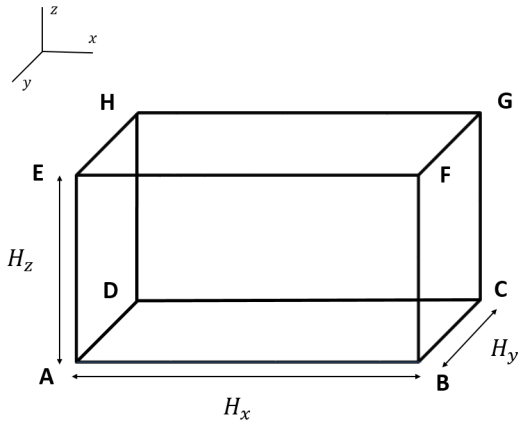

Figure 3.1 – *Problem geometry.*

iteration procedure continues until reaching the convergence characterized by

$$\frac{\left(\int_\Omega \left(\mathbf{P}_p^{k+1} \circ \mathbf{T}_p^{k+1} - \mathbf{P}_{p-1}^{k+1} \circ \mathbf{T}_{p-1}^{k+1}\right)^2 d\mathbf{x}\right)^{1/2}}{\left(\int_\Omega \left(\mathbf{P}_p^{k+1} \circ \mathbf{T}_p^{k+1}\right)^2 d\mathbf{x}\right)^{1/2}} < \epsilon, \tag{3.35}$$

where p refers to the fixed point iteration and ϵ is a small enough threshold value.

Similarly the enrichment procedure stops when the criterion

$$\frac{\left(\int_\Omega \left(\mathbf{U}_{xy}^{N_{k+1},k+1} \circ \mathbf{U}_z^{N_{k+1},k+1}\right)^2 d\mathbf{x}\right)^{1/2}}{\left(\int_\Omega \left(\mathbf{U}_{xy}^{1,k+1} \circ \mathbf{U}_z^{1,k+1}\right)^2 d\mathbf{x}\right)^{1/2}} < \tilde{\epsilon}, \tag{3.36}$$

is fulfilled, with $\tilde{\epsilon}$ another small enough threshold value.

3.1.4 Numerical validation

3.1.4.1 Dynamics of an homogeneous plate

We consider the problem defined in the domain Ω depicted in Fig. 3.1, with $H_x = H_y = 3m$ and $H_z = 0.1m$. In the first case study, the material occupying Ω is assumed homogeneous.

Boundary conditions are given by: $\mathbf{u} = (0,0,0)$ on the face ADHE; $\mathbf{u} = (free, 0, free)$ on the faces ABFE and DCGH; $\mathbf{F}(\mathbf{t}) = (0,0,A\sin(\omega t))$ on face BCGF, with $A = 10^8$, $\omega = 20\pi$ as depicted in Fig. 3.2.

The material properties are defined in Table 3.1, where E is the Young modulus, ν the Poisson coefficient and ρ the material density.

Figs. 3.3 and 3.4 compare the stability of standard explicit Q8-3D finite elements (fully explicit separated representations with equivalent discretizations lead to the same results) and the hybrid scheme just proposed, for different values of the

Table 3.1 – *Material properties.*

E (N/m^2):	$2\ 10^{11}$
ν:	0.25
ρ (kg/m^3):	8000

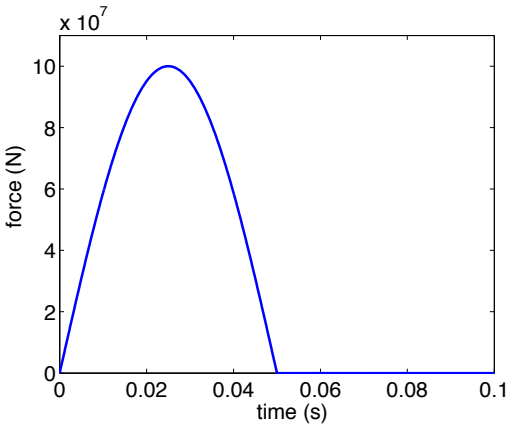

Figure 3.2 – *Loading.*

in-plane and out-of-plane mesh sizes, L_{xy} and L_z respectively. As it can noticed computed results reflect the stability conditions given by Eqs. (3.19) and (3.20). It is important to note that when considering fully explicit schemes, the stability is found being prescribed by the mesh size related to the thickness direction, however, when considering the hybrid schema the stability becomes given by the in-plane characteristic mesh size that, being much larger than the one related to the thickness, makes integration more efficient.

To validate the hybrid approach (only in what concerns accuracy and stability, because issues related to computing time savings were addressed in [Bognet *et al.* 2012]), the computed solution is compared with both explicit and implicit 3D finite elements integration with a time step (in the explicit case) guaranteeing the integration stability. The simulation parameters are the ones introduced previously concerning the material properties, and the ones concerning the remaining simulation parameters are indicated in Table 3.2, where N_x, N_y and N_z refer to the number of elements involved in the discretization of directions x, y and z.

Fig. 3.5 depicts the time evolution of the vertical displacement w at the central point on segment FG when using different integration schemes. The solution obtained by using the hybrid strategy agrees in minute with the one obtained by using the finite element method and considered as reference for comparison purposes.

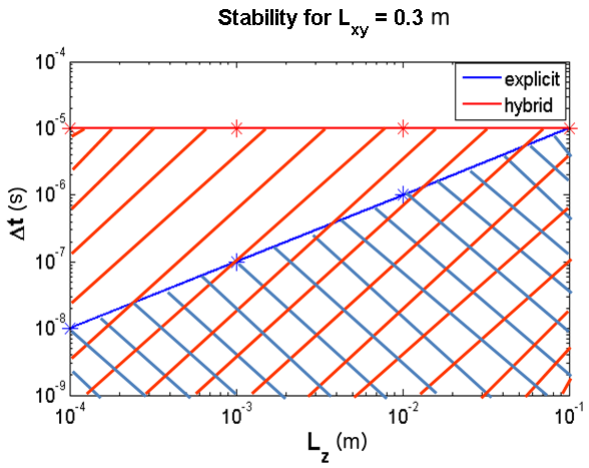

Figure 3.3 – *Stability analysis for a given in-plane characteristic mesh size* L_{xy}.

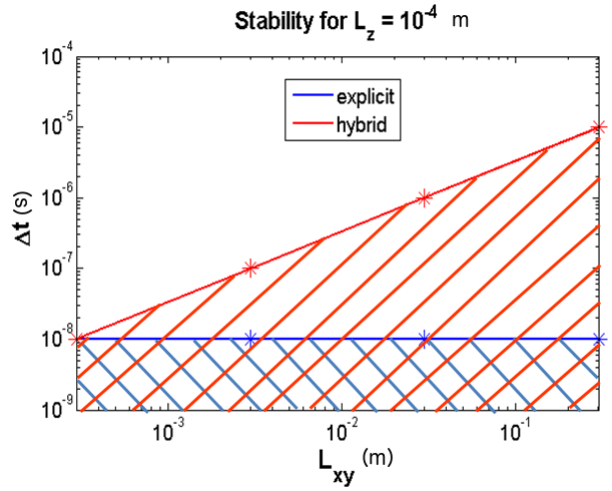

Figure 3.4 – *Stability analysis for a given out-of-plane characteristic mesh size* L_z.

Table 3.2 – *Simulation parameters.*

H_x:	$3\,m$
H_y:	$3\,m$
H_z:	$0.1\,m$
N_x:	10
N_y:	2
N_z:	10
Δt:	$10^{-6}\,s$

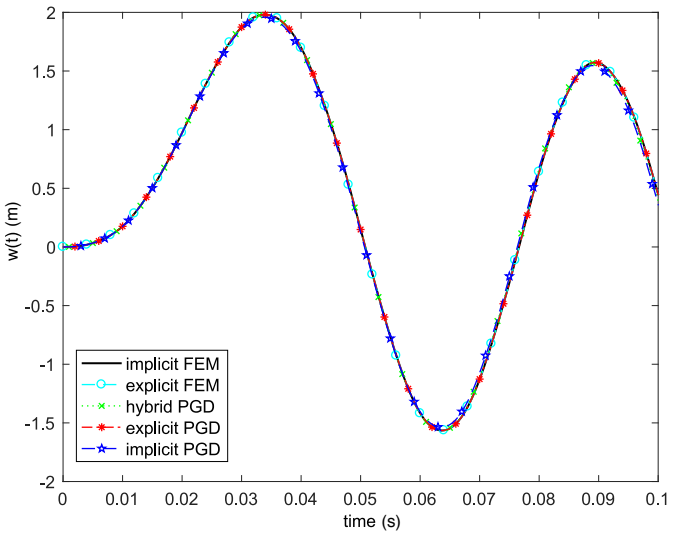

Figure 3.5 – *Vertical displacement at the central point of segment FG.*

3.1.4.2 Considering richer out-of-plane approximations

In order to check the stability of the proposed technique for addressing richer out-of-plane representations, we consider that the domain depicted in Fig. 3.1 consists now in a laminated composed of 8 anisotropic plies $[0, 45, -45, 90]_S$. The applied force now writes again $\mathbf{F}(\mathbf{t}) = \big(0, 0, A\sin(\omega t)\big)$ and applies on the face BCGF, with $A = 10^8$ but now with $\omega = 200\pi$, as depicted in Fig. 3.6.

The mechanical properties of the 0°-ply are given in Table 3.3, where E is the Young modulus, ν the Poisson coefficient, G the shear modulus and ρ the density. The subscripts indicate respectively the proprieties along the longitudinal direction of the fibers (1), the in-plane transverse direction (2) and the out-of-plane direction (3).

In the present case the elastic constitutive equation becomes orthotropic and using again Voigt notation it reads

$$\begin{bmatrix} \varepsilon_{xx} \\ \varepsilon_{yy} \\ \varepsilon_{zz} \\ \gamma_{yz} \\ \gamma_{xz} \\ \gamma_{xy} \end{bmatrix} = \begin{bmatrix} \frac{1}{E_1} & -\frac{\nu_{12}}{E_1} & -\frac{\nu_{13}}{E_1} & 0 & 0 & 0 \\ -\frac{\nu_{12}}{E_1} & \frac{1}{E_2} & -\frac{\nu_{23}}{E_2} & 0 & 0 & 0 \\ -\frac{\nu_{13}}{E_1} & -\frac{\nu_{23}}{E_2} & \frac{1}{E_3} & 0 & 0 & 0 \\ 0 & 0 & 0 & \frac{1}{G_{23}} & 0 & 0 \\ 0 & 0 & 0 & 0 & \frac{1}{G_{13}} & 0 \\ 0 & 0 & 0 & 0 & 0 & \frac{1}{G_{12}} \end{bmatrix} \begin{bmatrix} \sigma_{xx} \\ \sigma_{yy} \\ \sigma_{zz} \\ \sigma_{yz} \\ \sigma_{xz} \\ \sigma_{xy} \end{bmatrix}. \tag{3.37}$$

We compared the solution obtained using the hybrid strategy with the one obtained using implicit finite elements. An explicit finite element solution was not envisaged because the too small time step induced by the extremely fine through-the-thickness mesh. The simulation parameters are reported in Tables 3.3 and 3.4.

Fig. 3.7 compares the time evolution of the vertical displacement at the middle

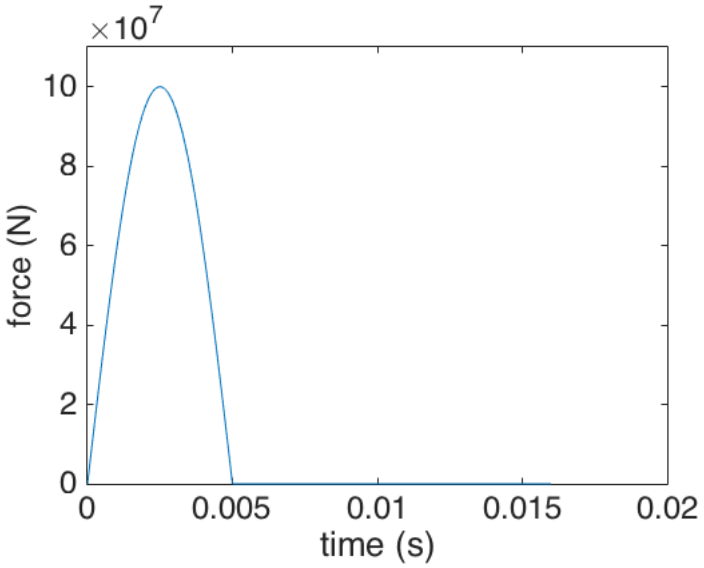

Figure 3.6 – *Loading applying in the composite laminate.*

Table 3.3 – *Mechanical properties of the* 0°*-ply.*

E_1 (N/mm^2):	$120 \cdot 10^3$
E_2 (N/mm^2):	$8.9 \cdot 10^3$
E_3 (N/mm^2):	$8.9 \cdot 10^3$
ν_{12}:	0.35
ν_{13}:	0.35
ν_{23}:	0.32
ν_{21}:	ν_{12}
ν_{31}:	ν_{13}
ν_{32}:	ν_{23}
G_{12} (N/mm^2):	$4.5 \cdot 10^3$
G_{13} (N/mm^2):	$4.5 \cdot 10^3$
G_{23} (N/mm^2):	$5.3 \cdot 10^3$
ρ (kg/m^3):	1750

Table 3.4 – *Simulation parameters.*

H_x:	$250\,mm$
H_y:	$100\,mm$
H_z:	$4\,mm$
N_x:	10
N_y:	2
N_z:	48 (6 elements per ply)
Δt:	$10^{-6}\,s$

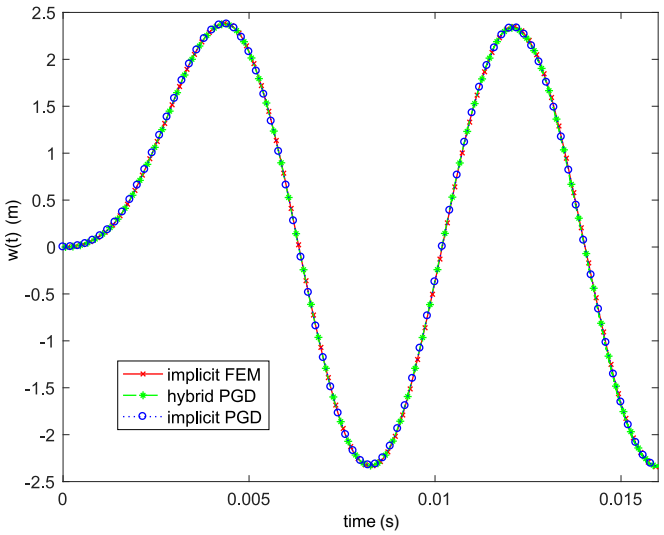

Figure 3.7 – *Vertical displacement at the middle of segment FG.*

of segment FG. It can be noticed again that the hybrid strategy provides an excellent solution compared with the implicit finite element considered as reference.

Finally Fig. 3.8 compares the time evolution of the stress component σ_{zz} at the same location calculated (middle of segment FG) using the finite element method and the implicit/explicit hybrid in-plane-out-of-plane decomposition. Again both solutions match perfectly.

3.1.5 Analysis of computational performances

In order to investigate the performances of the proposed technique we perform in this subsection different analyses. Before, we would like advertising on two facts. First, all computing times are referred to a Matlab implementation on a standard laptop. Thus, computed results allow comparing approaches but not to conclude on absolute performances. Second, for the sake of generality the problem linearity is not taken into account in the sense that at each time step a linear system is solved without taking advantage of the numerous computational profits that linearity offers in the finite element framework. This conservative approach allows extending the main conclusions to the nonlinear case.

We consider again the problem defined in the domain Ω depicted in Fig. 3.1, with $H_x = H_y = 3\,m$, $H_z = 0.1\,m$ and with the material properties defined in Table 3.1, considering the same boundary conditions than in Subsection 3.1.4.1 and the same loading, the last illustrated in Fig. 3.2. In the analyses here addressed, the PGD constructor stopping criterion is set to $\epsilon = \tilde{\epsilon} = 10^{-6}$.

First, we compare the hybrid PGD method with its fully implicit counterpart. The three different meshes defined in Table 3.5 are considered, where again N_x, N_y and N_z refer to the number of elements involved in the discretization of directions x, y and z respectively. For each mesh we compare the computing time employed by

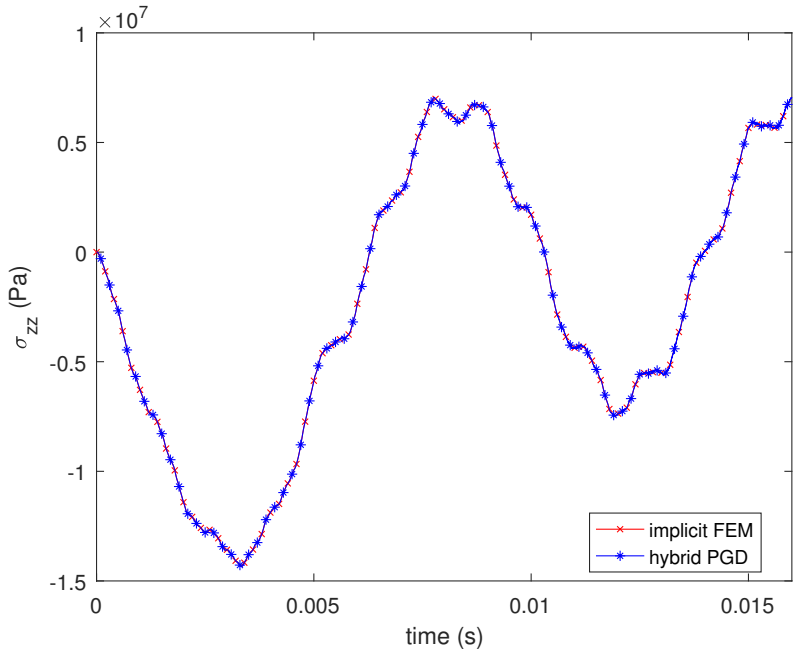

Figure 3.8 – *Stress component $\sigma_{zz}(t)$ at the central point of segment FG. Implicit and hybrid-based solutions are almost superimposed.*

Table 3.5 – *Meshes considered in the analysis of computational performances depicted in Fig. 3.9.*

	Mesh 1	Mesh 2	Mesh 3
N_x:	10	20	30
N_y:	10	20	30
N_z:	100	100	100

both the hybrid and the fully implicit PGD discretizations to solve the problem in the time interval $[0, 400\Delta t]$, with the time-step $\Delta t = \frac{10^{-5}}{3}\, s$ for all the simulations.

Results presented in Fig. 3.9 prove that, as expected, when using the same time-step the hybrid method proceeds faster than the implicit one. Later, in order to take advantage of the superior stability of fully implicit discretizations, time steps will be selected differently for ensuring an equivalent accuracy, in order to compare computing costs in a more appropriate manner.

Now, we perform a comparison between the three PGD formulations (explicit, hybrid and implicit) in the time interval $[0, 400\Delta t]$, with $\Delta t = 10^{-7}\, s$ to ensure the stability of the explicit time integration. Results for the three meshes in Table 3.6 are presented in Fig. 3.10. As expected the computational cost of the hybrid formulation is in between the one of explicit and implicit time integrations.

We have already proved in Figs. 3.3 and 3.4 that the stability domain of the

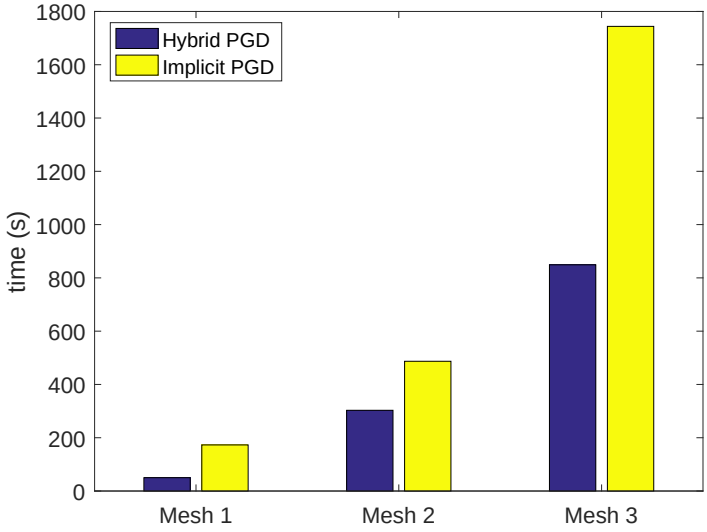

Figure 3.9 – *Hybrid versus implicit PGD formulations.*

Table 3.6 – *Meshes considered in the analysis of computational performances depicted in 3.10.*

	Mesh 4	Mesh 5	Mesh 6
N_x:	10	20	30
N_y:	10	20	30
N_z:	50	50	50

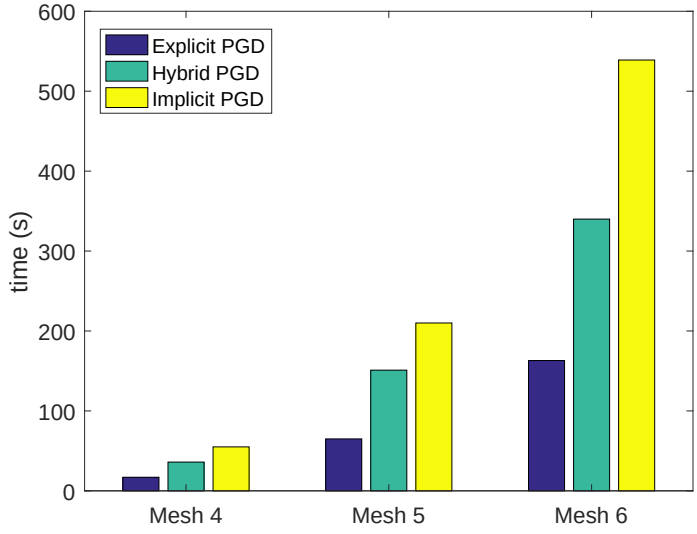

Figure 3.10 – *Comparing explicit, hybrid and implicit PGD formulations.*

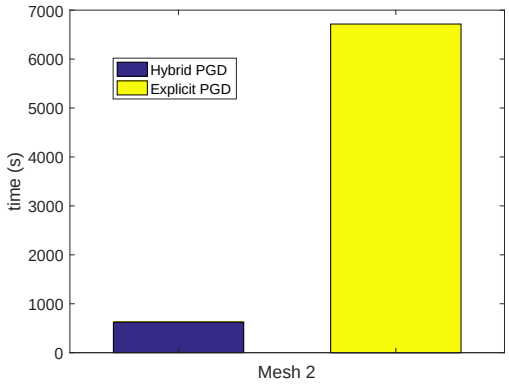

Figure 3.11 – *Hybrid versus explicit PGD formulations.*

hybrid formulation does not depend on the mesh size associated with the thickness direction, so that the hybrid simulation proceeds faster than the one performed using a fully explicit formulation by using a larger time step in the hybrid integration.

In order to prove it, we perform a simulation using 'Mesh 2" in Table 3.5, in the time interval $[0, 4]\,ms$. We use as time steps for the explicit and the hybrid methods respectively $\Delta t_{ex} = 10^{-7}\,s$ and $\Delta t_{hy} = 10^{-5}\,s$, ensuring the stability of both schemes. Results shown in Fig. 3.11 reveal as expected that the higher time step considered in the hybrid integration induces significant computing time savings.

The last analysis aims at taking advantage of the superior stability performances of the implicit formulation, that a priori can use larger time-steps than the ones of explicit and hybrid formulations that are only conditionally stables. However, here not only stability issues are addressed but also the accuracy of the computed solutions.

Thus, in the present numerical analysis we consider the mesh defined Table 3.7 and the time interval $[0, T]$ with $T = 6\,ms$, and consider as *reference solution* the one computed using an explicit FEM scheme with a very fine time-step $\Delta t = 10^{-7}\,s$, ensuring both stability and accuracy, both performances having been checked. Fig. 3.12 compares the computational cost related to FEM and PGD explicit time integrations. As expected the separated representation involved in the PGD formulation allows better performances.

Then the problem is solved using first the hybrid scheme with a time step $\Delta t = 2 \cdot 10^{-5}\,s$ that ensures its stability and implicit (PGD and FEM) time integrations using higher time steps. For each solution we consider the computational cost as well as the error E with respect to the reference solution, computed from

$$E = \frac{\left(\int_0^T \int_\Omega (\mathbf{u} - \mathbf{u}_{ref})^2 \, d\mathbf{x} dt\right)^{\frac{1}{2}}}{\left(\int_0^T \int_\Omega \mathbf{u}_{ref}^2 d\mathbf{x} dt\right)^{\frac{1}{2}}}. \tag{3.38}$$

Table 3.8 compares the different solutions, proving that: (i) implicit PGD and

Table 3.7 – *Mesh used in the results described in Fig. 3.12 and Table 3.8.*

	Mesh 7
N_x:	10
N_y:	10
N_z:	90

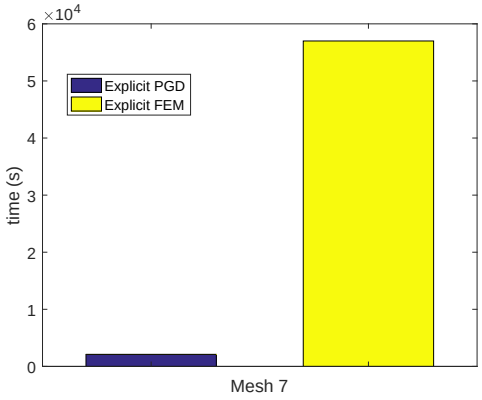

Figure 3.12 – *Explicit PGD versus explicit FEM.*

FEM integrations lead to almost the same solutions, being the ones related to PGD less computationally expensive; and (ii) implicit simulations related to the same computational cost than hybrid simulation produce larger errors, for the analyzed case.

3.1.6 Conclusions

This first part of the chapter proposed a new time discretization scheme for solving 3D dynamical problems defined in degenerated domains, that is, domains in which one of its characteristic dimensions is much smaller than the other ones, as it is the case when considering plates or shells.

A first complexity reduction is attained by considering an in-plane-out-of-plane separated representation that allows reducing the original 3D complexity to the one characteristic of 2D plate or shells models, even if the computed solution is fully 3D and any hypothesis is introduced. Such separated representation allows the use of extremely fine descriptions along the thickness direction.

However, such decomposition when combined with explicit time integrations has a major handicap, the too small size of the discretization involved in the thickness direction implies an extremely small time step for ensuring stability. In this work we circumvent such a drawback by using an implicit (unconditionally stable) through-the-thickness discretization whereas a standard explicit scheme is considered for treating the in-plane operators. Thus, the stability is dictated by the in-plane mesh

Table 3.8 – *Hybrid and implicit PGD integrations versus a standard implicit finite element formulation (using different time-steps).*

		Time	Error
$\Delta t = 2 \cdot 10^{-5}\, s$	Hybrid PGD:	$65\, s$	$8.3 \cdot 10^{-3}$
	Implicit PGD:	$203\, s$	$8.4 \cdot 10^{-3}$
	Implicit FEM:	$746\, s$	$8.4 \cdot 10^{-3}$
$\Delta t = 4 \cdot 10^{-5}\, s$	Implicit PGD:	$185\, s$	$1.66 \cdot 10^{-2}$
	Implicit FEM:	$363\, s$	$1.66 \cdot 10^{-2}$
$\Delta t = 6 \cdot 10^{-5}\, s$	Implicit PGD:	$145\, s$	$2.47 \cdot 10^{-2}$
	Implicit FEM:	$236\, s$	$2.47 \cdot 10^{-2}$
$\Delta t = 8 \cdot 10^{-5}\, s$	Implicit PGD:	$88\, s$	$3.27 \cdot 10^{-2}$
	Implicit FEM:	$174\, s$	$3.27 \cdot 10^{-2}$
$\Delta t = 10^{-4}\, s$	Implicit PGD:	$63\, s$	$4.05 \cdot 10^{-2}$
	Implicit FEM:	$146\, s$	$4.05 \cdot 10^{-2}$

size, much coarser than the one employed in the thickness direction. It is important to note that, even if a part of the whole scheme remains implicit, it only affects one dimension and then its solution is extremely fast and cheap.

The inclusion of progressive damage models combined with dynamical effects constitutes a work in progress, where the separated representations seems an appealing option to better represent damage effects along the laminate thickness and where explicit time integrations are usually employed in industrial applications.

3.2 From linear to nonlinear PGD-based parametric structural dynamics

Introduction The second part of the chapter analyzes different integration schemes of solid dynamics in the frequency domain involving the Proper Generalized Decomposition –PGD–. The last framework assumes for the solution a parametric dependency with respect to frequency. This procedure allowed introducing other parametric dependences related to loading, geometry and material properties. However, in these cases affine decompositions are required for an efficient computation of separated representations. A possibility for circumventing such difficulty consists in combining modal and harmonic analysis for defining an hybrid integration scheme. Moreover, such a procedure, as proved in the present work, can be easily generalized to address nonlinear parametric dynamics.

We revisit in next subsection, for a sake of completeness, the case of linear dynamics and the harmonic-modal hybrid approach developed in [Malik *et al.* 2018b].

This second part of the chapter and all the results presented in it correspond to

the following paper:

- G. Quaranta, C. Argerich Martin, R. Ibañez, J.L. Duval, E. Cueto, F. Chinesta, *From linear to nonlinear parametric structural dynamics*, Comptes rendus Mecanique, **347**:5, 2019.

3.2.1 Classical linear dynamics in the time and frequency domains

The general, semi-discretized form of the linear solid dynamics equations, writes

$$\mathbf{M}\frac{d^2\mathbf{U}(t)}{dt^2} + \mathbf{C}\frac{d\mathbf{U}(t)}{dt} + \mathbf{K}\mathbf{U}(t) = \mathbf{F}(t), \tag{3.39}$$

where $\mathbf{M}$, $\mathbf{C}$ and $\mathbf{K}$ are respectively the mass, damping and stiffness matrices. Mass and stiffness matrices are usually positive definite. $\mathbf{U}$ represents the vector that contains the nodal displacements and $\mathbf{F}$ the nodal excitations (forces). The problem boundary conditions were incorporated when the space discretization leading to Eq. (3.39) was performed. This equation can be obtained through any suitable mesh-based discretization technique like, for instance, the Finite Element Method, and can be solved as soon as the displacements and velocities are specified at the initial time.

By moving to the frequency-domain through the Fourier transform $\mathcal{F}(\bullet)$—denoting $\hat{\mathbf{F}}(\omega) = \mathcal{F}(\mathbf{F}(t))$ and $\hat{\mathbf{U}}(\omega) = \mathcal{F}(\mathbf{U}(t))$—, it results

$$\left(-\omega^2\mathbf{M} + \mathrm{i}\omega\mathbf{C} + \mathbf{K}\right)\hat{\mathbf{U}}(\omega) = \hat{\mathbf{F}}(\omega). \tag{3.40}$$

If damping vanishes, i.e., $\mathbf{C} = \mathbf{0}$ (if it is not the case, it is usually assumed to be proportional, $\mathbf{C} = a_0\mathbf{M} + a_1\mathbf{K}$), and one focuses on the free response of the system, $\hat{\mathbf{F}}(\omega) = \mathbf{0}$, Eq. (3.40) reduces to:

$$\mathbf{K}\hat{\mathbf{U}} = \omega^2\mathbf{M}\hat{\mathbf{U}}. \tag{3.41}$$

This defines an eigenproblem whose result is given by the eigenmodes $\mathbf{P}_i$ and the associated eigenfrequencies ω_i^2. The inverse transform allows coming back to the time domain, $\mathbf{U}(t) = \mathcal{F}^{-1}(\hat{\mathbf{U}}(\omega))$.

3.2.2 The hybrid harmonic-modal approach

When damping is neglected $\mathbf{C} = \mathbf{0}$ (or when proportional damping is considered $\mathbf{C} = a_0\mathbf{M} + a_1\mathbf{K}$) the single-parameter (frequency) dynamic equation reads

$$\left(-\omega^2\mathbf{M} + \mathbf{K}\right)\hat{\mathbf{U}}(\omega) = \hat{\mathbf{F}}(\omega). \tag{3.42}$$

We now consider matrix $\mathbf{P}$ diagonalizing matrices $\mathbf{M}$ and $\mathbf{K}$. In other words,

$$\begin{cases} \mathbf{P}^T\mathbf{M}\mathbf{P} = \mathbb{M} \\ \mathbf{P}^T\mathbf{K}\mathbf{P} = \mathbb{K} \end{cases},$$

where $\mathbb{M}_{ij} = m_{ii}\delta_{ij}$ and $\mathbb{K}_{ij} = k_{ii}\delta_{ij}$. Here, δ_{ij} represents the Kroenecker's delta, i.e., $\mathbb{M}$ and $\mathbb{K}$ become diagonal with entries m_{ii} and k_{ii}, respectively.

Such a choice implies that the system is no longer described in terms of its nodal degrees of freedom but rather in terms of the modal content. Both are formally related through the linear transformation

$$\hat{\mathbf{U}}(\omega) = \mathbf{P}\boldsymbol{\xi}(\omega). \tag{3.43}$$

Thus, the dynamical problem reduces to [Malik *et al.* 2018b]

$$\left(-\omega^2\mathbb{M} + \mathbb{K}\right)\boldsymbol{\xi}(\omega) = \mathbf{P}^T\hat{\mathbf{F}}(\omega) = \hat{\mathbf{f}}(\omega), \tag{3.44}$$

that results in a system of N_n decoupled algebraic equations (N_n being the size of matrices $\mathbf{M}$ and $\mathbf{K}$)

$$\left(-\omega^2 m_{ii} + k_{ii}\right)\xi_i(\omega) = \hat{f}_i(\omega), \qquad i = 1, 2, \ldots, N_n, \tag{3.45}$$

from which it results

$$\xi_i(\omega) = \frac{\hat{f}_i(\omega)}{(-\omega^2 m_{ii} + k_{ii})}, \qquad i = 1, 2, \ldots, N_n, \tag{3.46}$$

that allows calculating the nodal amplitudes from Eq. (3.43), i.e. $\hat{\mathbf{U}}(\omega) = \mathbf{P}\boldsymbol{\xi}(\omega)$.

Thus, the space-frequency separated representation reads

$$\hat{\mathbf{U}}(\omega) = \sum_{i=1}^{N_n} \mathbf{Z}_i\xi_i(\omega), \tag{3.47}$$

where $\mathbf{Z}_i$ is the i-column of matrix $\mathbf{P}$.

The obtention of $\hat{\mathbf{U}}(\omega)$ allows us to come back to the time domain $\mathbf{U}(t)$ by applying an inverse Fourier transform,

$$\mathbf{U}(t) = \mathcal{F}^{-1}(\hat{\mathbf{U}}(\omega)).$$

Remark. As it is usual when using harmonic analysis, the forced time response can be recovered at any time, except during the transient regime.

It is important to highlight—this will be crucial later when addressing nonlinear dynamics—that each term $\xi_i(\omega)$ involves transformed nodal forces, that is, nodal forces affected by the transformation matrix $\mathbf{P}$. Thus, Eq. (3.47) represents a canonical space-frequency-loading separated representation, that only makes use of a proportional damping assumption.

3.2.3 Nonlinear dynamics

In the nonlinear case, the general semi-discretized equilibrium equation writes

$$\mathbf{M}\frac{d^2\mathbf{U}(t)}{dt^2} + \mathbf{C}\frac{d\mathbf{U}(t)}{dt} + \mathbf{K}\mathbf{U}(t) - \mathbf{H}(\mathbf{U}) = \mathbf{F}(t),$$

where the nonlinear contribution is grouped in the vector $\mathbf{H}(\mathbf{U})$ and again a proportional damping is assumed.

The simplest linearization of this equation consists in an explicit evaluation of the nonlinear term $\mathbf{H}(\mathbf{U})$ at the last converged iteration. For the sake of notational simplicity it will be denoted by $\mathbf{U}^-(t)$. Thus, as soon as the nonlinear contribution is assumed known, it can be moved to the right hand member, i.e.,

$$\mathbf{M}\frac{d^2\mathbf{U}(t)}{dt^2} + \mathbf{C}\frac{d\mathbf{U}(t)}{dt} + \mathbf{K}\mathbf{U}(t) = \mathbf{H}(\mathbf{U}^-(t)) + \mathbf{F}(t). \tag{3.48}$$

An obvious possibility consists in computing the Fourier transform of the right-hand member of Eq. (3.48),

$$\hat{\mathbf{F}}(\omega) = \mathcal{F}(\mathbf{H}(\mathbf{U}^-(t)) + \mathbf{F}(t)),$$

and then to proceed exactly in the same way as in the linear case. However, in order to take benefit of model order reduction, in what follows we present an alternative but equivalent formulation, more adapted to the use of reduced bases.

By invoking the linearity of Fourier transform, we write

$$\hat{\mathbf{F}}(\omega) = \mathcal{F}\left(\mathbf{H}(\mathbf{U}^-(t)) + \mathbf{F}(t)\right) = \mathcal{F}\left(\mathbf{H}(\mathbf{U}^-(t))\right) + \mathcal{F}\left(\mathbf{F}(t)\right) = \hat{\mathbf{F}}^{\mathrm{H}}(\omega) + \hat{\mathbf{F}}^{\mathrm{F}}(\omega),$$

that could be expressed using a piecewise linear approximation basis $N_l(\omega)$ (like the usually considered one in linear finite element analyses)

$$\hat{\mathbf{F}}^{\mathrm{H}}(\omega) = \sum_{l=1}^{\mathtt{L}} \hat{\mathbf{F}}^{\mathrm{H}}(\omega_l) N_l(\omega),$$

or

$$\hat{\mathbf{f}}^{\mathrm{H}}(\omega) = \mathbf{P}^T \hat{\mathbf{F}}^{\mathrm{H}}(\omega).$$

In turn,

$$\hat{\mathbf{F}}^{\mathrm{F}}(\omega) = \sum_{l=1}^{\mathtt{L}} \hat{\mathbf{F}}^{\mathrm{F}}(\omega_l) N_l(\omega),$$

or

$$\hat{\mathbf{f}}^{\mathrm{F}}(\omega) = \mathbf{P}^T \hat{\mathbf{F}}^{\mathrm{F}}(\omega),$$

each one contributing to the solution $\boldsymbol{\xi}(\omega)$ according to

$$\boldsymbol{\xi}(\omega) = \boldsymbol{\xi}^{\mathrm{H}}(\omega) + \boldsymbol{\xi}^{\mathrm{F}}(\omega), \tag{3.49}$$

with

$$\xi_i^{\mathrm{H}}(\omega) = \frac{\sum_{l=1}^{\mathtt{L}} \hat{f}_i^{\mathrm{H}}(\omega_l) N_l(\omega)}{(-\omega^2 m_{ii} + k_{ii})}, \qquad i = 1, 2, \cdots, N_n, \tag{3.50}$$

$$\xi_i^{\mathrm{F}}(\omega) = \frac{\sum_{l=1}^{\mathtt{L}} \hat{f}_i^{\mathrm{F}}(\omega_l) N_l(\omega)}{(-\omega^2 m_{ii} + k_{ii})}, \qquad i = 1, 2, \cdots, N_n. \tag{3.51}$$

Thus, it finally results

$$\hat{\mathbf{U}}(\omega) = \mathbf{P}\boldsymbol{\xi}(\omega) = \hat{\mathbf{U}}^{\mathrm{H}}(\omega) + \hat{\mathbf{U}}^{F}(\omega) = \mathbf{P}\boldsymbol{\xi}^{\mathrm{H}}(\omega) + \mathbf{P}\boldsymbol{\xi}^{F}(\omega),$$

being its time-dependent counterpart

$$\mathbf{U}(t) = \mathbf{U}^{\mathrm{H}}(t) + \mathbf{U}^{\mathrm{F}}(t) = \mathcal{F}^{-1}(\mathbf{P}\boldsymbol{\xi}^{\mathrm{H}}(\omega)) + \mathcal{F}^{-1}(\mathbf{P}\boldsymbol{\xi}^{\mathrm{F}}(\omega)).$$

It is important to highlight that the inverse transform involves terms $\mathcal{T}_{il}$, $i = 1, \ldots, N_n$ and $l = 1, \ldots, \mathtt{L}$, whose form reads

$$\mathcal{T}_{il} \equiv \mathcal{F}^{-1}\left(\frac{N_l(\omega)}{-\omega^2 m_{ii} + k_{ii}}\right),$$

that can be computed offline and stored in memory.

Our numerical experiments reveal that this offline-online procedure does not allow for significant computing time savings when one considers a standard piecewise linear approximation bases. However, by considering reduced bases to approximate functions $\hat{\mathbf{F}}^{\mathrm{H}}(\omega)$ and $\hat{\mathbf{F}}^{\mathrm{F}}(\omega)$, the number of integrals to be performed drastically reduces and the offline-online becomes valuable. These reduced basis are computed offline after an adequate training stage. Moreover, the computational cost for the evaluation of the nonlinear term in the time domain, $\mathbf{H}(\mathbf{U}^{-}(t))$, can be drastically reduced by using empirical interpolation techniques [Barrault *et al.* 2004, Chaturantabut & C. Sorensen 2010, Aguado *et al.* 2017b].

As soon as reduced bases are available in the frequency domain, their counterpart in the time domain is easily computable, and from it, direct Fourier transform could be also computed offline. The use of strategies based on the use of reduced bases constitutes a work in progress.

3.2.4 Numerical results

In this section we use the proposed strategy to address 1D and 2D dynamics. The 1D problem consists in a rod of length L, cross section A, clamped at its left boundary and subjected to an axial load applied on its right boundary as depicted in Fig. 3.13, subjected to homogeneous displacement and velocity initial conditions.

If a linear elastic behavior is assumed, the relation between the stress σ and the strain ε reads

$$\sigma = E\,\varepsilon,$$

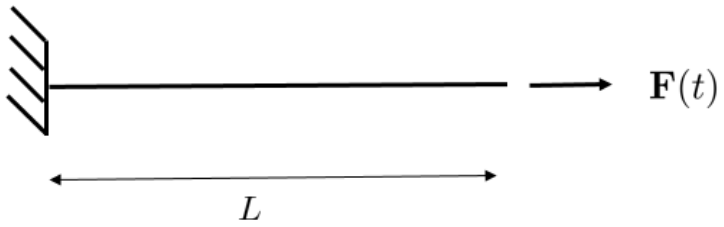

Figure 3.13 – *Simple 1D case study.*

where E is the Young modulus. In the simulations we used $L = 1m$, $E = 2\,10^{11} N/m^2$ and $\rho = 8000 kg/m^3$, where ρ is the density. When damping vanishes or when proportional damping is assumed, the mechanical response is computed from the discrete system

$$\mathbf{M}\frac{d^2\mathbf{U}(t)}{dt^2} + \mathbf{K}\mathbf{U}(t) = \mathbf{F}(t), \tag{3.52}$$

whose expression in the frequency domain is given by Eq. (3.42). However when a nonlinear elastic behavior is assumed, the stress-strain relation reads

$$\sigma = \mathcal{C}(\varepsilon),$$

where $\mathcal{C}$ is a non-linear function of ε. In the numerical test here addressed it is assumed that

$$\sigma = E\,(\varepsilon + c\,\varepsilon^3), \tag{3.53}$$

where c can be considered as a parameter (obviously, when $c = 0$ the nonlinear case reduces to the linear case).

Recalling the linearization described in Subsection 3.2.3, the mechanical response is computed from the discrete system

$$\mathbf{M}\frac{d^2\mathbf{U}(t)}{dt^2} + \mathbf{C}\frac{d\mathbf{U}(t)}{dt} + \mathbf{K}\mathbf{U}(t) = c\,\mathbf{H}(t) + \mathbf{F}(t), \tag{3.54}$$

where $\mathbf{H}(t)$ accounts for the nonlinear contribution.

Thus, using the notation introduced in the previous section, the frequency and time domain solutions read

$$\hat{\mathbf{U}}(\omega; c) = \hat{\mathbf{U}}^{\mathrm{F}}(\omega) + c\hat{\mathbf{U}}^{\mathrm{H}}(\omega), \tag{3.55}$$

that can be seen as a parametric solution involving both the frequency ω and the parameter c controlling the nonlinearity, with its time counterpart expressed from

$$\mathbf{U}(t, c) = \mathcal{F}^{-1}(\hat{\mathbf{U}}^{\mathrm{F}}(\omega)) + c\mathcal{F}^{-1}(\hat{\mathbf{U}}^{\mathrm{H}}(\omega)). \tag{3.56}$$

Both formulations, the one defined in the time domain and the harmonic-modal hybrid formulations are solved in the time interval $I = [0, T]$ with $T = 4s$, the first by using a standard Newmark time-stepping (with time step $\Delta t = 10^{-2}s$)

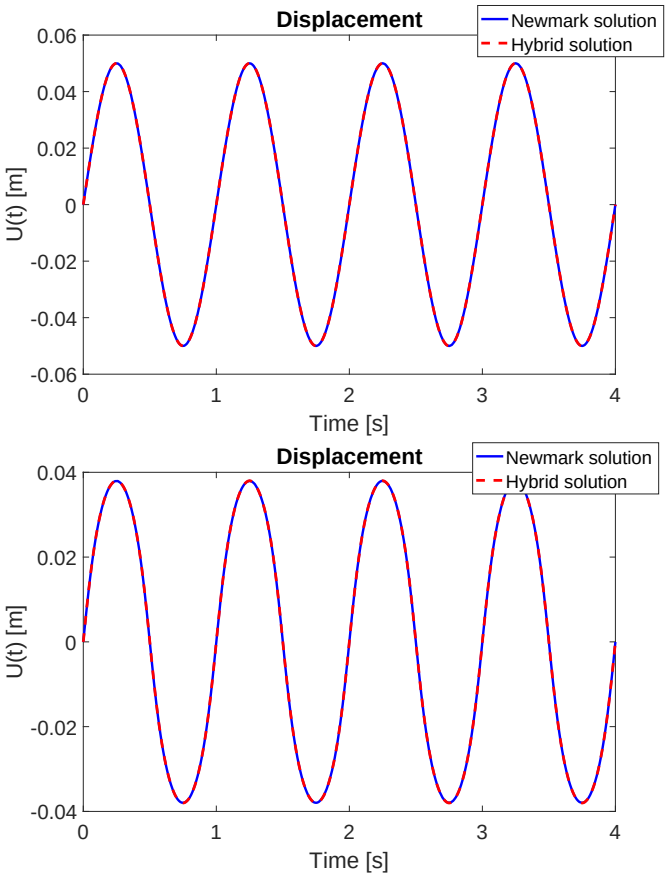

Figure 3.14 – *Displacement at the rod right border for two different values of c: (top) $c = 0$, that corresponds to the linear case and (bottom) $c = 220$.*

[Newmark 1959].

Fig. 3.14 compares both solutions for two different values of the parameter c: $c = 0$ that corresponds to the linear case and for $c = 220$ for the simple harmonic loading $F(t) = 10^{10}\sin(2\pi t)$. The computed results agree perfectly, but when using the hybrid solver significant computing time savings are noticed. These are summarized in Tables 3.9 and 3.10. Moreover, Table 3.9 also reflects the fact that the computing time saving remains almost independent of the considered mesh size.

We also consider a more complex loading scenario, as depicted in Fig. 3.15. It contains a richer frequency spectrum, with $c = 0$ and $c = 4000$. The solutions when using the Newmark ($\Delta t = 10^{-3}\,s$) versus the harmonic-modal hybrid schemes are again in perfect agreement, as Fig. 3.16 reveals, with similar computing time savings, reported in Tables 3.11 and 3.12.

Finally we consider the 2D dynamics of a plate $\Omega = [0, L_x] \times [0, L_y]$, clamped at its left boundary and subjected to an horizontal load applied on its right boundary as depicted in Fig. 3.17, subjected to homogeneous displacement and velocity initial conditions. When a linear elastic behavior is assumed the relation between the stress

Table 3.9 – *Hybrid vs Newmark methods,* $T = 4\,s$.

	Hybrid	Newmark
$N_n = 100$	$1.34\,s$	$5.97\,s$
$N_n = 250$	$3.26\,s$	$14.29\,s$
$N_n = 500$	$7.19\,s$	$39.08\,s$
$N_n = 750$	$11.70\,s$	$68.12\,s$
$N_n = 1000$	$16.33\,s$	$100.75\,s$

Table 3.10 – *Hybrid vs Newmark method,* $N_n = 100$.

	Hybrid	Newmark
$T = 4\,s$:	$1.34\,s$	$5.97\,s$
$T = 8\,s$:	$2.44\,s$	$12.20\,s$
$T = 20\,s$:	$6.32\,s$	$29.75\,s$
$T = 40\,s$:	$13.54\,s$	$59.30\,s$

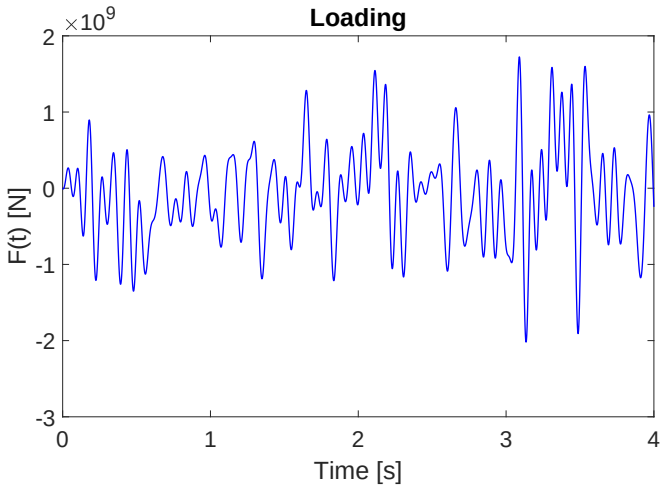

Figure 3.15 – *Loading containing a richer frequency spectrum.*

Table 3.11 – *Hybrid vs Newmark method,* $T = 4\,s$.

	Hybrid	Newmark
$N_n = 100$:	$2.49\,s$	$9.68\,s$
$N_n = 250$:	$6.90\,s$	$23.38\,s$
$N_n = 500$:	$14.28\,s$	$48.26\,s$
$N_n = 750$:	$21.90\,s$	$69.72\,s$
$N_n = 1000$:	$30.13\,s$	$93.11\,s$

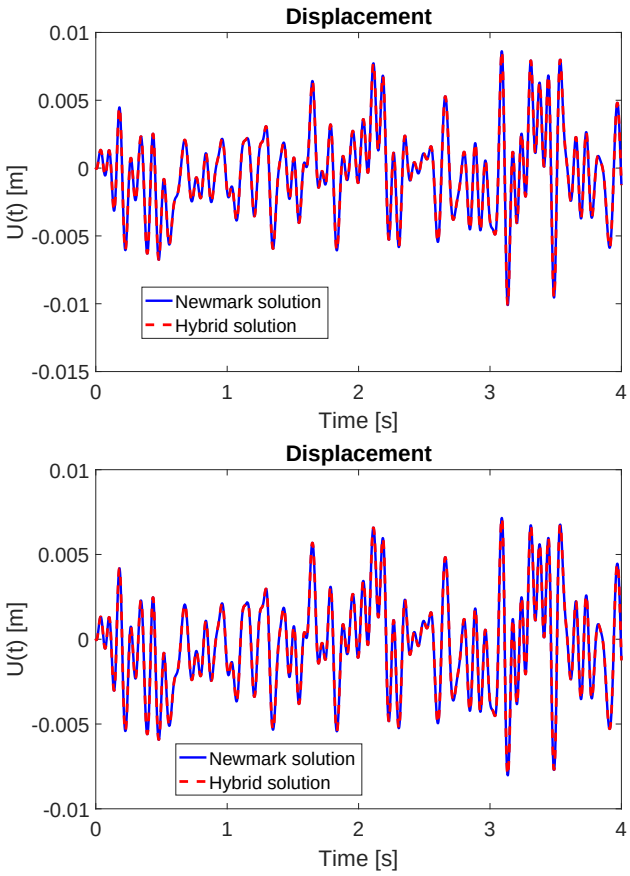

Figure 3.16 – *Displacement at the rod right border for two different values of c: (top)* $c = 0$*, that corresponds to the linear case and (bottom)* $c = 4000$*.*

Table 3.12 – *Hybrid vs Newmark method,* $N_n = 100$*.*

	Hybrid	Newmark
$T = 4\,s$:	$2.49\,s$	$9.68\,s$
$T = 8\,s$:	$4.95\,s$	$21.32\,s$
$T = 20\,s$:	$13.57\,s$	$59.48\,s$
$T = 40\,s$:	$28.29\,s$	$122.23\,s$

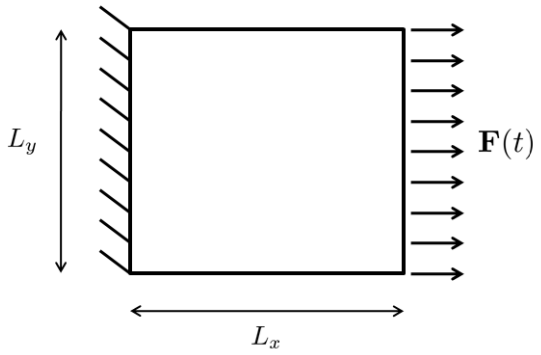

Figure 3.17 – *Simple 2D case study.*

$\boldsymbol{\sigma}$ and the strain $\boldsymbol{\varepsilon}$ reads, by using Voigt notation and plane stress conditions,

$$\begin{bmatrix}\sigma_{xx}\\ \sigma_{yy}\\ \sigma_{xy}\end{bmatrix} = \frac{E}{1-\nu^2}\begin{bmatrix}1 & \nu & 0\\ \nu & 1 & 0\\ 0 & 0 & (1-\nu)/2\end{bmatrix}\begin{bmatrix}\varepsilon_{xx}\\ \varepsilon_{yy}\\ \gamma_{xy}\end{bmatrix}. \tag{3.57}$$

where E is the Young modulus and ν the Poisson coefficient. In the simulations we used $L_x = L_y = 0.5m$, $E = 2\ 10^{11} N/m^2$, $\nu = 0.3$ and $\rho = 8000 kg/m^3$. Similarly to the 1D case, when a nonlinear elastic behavior is assumed, in the numerical test here addressed it is assumed that

$$\begin{bmatrix}\sigma_{xx}\\ \sigma_{yy}\\ \sigma_{xy}\end{bmatrix} = \frac{E}{1-\nu^2}\begin{bmatrix}1 & \nu & 0\\ \nu & 1 & 0\\ 0 & 0 & (1-\nu)/2\end{bmatrix}\begin{bmatrix}\varepsilon_{xx}+c\,\varepsilon_{xx}^3\\ \varepsilon_{yy}+c\,\varepsilon_{yy}^3\\ \gamma_{xy}+c\,\gamma_{xy}^3\end{bmatrix} \tag{3.58}$$

where c can be considered as a parameter (again when $c = 0$ the nonlinear case reduces to the linear case).

As before, both formulations, the one defined in the time domain and the harmonic-modal hybrid formulations are solved in the time interval $I = [0, T]$ with $T = 4s$, the first by using a standard Newmark time-stepping (with time step $\Delta t = 10^{-2}s$).

Figs. 3.18 and 3.19 compares respectively the horizontal displacement along the time at the domain bottom right hand corner and the 2D displacement at a fixed time ($t = 0.27s$) of both solutions for two different values of the parameter c: $c = 0$, that corresponds to the linear case, and $c = 1.5$ for the simple horizontal harmonic loading $F(t) = 10^{11}\sin(2\pi t)$. Again the computed results agree perfectly, but the hybrid solver allows significant computing time savings. These are summarized in Tables 3.13 and 3.14.

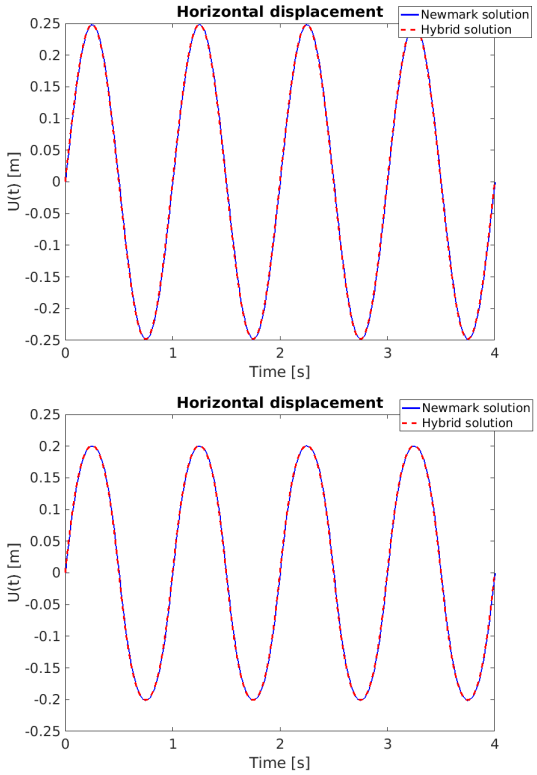

Figure 3.18 – *Horizontal displacement at the domain bottom right hand corner for two different values of c: (top)* $c = 0$*, that corresponds to the linear case and (bottom)* $c = 1.5$.

Table 3.13 – *Hybrid vs Newmark method,* $T = 4\,s$.

	Hybrid	Newmark
$N_n = 2 \cdot 6^2$:	$1.80\,s$	$15.81\,s$
$N_n = 2 \cdot 12^2$:	$6.56\,s$	$69.80\,s$
$N_n = 2 \cdot 18^2$:	$15.15\,s$	$181.25\,s$
$N_n = 2 \cdot 24^2$:	$48.87\,s$	$395.90\,s$

Table 3.14 – *Hybrid vs Newmark method,* $N_n = 2 \cdot 12^2$.

	Hybrid	Newmark
$T = 4\,s$:	$6.56\,s$	$69.80\,s$
$T = 8\,s$:	$9.34\,s$	$127.77\,s$
$T = 12\,s$:	$12.45\,s$	$192.63\,s$
$T = 16\,s$:	$17.54\,s$	$256.60\,s$

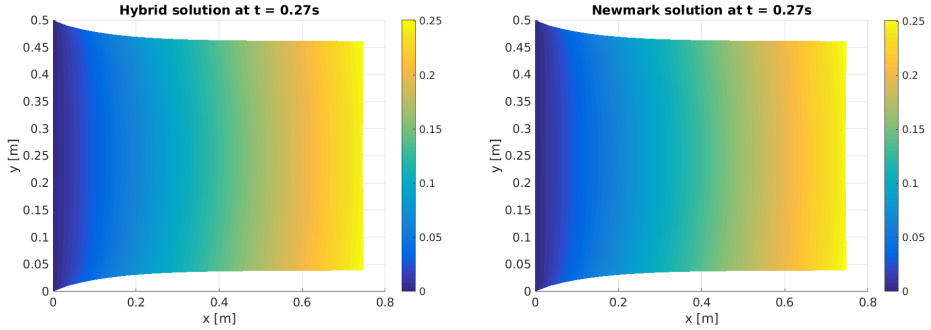

(a)

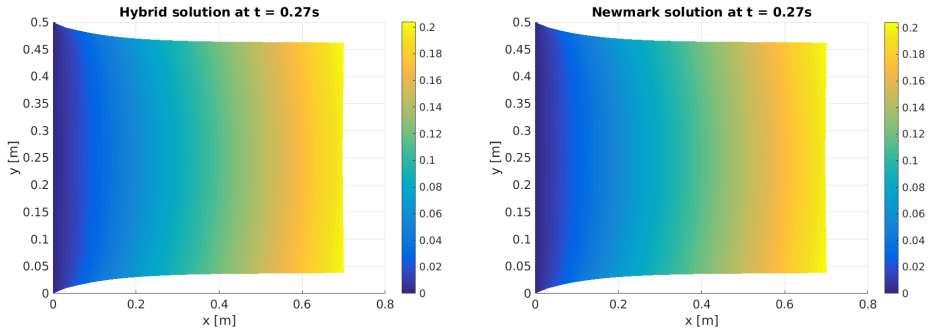

(b)

Figure 3.19 – *Displacement field at* $t = 0.27s$ *for two different values of* c*: (a)* $c = 0$*, that corresponds to the linear case and (b)* $c = 1.5$*.*

3.2.5 Conclusions

In this second part of the chapter we proposed an extension of the hybrid methodology combining harmonic and modal analyses for treating nonlinear parametric dynamics.

The main contribution of the present work is the derivation of a parametric solution in the frequency space. Apart from its natural dependence on the frequency, the just developed method also accounts for other model parameters. More importantly, it explicitly decouples the dependence on the amplitude of nodal loading and it makes possible the solution of nonlinear models combined with simple linearizations.

Preliminary numerical results evidence the potentialities of the proposed technique, while proving its computational efficiency.

Chapter 4

Minimally intrusive MOR techniques in computational structural mechanics of plate geometries

Contents

As we said in the previous chapter most of mechanical systems and complex structures exhibit plate and shell components. Therefore, 2D simulation, based on plate and shell theory, appears as an appealing choice in structural analysis as it allows reducing the computational complexity. Nevertheless, this 2D framework fails for capturing rich physics compromising the usual hypotheses considered when deriving standard plate and shell theories. To circumvent, or at least alleviate this issue, the in-plane-out-of-plane separated representation can be used; that is able to capture rich 3D behaviors while keeping the computational complexity of 2D simulations. However, that procedure it was revealed to be too intrusive for being introduced into existing commercial softwares that generally propose different plate

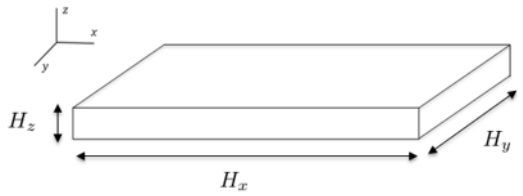

Figure 4.1 – *Example of a plate domain.*

and shell finite elements, even in the case of multilayered composites plates or shells. For this reason in this chapter we propose minimally-intrusive methods which allow integrating 3D descriptions in plate or shell models implemented in any software, without affecting its computational complexity that remains the one related to standard 2D analyses.

4.1 On the coupling of local 3D solutions and global 2D shell theory in structural mechanics

Introduction As experience indicated that in many situations the enriched descriptions are only compulsory locally, in some regions or structure components, in the first part of the chapter we propose an enrichment procedure able to address 3D local behaviors, preserving the direct minimally-invasive coupling with existing plate and shell discretizations. The proposed strategy will be extended to inelastic behaviors and structural dynamics.

This first part of the chapter and all the results presented in it correspond to the following paper:

- G. Quaranta, M. Ziane, F. Daim, E. Abisset-Chavanne, J.L. Duval, F. Chinesta, *On the coupling of local 3D solutions and global 2D shell theory in structural mechanics*, Advanced Modeling and Simulation in Engineering Sciences, **6**:1, 2019.

4.1.1 Elastostatic problem definition

We consider the linear elastostatic problem defined in the plate domain depicted in Fig. 4.1, $\Omega = \Omega_{xy} \times \Omega_z$, with $\Omega_{xy} = [0, H_x] \times [0, H_y]$ and $\Omega_z = [0, H_z]$ in which the thickness (out-of-plane) dimension is much lower than the other ones, i.e. $H_z \ll H_x, H_y$.

As we have already seen in the previous chapters, the linear elastic behavior relating the Cauchy's stress $\boldsymbol{\sigma}$ and the strain $\boldsymbol{\varepsilon}$ tensors reads

$$\boldsymbol{\sigma} = \mathbb{C}\,\boldsymbol{\varepsilon}, \tag{4.1}$$

where $\mathbb{C}$ is the Hooke's fourth order tensor. The relation between strain $\boldsymbol{\varepsilon}$ and displacement $\mathbf{u}$ (with components $\mathbf{u} = (u, v, w)$) writes

$$\boldsymbol{\varepsilon} = \nabla_s \mathbf{u} = \mathbf{G}\mathbf{u}, \tag{4.2}$$

where $\mathbf{G} = \nabla_s \bullet$ is the symmetric gradient operator. Considering an homogeneous and isotropic material and using the Voigt notation, the Hooke's tensor can be written as

$$\mathbf{C} = \frac{E}{(1+\nu)(1-2\nu)} \begin{bmatrix} 1-\nu & \nu & \nu & 0 & 0 & 0 \\ \nu & 1-\nu & \nu & 0 & 0 & 0 \\ \nu & \nu & 1-\nu & 0 & 0 & 0 \\ 0 & 0 & 0 & \frac{(1-2\nu)}{2} & 0 & 0 \\ 0 & 0 & 0 & 0 & \frac{(1-2\nu)}{2} & 0 \\ 0 & 0 & 0 & 0 & 0 & \frac{(1-2\nu)}{2} \end{bmatrix}. \tag{4.3}$$

In absence of volumetric body forces, the displacement field evolution $\mathbf{u}(\mathbf{x})$ for $\mathbf{x} \in \Omega$ is described by the linear momentum balance equation

$$\nabla \cdot \boldsymbol{\sigma} = \mathbf{0}. \tag{4.4}$$

The domain boundary $\partial\Omega$ is partitioned into Dirichlet, Γ_D, and Neumann, Γ_N, boundaries, where displacement $\mathbf{u}_g$ and tractions $\mathbf{T}$ are enforced respectively.

The problem weak form associated to the strong form (4.4) lies in looking for the displacement field $\mathbf{u}$ verifying the Dirichlet boundary conditions such that the weak form

$$\int_\Omega \boldsymbol{\varepsilon}(\mathbf{u}^*) \cdot (\mathbf{C}\,\boldsymbol{\varepsilon}(\mathbf{u}))\, d\mathbf{x} = \int_{\Gamma_N} \mathbf{u}^* \cdot \mathbf{T}\, d\mathbf{x} \tag{4.5}$$

fulfills for any test function $\mathbf{u}^*$, with the trial and test fields defined in appropriate functional spaces.

In this type of domains, plate theory is usually used in order to reduce the general 3D mechanical problem to a 2D one involving the in-plane coordinates only. Two kinds of theories exist: the thin plate theory proposed by Kirchoff [Kirchhoff 1850] which establishes that the normal remains straight and orthogonal to the middle plane after deformation and the thick plate theory proposed by Reissner [Reissner 1945] and Mindlin [Mindlin 1951] which assumes that normals remain straight, but not necessarily orthogonal to the middle plane after deformation.

In both theories the middle plane is taken as the reference plane ($z = 0$) for deriving the plane kinematic equations. In this work, we consider the Reissner-Mindlin theory whose fundamental hypotheses are the following: (i) on the middle plane ($z = 0$) the in-plane displacements vanish, i.e. $u(x, y, z = 0) = v(x, y, z = 0) = 0$, that implies that points located in the middle-plane only moves vertically; (iii) the plate thickness remains unchanged; (iv) the plane stress assumption remains valid,

i.e. $\sigma_{zz} = 0$ and (v) a straight line normal to the undeformed middle plane remains straight but not necessarily orthogonal to the middle plane after deformation.

From these assumptions the displacement field can be written as:

$$\begin{cases} u(x,y,z) = -z\theta_x(x,y) \\ v(x,y,z) = -z\theta_y(x,y) \\ w(x,y,z) = w(x,y) \end{cases} \tag{4.6}$$

where w is the vertical displacement (deflection) of the points on the middle plane and the rotations θ_x and θ_y coincide with the angles followed by the normal vectors contained in the planes xz and yz respectively in their motions.

We define the generalized displacement vector $\hat{\mathbf{u}}$

$$\hat{\mathbf{u}} = [\theta_x, \theta_y, w]^T \tag{4.7}$$

defined at any point on the middle plane.

Injecting plate theory assumptions into the 3D elastostatic problem weak form, Eq. (4.5) reduces to the following 2D formulation [Oñate 2010]

$$\int_{\Omega_{xy}} \hat{\boldsymbol{\varepsilon}}(\hat{\mathbf{u}}^*) \cdot \left(\hat{\mathbf{C}}\, \hat{\boldsymbol{\varepsilon}}(\hat{\mathbf{u}}) \right) d\mathbf{x} = \int_{\partial_N \Omega_{xy}} \hat{\mathbf{u}}^* \cdot \hat{\mathbf{T}}\, d\mathbf{x}, \tag{4.8}$$

whose standard finite element discretization leads to

$$\mathbf{KU} = \mathbf{F} \tag{4.9}$$

where, for notational simplicity, the hat symbol ($\hat{\bullet}$) is omitted. In the previous expression (4.9), $\mathbf{K}$ is the stiffness matrix and $\mathbf{U}$ and $\mathbf{F}$ are the vector of the generalized displacements and forces, the former containing nodal rotations and deflections and the last the dual quantities: the nodal moments and vertical nodal forces. The 3D displacement field can be then recovered by using the relations (4.6).

In many cases, the complexity of the solution makes impossible the introduction of pertinent hypotheses for reducing the dimensionality of the model from 3D to 2D. In that case a fully 3D description seems compulsory and the in-plane-out-of-plane separated representations become particularly suitable.

4.1.2 Enriched formulations

4.1.2.1 PGD-based enriched elements

We assume the 2D mesh defined on the middle plane of a plate geometry Ω, depicted in Fig. 4.2. Our goal here is to address one element of the mesh, for example the one whose boundary is highlighted in red and that is noted by Ω_e, by using a fully 3D description in order to extract its homogenized 9×9 element stiffness matrix corresponding to Ω_e, and therefore fully compatible with the plate kinematics enforced on the element boundary $\partial\Omega_e$.

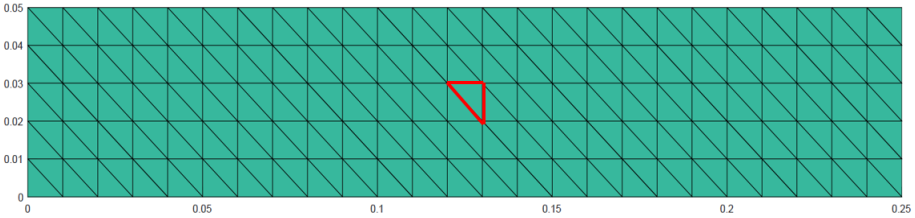

Figure 4.2 – *Plate domain* Ω *and its associated mesh.*

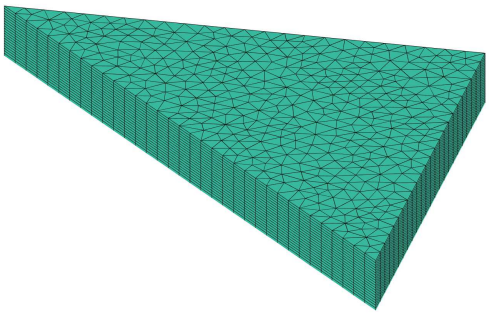

Figure 4.3 – *3D mesh of element* Ω_e.

For that purpose, Ω_e is 3D resolved using the PGD-based in plane-out-of-plane separated representation [Bognet *et al.* 2012, Bognet *et al.* 2014]

$$\mathbf{u}(x,y,z) = \begin{pmatrix} u^e(x,y,z) \\ v^e(x,y,z) \\ w^e(x,y,z) \end{pmatrix} \approx \sum_{i=1}^{N} \begin{pmatrix} u_{xy}^{e,i}(x,y) \cdot u_z^{e,i}(z) \\ v_{xy}^{e,i}(x,y) \cdot v_z^{e,i}(z) \\ w_{xy}^{e,i}(x,y) \cdot w_z^{e,i}(z) \end{pmatrix}. \tag{4.10}$$

or, by using the Hadamard (component-to-component) product,

$$\mathbf{u}^e(x,y,z) \approx \sum_{i=1}^{N} \mathbf{U}_{xy}^{e,i}(x,y) \circ \mathbf{U}_z^{e,i}(z), \tag{4.11}$$

while a kinematics compatible with the plate kinematics (4.6) is enforced on the element boundary. All the other elements in Ω depicted in Fig. 4.2 are described using the standard plate theory, the only 3D resolved is just the Ω_e whose 3D mesh is depicted in Fig. 4.3. The separated representation of the 3D displacement field in Ω_e is denoted by $\mathbf{u}^e = (u^e, v^e, w^e)$, whose first mode consists of the standard plate

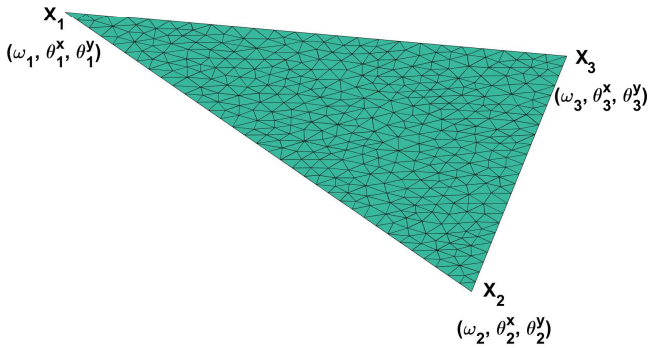

Figure 4.4 – *Nodal degrees of freedom defining the kinematics on* $\partial\Omega_e$.

kinematics

$$\begin{cases} u_{xy}^{e,1}(x,y) = \theta_1^x N_1(x,y) + \theta_2^x N_2(x,y) + \theta_3^x N_3(x,y) \\ v_{xy}^{e,1}(x,y) = \theta_1^y N_1(x,y) + \theta_2^y N_2(x,y) + \theta_3^y N_3(x,y) \\ w_{xy}^{e,1}(x,y) = \omega_1 N_1(x,y) + \omega_2 N_2(x,y) + \omega_3 N_3(x,y) \\ u_z^{e,1}(z) = -z \\ v_z^{e,1}(z) = -z \\ w_z^{e,1}(z) = 1 \end{cases} \tag{4.12}$$

where $N_1(x,y)$, $N_2(x,y)$ and $N_3(x,y)$ are the shape functions related to the 2D linear triangular element Ω_e, and

$$\mathbf{U^e} = (\omega_1, \theta_1^x, \theta_1^y, \omega_2, \theta_2^x, \theta_2^y, \omega_3, \theta_3^x, \theta_3^y) \tag{4.13}$$

are the nine degrees of freedom associated to its three vertices, depicted in Fig. 4.4.

Once the first mode has been imposed, the following modes are constructed as described in Chapter 3 while ensuring that they vanish on the element boundary $\partial\Omega_e$. The last condition can be enforced by using the so-called bubble function that results from the product of the three triangle shape functions $\mathcal{B}(x,y) = N_1(x,y)N_2(x,y)N_3(x,y)$ (even if other alternatives exist for that purpose [Chinesta *et al.* 2014a]), i.e. $\forall i > 1$

$$\begin{cases} u_{xy}^{e,i}(x,y) = \mathcal{B}(x,y) P_x^i(x,y) \\ v_{xy}^{e,i}(x,y) = \mathcal{B}(x,y) P_y^i(x,y) \\ w_{xy}^{e,i}(x,y) = \mathcal{B}(x,y) P_z^i(x,y) \\ u_z^{e,i}(z) = T_x^i(z) \\ v_z^{e,i}(z) = T_y^i(z) \\ w_z^{e,i}(z) = T_z^i(z) \end{cases} \tag{4.14}$$

Thus, the solution on the triangle boundary $\partial\Omega_e$ is given by the first mode, that is the standard plate kinematics, whereas inside Ω_e the solution becomes enriched with models that can describe richer kinematics than the one related to standard

plate kinematics.

In order to extract the effective enriched 9×9 element stiffness $\mathbf{K}^e$ (related to element Ω_e) to be assembled into the global stiffness matrix involved in the algebraic system (4.9), we consider the element average

$$\langle \bullet \rangle = \int_{\Omega_e} \bullet \, d\mathbf{x}, \tag{4.15}$$

from which the element elastic energy $\mathcal{U}^e$ becomes

$$\mathcal{U}^e = \left\langle \boldsymbol{\varepsilon}^{e^T} \boldsymbol{\sigma}^e \right\rangle = \left\langle \boldsymbol{\varepsilon}^{e^T} \mathbf{C} \boldsymbol{\varepsilon}^e \right\rangle. \tag{4.16}$$

Now, with the strain defined from (4.2) we assume the existence of a localization tensor $\mathbf{L}$ such that

$$\mathbf{u}^e = \mathbf{L}\mathbf{U}^e, \tag{4.17}$$

that using Eq. (4.2) results

$$\boldsymbol{\varepsilon}^e = \nabla_s \mathbf{u}^e = \mathbf{G}\mathbf{L}\mathbf{U}^e, \tag{4.18}$$

where $\mathbf{U}^e$, as previously indicated, represents the plate generalized displacement degrees of freedom defined in (4.13).

Thus, the components of the localization tensor result from the elastic problem solution in Ω_e by prescribing the canonical boundary displacements, i.e. $\mathbf{U}_1^e = (1,0,0,0,0,0,0,0,0)$, $\mathbf{U}_2^e = (0,1,0,0,0,0,0,0,0)$, and so on, with nine associated 3D elastic problems solved by using the PGD-based in-plane-out-of-plane separated representation.

Then, by defining $\mathbf{M} = \mathbf{G}\mathbf{L}$ we obtain

$$\mathcal{U}^e = \left\langle \mathbf{U}^{e^T} \mathbf{M}^T \mathbf{C} \mathbf{M} \mathbf{U}^e \right\rangle = \mathbf{U}^{e^T} \left\langle \mathbf{M}^T \mathbf{C} \mathbf{M} \right\rangle \mathbf{U}^e, \tag{4.19}$$

which allows defining the element stiffness matrix $\mathbf{K}^e$ as

$$\mathbf{K}^e = \left\langle \mathbf{M}^T \mathbf{C} \mathbf{M} \right\rangle. \tag{4.20}$$

In order to check the procedure, the stiffness matrix $\mathbf{K}^e$ obtained using the first mode of the displacement expansion is compared to that one corresponding to the plate kinematics. In that case, the resulting stiffness matrix is, as expected, the one related to standard plate theory.

Of course, when considering more modes in the separated representation of the 3D displacement field $\mathbf{u}^e$, the resulting stiffness matrix $\mathbf{K}^e$ differs from the one associated to standard plate theory by including eventual 3D effects ignored in standard plate kinematics. However, in that case the expression of the effective enriched stiffness matrix $\mathbf{K}^e$ depends on the element geometry. To avoid the necessity of calculating online stiffness matrices for each triangle, the PGD rationale allows including different parameters into the separated representation

as mentioned in the previous chapters, [Chinesta *et al.* 2011, Chinesta *et al.* 2013b, Chinesta *et al.* 2015, Bur *et al.* 2016, Chinesta *et al.* 2014b]. The interested reader can refer to [Chinesta *et al.* 2014a] and [Borzacchiello *et al.* 2017] for an intrusive and a non-intrusive approach, respectively (some details for the non-intrusive approach by using the Sparse Subspace Learning – SSL – method are given in Appendix A). In the case here addressed, the natural choice consists of considering the triangle geometry as parameters, and then as extra-coordinates within the PGD rationale.

4.1.2.2 Static condensation based enrichment

In this section, we consider an alternative procedure for computing the homogenized element stiffness matrix using static condensation [Wilson 1974].

We consider again the problem defined in the domain Ω_e depicted in Fig. 4.3. The nodal degrees of freedom used for discretizing the displacement field $\mathbf{u}^e$, $\mathbb{U}^e$, can be decomposed in the ones related to internal nodes $\mathbb{U}_i^e$ and the ones related to nodes located on $\partial\Omega_e$, $\mathbb{U}_b^e$.

Thus, the standard 3D finite element formulation

$$\mathbb{K}^e\mathbb{U}^e = \mathbb{F}^e, \tag{4.21}$$

with

$$\mathbb{K}^e = \begin{pmatrix} \mathbb{K}_{ii}^e & \mathbb{K}_{ib}^e \\ \mathbb{K}_{bi}^e & \mathbb{K}_{bb}^e \end{pmatrix}, \tag{4.22}$$

$$\tag{4.23}$$

can be expressed as

$$\begin{pmatrix} \mathbb{K}_{ii}^e & \mathbb{K}_{ib}^e \\ \mathbb{K}_{bi}^e & \mathbb{K}_{bb}^e \end{pmatrix} \begin{pmatrix} \mathbb{U}_i^e \\ \mathbb{U}_b^e \end{pmatrix} = \begin{pmatrix} \mathbb{F}_i^e \\ \mathbb{F}_b^e \end{pmatrix}. \tag{4.24}$$

Now, by developing the first row of the previous system, the internal degrees of freedom can be expressed from the ones on the element border,

$$\mathbb{U}_i^e = \mathbb{K}_{ii}^{e^{-1}} \left(\mathbb{F}_i^e - \mathbb{K}_{ib}^e \mathbb{U}_b^e\right), \tag{4.25}$$

that inserted in the second leads to

$$\mathcal{K}_{bb}^e \mathbb{U}_b^e = \mathcal{F}_b^e, \tag{4.26}$$

with

$$\mathcal{K}_{bb}^e = \mathbb{K}_{bb}^e - \mathbb{K}_{bi}^e \mathbb{K}_{ii}^{e^{-1}} \mathbb{K}_{ib}^e \tag{4.27}$$

$$\mathcal{F}_b^e = \mathbb{F}_b^e - \mathbb{K}_{bi}^e \mathbb{K}_{ii}^{e^{-1}} \mathbb{F}_i^e. \tag{4.28}$$

Now we enforce on the element border a kinematic compatible with the one of the plate theory, that is, the border nodal displacements $\mathbb{U}_b^e$ are expressed from $\mathbf{U}^e$

Table 4.1 – *Problem parameters.*

H_x: Length in the x direction (mm)	250
H_y: Length in the y direction (mm)	50
H_z: Length in the z direction (mm)	2
E: Young modulus (N/m^2)	$2 \cdot 10^{11}$
ν: Poisson coefficient	0.25

(the plate theory degrees of freedom defined at the triangle vertices as expressed in Eq. (4.13)), according to Eq. (4.6), relation that is expressed in matrix form from $\mathbb{U}_b^e = \mathbf{B}\mathbf{U}^e$.

Thus, Eq. (4.26) can be rewritten as

$$\mathcal{K}_{bb}^e \mathbf{B}\mathbf{U}^e = \mathcal{F}_b^e, \tag{4.29}$$

that premultiplying by $\mathbf{B}^T$ (looking for the Galerkin based discrete system) results

$$\mathbf{B}^T \mathcal{K}_{bb}^e \mathbf{B}\mathbf{U}^e = \mathbf{B}^T \mathcal{F}_b^e, \tag{4.30}$$

that allows extracting the expression of the effective plate element stiffness matrix $\tilde{\mathbf{K}}^e$ and the effective plate nodal forces $\tilde{\mathbf{F}}^e$

$$\tilde{\mathbf{K}}^e = \mathbf{B}^T \mathcal{K}_{bb}^e \mathbf{B} \tag{4.31}$$

$$\tilde{\mathbf{F}}^e = \mathbf{B}^T \mathcal{F}^e. \tag{4.32}$$

Our numerical simulation allowed proving that the effective plate element stiffness matrix $\tilde{\mathbf{K}}^e$ obtained using the just described rationale based on the static condensation coincides with the one previously obtained by using the PGD-based separated representation $\mathbf{K}^e$.

An additional advantage of this second route is the fact of deriving an expression for the effective plate nodal forces that will be advantageously considered when addressing inelastic and dynamic behaviors.

4.1.3 Numerical validation

We solve the elastic problem in the plate domain depicted in Fig. 4.5 and compare the solutions obtained using 3D FEM, the standard plate theory and the enriched formulations considered in the previous section. The domain geometry $\Omega = [0, H_x] \times [0, H_y] \times [0, H_z]$ is defined in Table 4.1 whereas Table 4.2 specifies the considered mesh. On the domain right face (blue area in Fig. 4.5) a vertical traction is applied, $\mathbf{T} = (0, 0, 10000) N/m^2$ whereas the displacement is prevented on the opposite face.

Fig. 4.6 compares the different computed solutions. In that figure "3D solution" refers to the solution obtained using 3D elements according to the mesh specified in Table 4.2. As reference solution we consider a 3D finite element solution using a

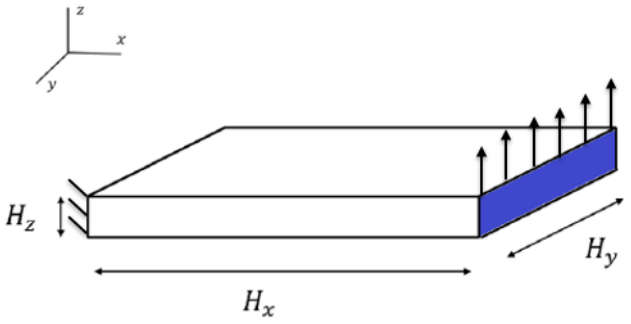

Figure 4.5 – *Elastic problem defined in a plate domain.*

Table 4.2 – *Parameters values used in the simulation.*

N_x (number of elements in the x direction): 25
N_y (number of elements in the y direction): 5
N_z (number of elements in the z direction): 11

much finer mesh (the one defined in Table 4.3).

The number of elements with enriched behavior (according to the procedures described in the previous section) can be arbitrarily increased, and it was noted that, as expected, by increasing it the solution approaches the reference one.

It is important to note that even when all the elements are enriched, the solution exhibits a gap with respect to the reference solution. This gap can be explained by the fact that, despite of the valuable enrichments introduced at the elements level, at the elements boundaries standard plate kinematics is enforced with its consequent impact on the resulting kinematics that continues to be too constrained with respect to a fully 3D kinematics.

Thus one could conclude that the proposed technique could become advantageous when used for enriching the mechanical description inside an element or patch (as discussed later) but whose effects remain confined in the interior of that element (or patch) and when approaching to the element border the plate kinematic is accurate enough.

In the case here discussed plate theory and coarse 3D finite element solutions

Table 4.3 – *Parameters values used in the simulation for the reference solution.*

N_x (number of elements in the x direction): 60
N_y (number of elements in the y direction): 12
N_z (number of elements in the z direction): 11

are closer one to the other, whereas the enriched one is the closest to the reference one (refined 3D finite element solution).

We consider now the same problem as in the previous example but we suppose that in the 3D element there is an hole as depicted in Fig. 4.7 (in the other elements we consider the enrichment presented before in absence of holes).

Here, there is clearly a double advantage in using the enrichment methodology. First, if the effect of the hole remains confined inside the element, vanishing when approaching the element boundary, the element enriched suffices and the plate meshing can be alleviated because the hole only exists for the element that will be accordingly enriched, but remains invisible at the plate level. On the other hand, its local 3D effects will be described very accurately.

Once the holed element stiffness matrix $\mathbf{K}^e$ is computed using the procedure presented in the previous section, the problem is solved and the generalized displacement field $\mathbf{U}^e$ can be extracted at the vertices of the holed triangle. Then the 3D solution inside the element can be easily computed by using (4.17). Fig. 4.8 depicts different solutions. Even if Ω_e accounts the hole presence (the PGD and static condensation based enrichment proceed on a mesh that describe the hole presence), the plate mesh becomes unaltered.

As discussed, after solving the problem at the plate level, using the enriched stiffness matrices for the different elements, 3D fields can be reconstructed. Thus, Figs. 4.9, 4.10 and 4.11 represent the out-of-plane stress tensor components, including the component σ_{zz} that is neglected when using standard plate theory. Moreover, a parabolic evolution of the components σ_{xz} and σ_{yz} along the domain thickness, typical of a 3D solution, can be noticed in Fig. 4.11.

4.1.4 Extension of the method to patches

In this section we extend the method previously presented to the construction of an enriched patch (super-element). In fact a single triangle element is too small for capturing rich events which can occur on a large area of the domain. Our goal is to select the patch delimited by the red line in Fig. 4.12, Ω_p, treat it using a 3D description by employing one of the two procedures previously presented (the PGD in-plane-out-of-plane separated representation or the static condensation procedure) and then construct the $(3\mathcal{N}_b)\times(3\mathcal{N}_b)$ patch stiffness matrix (being $\mathcal{N}_b$ the number of nodes in the border of the enriched patch). In the case here addressed numerically, the stiffness matrix size will be 84×84. In the construction procedure it is assumed that on the patch border the kinematics is the standard plate kinematics applied in the surrounding elements.

In the present case the generalized patch displacement reads

$$\mathbf{U} = (\theta_1^x, \theta_1^y, \omega_1, \theta_2^x, \theta_2^y, \omega_2, \ldots, \theta_{\mathcal{N}_b}^x, \theta_{\mathcal{N}_b}^y, \omega_{\mathcal{N}_b}), \tag{4.33}$$

with $\mathcal{N}_b = 28$. Figs. 4.12, 4.13 and 4.14 depict respectively the patch location, its 3D representations and its connection with the surrounding plate elements.

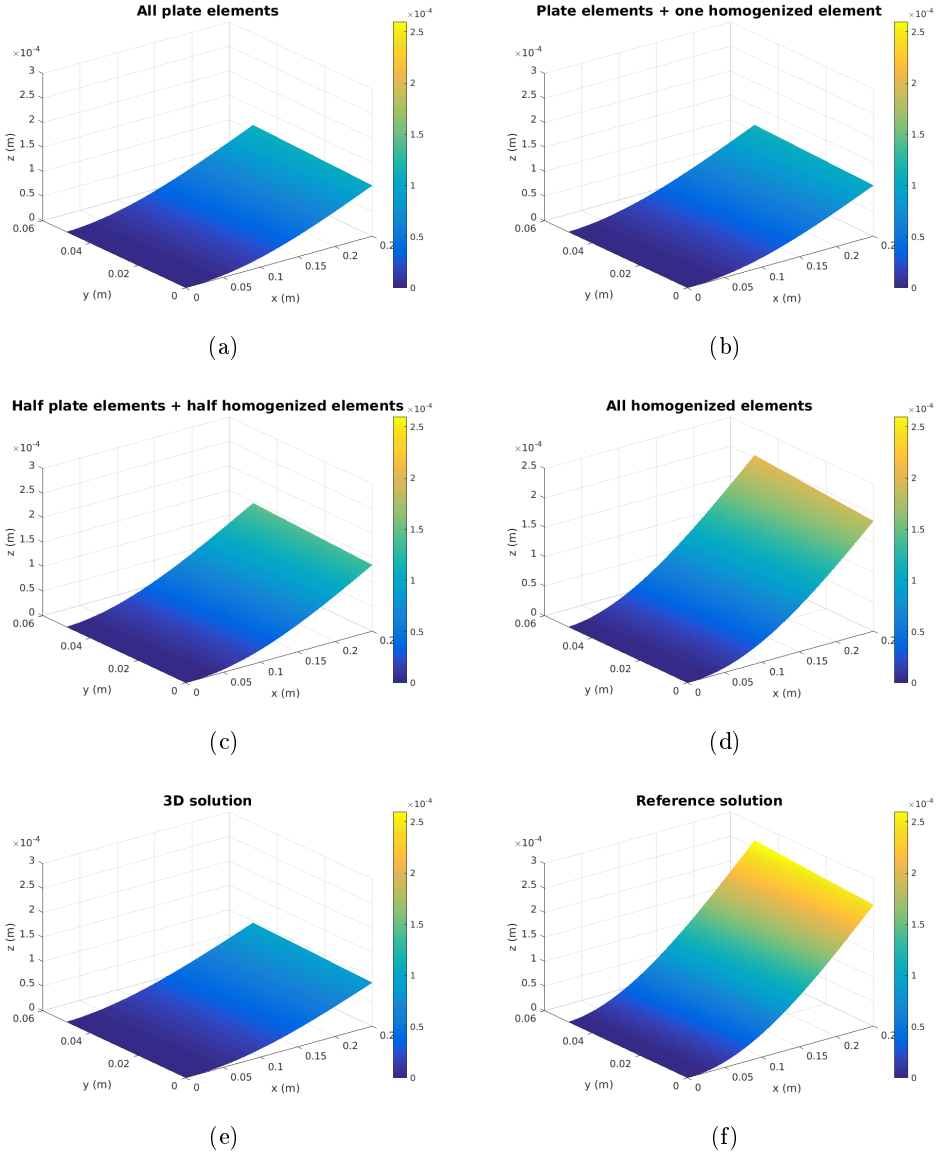

Figure 4.6 – *Displacement of the plate middle plane using plate theory (a), all plate theory elements except the homogenized (enriched) element (b), half plate theory elements (the triangles of the mesh in Fig. 4.2 with the right angle on the bottom) and half homogenized (enriched) elements (the triangles of the mesh in Fig. 4.2 with the right angle on the top) (c), all homogenized (enriched) elements (d), fully 3D FEM on a coarse mesh (e), fully 3D FEM on fine mesh (f).*

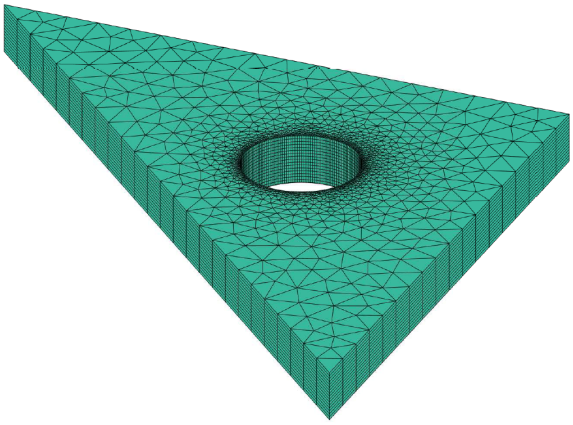

Figure 4.7 – *Holed 3D triangular element and its associated mesh.*

Table 4.4 – *Model parameters.*

H_x: Length in the x direction (mm)	250
H_y: Length in the y direction (mm)	250
H_z: Length in the z direction (mm)	2
E: Young modulus (N/m^2)	$2\ 10^{11}$
ν: Poisson coefficient	0.25

In the numerical validation we consider again the problem depicted in Fig. 4.5, where the geometrical and mechanical properties are defined in Table 4.4. On the right face (the blue area in Fig. 4.5) a vertical traction is applied, $T = (0, 0, 1100000)N/m^2$ whereas on the opposite face the displacement is prevented.

Fig. 4.15 depicts the different solutions, where 3D FEM coarse and refined (reference) solutions are related to the meshes specified respectively in Tables 4.5 and 4.6. The solution referred as “with all patch elements" refers to the solution computed replacing all the plate elements with the 9 patches (super-elements) depicted in Fig. 4.16. The 3D reference solution has been computed using a mesh as fine as the one considered to describe the enriched solution at the patch level.

The solution involving the nine patches is the closest to the reference solution.

Table 4.5 – *Coarse 3D FEM.*

N_x (number of elements in the x direction): 21
N_y (number of elements in the y direction): 21
N_z (number of elements in the z direction): 5

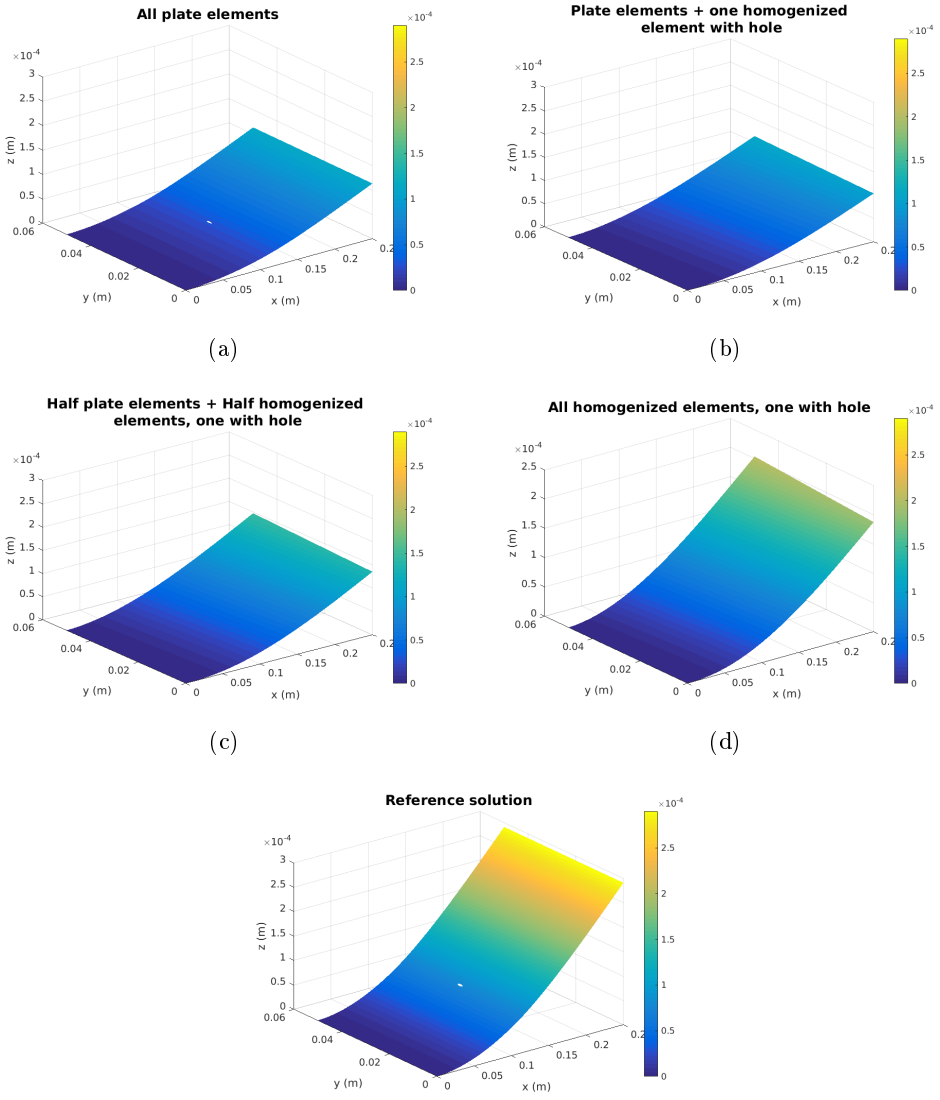

Figure 4.8 – *Displacement of the plate middle plane using plate theory (a), all plate theory elements except the homogenized (enriched) holed element (b), half plates theory elements (the triangles of the mesh in Fig. 4.2 with the right angle on the bottom) and half homogenized elements (the triangles of the mesh in Fig. 4.2 with the right angle on the top), one of them holed (c), all homogenized elements, one of them holed (d), fully 3D theory on the fine mesh (e).*

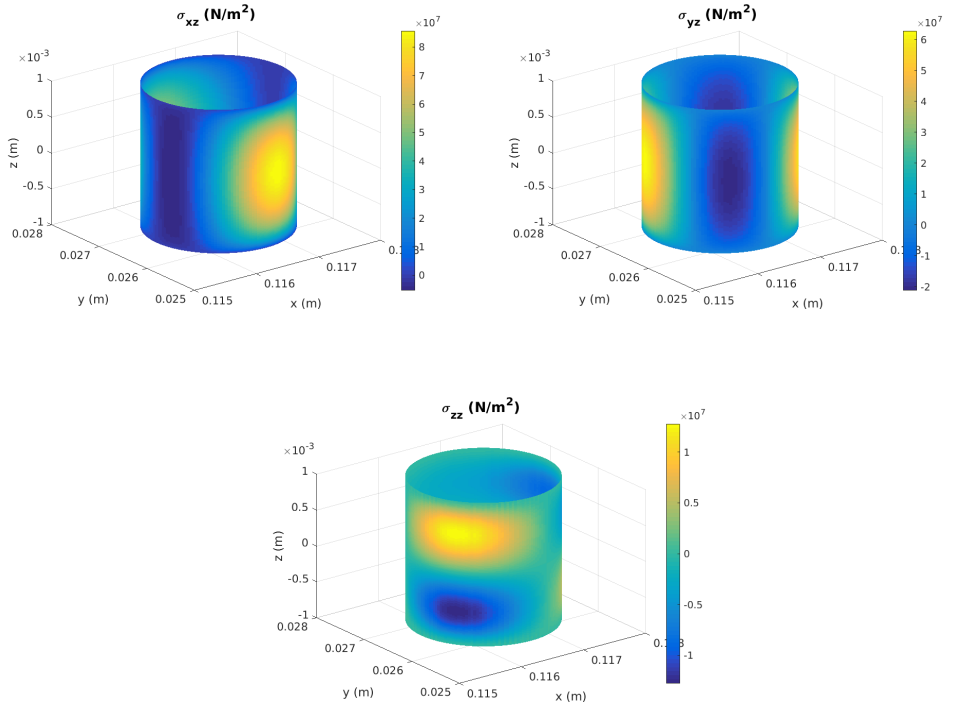

Figure 4.9 – *Out-of-plane components of the stress tensor around the hole.*

Table 4.6 – *Refined 3D FEM considered for defining the reference solution.*

N_x (number of elements in the x direction): 63
N_y (number of elements in the y direction): 63
N_z (number of elements in the z direction): 5

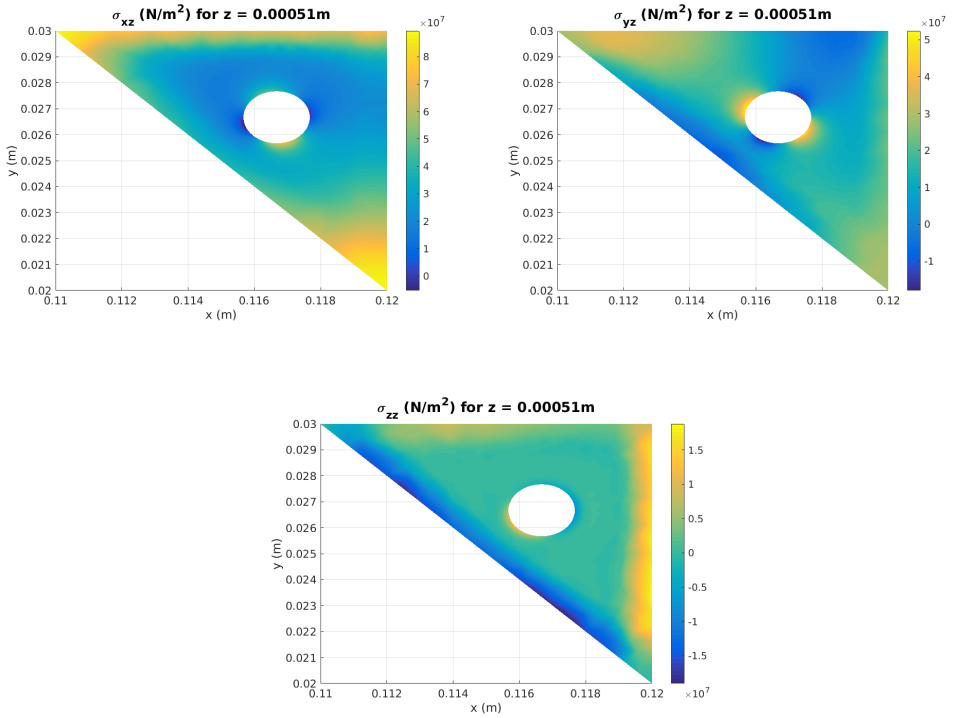

Figure 4.10 – *Out-of-plane components of the stress tensor on the plane* $z = 0.51$ *mm.*

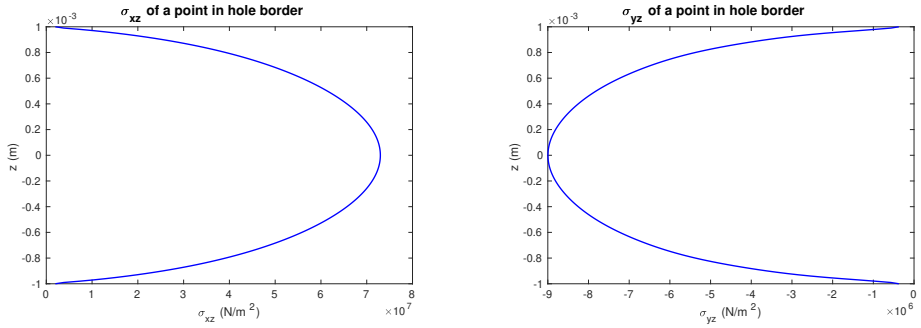

Figure 4.11 – *Out-of-plane components of the stress tensor through the domain thickness in the hole neighborhood.*

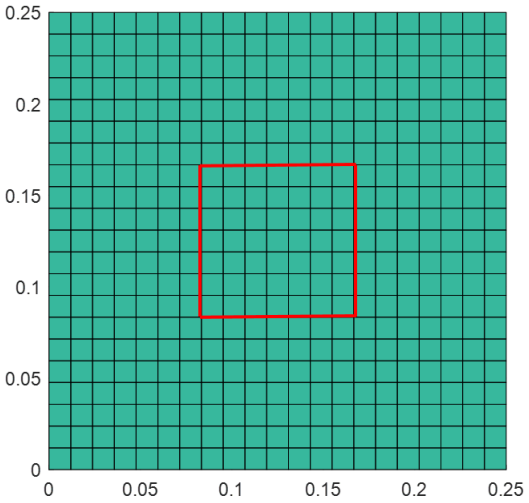

Figure 4.12 – *Plate mesh.*

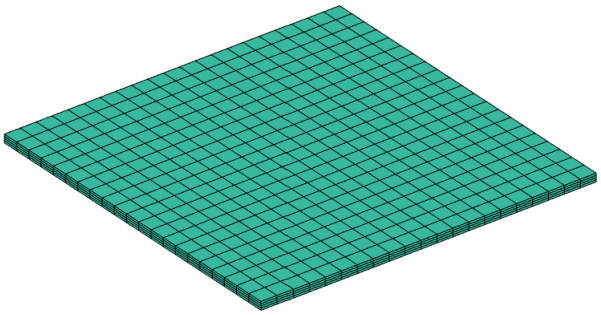

Figure 4.13 – *3D patch mesh.*

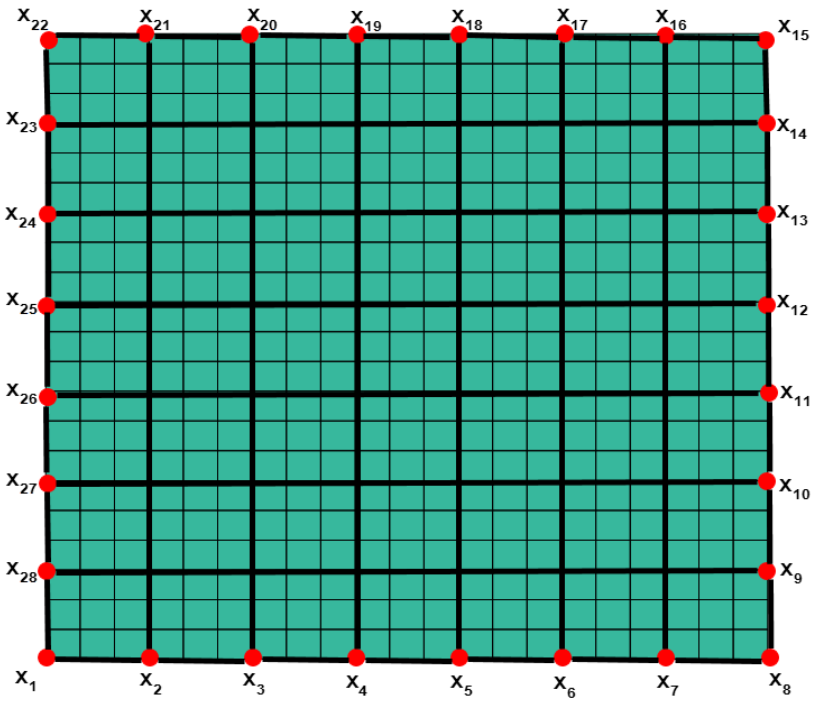

Figure 4.14 – *Patch discretization.*

However, since at the border of the patches the usual plate kinematics is enforced, a gap between the nine-patches solution and the refined 3D FEM solution (reference solution) persists. In any case, as the patches solution involved less constraints (plate kinematics) than the one related to enriched elements, where the kinematic constrains are applied to all the elements boundaries, its accuracy is superior.

Since it is not pretended that plates should be discretized using enriched super-elements, our main interest is adopting accurate descriptions of rich behaviors that could be assumed confined inside a region (our patch). This is the route retained for replacing 3D FEM discretization in regions exhibiting rich behaviors by enriched super-elements keeping its 2D computational complexity.

4.1.5 Extension of the method to plasticity

In this section we extend the method to problems in which plastic behavior can occur. In fact localized plasticity phenomena can occur in several situation, as in spot-welds during crash simulations.

In its general form the infinitesimal relation between the stress increment $d\boldsymbol{\sigma}$ and the elastic strain $d\boldsymbol{\varepsilon}^e$ increment reads [Owen & Hinton 1980]

$$d\boldsymbol{\sigma} = \mathbf{C}d\boldsymbol{\varepsilon}^e = \mathbf{C}(d\boldsymbol{\varepsilon} - d\boldsymbol{\varepsilon}^p), \tag{4.34}$$

where $\mathbf{C}$ is the Hooke tensor, $d\boldsymbol{\varepsilon}$ is total strain and $d\boldsymbol{\varepsilon}^p$ is the plastic strain.

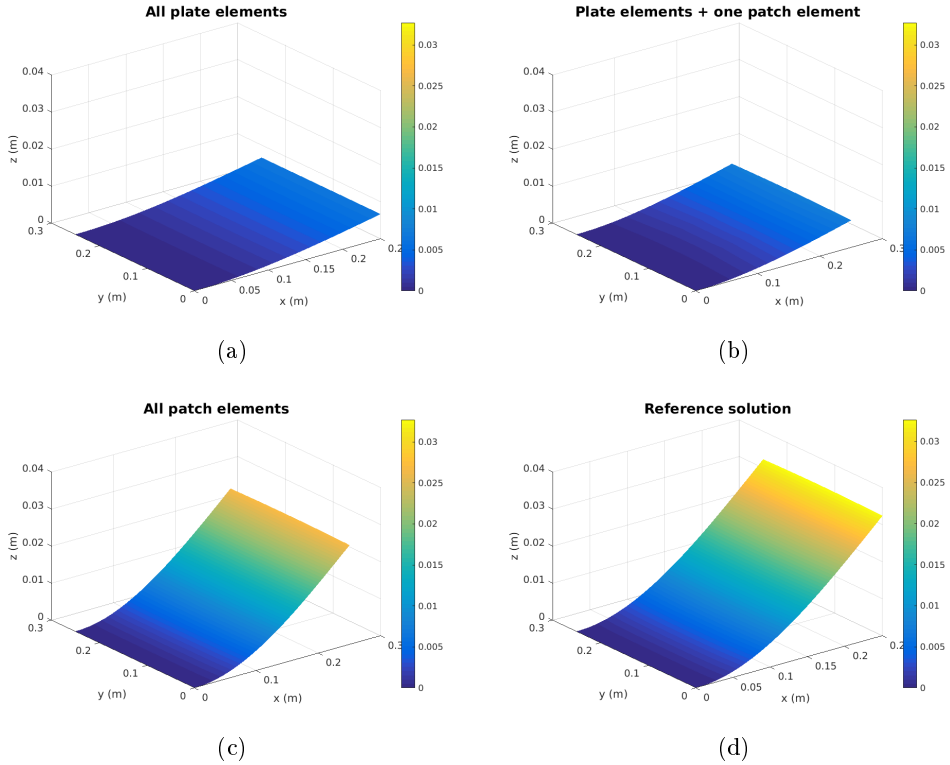

Figure 4.15 – *Displacement using plate theory (a), all plate theory elements except the patch super-element (b), all patches as depicted in Fig. 4.16 (c), fully 3D refined FEM (d).*

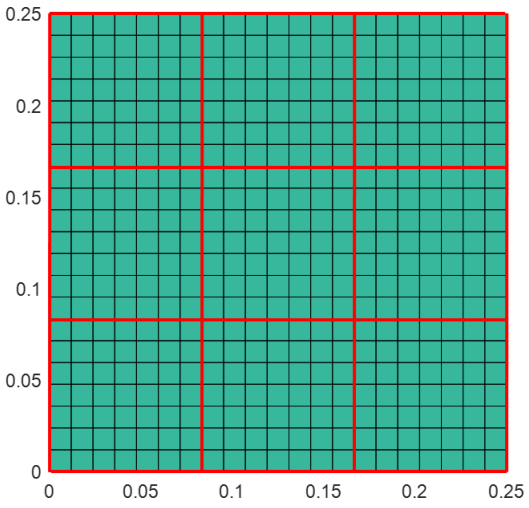

Figure 4.16 – *Super-elements discretization.*

In plasticity yielding can occur only if the stresses satisfy a general yield criterion; in the considered examples, for the sake of simplicity, we use the Von Mises criterion [Mises 1913], assuming perfect plasticity. Ignoring volumetric body forces, the weak form of the problem, in its finite incremental form, associated to the strong form (4.4) lies in looking for the displacement field increment $\Delta\mathbf{u}$ verifying the Dirichlet boundary conditions, verifying

$$\int_\Omega \boldsymbol{\varepsilon}(\mathbf{u}^*) \cdot \left(\mathbf{C}\left(\Delta\boldsymbol{\varepsilon}(\Delta\mathbf{u}) - \Delta\boldsymbol{\varepsilon}^p(\Delta\mathbf{u})\right)\right) \, d\mathbf{x} = \int_{\Gamma_N} \mathbf{u}^* \cdot \Delta\mathbf{T} \, d\mathbf{x} \tag{4.35}$$

for any test function $\mathbf{u}^*$ in an appropriate functional space.

In order to solve the resulting nonlinear problem, various computational procedures have been proposed and extensively used, among them [Zienkiewicz *et al.* 1969, Gallagher 1962, Argyris 1965, Swedlow *et al.* 1965, Pope 1966, Reyes & Deere 1966, Marcal & King 1967, Popov *et al.* 1967].

In this work we consider a simple implicit approach [Zienkiewicz *et al.* 1969] that at the n load step solves

$$\int_\Omega \boldsymbol{\varepsilon}(\mathbf{u}^*) \cdot \left(\mathbf{C}\,\Delta_n^1\boldsymbol{\varepsilon}\right) \, d\mathbf{x} = \int_{\Gamma_N} \mathbf{u}^* \cdot \Delta_n\mathbf{T} \, d\mathbf{x}. \tag{4.36}$$

From $\Delta_n^1\boldsymbol{\varepsilon}$, the stress increment $\Delta_n^1\boldsymbol{\sigma}$ results

$$\Delta_n^1\boldsymbol{\sigma} = \mathbf{C}\Delta_n^1\boldsymbol{\varepsilon} \tag{4.37}$$

that allows updating the stress

$$\boldsymbol{\sigma}_n^1 = \boldsymbol{\sigma}_{n-1} + \Delta_n^1\boldsymbol{\sigma}, \tag{4.38}$$

and from it computing the plastic strain increment $\Delta_n^1\boldsymbol{\varepsilon}^p$ using well known procedures (some details are given in Appendix B). Then, the stress is updated according to

$$\boldsymbol{\sigma}_n^1 = \boldsymbol{\sigma}_n^1 - \mathbf{C}\Delta_n^1\boldsymbol{\varepsilon}^p. \tag{4.39}$$

Then, $\Delta_n^2\boldsymbol{\varepsilon}$ is calculated from

$$\int_\Omega \boldsymbol{\varepsilon}(\mathbf{u}^*) \cdot \left(\mathbf{C}\,\Delta_n^2\boldsymbol{\varepsilon}\right) \, d\mathbf{x} = \int_\Omega \boldsymbol{\varepsilon}(\mathbf{u}^*) \cdot \left(\mathbf{C}\,\Delta_n^1\boldsymbol{\varepsilon}^p\right) \, d\mathbf{x}, \tag{4.40}$$

and the stress update from

$$\boldsymbol{\sigma}_n^2 = \boldsymbol{\sigma}_n^1 + \Delta_n^2\boldsymbol{\sigma}, \tag{4.41}$$

and from it computing the plastic strain increment $\Delta_n^2\boldsymbol{\varepsilon}^p$. Then, the stress is updated according to

$$\boldsymbol{\sigma}_n^2 = \boldsymbol{\sigma}_n^2 - \mathbf{C}\Delta_n^2\boldsymbol{\varepsilon}^p. \tag{4.42}$$

At iteration j the problem to be solved reads

$$\int_\Omega \boldsymbol{\varepsilon}(\mathbf{u}^*) \cdot \left(\mathbf{C}\, \Delta_n^j \boldsymbol{\varepsilon}\right)\, d\mathbf{x} = \int_\Omega \boldsymbol{\varepsilon}(\mathbf{u}^*) \cdot \left(\mathbf{C}\, \Delta_n^{j-1} \boldsymbol{\varepsilon}^p\right)\, d\mathbf{x}, \tag{4.43}$$

where it can be noticed that the problem structure remains unaltered, with the left-hand member encountered when addressing elastic behaviors and the inelastic behavior appearing as a body force. Thus, the enrichment procedure based on the static condensation seems specially suitable.

For validating the proposed strategy we consider the same problem as in the previous section, sketched in Fig. 4.5, with geometrical and mechanical properties specified in Table 4.4 and the considered mesh defined in Table 4.5. On the right face of the domain (blue area in Fig. 4.5) a vertical traction is applied, $T = (0, 0, 1100000) N/m^2$, and on the opposite face displacement is prevented. The considered uniaxial stress yield is $\bar{\sigma}_0 = 250 \cdot 10^6 N/m^2$. Again, Fig. 4.17 depicts the usual different solutions. Again "all patch elements" refers to the case in which the domain is composed by the nine super-elements shown in Fig. 4.16. The 3D reference solution has been computed using a mesh as fine as with the one used in the patch description (Table 4.6). Again, the nine-patches solution is the most accurate (when compared with the reference solution).

4.1.6 Extension to structural dynamics

In this section we address structural dynamics, again ignoring body forces without loss of generality. Thus, the displacement field evolution $\mathbf{u}(\mathbf{x}, t)$ in the domain Ω and time interval $t \in I = (0, T]$ is described by the linear momentum balance equation

$$\rho \ddot{\mathbf{u}}(\mathbf{x}, t) = \nabla \cdot \boldsymbol{\sigma}, \tag{4.44}$$

where ρ is the density (kg/m^3).

The boundary $\partial\Omega$ is decomposed according to $\partial\Omega = \partial_D\Omega \cup \partial_N\Omega$ where displacement and tractions are prescribed.

In the elastic case the problem weak form associated with the strong form (4.44) results in looking for the displacement field $\mathbf{u}$ verifying the initial and Dirichlet boundary conditions, and fulfilling

$$\rho \int_\Omega \mathbf{u}^* \cdot \ddot{\mathbf{u}}\, d\mathbf{x} + \int_\Omega \boldsymbol{\varepsilon}(\mathbf{u}^*) \cdot (\mathbf{C}\, \boldsymbol{\varepsilon}(\mathbf{u}))\, d\mathbf{x} = \int_{\Gamma_N} \mathbf{u}^* \cdot \mathbf{T}(t)\, d\mathbf{x} \tag{4.45}$$

for any test function $\mathbf{u}^*$ in an appropriate functional space.

The standard FEM space discretization reads

$$\mathbf{M}\mathbf{a}(t) + \mathbf{K}\mathbf{u}(t) = \mathbf{F}(t), \tag{4.46}$$

where $\mathbf{a}(t)$ represents the acceleration. The time stepping consists in calculating the acceleration and displacement at each time step $t_{j+1} = (j+1)\Delta t$ from the ones

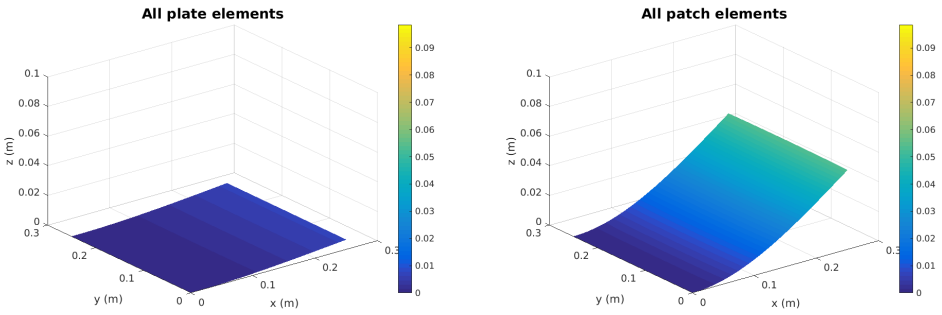

(a) (b)

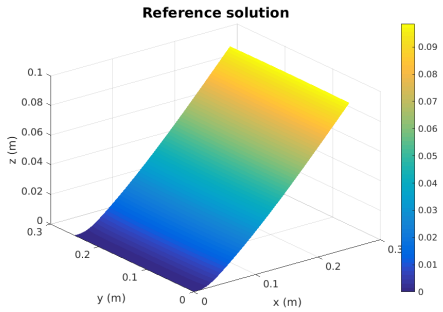

(c)

Figure 4.17 – *Plate theory displacement (a), all patch elements according to Fig. 4.16 (b) and refined 3D FEM (reference solution) (c).*

Table 4.7 – *Model parameters.*

H_x: Length in the x direction (m)	3
H_y: Length in the y direction (m)	3
H_z: Length in the z direction (m)	0.1
E: Young modulus (N/m^2)	$2\ 10^{11}$
ν: Poisson coefficient	0.25

existing at the previous time step $t_j = j\Delta t$.

A widely considered choice consists of the Newmark method [Newmark 1959], in which the velocity and the displacement fields at time t_{j+1} read

$$\mathbf{v}_{j+1} = \mathbf{v}_j + \Delta t\left((1-\gamma)\mathbf{a}_j + \gamma\mathbf{a}_{j+1}\right), \tag{4.47}$$

and

$$\mathbf{u}_{j+1} = \mathbf{u}_j + \Delta t\mathbf{v}_j + \frac{\Delta t^2}{2}\left((1-2\beta)\mathbf{a}_j + 2\beta\mathbf{a}_{j+1}\right), \tag{4.48}$$

so that at each time step the acceleration field can be obtained by solving the linear system

$$\mathbf{K}^*\mathbf{a}_{j+1} = \mathbf{p}^*_{j+1} \tag{4.49}$$

where

$$\mathbf{K}^* = \mathbf{M} + \beta\Delta t^2\mathbf{K} \tag{4.50}$$

and

$$\mathbf{p}^*_{j+1} = \mathbf{F}_{j+1} - \mathbf{K}\mathbf{u}_j - \Delta t\mathbf{K}\mathbf{v}_j - \frac{\Delta t^2}{2}(1-2\beta)\mathbf{K}\mathbf{a}_j. \tag{4.51}$$

According to the values of β and γ the method can be explicit (conditionally stable) or implicit (unconditionally stable). In our numerical examples we considered $\beta = 1/4$ and $\gamma = 1/2$ defining an implicit method. As soon as the acceleration is available, the velocity and displacement field can be computed using Eqs. 4.47 and 4.48 respectively.

An enriched stiffness can be derived at the element or patch levels, where the use of the procedure based on the condensation allows properly addressing the forces $\mathbf{p}^*_{j+1}$, and therefore combining dynamics and plasticity.

For evaluating the performances of the proposed enrichment procedure, we consider again the problem defined in Fig. 4.5 and Table 4.7.

On the right face (the blue area in Fig. 4.5) a vertical traction is enforced, $\mathbf{T}(t) = (0, 0, 4.1 \cdot 10^6 \sin(2\pi\omega t))N/m^2$, whereas on the opposite face displacement is prevented. Without loss of generality homogeneous initial conditions $\mathbf{u}(\mathbf{x}, t = 0) = 0$ and $\mathbf{v}(\mathbf{x}, t = 0) = 0$ are assumed. Table 4.8 reports the considered coarse mesh whereas Table 4.9 defined the refined one from which the reference solution is calculated.

Figs. 4.18 and 4.19 depict respectively the solutions computed using the different

Table 4.8 – *Coarse FEM mesh.*

N_x (number of elements in the x direction): 21
N_y (number of elements in the y direction): 21
N_z (number of elements in the z direction): 5

Table 4.9 – *Refined FEM mesh considered for computing the reference solution.*

N_x (number of elements in the x direction): 63
N_y (number of elements in the y direction): 63
N_z (number of elements in the z direction): 5

techniques at four different times and the vertical displacement time evolution at the right border. Figs. 4.20 and 4.21 present similar results but in a case where plasticity takes place. Again the best solutions are the ones related to a nine-patches discretization for the reasons widely exposed before.

4.1.7 Conclusions

This first part of the chapter proposed two different procedures to capture local 3D behaviors by enriching elements (or super-elements) connected to plate discretization. This goal is performed by integrating, in a non-intrusive manner, 3D elements (or patches) in plate or shell based commercial codes. In order to compute this enriched 2D element, two different techniques were presented: one based on the PGD in-plane-out-of-plane separated representation and the other on the static condensation. The method was firstly developed in linear elastic settings and then successfully extended to structures exhibiting inelastic behaviors or dynamics.

4.2 A minimally-intrusive fully 3D separated plate formulation in computational structural mechanics

Introduction The second part of the chapter addresses problems in which enriched descriptions are compulsory in all the domain and it proposes a more general method which allows efficient integration of fully 3D descriptions into existing plate softwares.

This second part of the chapter and all the results presented in it constitute a submitted paper:

- G. Quaranta, M. Ziane, E. Haug, J.L. Duval, F. Chinesta, *A minimally-intrusive fully 3D separated plate formulation in computational structural mechanics*, Advanced Modeling and Simulation in Engineering Sciences, (submitted).

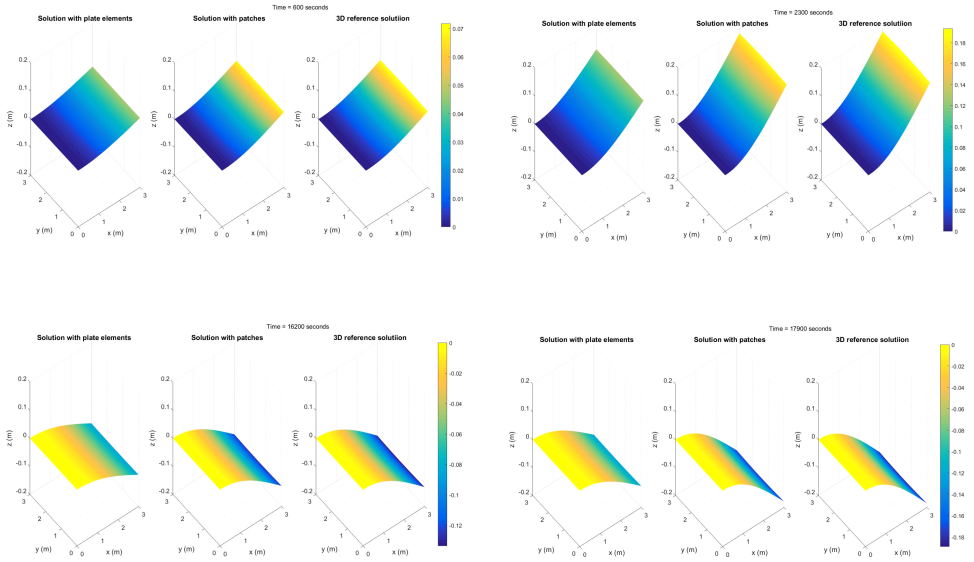

Figure 4.18 – *Elastic displacement using plate theory, nine-patches and 3D FEM on the refined mesh at four different time-steps.*

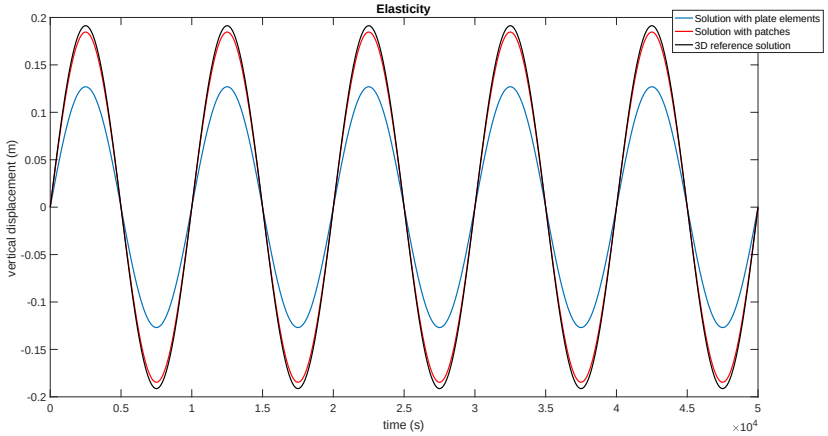

Figure 4.19 – *Vertical elastic displacement evolution in time at the right border.*

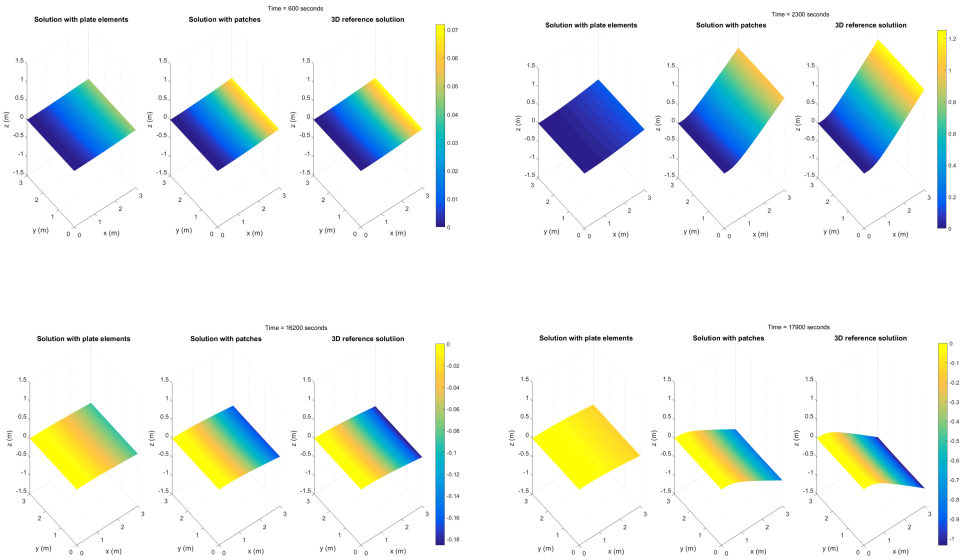

Figure 4.20 – *Elasto-plastic displacement using plate theory, nine-patches and 3D FEM on the refined mesh at four different time-steps.*

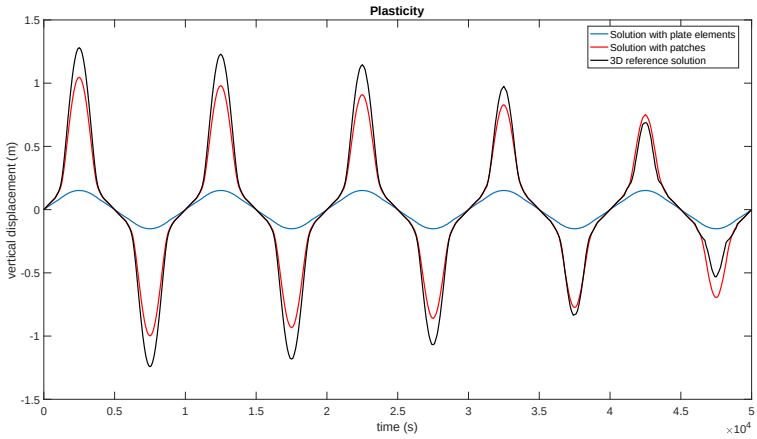

Figure 4.21 – *Vertical elasto-plastic displacement evolution in time at the right border.*

4.2.1 Elastostatic problem definition

We consider, as in the first part of the chapter, the linear elastostatic problem defined in the plate domain $\Omega = \Omega_{xy} \times \Omega_z$, with $\Omega_{xy} = [0, H_x] \times [0, H_y]$ and $\Omega_z = [0, H_z]$.

The linear elastic behavior relating the Cauchy's stress $\boldsymbol{\sigma}$ and the strain $\boldsymbol{\varepsilon}$ reads as (4.1) and the relation between strain $\boldsymbol{\varepsilon}$ and displacement $\mathbf{u}$ (with components $\mathbf{u} = (u, v, w)$) writes as (4.2). Considering an homogeneous and isotropic material and using Voigt notation the behavior writes as (4.3).

With $\mathbf{g}(\mathbf{x})$ the body forces, the displacement field $\mathbf{u}(\mathbf{x})$ for $\mathbf{x} \in \Omega$ is described by the linear momentum balance equation

$$\nabla \cdot \boldsymbol{\sigma} + \mathbf{g} = \mathbf{0}. \tag{4.52}$$

The domain boundary $\partial\Omega$ is partitioned into Dirichlet, Γ_D, and Neumann, Γ_N, boundaries, where displacement $\mathbf{u}_g$ and tractions $\mathbf{T}$ are enforced respectively. For the sake of simplicity, in what follows and without loss of generality we assume $\mathbf{T} = \mathbf{0}$

The problem weak form associated to the strong form (4.52) lies in looking for the displacement field $\mathbf{u}$ verifying the Dirichlet boundary conditions such that the weak form

$$\int_\Omega \boldsymbol{\varepsilon}(\mathbf{u}^*) \cdot (\mathbf{C} \cdot \boldsymbol{\varepsilon}(\mathbf{u}))\, d\mathbf{x} = \int_\Omega \mathbf{u}^* \cdot \mathbf{g}\, d\mathbf{x}, \tag{4.53}$$

fulfills for any test function $\mathbf{u}^*$, with the trial and test fields defined in appropriate functional spaces.

Using the Reissner-Mindlin theory the displacement field can be written as (4.6) and the generalized displacement vector $\hat{\mathbf{u}}$ as (4.7) at any point on the middle plane.

Injecting plate theory assumptions into the 3D elastostatic problem weak form, Eq. (4.53) reduces to the following 2D formulation

$$\int_{\Omega_{xy}} \hat{\boldsymbol{\varepsilon}}(\hat{\mathbf{u}}^*) \cdot \left(\hat{\mathbf{C}}\hat{\boldsymbol{\varepsilon}}(\hat{\mathbf{u}})\right) d\mathbf{x} = \int_{\Omega_{xy}} \hat{\mathbf{u}}^* \cdot \hat{\mathbf{g}}\, d\mathbf{x}, \tag{4.54}$$

whose standard finite element discretization leads to

$$\mathbf{K}_{xy}\mathbf{U} = \mathbf{B}_{xy} \tag{4.55}$$

where for notational simplicity the hat symbol ($\hat{\bullet}$) is omitted. In the previous expression (4.55), $\mathbf{K}_{xy}$ is the stiffness matrix and $\mathbf{U}$ and $\mathbf{B}_{xy}$ are the vector of the generalized displacements and forces, the former containing nodal rotations and deflections and the last the dual quantities: the nodal moments and vertical nodal forces.

As we have already said when the complexity of the solution makes impossible the introduction of pertinent hypotheses for reducing the dimensionality of the model from 3D to 2D, a fully 3D description seems compulsory and the in-plane-out-of-plane separated representation (4.10) becomes particularly suitable.

4.2.2 Enriched formulations

As reported in the previous section plate kinematics can be written as a single-term separated decomposition

$$\begin{cases} u(x,y,z) = \theta^x(x,y) f^x(z) \\ v(x,y,z) = \theta^y(x,y) f^y(z) \\ w(x,y,z) = w(x,y) f^z(z) \end{cases}, \tag{4.56}$$

with $f^x(z) = -z$, $f^y(z) = -z$ and $f^z(z) = 1$.

For the sake of generality we consider now generic functions $f^x(z)$, $f^y(z)$ and $f^z(z)$ assumed known, but than can be different to the ones related to the standard Reissner-Mindlin plate theory, and its associated 3D kinematics given by Eq. (4.56). Consequently θ^x, θ^y and w do not represent rotations and deflection anymore.

The displacements gradient becomes

$$\nabla \mathbf{u} = \begin{pmatrix} \frac{\partial u}{\partial x} \\ \frac{\partial u}{\partial y} \\ \frac{\partial u}{\partial z} \\ \frac{\partial v}{\partial x} \\ \frac{\partial v}{\partial y} \\ \frac{\partial v}{\partial z} \\ \frac{\partial w}{\partial x} \\ \frac{\partial w}{\partial y} \\ \frac{\partial w}{\partial z} \end{pmatrix} = \begin{pmatrix} \frac{\partial \theta^x}{\partial x} \\ \frac{\partial \theta^x}{\partial y} \\ \theta^x \\ \frac{\partial \theta^y}{\partial x} \\ \frac{\partial \theta^y}{\partial y} \\ \theta^y \\ \frac{\partial w}{\partial x} \\ \frac{\partial w}{\partial x} \\ w \end{pmatrix} \circ \begin{pmatrix} f^x \\ f^x \\ \frac{df^x(z)}{dz} \\ f^y \\ f^y \\ \frac{df^y(z)}{dz} \\ f^z \\ f^z \\ \frac{df^z}{\partial z} \end{pmatrix}, \tag{4.57}$$

that allows defining the strain separated form, that, taking into account its symmetry, reads

$$\boldsymbol{\varepsilon} = \begin{pmatrix} \frac{\partial u}{\partial x} \\ \frac{\partial v}{\partial y} \\ \frac{\partial w}{\partial z} \\ \frac{\partial u}{\partial y} + \frac{\partial v}{\partial x} \\ \frac{\partial u}{\partial z} + \frac{\partial w}{\partial x} \\ \frac{\partial v}{\partial y} + \frac{\partial v}{\partial y} \end{pmatrix} = \begin{pmatrix} \frac{\partial \theta^x}{\partial x} \\ \frac{\partial \theta^y}{\partial y} \\ w \\ \frac{\partial \theta^x}{\partial y} \\ \theta^x \\ \theta^y \end{pmatrix} \circ \begin{pmatrix} f^x \\ f^y \\ \frac{df^z}{dz} \\ f^x \\ \frac{df^x}{dz} \\ \frac{df^y}{dz} \end{pmatrix} + \begin{pmatrix} 0 \\ 0 \\ 0 \\ \frac{\partial \theta^y}{\partial x} \\ \frac{\partial w}{\partial x} \\ \frac{\partial w}{\partial y} \end{pmatrix} \circ \begin{pmatrix} 0 \\ 0 \\ 0 \\ f^y \\ f^z \\ f^z \end{pmatrix} \tag{4.58}$$

$$= \boldsymbol{\Theta}^1(x,y) \circ \mathbf{F}^1(z) + \boldsymbol{\Theta}^2(x,y) \circ \mathbf{F}^2(z). \tag{4.59}$$

In the case of a general material the Hooke tensor can also be written as

$$\mathbf{C}(x,y,z) = \sum_{i=1}^{M} \mathbf{C}^i_{xy}(x,y) \circ \mathbf{C}^i_z(z). \tag{4.60}$$

For an homogeneous material we have simply

$$\mathbf{C} = \mathbf{C}^i_{xy} \circ \mathbf{C}^i_z. \tag{4.61}$$

where $\mathbf{C}_z$ is given by (4.3) and $\mathbf{C}_{xy}$ is a tensor whose all the entries are 1,

$$\mathbf{C}_{xy} = \begin{bmatrix} 1 & 1 & 1 & 1 & 1 & 1 \\ 1 & 1 & 1 & 1 & 1 & 1 \\ 1 & 1 & 1 & 1 & 1 & 1 \\ 1 & 1 & 1 & 1 & 1 & 1 \\ 1 & 1 & 1 & 1 & 1 & 1 \\ 1 & 1 & 1 & 1 & 1 & 1 \end{bmatrix}. \tag{4.62}$$

Taking this into consideration the method that we are going to explain can be used both for homogeneous and not homogeneous materials. For the sake of simplicity we are going to present it in the case where in expression (4.60) only one term appears in the sum, but it can be easily extended to involve more terms. The virtual work principle, expressed using a matrix notation, involves the internal work

$$\begin{aligned}
&\boldsymbol{\varepsilon}^{*T}\boldsymbol{\sigma} = \boldsymbol{\varepsilon}^{*T}\mathbf{C}\boldsymbol{\varepsilon} \\
&= \{\boldsymbol{\Theta}^{1*}(x,y)\circ\mathbf{F}^1(z) + \boldsymbol{\Theta}^{2*}(x,y)\circ\mathbf{F}^2(z)\}^T\{\mathbf{C}_{xy}(x,y)\circ\mathbf{C}_z(z)\} \\
&\{\boldsymbol{\Theta}^1(x,y)\circ\mathbf{F}^1(z) + \boldsymbol{\Theta}^2(x,y)\circ\mathbf{F}^2(z)\} \\
&= \boldsymbol{\Theta}^{1*T}(x,y)\{\mathbf{C}_{xy}(x,y)\circ\hat{\mathbf{C}}_z^{11}(z)\}\boldsymbol{\Theta}^1(x,y) + \boldsymbol{\Theta}^{1*T}(x,y)\{\mathbf{C}_{xy}(x,y)\circ\hat{\mathbf{C}}_z^{12}(z)\} \\
&\boldsymbol{\Theta}^2(x,y) + \boldsymbol{\Theta}^{2*T}(x,y)\{\mathbf{C}_{xy}(x,y)\circ\hat{\mathbf{C}}_z^{21}(z)\}\boldsymbol{\Theta}^1(x,y) + \boldsymbol{\Theta}^{2*T}(x,y) \\
&\{\mathbf{C}_{xy}(x,y)\circ\hat{\mathbf{C}}_z^{22}(z)\}\boldsymbol{\Theta}^2(x,y).
\end{aligned} \tag{4.63}$$

In the previous expression matrices $\hat{\mathbf{C}}_z^{ij}(z)$ results

$$\hat{\mathbf{C}}_{z_{kl}}^{ij}(z) = \mathbf{C}_{z_{kl}}(z)\mathbf{F}_k^i(z)\mathbf{F}_l^j(z), \quad i,j\in[1,2]\ \&\ \ k,l\in[1,\cdots,6]. \tag{4.64}$$

Now, the virtual work integral reads

$$\begin{aligned}
&\int_{\Omega_{xy}\times\Omega_z}\sum_{i=1}^{2}\sum_{j=1}^{2}\boldsymbol{\Theta}^{i*T}(x,y)\{\mathbf{C}_{xy}(x,y)\circ\hat{\mathbf{C}}_z^{ij}(z)\}\boldsymbol{\Theta}^j(x,y)\ dz\ dx\ dy \\
&= \int_{\Omega_{xy}}\sum_{i=1}^{2}\sum_{j=1}^{2}\boldsymbol{\Theta}^{i*T}(x,y)\mathbf{D}^{ij}(x,y)\boldsymbol{\Theta}^j(x,y)\ dx\ dy,
\end{aligned} \tag{4.65}$$

where

$$\mathbf{D}^{ij}(x,y) = \mathbf{C}_{xy}(x,y)\circ\int_{\Omega_z}\hat{\mathbf{C}}_z^{ij}(z)\ dz. \tag{4.66}$$

Now, if we assume an approximation based on a piecewise linear interpolation on a triangular finite element, related to an in-plane mesh of $\Omega_{xy} = \cup_{e=1}^{\mathtt{E}}\Omega_{xy}^e$, with the shape functions defined by $N_i^e(x,y),\ i=1,2,3;\ e=1,\cdots,\mathtt{E}$; it results

$$\begin{cases}
\theta^{x,e}(x,y) = N_1^e(x,y)\theta_1^{x,e} + N_2^e(x,y)\theta_2^{x,e} + N_3^e(x,y)\theta_3^{x,e} \\
\theta^{y,e}(x,y) = N_1^e(x,y)\theta_1^{y,e} + N_2^e(x,y)\theta_2^{y,e} + N_3^e(x,y)\theta_3^{y,e} \\
w^e(x,y) = N_1^e(x,y)w_1^e + N_2^e(x,y)w_2^e + N_3^e(x,y)w_3^e
\end{cases} \tag{4.67}$$

Using that approximation we can express vectors $\boldsymbol{\Theta}^i(x,y)$ in each element Ω^e from the generalized nodal displacements

$$\mathbf{U}^{eT} = (\theta_1^{x,e}, \theta_1^{y,e}, w_1^e, \theta_2^{x,e}, \theta_2^{y,e}, w_2^e, \theta_3^{x,e}, \theta_3^{y,e}, w_3^e), \tag{4.68}$$

from

$$\boldsymbol{\Theta}^i((x,y) \in \Omega_{xy}^e) = \mathbf{B}^{i,e}(x,y)\mathbf{U}^e, \tag{4.69}$$

where $\mathbf{B}^{i,e}(x,y)$ contains the shape functions and theirs derivatives, according to the expressions involved in the components of $\boldsymbol{\Theta}^i(x,y),\ i = 1,2$. Thus, integral (4.65) reads

$$\sum_{e=1}^{\mathtt{E}} \mathbf{U}^{e*T} \left\{ \int_{\Omega_{xy}^e} \sum_{i=1}^{2}\sum_{j=1}^{2} \mathbf{B}^{i,eT}(x,y)\mathbf{D}^{ij}(x,y)\mathbf{B}^{j,e}(x,y)\ dx\ dy \right\} \mathbf{U}^e$$

$$= \sum_{e=1}^{\mathtt{E}} \mathbf{U}^{e*T}\mathbf{K}_{xy}^e\mathbf{U}^e = \mathbf{U}^{*T}\mathbf{K}_{xy}\mathbf{U}. \tag{4.70}$$

Now, if we consider the virtual work of the body forces $\mathbf{g}(\mathbf{x})$, it involves

$$\mathbf{u}^{*T}\mathbf{g}(\mathbf{x}), \tag{4.71}$$

where without loss of generality we assume

$$\mathbf{u}(x,y,z) = \mathbf{V} \circ \mathbf{W}, \tag{4.72}$$

with $\mathbf{V}^T = (\theta^x, \theta^y, w)$ and $\mathbf{W}^T = (f^x(z), f^y(z), f^z(z))$, and the single-mode decomposition of the body forces given by

$$\mathbf{g}(x,y,z) = \mathbf{G} \circ \mathbf{H}, \tag{4.73}$$

with $\mathbf{G}^T = (M^x(x,y), M^y(x,y), T(x,y))$ and $\mathbf{H}^T = (h^x(z), h^y(z), h^z(z))$. The fact of considering a single mode in the decomposition of the body force is not restrictive as discussed later. The virtual work (4.71) can be expressed as

$$\mathbf{u}^{*T}\mathbf{g}(\mathbf{x}) = \mathbf{V}^{*T}(x,y)\hat{\mathbf{J}}(z)\mathbf{G}(x,y), \tag{4.74}$$

where matrix $\hat{\mathbf{J}}$ reads

$$\hat{\mathbf{J}}_{kl}(z) = \mathbf{I}_{kl}\mathbf{W}_k(z)\mathbf{H}_l(z), \tag{4.75}$$

with $\mathbf{I}$ the identity matrix. Now, the integral results

$$\int_{\Omega_{xy}\times\Omega_z} \mathbf{u}^{*T}\mathbf{g}(\mathbf{x})\ dz\ dx\ dy = \int_{\Omega_{xy}} \mathbf{V}^{*T}(x,y)\mathbf{J}\mathbf{G}(x,y)\ dx\ dy, \tag{4.76}$$

with

$$\mathbf{J} = \int_{\Omega_z} \hat{\mathbf{J}}(z)\ dz. \tag{4.77}$$

Integrating in the mesh $\Omega_{xy} = \cup_{e=1}^{\mathtt{E}} \Omega_{xy}^e$,

$$\int_{\Omega_{xy}} \mathbf{V}^{*T}(x,y)\mathbf{J}\mathbf{G}(x,y)\ dx\ dy = \sum_{e=1}^{\mathtt{E}} \int_{\Omega_{xy}^e} \mathbf{V}^{e*T}(x,y)\mathbf{J}\mathbf{G}^e(x,y)\ dx\ dy, \tag{4.78}$$

where $\mathbf{V}^e(x,y)$ and $\mathbf{G}^e(x,y)$ are approximated respectively from

$$\mathbf{V}^e(x,y) = \mathbf{N}(x,y)\mathbf{U}^e, \tag{4.79}$$

and

$$\mathbf{G}^e(x,y) = \mathbf{N}(x,y)\mathbf{R}^e, \tag{4.80}$$

with $\mathbf{R}^e$ containing the nodal values of $\mathbf{G}(x,y)$ and $\mathbf{N}(x,y) = [\mathbf{N}_1(x,y)\ \mathbf{N}_2(x,y)\ \mathbf{N}_3(x,y)]$, and

$$\mathbf{N}_i = \begin{pmatrix} N_i^e(x,y) & 0 & 0 \\ 0 & N_i^e(x,y) & 0 \\ 0 & 0 & N_i^e(x,y) \end{pmatrix}. \tag{4.81}$$

Thus, it results

$$\sum_{e=1}^{\mathtt{E}} \int_{\Omega_{xy}^e} \mathbf{V}^{e*T}(x,y)\mathbf{J}\mathbf{G}^e(x,y)\ dx\ dy = \sum_{e=1}^{\mathtt{E}} \mathbf{U}^{e*T} \left\{ \int_{\Omega_{xy}^e} \mathbf{N}^T\mathbf{J}\mathbf{N}\ dx\ dy \right\} \mathbf{R}^e$$

$$= \sum_{e=1}^{\mathtt{E}} \mathbf{U}^{e*T}\mathbf{A}_{xy}^e\mathbf{R}^e = \sum_{e=1}^{\mathtt{E}} \mathbf{U}^{e*T}\mathbf{B}_{xy}^e = \mathbf{U}^{*T}\mathbf{B}_{xy}, \tag{4.82}$$

from which, the principle of virtual works reads

$$\mathbf{U}^{*T}\mathbf{K}_{xy}\mathbf{U} = \mathbf{U}^{*T}\mathbf{B}_{xy}. \tag{4.83}$$

Remark 1. In general the displacement decomposition within the PGD rationale involves more than a single mode, however, within the updating process, when calculating the n mode, the $n-1$ already computed move to the right hand member, acting as generalized body force.

Remark 2. Thus, the in-plane functions determining the kinematics can be obtained from a standard plate theory software by using the elementary rigidity and forces given respectively by $\mathbf{K}_{xy}^e$ and $\mathbf{B}_{xy}^e$ considered in expression (4.70) and (4.82).

Remark 3. If traction $\mathbf{T} \neq \mathbf{0}$ the same procedure can be applied to treat the corresponding terms.

4.2.3 Calculation of the out-of plane functions

The expression of the solution obtained in the previous section is given by

$$\mathbf{u}(x,y,z) = \begin{pmatrix} u(x,y,z) \\ v(x,y,z) \\ w(x,y,z) \end{pmatrix} = \begin{pmatrix} \theta^x(x,y)f^x(z) \\ \theta^y(x,y)f^y(z) \\ w(x,y)f^z(z) \end{pmatrix} = \mathbf{V}(x,y) \circ \mathbf{W}(z), \tag{4.84}$$

where

$$\mathbf{V}(x,y) = \begin{pmatrix} \theta^x(x,y) \\ \theta^y(x,y) \\ w(x,y) \end{pmatrix} \tag{4.85}$$

and

$$\mathbf{W}(z) = \begin{pmatrix} f^x(z) \\ f^x(z) \\ f^z(z) \end{pmatrix}. \tag{4.86}$$

Now, we proceed to update the out-of-plane functions involved in $\mathbf{W}(z)$ from the just calculated in-plane functions $\mathbf{V}(x,y)$ by considering again the principle of virtual work

$$\int_{\Omega_{xy}\times\Omega_z} \boldsymbol{\varepsilon}(\mathbf{u}^*) \cdot (\mathbf{C} \cdot \boldsymbol{\varepsilon}(\mathbf{u})\ d\mathbf{x} = \int_{\Omega_{xy}\times\Omega_z} \mathbf{u}^* \cdot \mathbf{f}\, d\mathbf{x} \tag{4.87}$$

where now in Eq. (4.84) the in-plane functions are assumed known and we look for the ones involved in the out-of-plane contribution $\mathbf{W}(z)$. Thus, Eq. (4.87) can be integrated on Ω_{xy} and it reduces to a one dimensional problem in Ω_z involving as unknown functions $f^x(z)$, $f^y(z)$ and $f^z(z)$.

The same rationale that was previously addressed when performing the in-plane calculations is considered again but now with the test functions given by

$$\boldsymbol{\varepsilon}^* = \boldsymbol{\Theta}^1(x,y) \circ \mathbf{F}^{1*}(z) + \boldsymbol{\Theta}^2(x,y) \circ \mathbf{F}^{2*}(z), \tag{4.88}$$

and

$$\mathbf{u}^*(x,y,z) = \mathbf{V}(x,y) \circ \mathbf{W}^*(z). \tag{4.89}$$

Now, from the updated out-of-plane functions in $\mathbf{W}(z)$, the in-plane functions in $\mathbf{V}(x,y)$ are again updated and the procedure repeats until reaching the convergence (fixed point). The procedure for computing the out-of-plane components in this minimally-intrusive way is detailed in Appendix C.

4.2.4 Numerical results

The problem taken into consideration is depicted in Fig. 4.22. The geometrical and mechanical properties of the plate domain $\Omega = [0, H_x] \times [0, H_y] \times [0, H_z]$ are defined in Table 4.10 On the right boundary face of the domain (the blue zone in Fig. 4.22) a vertical traction is enforced, $\mathbf{T} = (0, 0, 8 \cdot 10^9) N/m^2$ and on the opposite face homogeneous Dirichlet boundary conditions are imposed. No volumetric body

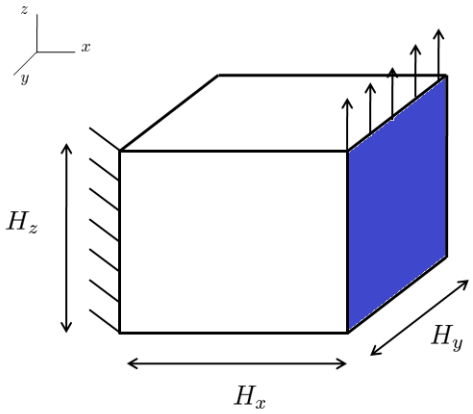

Figure 4.22 – *The problem taken into consideration*

Table 4.10 – *Model parameters.*

H_x: Length in the x direction (mm)	250
H_y: Length in the y direction (mm)	250
H_z: Length in the z direction (mm)	250
E: Young modulus (N/m^2)	$2 \cdot 10^{11}$
ν: Poisson coefficient	0.25

forces are considered. As in the considered domain the thickness (out-of-plane) dimension is not much lower than the other ones (in-plane dimensions), the linear variation of the displacement field along the thickness described by (4.6) is not more true as we can notice in Fig. 4.23. In this figure the plate solution differs from the fully 3D solution. However using the just proposed minimally-intrusive fully 3D separated plate formulation we can notice how the solution is improved. In Fig. 4.24 it is also possible to see the error of the solution respect to the 3D FEM solution, computed as

$$\xi(\mathbf{u}) = \frac{\left(\int_\Omega \left(\mathbf{u} - \mathbf{u}_{FEM}\right)^2 d\,\mathbf{x}\right)^{\frac{1}{2}}}{\left(\int_\Omega \left(\mathbf{u}_{FEM}\right)^2 d\,\mathbf{x}\right)^{\frac{1}{2}}}, \tag{4.90}$$

as a function of the number of modes. The error of the plate theory solution would be $\xi(\mathbf{u}_{plate}) = 0.0633$.

We consider now the same problem as the previous example but this time we suppose that there is an hole in the domain. As in the previous example, in Fig. 4.25 it is depicted the solution computed using the different techniques. Moreover in Figs. 4.26, 4.27 and 4.28 different perspectives of the out-of-plane stress tensor components are depicted. Let's note how the proposed method is able to take into consideration the σ_{zz} components, which is considered negligible in the plate the-

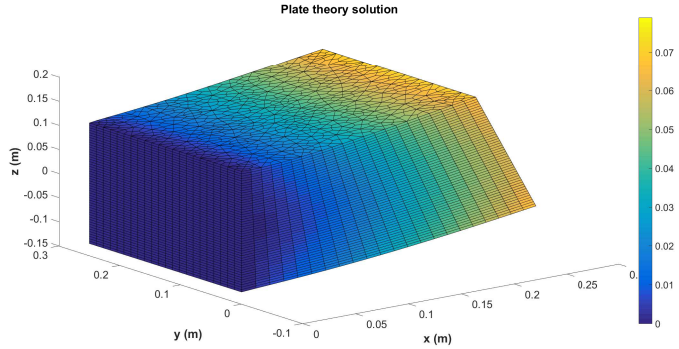

(a)

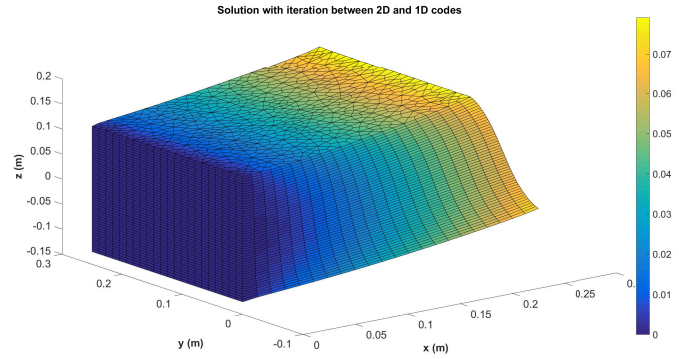

(b)

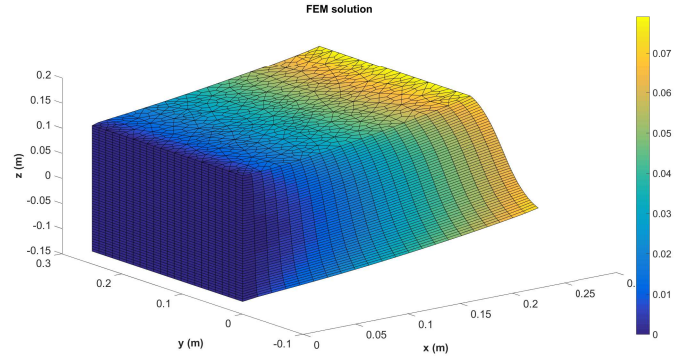

(c)

Figure 4.23 – *Displacement field using: plate theory (a), minimally-intrusive fully 3D separated plate formulation (b), 3D FEM (c).*

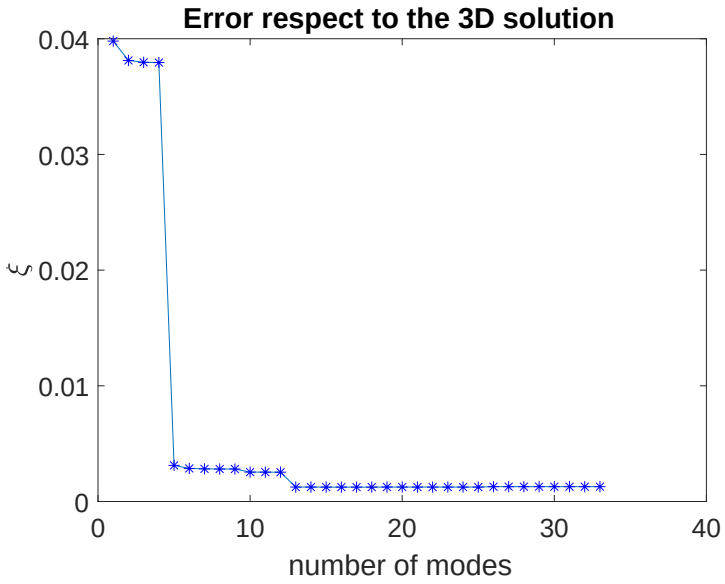

Figure 4.24 – *Error of the enriched solution respect to the 3D solution for different number of modes.*

ory, and to obtain the parabolic evolution around the thickness for the σ_{xz} and σ_{yz} typical of a 3D solution (Fig. 4.28).

In Figs. 4.29, 4.30 and 4.31 the same quantities are computed using a 3D finite element method, proving the good results of the proposed method.

Again, in Fig. 4.32 it is possible to see the error of the solution respect to the 3D FEM solution as a function of the number of modes. The error of the plate theory solution would be $\xi(\mathbf{u}_{plate}) = 0.0638$.

4.2.5 Extension of the method to elasto-plastic dynamics

In this section we extend the method to dynamics problem in which plastic behavior can occur. With $\mathbf{g}(\mathbf{x}, t)$ the body forces, the displacement field evolution $\mathbf{u}(\mathbf{x}, t)$ in the domain Ω and time interval $t \in I = (0, T]$ is described by the linear momentum balance equation

$$\rho\ddot{\mathbf{u}}(\mathbf{x}, t) = \nabla \cdot \boldsymbol{\sigma} + \mathbf{g}, \tag{4.91}$$

where ρ is the density (kg/m^3).

The boundary $\partial\Omega$ is decomposed according to $\partial\Omega = \Gamma_D \cup \Gamma_N$ where displacement and tractions $\mathbf{T}(t)$ are prescribed.

The behavior relating the Cauchy's stress $\boldsymbol{\sigma}$ and the elastic strain $\boldsymbol{\varepsilon}^e$ reads

$$\boldsymbol{\sigma} = \mathbf{C}\boldsymbol{\varepsilon}^e = \mathbf{C}(\boldsymbol{\varepsilon} - \boldsymbol{\varepsilon}^p), \tag{4.92}$$

where $\mathbf{C}$ is the Hooke tensor, $\boldsymbol{\varepsilon}$ is total strain and $\boldsymbol{\varepsilon}^p$ is the plastic strain.

The problem weak form associated with the strong form (4.91) results in looking

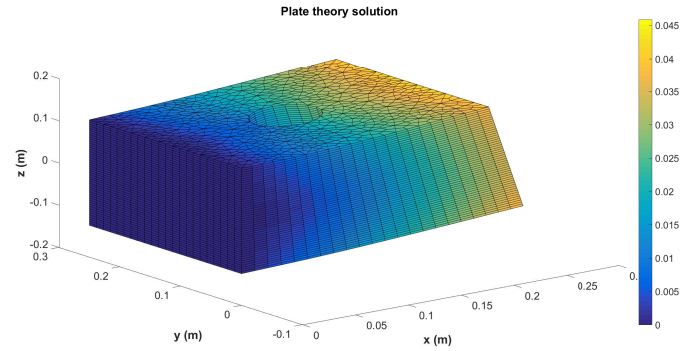

(a)

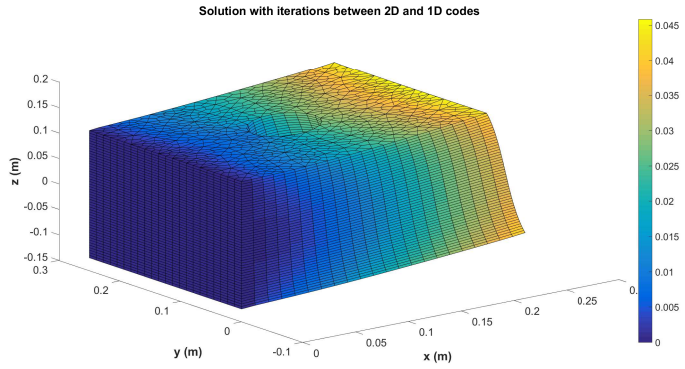

(b)

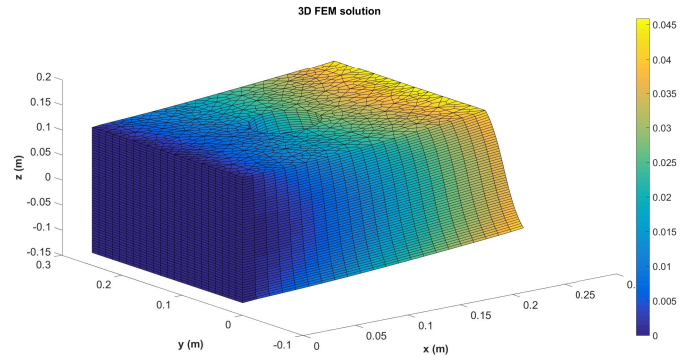

(c)

Figure 4.25 – *Displacement field using: plate theory (a), minimally-intrusive fully 3D separated plate formulation (b), 3D FEM (c).*

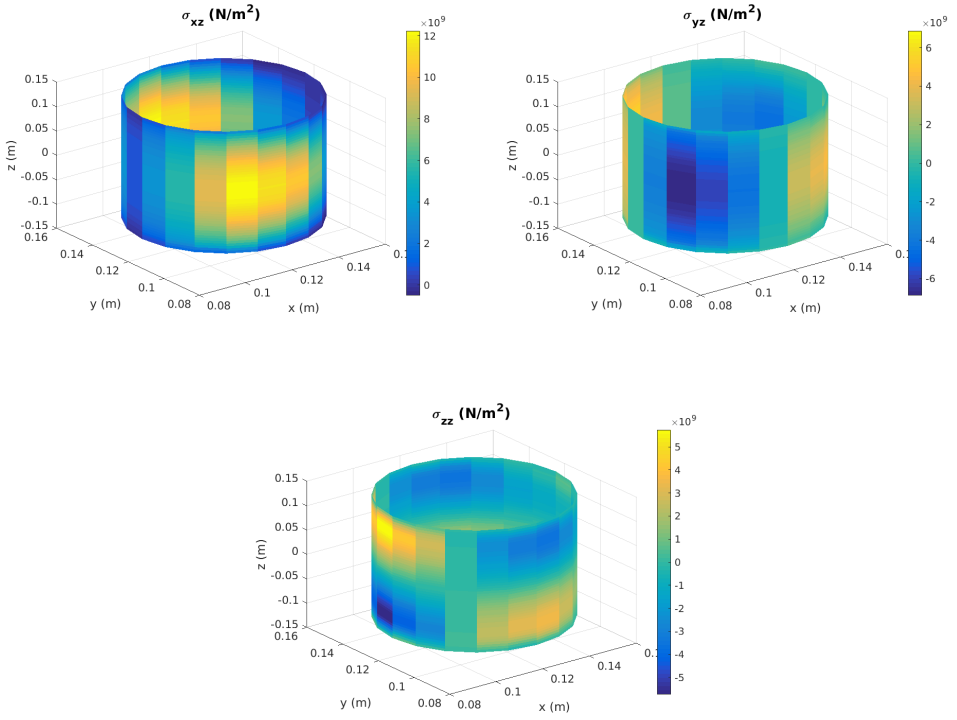

Figure 4.26 – *Out-of-plane stress tensor components around the hole using the minimally-intrusive fully 3D separated plate formulation.*

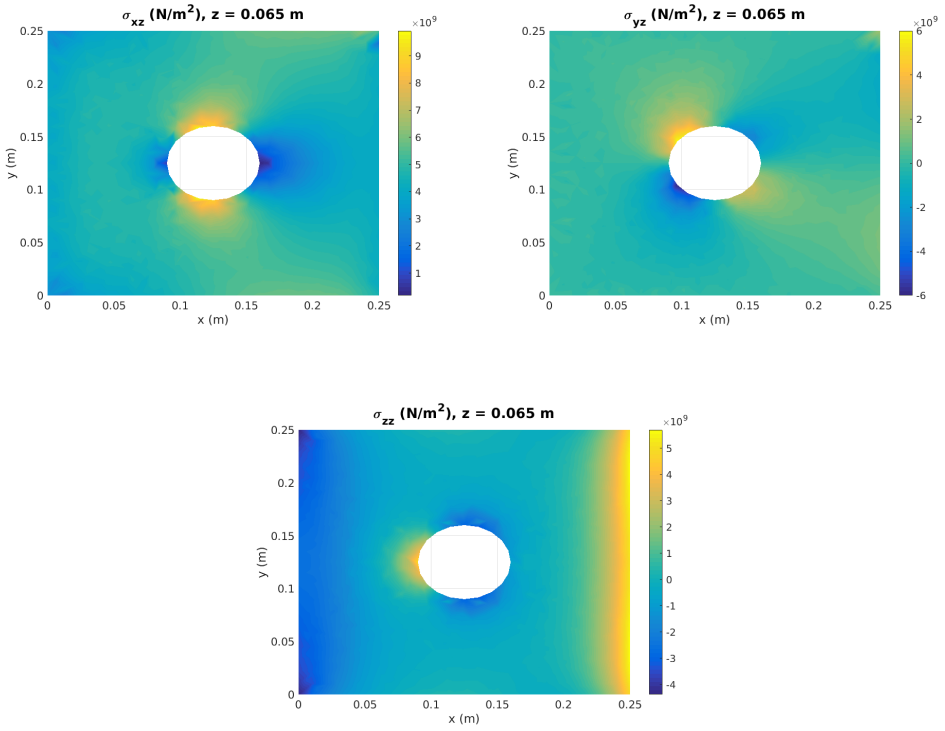

Figure 4.27 – *Out-of-plane stress tensor components in the $z = 65mm$ plane using the minimally-intrusive fully 3D separated plate formulation.*

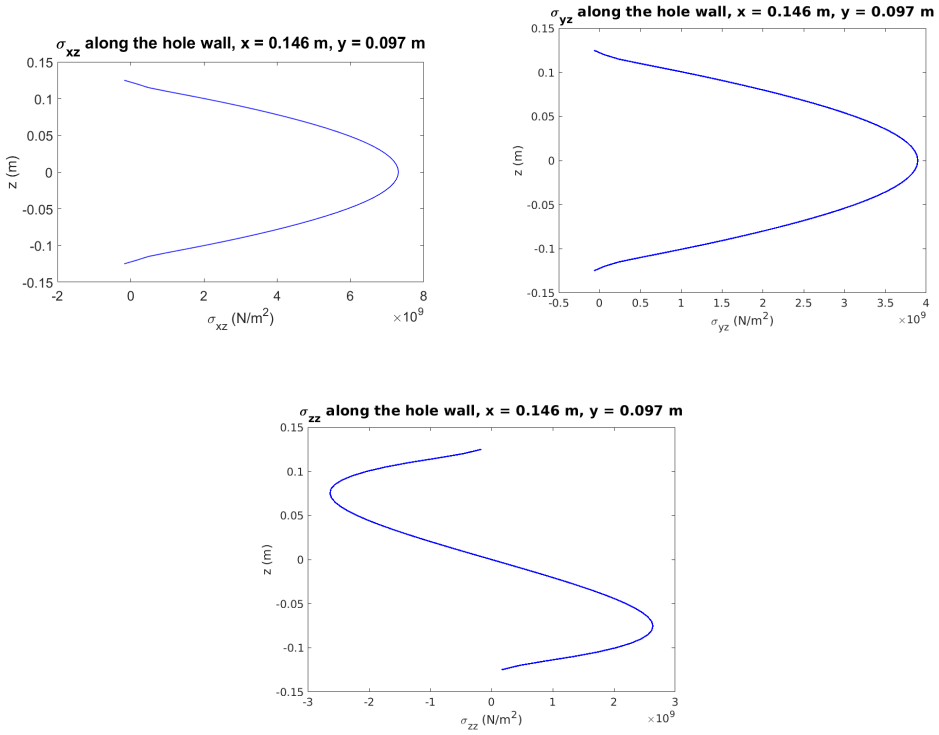

Figure 4.28 – *Out-of-plane stress tensor components around the hole for* $x = 146mm$ *and* $y = 97mm$ *using the minimally-intrusive fully 3D separated plate formulation.*

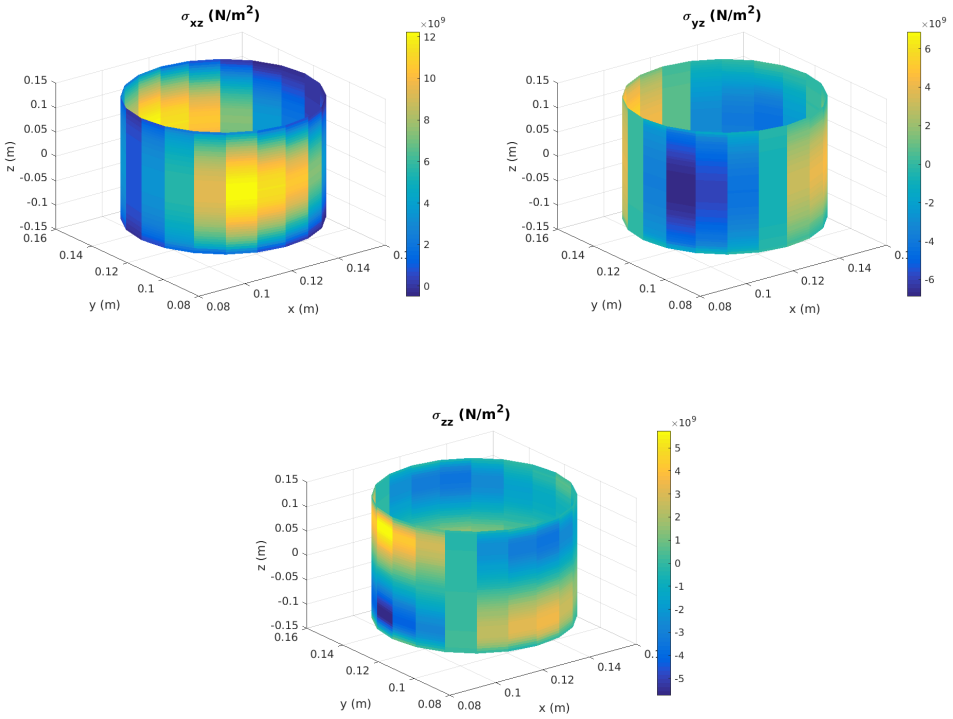

Figure 4.29 – *Out-of-plane stress tensor components around the hole using 3D FEM.*

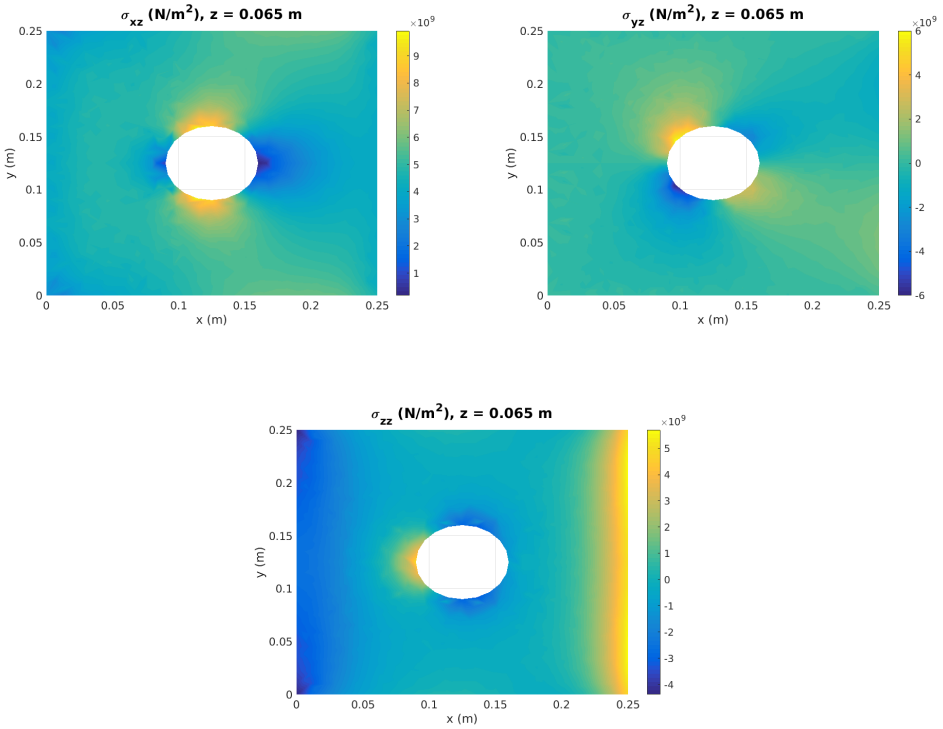

Figure 4.30 – *Out-of-plane stress tensor components in the* $z = 65mm$ *plane using 3D FEM.*

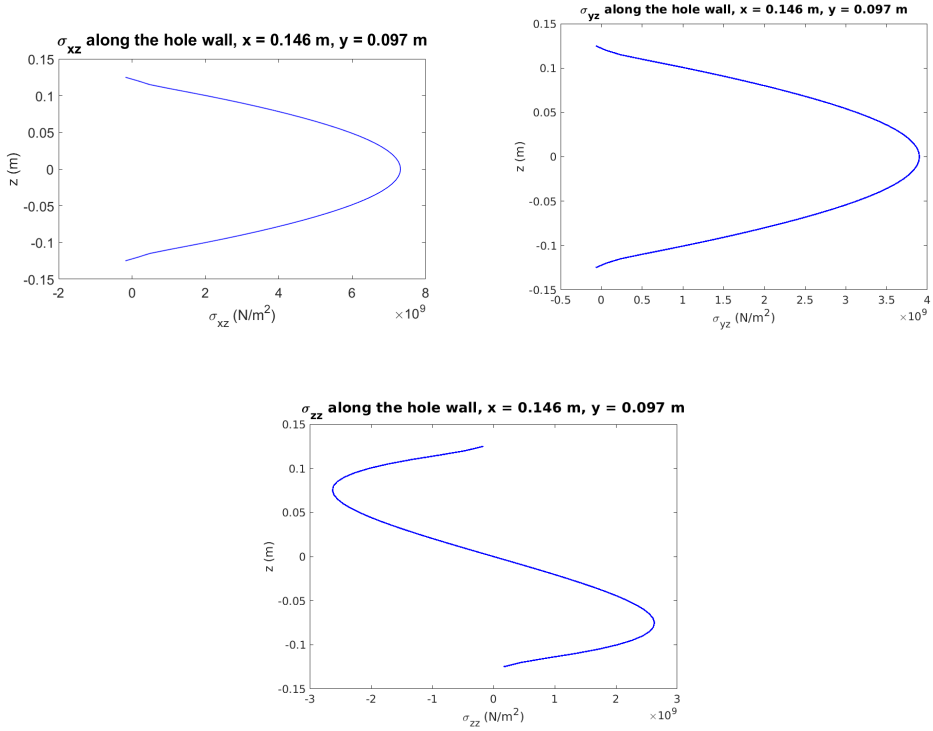

Figure 4.31 – *Out-of-plane stress tensor components around the hole for* $x = 146mm$ *and* $y = 97mm$ *using 3D FEM.*

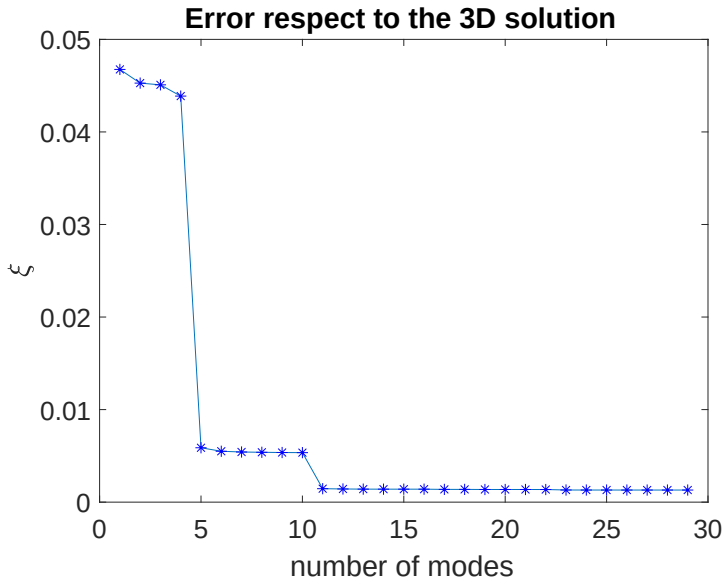

Figure 4.32 – *Error of the enriched solution respect to the 3D solution for different number of modes.*

for the displacement field $\mathbf{u}$ verifying the initial and Dirichlet boundary conditions, and fulfilling

$$\rho \int_\Omega \mathbf{u}^* \cdot \ddot{\mathbf{u}}\, d\mathbf{x} + \int_\Omega \boldsymbol{\varepsilon}(\mathbf{u}^*) \cdot (\mathbf{C}\ (\boldsymbol{\varepsilon}(\mathbf{u}) - \boldsymbol{\varepsilon}^p(\mathbf{u})))\ d\mathbf{x} = \int_\Omega \mathbf{u}^* \cdot \mathbf{g}\, d\mathbf{x} + \int_{\Gamma_N} \mathbf{u}^* \cdot \mathbf{T}(t)\, d\mathbf{x} \tag{4.93}$$

for any test function $\mathbf{u}^*$ in an appropriate functional space. We consider at time t_{j+1} the standard explicit time integration [Bathe 2006] (widely considered in commercial codes) already presented in previous chapters and given by

$$\rho \int_\Omega \mathbf{u}^* \cdot \frac{\mathbf{u}^{j+1} - 2\mathbf{u}^j + \mathbf{u}^{j-1}}{\Delta t^2} d\mathbf{x} + \int_\Omega \boldsymbol{\varepsilon}(\mathbf{u}^*) \cdot \left(\mathbf{C}\ \left(\boldsymbol{\varepsilon}(\mathbf{u}^j) - \boldsymbol{\varepsilon}^p(\mathbf{u}^j)\right)\right) d\mathbf{x} = \int_\Omega \mathbf{u}^* \cdot \mathbf{g}^j\, d\mathbf{x} + \int_{\Gamma_N} \mathbf{u}^* \cdot \mathbf{T}^j d\mathbf{x}, \tag{4.94}$$

or, by putting all the explicit terms at the right hand side,

$$\rho \int_\Omega \mathbf{u}^* \cdot \mathbf{u}^{j+1} d\mathbf{x} = \rho \int_\Omega \mathbf{u}^* \cdot \left(2\mathbf{u}^j - \mathbf{u}^{j-1}\right) d\mathbf{x} - \Delta t^2 \Big(\int_\Omega \boldsymbol{\varepsilon}(\mathbf{u}^*) \cdot \left(\mathbf{C}\ \left(\boldsymbol{\varepsilon}(\mathbf{u}^j) - \boldsymbol{\varepsilon}^p(\mathbf{u}^j)\right)\right) d\mathbf{x} + \int_\Omega \mathbf{u}^* \cdot \mathbf{g}^j\, d\mathbf{x} + \int_{\Gamma_N} \mathbf{u}^* \cdot \mathbf{T}^j d\mathbf{x} \Big). \tag{4.95}$$

Recalling (4.72) we can write

$$\mathbf{u}^{j+1}(x, y, z) = \mathbf{V}^{j+1} \circ \mathbf{W}^{j+1}. \tag{4.96}$$

Supposing the out-of-plane functions known, the left hand side term in (4.95) can be expressed as

$$\mathbf{u}^{*T}\mathbf{u}^{j+1}(\mathbf{x}) = \mathbf{V}^{j+1,*T}(x, y)\hat{\mathbf{J}}^{j+1}(z)\mathbf{V}^{j+1}(x, y), \tag{4.97}$$

where matrix $\hat{\mathbf{J}}^{j+1}$ reads

$$\hat{\mathbf{J}}^{j+1}_{kl}(z) = \mathbf{I}_{kl}\mathbf{W}^{j+1}_k(z)\mathbf{W}^{j+1}_l(z), \tag{4.98}$$

with $\mathbf{I}$ the identity matrix. Now, the integral results

$$\rho \int_\Omega \mathbf{u}^* \cdot \mathbf{u}^{j+1}\ dz\ dx\ dy = \int_{\Omega_{xy}} \mathbf{V}^{j+1,*T}(x, y)\mathbf{J}^{j+1}\mathbf{V}^{j+1}(x, y)\ dx\ dy, \tag{4.99}$$

with

$$\mathbf{J}^{j+1} = \int_{\Omega_z} \hat{\mathbf{J}}^{j+1}(z)\ dz, \tag{4.100}$$

Integrating in the mesh $\Omega_{xy} = \cup_{e=1}^{\mathtt{E}} \Omega^e_{xy}$,

$$\int_{\Omega_{xy}} \mathbf{V}^{j+1,*T}\mathbf{J}^{j+1}\mathbf{V}^{j+1}\ dx\ dy = \sum_{e=1}^{\mathtt{E}} \int_{\Omega^e_{xy}} \mathbf{V}^{j+1,e*T}\mathbf{J}^{j+1}\mathbf{V}^{j+1,e}\ dx\ dy, \tag{4.101}$$

Table 4.11 – *Model parameters.*

H_x: Length in the x direction (mm)	250
H_y: Length in the y direction (mm)	250
H_z: Length in the z direction (mm)	20
E: Young modulus (N/m^2)	$6.68 \cdot 10^{10}$
ν: Poisson coefficient	0.35
ρ: Density (kg/m^3)	2700

where $\mathbf{V}^{j+1,e}(x,y)$ is approximated from

$$\mathbf{V}^{j+1,e}(x,y) = \mathbf{N}(x,y)\mathbf{U}^{j+1,e}, \tag{4.102}$$

with $\mathbf{N}(x,y) = [\mathbf{N}_1(x,y)\ \mathbf{N}_2(x,y)\ \mathbf{N}_3(x,y)]$, and

$$\mathbf{N}_i = \begin{pmatrix} N_i^e(x,y) & 0 & 0 \\ 0 & N_i^e(x,y) & 0 \\ 0 & 0 & N_i^e(x,y) \end{pmatrix}. \tag{4.103}$$

Thus, it results

$$\sum_{e=1}^{\mathtt{E}} \int_{\Omega_{xy}^e} \mathbf{V}^{j+1,e*T}\mathbf{J}^{j+1}\mathbf{V}^{j+1,e}\ dx\ dy = \sum_{e=1}^{\mathtt{E}} \mathbf{U}^{j+1,e*T} \left\{ \int_{\Omega_{xy}^e} \mathbf{N}^T\mathbf{J}^{j+1}\mathbf{N}\ dx\ dy \right\} \mathbf{U}^{j+1,e}$$

$$= \sum_{e=1}^{\mathtt{E}} \mathbf{U}^{j+1,e*T} M_{xy}^{j+1,e}\mathbf{U}^{j+1,e} = \mathbf{U}^{j+1,*T}\mathbf{M}_{xy}^{j+1}\mathbf{U}^{j+1}. \tag{4.104}$$

The different terms at the right hand side of (4.95) can be treated in a similar way, as already explained for the static case, so that at each time step j the virtual work principle reads

$$\mathbf{U}^{j+1,*T}\mathbf{M}_{xy}^{j+1}\mathbf{U}^{j+1} = \mathbf{U}^{j+1,*T}\mathbf{B}_{xy}^{j}. \tag{4.105}$$

Remark 4. As for the static case, the in-plane functions determining the kinematics can be obtained from a standard plate theory software by using the elementary mass and forces given respectively by $\mathbf{M}_{xy}^{j+1,e}$ and $\mathbf{B}_{xy}^{j,e}$.

Remark 5. Again the out-of-plane functions can be obtained in a similar manner as already explained in the static case.

For evaluating the performances of the method we consider the problem defined in Fig. 4.33. The geometrical and mechanical properties of the plate domain are defined in Table 4.11 On the right boundary face of the domain (the blue zone in Fig. 4.33) an horizontal traction is enforced, $\mathbf{T} = (2.7 \cdot 10^8, 0, 0) N/m^2$ and on the op-

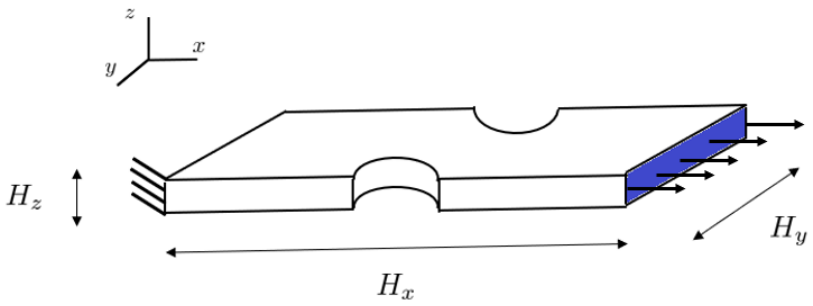

Figure 4.33 – *The elasto-plastic dynamical problem taken into consideration*

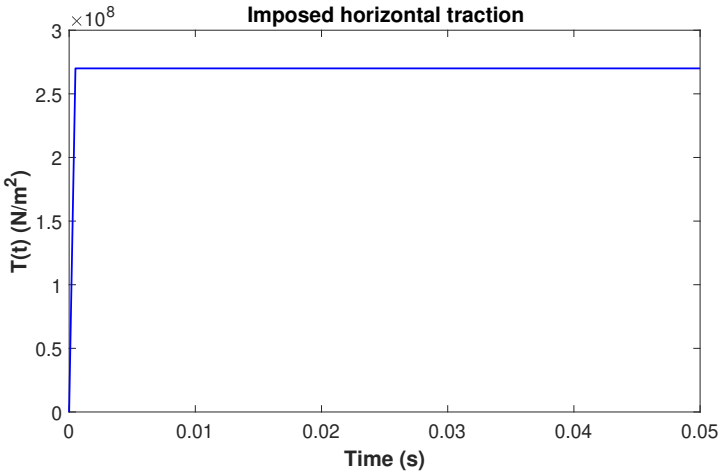

Figure 4.34 – *Horizontal loading for the elasto-plastic dynamical problem.*

posite face homogeneous Dirichlet boundary conditions are imposed. No volumetric body forces are considered. For the sake of simplicity, we use the Von Mises criterion [Mises 1913], assuming a Krupkowky isotropic hardening [Siser & Slota 2016] given by the formula:

$$\bar{\sigma} = K\left(\bar{\varepsilon}_0 + \bar{\varepsilon}_p\right)^p \tag{4.106}$$

where $\bar{\varepsilon}_0 = 0.008$ is the initial equivalent plastic strain, $\bar{\varepsilon}_p$ is the equivalent plastic strain, $K = 0.4619\,GPa$ is a strength coefficient and $p = 0.1$ is the strain hardening exponent [Wilkins *et al.* 1980]. The problem is solved in the time interval $[0, 50]\,ms$ with a time step $\Delta t = 10^{-4}\,ms$ which ensures the stability of the explicit method. In order to get the stationary solution, the traction is applied gradually as depicted in Fig. 4.34 and a Rayleigh damping (proportional to the mass) is used. Figs. 4.35, 4.36 and 4.37 compares the solution obtained with the three methods at different times. For this problem the 2D solution is given by shell theory [Oñate 2010] as

$$\begin{cases} u(x,y,z) = u_0(x,y) - z\theta_x(x,y) \\ v(x,y,z) = v_0(x,y) - z\theta_y(x,y) \\ w(x,y,z) = w_0(x,y) \end{cases} \tag{4.107}$$

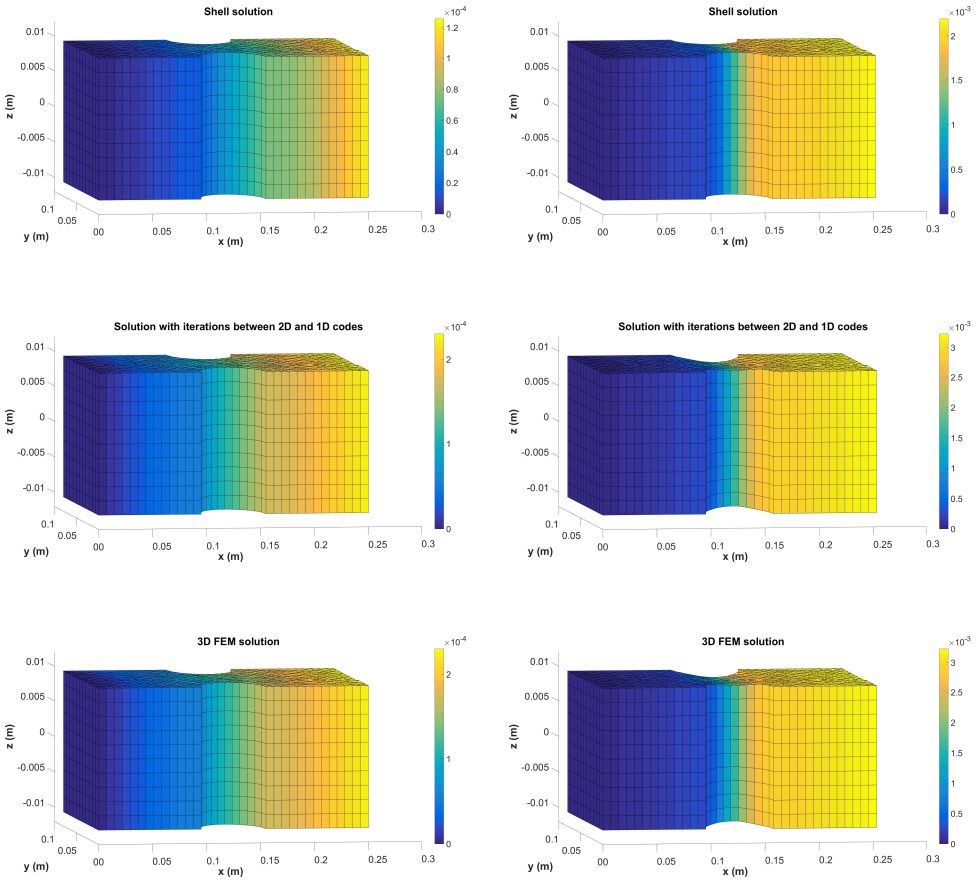

Time $= 0.1\,ms$ Time $= 0.5\,ms$

Figure 4.35 – *Displacement field using the three methods for* $t = 0.1\,ms$ *and* $t = 0.5\,ms$.

where u_0, v_0 and w_0 are the displacements of the points on the middle plane along x, y and z respectively and the rotations θ_x and θ_y coincide with the angles followed by the normal vectors contained in the planes xz and yz respectively in their motions. Again the solution computed using the proposed method is able to get a 3D behavior (as the one of the 3D FEM solution) with the striction along the thickness in the zone with a smaller section, which is typical of a 3D plastic solution.

4.2.6 Conclusions

This second part of the chapter proposed a minimally intrusive formulation of mechanical problems (linear, elasto-plastic, static and dynamic) defined in separable domains, enabling 3D solutions expressed as a finite sum decomposition involving the product of functions defined in the plane and in the thickness. The main contribution of the present work is that the calculation of functions defined in the plane, the most expensive computationally, can be ensured by a standard plate solver,

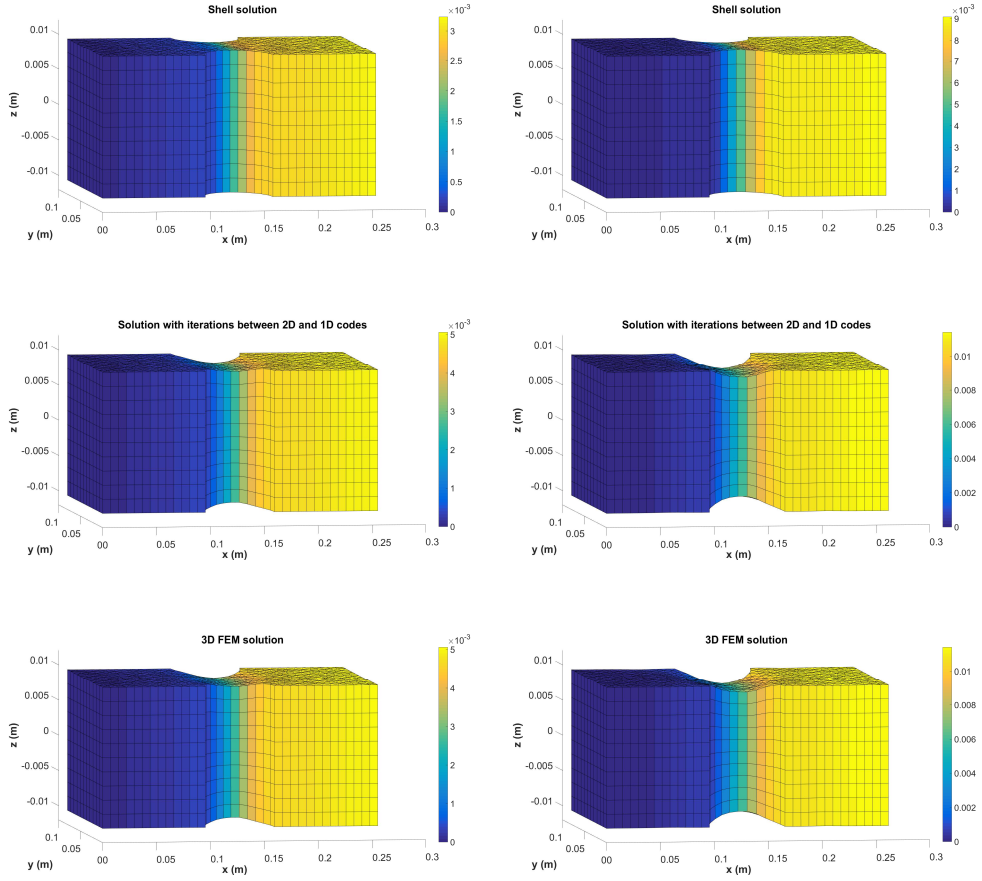

Figure 4.36 – *Displacement field using the three methods for* $t = 1\,ms$ *and* $t = 5\,ms$.

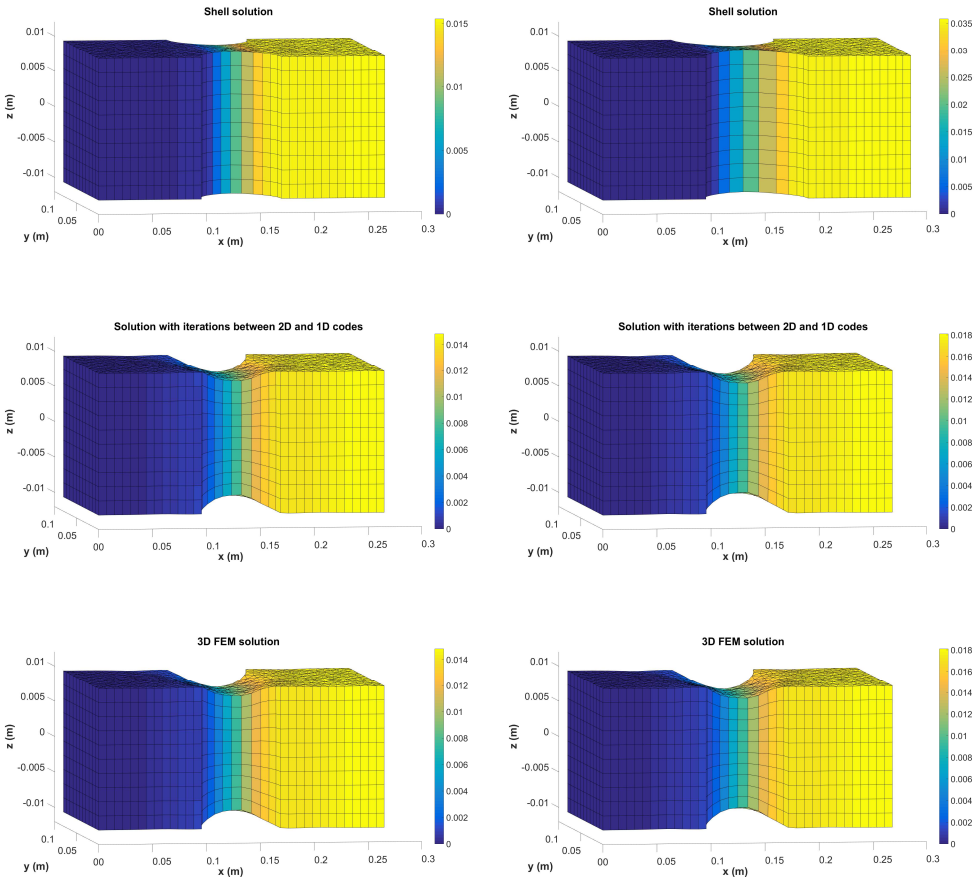

Time $= 10\,ms$ Time $= 30\,ms$

Figure 4.37 – *Displacement field using the three methods for* $t = 10\,ms$ *and* $t = 30\,ms$.

whereas the solution of those defined in the thickness, defining 1D problems extremely simple and cheap, is externalized and ensured by a function called by the plate solver.

The different numerical examples prove the procedure efficiency that allows computing 3D solutions while keeping the computational cost the one characteristic of standard 2D plate and shell calculations.

Chapter 5

Parametric evaluation of part distortion in additive manufacturing processes

Contents

Introduction Additive manufacturing is a mechanical process the more and more considered in industry, however efficient simulation tools able to perform accurate predictions are still quite limited. The main difficulties for an efficient simulation are related to the multiple scales, the multiple and complex physics involved, as well as the strong dependency on the process trajectory. This chapter aims at proposing a simplified parametric modeling and its subsequent parametric solution for evaluating parametrically the manufactured part distortion. The involved parameters are the ones parametrizing the process trajectories, the thermal shrinkage intensity and anisotropy (the former depending on several material and process parameters and the last directly depending on the process trajectory) and the deposited layers. The resulting simulation tool allows evaluating in real-time the impact of the parameters just referred on the part distortion, and proceed to the required geometrical compensation. Moreover optimization, sensitivity analysis and uncertainty propagation can also be performed.

This chapter and all the results presented in it correspond to the following paper:

- G. Quaranta, E. Haug, J.L. Duval, F. Chinesta, *Parametric evaluation of part distortion in additive manufacturing processes*, International Journal of Material Forming, **12**:1, 2019,

and to the following conference proceedings paper:

- G. Quaranta, E. Haug, J.L. Duval, E. Cueto, F. Chinesta, *Parametric Numerical Solutions of Additive Manufacturing Processes*, ESAFORM2019 Conference, AIP Conference Proceedings, 2019 (in press).

Figure 5.1 – *One-parameter process trajectories*

5.1 Parametrizing trajectories

Additive Manufacturing is an incremental process requiring the definition of the process trajectory. In order to efficiently evaluate the impact of the different possible trajectories on the part distortion, for optimizing or controlling the process, one should be able to simulate in almost real-time the process, possibility that remains nowadays out of reach. Alternatively one could create offline the parametric solution of the process, that is the output of interest, the part distortion in our case, for any possible process trajectory. Thus, the expensive offline calculation (the *vademecum* construction) will be largely compensated by its online use in almost real-time, because only particularizations of the parametric solutions are required.

In former works based on the Proper Generalized Decomposition method [Chinesta *et al.* 2011, Chinesta *et al.* 2013b, Chinesta *et al.* 2014a, Chinesta *et al.* 2015, Bur *et al.* 2016, Chinesta *et al.* 2014b] a panoply of different type parameters $\mu_1, \ldots, \mu_{\mathtt{Q}}$ were introduced as extra-coordinates in the model, leading to a parametric solution or *computational vademecums* like

$$u(\boldsymbol{x}, t, \mu_1, \ldots, \mu_{\mathtt{Q}}) \approx \sum_{i=1}^{\mathtt{M}} X_i(\boldsymbol{x}) T_i(t) \prod_{j=1}^{\mathtt{Q}} M_i^j(\mu_j), \tag{5.1}$$

in order to compute parametric solutions of models representing complex processes, structures and systems. In that expression parameters μ_i can be material parameters, process parameters (including initial and boundary conditions) and even parameters related to the geometry.

Sometimes parameters are not discrete but continuous, for example material parameters can evolve in space and/or time. In that case the solution retained was assuming an appropriate parametrization of these fields, and then including the coefficients of those approximations as model parameters and consequently, within the PGD rationale, as problem extra-coordinates.

This option was possible when the field describing the space and/or time evolution of the parameters involved few terms, however in the case of a trajectory the situation is radically different because any two points $\boldsymbol{P}$ and $\boldsymbol{Q}$, and independently on the distance between them, can be joined by an infinity of curves and then parametrizing a trajectory has no sense. Thus, rather than looking for all possible trajectories, one must restrict to a family of them.

To fix ideas we first consider the additive manufacturing process of a solid cuboid shape and the addition of a new rectangular layer on its top surface. A family of trajectories, for covering all its surface, could consist of straight lines parametrized by a single parameter, e.g. the angle θ with respect to the rectangle base, as depicted in Fig. 5.1. However, such a parametrization does not allow other usual process trajectories as the one illustrated in Fig. 5.2.

A general approach consists in associating the trajectories to the iso-field curves $\phi = \text{cte}$

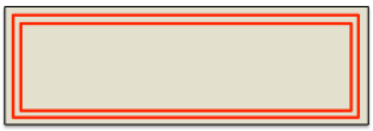

Figure 5.2 – *Concentric-like trajectories*

related to a certain parametrized partial differential equation involving the scalar field $\phi(x, y)$. For that purpose we propose considering the Poisson equation defined in the rectangular domain $\Omega = (0, L) \times (0, H)$

$$\Delta\phi(x, y) = s(x, y), \tag{5.2}$$

with the parametrized Dirichlet boundary conditions

$$\begin{cases} \phi(x, y = 0) = \mu_1 + (\mu_2 - \mu_1)\frac{x}{L} \\ \phi(x, y = H) = \mu_4 + (\mu_3 - \mu_4)\frac{x}{L} \\ \phi(x = 0, y) = \mu_1 + (\mu_4 - \mu_1)\frac{y}{H} \\ \phi(x = L, y) = \mu_2 + (\mu_3 - \mu_2)\frac{y}{H} \end{cases}, \tag{5.3}$$

that represent linear variations on each rectangle side, parametrized by the values at the corners $\phi(0, 0) = \mu_1$, $\phi(L, 0) = \mu_2$, $\phi(L, H) = \mu_3$ and $\phi(0, H) = \mu_4$. When all these parameters defining the boundary condition vanish, and the source term takes a unit value, i.e. $s(x, y) = 1$, the solution iso-curves are expected representing concentric trajectories.

The parametric solution of this problem is easily computable because of its linearity, and consequently the use of the standard constructor of PGD parametric solutions is not compulsory. One must simply solve the following five boundary value problems:

$$\Delta\phi^1(x, y) = s(x, y), \text{ with } s(x, y) = 0 \ \& \ \mu_1 = 1, \mu_2 = \mu_3 = \mu_4 = 0, \tag{5.4}$$

$$\Delta\phi^2(x, y) = s(x, y), \text{ with } s(x, y) = 0 \ \& \ \mu_2 = 1, \mu_1 = \mu_3 = \mu_4 = 0, \tag{5.5}$$

$$\Delta\phi^3(x, y) = s(x, y), \text{ with } s(x, y) = 0 \ \& \ \mu_3 = 1, \mu_1 = \mu_2 = \mu_4 = 0, \tag{5.6}$$

$$\Delta\phi^4(x, y) = s(x, y), \text{ with } s(x, y) = 0 \ \& \ \mu_4 = 1, \mu_1 = \mu_2 = \mu_3 = 0, \tag{5.7}$$

and

$$\Delta\phi^5(x, y) = s(x, y), \text{ with } s(x, y) = 1 \ \& \ \mu_1 = \mu_2 = \mu_3 = \mu_4 = 0. \tag{5.8}$$

Now, any other solution for any choice of parameters $\mu_1, \cdots, \mu_4$ and $\mu_5 = s(x, y)$ can be obtained from

$$\phi(x, y, \mu_1, \cdots, \mu_5) = \mu_1\phi^1(x, y) + \cdots + \mu_5\phi^5(x, y). \tag{5.9}$$

Obviously richer parametrizations of the boundary conditions as well as of the source term can be envisaged. Even other linear and nonlinear parametrized partial differential equations could be adopted, where in the nonlinear case, where superposition fails, the usual greedy PGD constructor should be considered for circumventing the curse of dimensionality.

Fig. 5.3 depicts different scenarios, where parameters $\mu_1, \cdots, \mu_4$ and $\mu_5 = s(x, y)$ are noted by $P1, \cdots, P5$. The developed GUI application allows evaluating any possible trajectory related to the problem defined above in almost real-time.

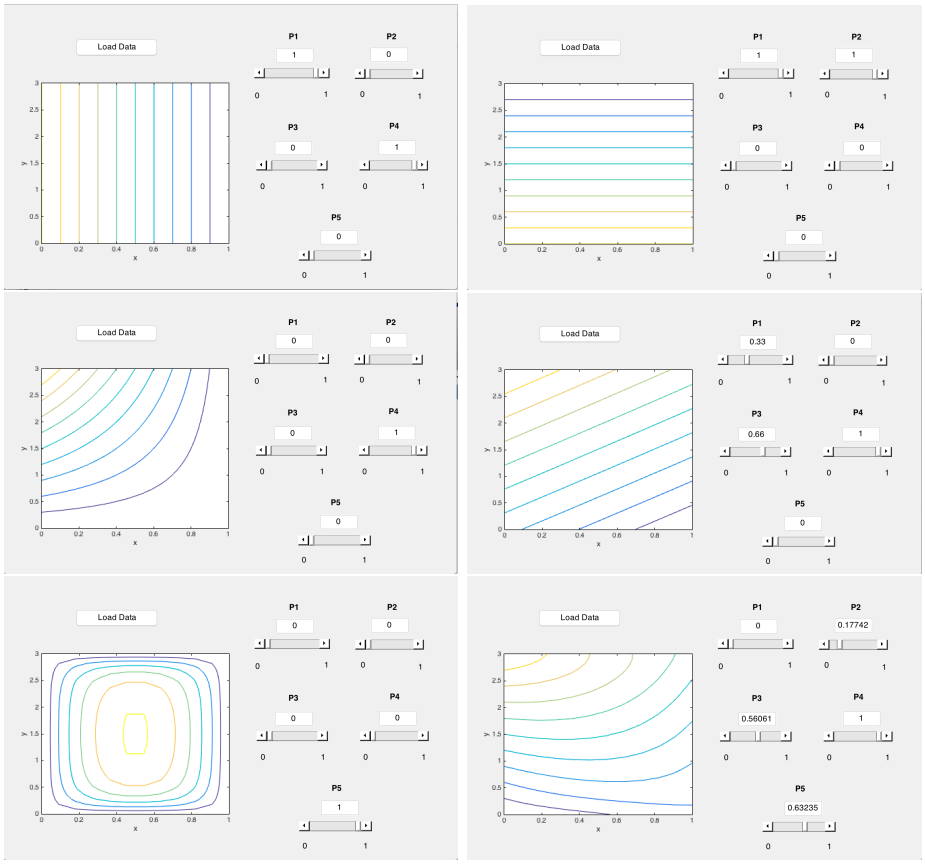

Figure 5.3 – *Trajectories for: (top-left)* $\mu_1 = 1,\ \mu_2 = 0,\ \mu_3 = 0,\ \mu_4 = 1,\ \mu_5 = 0$*; (top-right)* $\mu_1 = 1,\ \mu_2 = 1,\ \mu_3 = 0,\ \mu_4 = 0,\ \mu_5 = 0$*; (middle-left)* $\mu_1 = 0,\ \mu_2 = 0,\ \mu_3 = 0,\ \mu_4 = 1,\ \mu_5 = 0$*; (middle-right)* $\mu_1 = 0.33,\ \mu_2 = 0,\ \mu_3 = 0.66,\ \mu_4 = 1,\ \mu_5 = 0$*; (bottom-left)* $\mu_1 = 0,\ \mu_2 = 0,\ \mu_3 = 0,\ \mu_4 = 0,\ \mu_5 = 1$ *and (bottom-right)* $\mu_1 = 0,\ \mu_2 = 0.2,\ \mu_3 = 0.5,\ \mu_4 = 1,\ \mu_5 = 0.6$*. Dimensions:* $\times 10cm$.

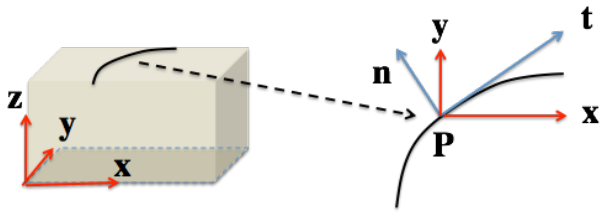

Figure 5.4 – *Wired model for the installed residual stresses*

5.2 A simplified parametric thermo-mechanical model

In this section we address parametrized thermal shrinkage. Many simplified AM simulators consider that as soon as a layer or several layers are assumed deposited at a certain temperature, from which the cooling process occurs, and being the thermal shrinkage constrained by the already solid part, residuals stress are induced.

In this work, among the numerous possibilities we are assuming a wired model that considers that thermal shrinkage follows the deposition trajectory as sketched in Fig. 5.4.

Thus, in the local system of coordinates, shrinkage strains are expected having the expression

$$\tilde{\varepsilon}_0(\mathbf{P}) = \begin{pmatrix} \lambda & 0 & 0 \\ 0 & 0 & 0 \\ 0 & 0 & 0 \end{pmatrix}. \tag{5.10}$$

It is important to note that when the wired hypothesis is expected working inappropriately, one could consider a richer parametrization of the shrinkage strain tensor, coming from an appropriate micro-to-macro upscaling modeling and assuming, in the most general case, an expression containing six parameters (the six components of the symmetric shrinkage strain tensor). In the general case the strain tensor could also depend on the space coordinates. These spatial dependence will result from a micro-mechanical analysis and will require a richer parametric expression by invoking the PGD rationale.

The global equilibrium requires expressing shrinkage strains, given at each point by expression (5.10) in the local coordinate system related to the local trajectory, in the global coordinate systems (x, y, z) depicted in Fig. 5.4. For that purpose we should consider the rotation of it according to

$$\boldsymbol{\varepsilon}_0(\mathbf{P}) = \mathbf{R}^T \tilde{\boldsymbol{\varepsilon}}_0(\mathbf{P})\mathbf{R}, \tag{5.11}$$

with $\mathbf{R}$ the rotation matrix. Shrinkage stresses would then be given by

$$\boldsymbol{\sigma}_0(\mathbf{P}) = \mathbb{C}\,\boldsymbol{\varepsilon}_0(\mathbf{P}), \tag{5.12}$$

where $\mathbb{C}$ is the Hooke's fourth order tensor.

It is expected that, when considering the model just described, shrinkage stresses depend parametrically on the trajectory (that controls its anisotropy) and also eventually on space from thermal couplings here ignored.

One could imagine the possibility of expressing the shrinkage tensor parametrically as was the case for the trajectories. Thus, by noting $\boldsymbol{\sigma}^i(\mathbf{P})$ the shrinkage tensor related to the parameters choice $\mu_j = \delta_{ij}$, with δ the Kroneker delta, the thermal shrinkage tensor could be expected expressing as

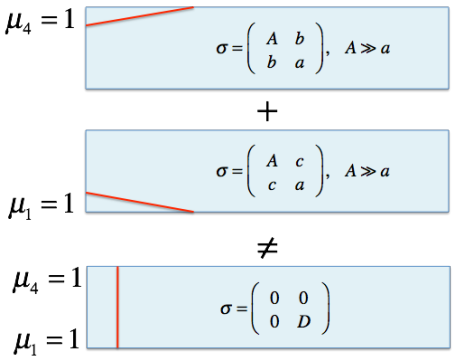

Figure 5.5 – *Shrinkage tensor interpolation issues*

$$\boldsymbol{\sigma}_0(\mathbf{P};\mu_1,\cdots,\mu_5) = \mu_1\boldsymbol{\sigma}^1(\mathbf{P}) + \cdots + \mu_5\boldsymbol{\sigma}^5(\mathbf{P}). \tag{5.13}$$

However, such a natural option fails because the limitations of tensor interpolations as Fig. 5.5 illustrates.

For circumventing the just mentioned difficulties we proceed by expressing the rotation matrix parametrically. For that purpose we proceed from the parametric trajectories expression

$$\phi(x,y,\mu_1,\cdots,\mu_5) = \sum_{i=1}^{5}\mu_i\phi^i(x,y), \tag{5.14}$$

whose normalized gradient defines the normal direction to the trajectory, according to

$$\boldsymbol{n} = \frac{\nabla\phi}{||\nabla\phi||}, \tag{5.15}$$

with

$$\nabla\phi(x,y,\mu_1,\cdots,\mu_5) = \sum_{i=1}^{5}\mu_i\nabla\phi^i(x,y), \tag{5.16}$$

where the gradient of solutions $\phi^i(x,t)$ can be computed offline.

Now, the tangent vector $\boldsymbol{t}$ comes from the normality condition $\boldsymbol{t}\cdot\boldsymbol{n} = 0$. These expressions allow determining the parametric expression of the rotation tensor and from it, the one of the shrinkage tensor, by using the standard PGD technology, even if the computation could be perfectly performed online in real-time without requiring precomputing a parametric expression of expression (5.12).

Now, the virtual work principle, assuming without loss of generality small displacements and strains, writes

$$\int_\Omega \boldsymbol{\varepsilon}^* : (\boldsymbol{\sigma} - \boldsymbol{\sigma}_0)\ d\boldsymbol{x} = 0, \tag{5.17}$$

where without loss of generality surface and volume forces are neglected. This expression applies for any kinematically admissible deformation $\boldsymbol{\varepsilon}^*$, i.e. related to test displacements vanishing in the part of the boundary of Ω where displacements are prescribed, in general the bottom basis of the part.

It can be noticed from Eq. (5.17) that shrinkage acts as a volume force and consequently in the resulting linear system (after discretization) it appears at the right-hand member,

that can be expressed using the most usual notation as

$$\mathbf{KU} = \mathbf{F}(\mu_1, \cdots, \mu_5). \tag{5.18}$$

As soon as the problem is linear, $\mathbf{K}^{-1}$ can be computed and used for evaluating online the parametric displacements according to

$$\mathbf{U}(\mu_1, \cdots, \mu_5) = \mathbf{K}^{-1}\mathbf{F}(\mu_1, \cdots, \mu_5). \tag{5.19}$$

At this point it is important to make two observations:

- When considering nonlinear behaviors, in particular large strain / displacements, the best option consists of applying directly the PGD rationale for computing the parametric displacement field for each intermediate configuration, i.e. number of deposited layers, or applying the procedure just described operating at the discrete level (Eqs. (5.18) and (5.19)) but decomposing the stiffness matrix in a linear and nonlinear parts, i.e. $\mathbf{K} = \mathbf{K}_L + \mathbf{K}_{NL}$ and proceeding until convergence within the iteration scheme

$$\mathbf{U}^n(\mu_1, \cdots, \mu_5) = \mathbf{K}_L^{-1}\left(-\mathbf{K}_{NL}^{n-1}\mathbf{U}^{n-1}(\boldsymbol{\mu}) + \mathbf{F}(\mu_1, \cdots, \mu_5)\right), \tag{5.20}$$

  with $\mathbf{U}^{n-1}(\boldsymbol{\mu}) = \mathbf{U}^{n-1}(\mu_1, \cdots, \mu_5)$.

- In all cases the linear and nonlinear matrices must be evaluated for different stages of the process, that is, for different numbers of deposited layers. Thus, later, the number of layers will be introduced as an extra-parameter in the parametric solution.

Fig. 5.6 depicts, for a given shrinkage intensity λ, for the final configuration and for the different scenarios considered in Fig. 5.3, where parameters $\mu_1, \cdots, \mu_4$ and $\mu_5 = s(x, y)$ are noted by $P1, \cdots, P5$, the considered solid cuboid part distortion from its target geometry. This GUI application allows evaluating distortions associated to any possible trajectory in almost real-time.

5.3 Distortion compensation

As soon as the distortion is evaluated for a choice of the parameters, one could expect that by applying that displacement field with opposite sign to the target configuration, the final geometry after shrinkage should almost correspond to the target geometry. For evaluating this simple compensation procedure we consider again the part addressed in the previous section and we evaluate its distortion for the parameters indicated in Fig. 5.7. Now, by applying to the target geometry the opposite of the displacement field illustrated in Fig. 5.7, it results the geometry displayed in Fig. 5.8. Now, using the same process parameters, the distorted part associated with the target geometry shown in Fig. 5.8 results in the one displayed in Fig. 5.9.

In the just analyzed case the geometry ensured that the simplest compensation procedure works perfectly, however this simple procedure could fail in more complex geometries. In that case it is obvious that the fact of evaluating in real-time (almost instantaneously) the displacement could allow to implement more sophisticated compensation algorithms dialoging with our *computational vademecum*.

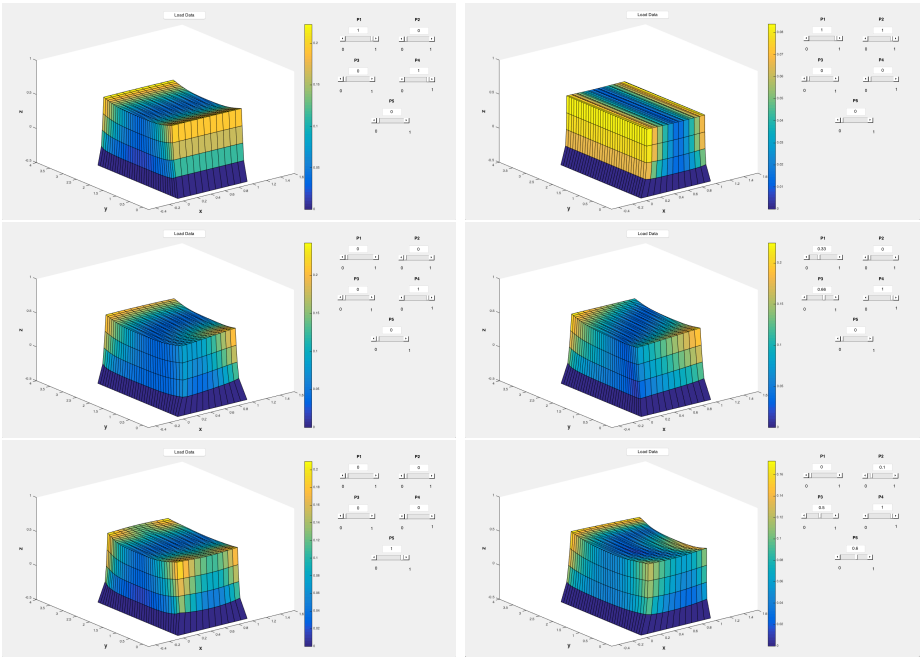

Figure 5.6 – *Parametric distortions for: (top-left)* $\mu_1 = 1,\ \mu_2 = 0,\ \mu_3 = 0,\ \mu_4 = 1,\ \mu_5 = 0$*; (top-right)* $\mu_1 = 1,\ \mu_2 = 1,\ \mu_3 = 0,\ \mu_4 = 0,\ \mu_5 = 0$*; (middle-left)* $\mu_1 = 0,\ \mu_2 = 0,\ \mu_3 = 0,\ \mu_4 = 1,\ \mu_5 = 0$*; (middle-right)* $\mu_1 = 0.33,\ \mu_2 = 0,\ \mu_3 = 0.66,\ \mu_4 = 1,\ \mu_5 = 0$*; (bottom-left)* $\mu_1 = 0,\ \mu_2 = 0,\ \mu_3 = 0,\ \mu_4 = 0,\ \mu_5 = 1$ *and (bottom-right)* $\mu_1 = 0,\ \mu_2 = 0.1,\ \mu_3 = 0.5,\ \mu_4 = 1,\ \mu_5 = 0.6$*. The depicted mesh is only for visualization purposes, the one related to the calculations is finer. Dimensions:* $\times 10cm$*. Displacements in cm.*

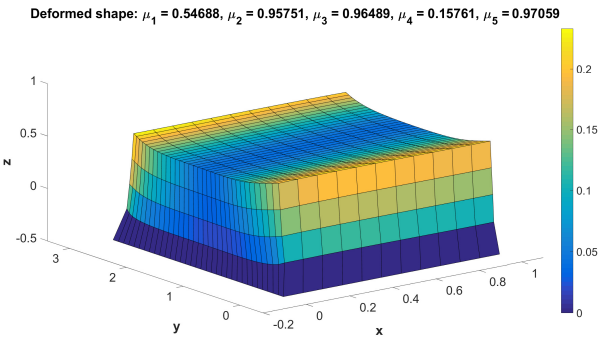

Figure 5.7 – *Distorted geometry for the indicated parameters defining the process trajectory. Dimensions:* $\times 10cm$*. Displacements in cm.*

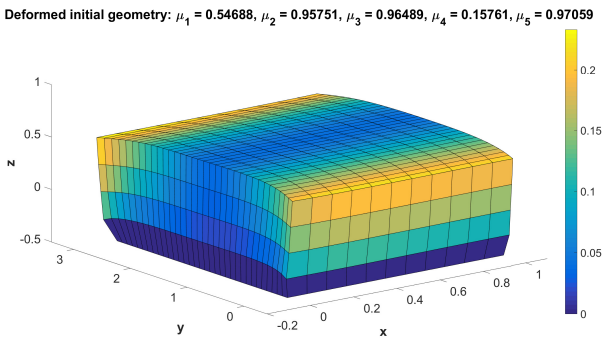

Figure 5.8 – *Compensated geometry. Dimensions:* $\times 10cm$. *Displacements in cm.*

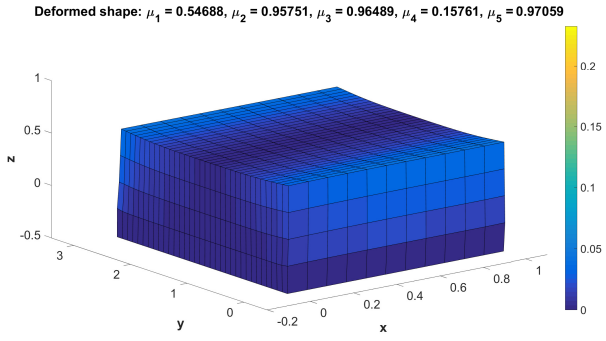

Figure 5.9 – *Distortion applying on the compensated geometry. Dimensions:* $\times 10cm$. *Displacements in cm.*

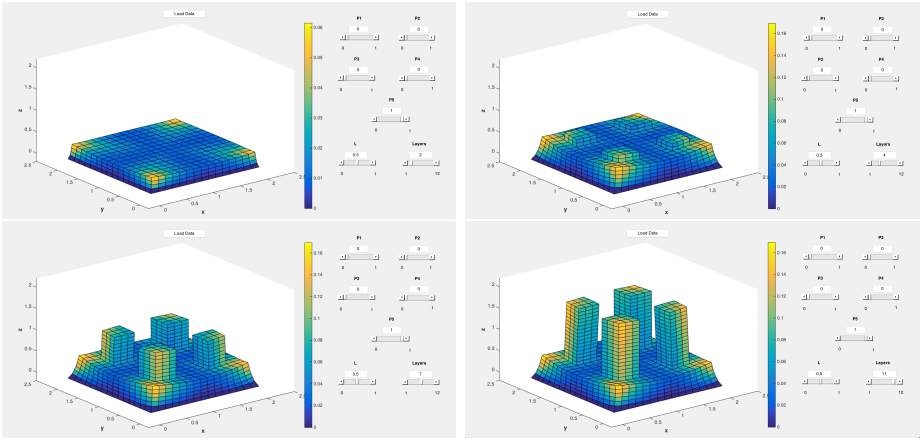

Figure 5.10 – *Parametric distortions for* $\mu_1 = 0,\ \mu_2 = 0,\ \mu_3 = 0,\ \mu_4 = 0,\ \mu_5 = 1, \lambda = L = 0.5$ *and: (top-left)* layers $= 2$*; (top-right)* layers $= 4$*; (bottom-left)* layers $= 7$ *and (bottom-right)* layers $= 11$. *Dimensions:* $\times 10cm$. *Displacements in* cm.

5.4 Numerical results

In this section we are considering a quite more complex geometry and introducing two new parameters into the parametric solution (*computational vademecum*): (i) the one related to the thermal shrinkage intensity λ (noted in the GUI application shown later by L) and (ii) the process progression, that is, the number of deposited layers.

Fig. 5.10 depicts the deformed geometry for four different process stages where different number of layers were deposited. Here the only parameter that varies is the number of layers. It can be noticed that the greater is the number of layers the higher is the distortion. Fig. 5.11 shows the effect of the thermal shrinkage intensity, a certain value multiplied by parameter $L \equiv \lambda$, from a null value for with distortions vanish to its highest value $L = 1$ exhibiting the largest distortions.

Moreover, in order to show how the PGD rationale can be used to compute the parametric solution, in Fig. 5.12 we compare the solution computed using the non-intrusive PGD procedures, the Sparse Subspace Learning (SSL) method [Borzacchiello *et al.* 2017] (some details about this method are given in Appendix A), and the solution computed using 3D finite element for $L = 1$ and three different combinations of the parameters related to the deposition trajectories. The results between the two methods are in perfect agreement.

5.4.1 Geometry compensation

For evaluating in the present case study the compensation procedure, we evaluate its distortion for the parameters indicated in Fig. 5.13. Now, by applying to the target geometry the opposite of the displacement field illustrated in Fig. 5.13, it results the geometry displayed in Fig. 5.14. Now, using te same process parameters, the distorted part associated with the target geometry shown in Fig. 5.14 results in the one displayed in Fig. 5.15.

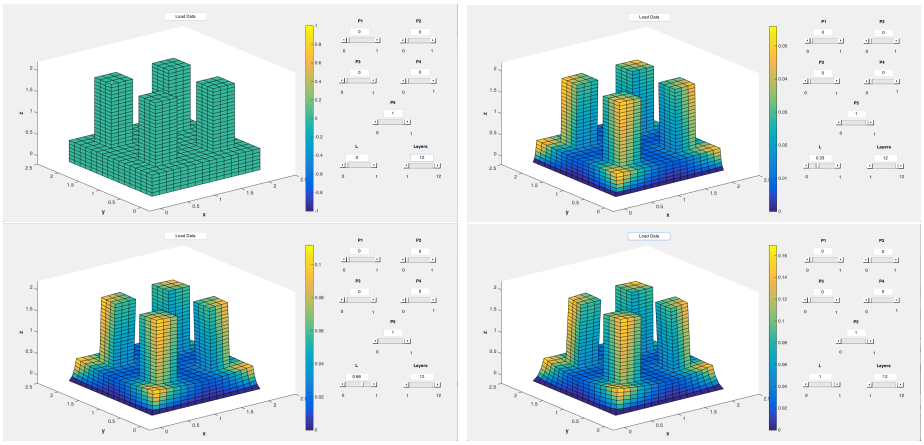

Figure 5.11 – *Parametric distortions for* $\mu_1 = 0,\ \mu_2 = 0,\ \mu_3 = 0,\ \mu_4 = 0,\ \mu_5 = 1, \text{layers} = 12$ *and: (top-left)* $L = \lambda = 0$*; (top-right)* $L = \lambda = 0.33$*; (bottom-left)* $L = \lambda = 0.66$ *and (bottom-right)* $L = \lambda = 1$*. Dimensions:* $\times 10cm$*. Displacements in* cm*.*

5.4.2 Optimization, sensitivity analysis and uncertainty propagation

We address now the use of the parametric solution with three different purposes: (i) evaluating the parameters related to the deposition trajectories leading to the minimal part distortion (in the range of parameters used for the parametrization); (ii) evaluating the solution sensitivity to the different parameters, and in particular to the ones related to the deposition trajectory; and (iii) propagating the uncertainty related to the intensity of the thermal shrinkage. The parameters μ_i, $i = 1, \cdots, 5$, defining the deposition trajectory, which define the trajectory minimizing part distortion are computed with the Trust Region Reflective Algorithm [Branch *et al.* 1999]. That optimal solution is depicted in Fig. 5.16. Fig. 5.17 depicts the derivative of the displacement with respect to parameters μ_1 and μ_5 for the parameters related to the optimal process leading to the part shown in Fig. 5.16. Finally, if the thermal shrinkage intensity λ is assumed normally distributed (Fig. 5.18 (left)), the norm of the distortion becomes distributed as depicted in Fig. 5.18(right).

5.4.3 Qualitative validation

For a first qualitative validation we considered the deposition of a thin wall on a thin plate with a prescribed null displacements at one of its lateral bases. Figs. 5.19-5.21 depict the distorted structure for respectively different shrinkage intensities, number of deposited layers and process trajectories. Fig. 5.22 shows the experimental result when the process is operated by using trajectories expressed by $\mu_1 = \mu_2 = 1$ and $\mu_3 = \mu_4 = \mu_5 = 0$.

5.5 Conclusions

This chapter presented a simplified parametric modeling of distortions occurring in parts manufactured by additive manufacturing. After having introduced a parametrization of the process trajectories as the iso-values of a parametrized partial differential equation, thermal shrinkage was expressed parametrically with respect to the process trajectory. Finally two

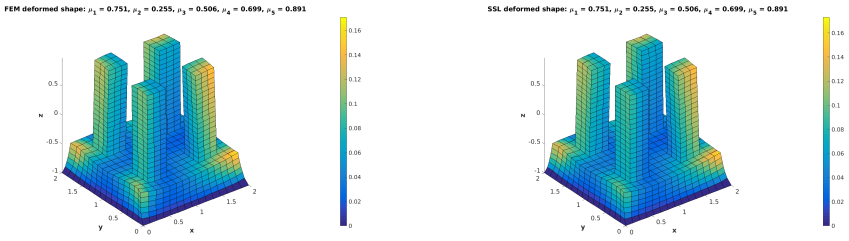

(a)

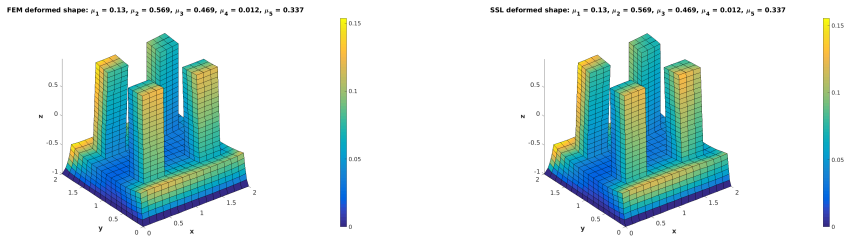

(b)

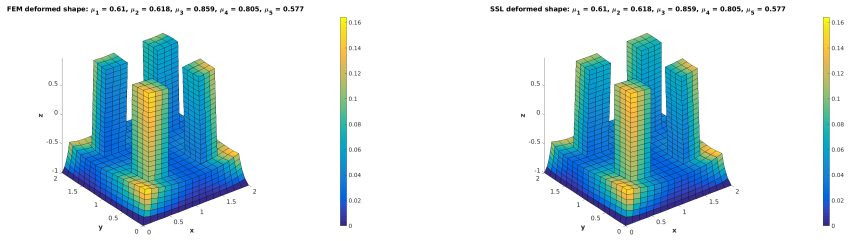

(c)

Figure 5.12 – *Comparison between FEM (left) and SSL (right) solutions for three different combinations of the parameters defining the trajectories.*

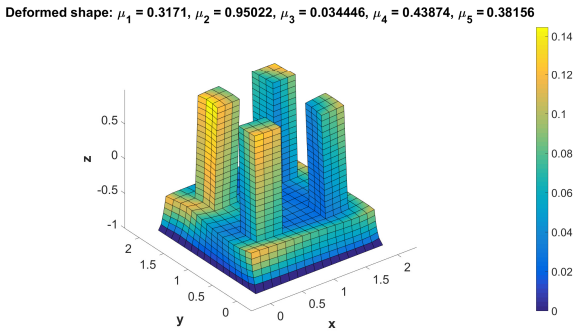

Figure 5.13 – *Distorted final geometry for the indicated parameters defining the process trajectory. Dimensions:* $\times 10$*cm. Displacements in cm.*

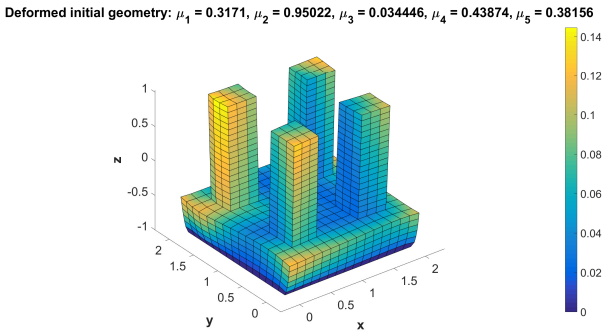

Figure 5.14 – *Compensated geometry. Dimensions:* $\times 10cm$. *Displacements in cm.*

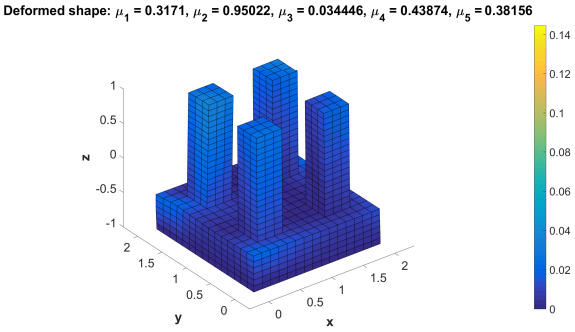

Figure 5.15 – *Distortion applying on the compensated geometry. Dimensions:* $\times 10cm$. *Displacements in cm.*

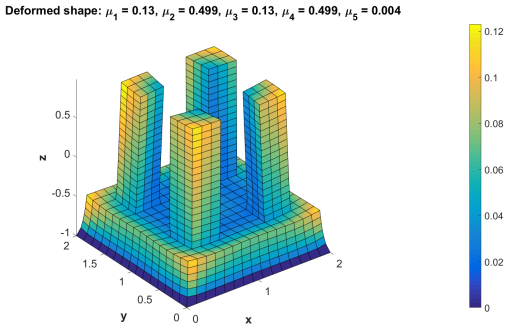

Figure 5.16 – *Optimal process minimizing part distortion.*

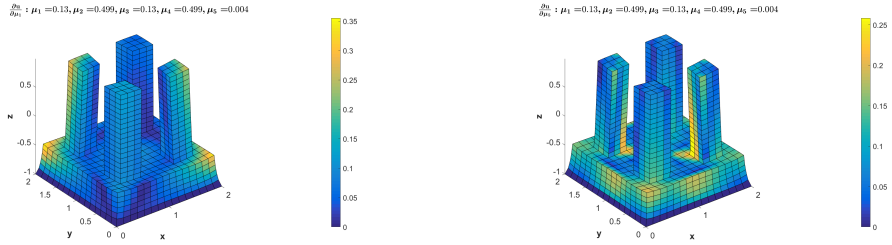

Figure 5.17 – *Sensitivity analysis: Displacement derivative with respect parameter* μ_1 *(left) and* μ_5 *(right).*

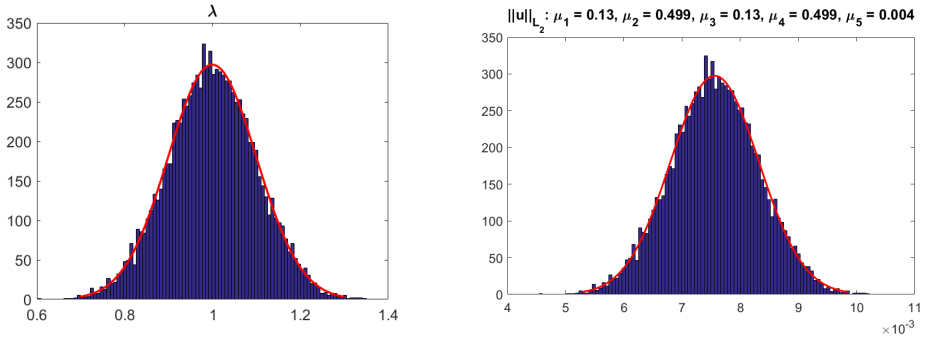

Figure 5.18 – *Uncertainty propagation related to the thermal shrinkage.*

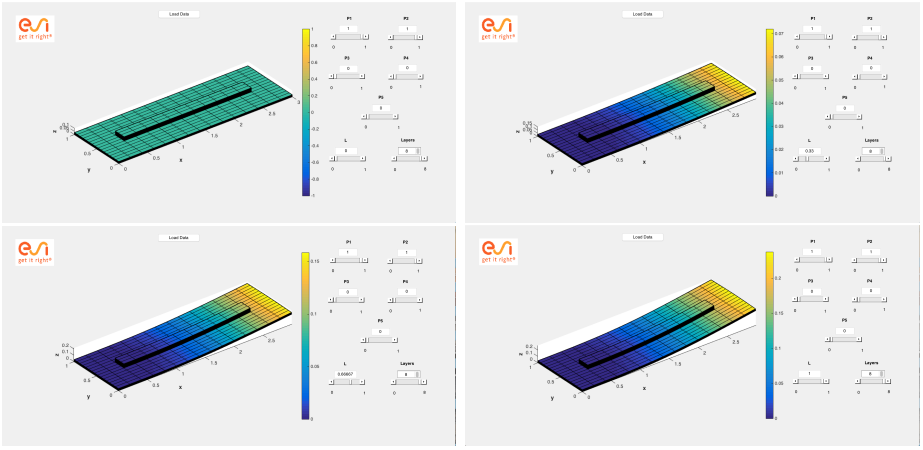

Figure 5.19 – *Parametric distortions for* $\mu_1 = 1$, $\mu_2 = 1$, $\mu_3 = 0$, $\mu_4 = 0$, $\mu_5 = 0$, layers $= 8$ *and: (top-left)* $L = \lambda = 0$*; (top-right)* $L = \lambda = 0.33$*; (bottom-left)* $L = \lambda = 0.66$ *and (bottom-right)* $L = \lambda = 1$*. Dimensions:* $\times 10cm$*. Displacements:* $\times 10cm$*.*

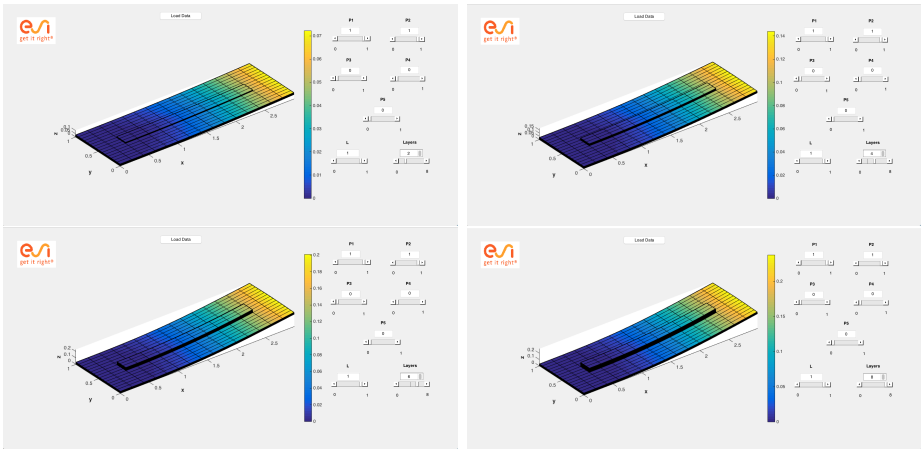

Dimensions: $\times 10cm$. Displacements in $\times 10cm$.

Figure 5.20 – *Parametric distortions for* $\mu_1 = 1$, $\mu_2 = 1$, $\mu_3 = 0$, $\mu_4 = 0$, $\mu_5 = 0$, $\lambda = L = 1$ *and: (top-left)* layers $= 2$*; (top-right)* layers $= 4$*; (bottom-left)* layers $= 6$ *and (bottom-right)* layers $= 8$. *Dimensions:* $\times 10cm$. *Displacements:* $\times 10cm$.

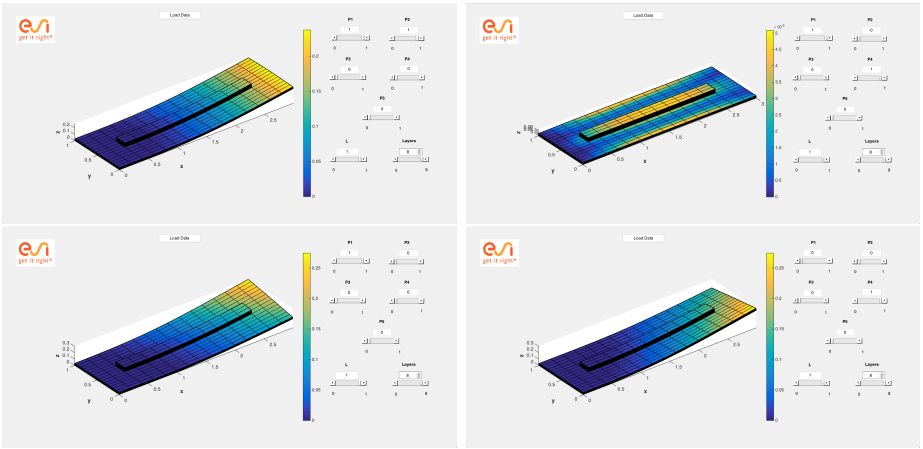

Figure 5.21 – *Parametric distortions for* layers $= 8$, $\lambda = L = 1$ *and: (top-left)* $\mu_1 = 1$, $\mu_2 = 1$, $\mu_3 = 0$, $\mu_4 = 0$, $\mu_5 = 0$*; (top-right)* $\mu_1 = 1$, $\mu_2 = 0$, $\mu_3 = 0$, $\mu_4 = 0$, $\mu_5 = 0$*; (bottom-left)* $\mu_1 = 0$, $\mu_2 = 0$, $\mu_3 = 0$, $\mu_4 = 0$, $\mu_5 = 0$ *and (bottom-right)* $\mu_1 = 0$, $\mu_2 = 0$, $\mu_3 = 0$, $\mu_4 = 1$, $\mu_5 = 0$. *Dimensions:* $\times 10cm$. *Displacements:* $\times 10cm$.

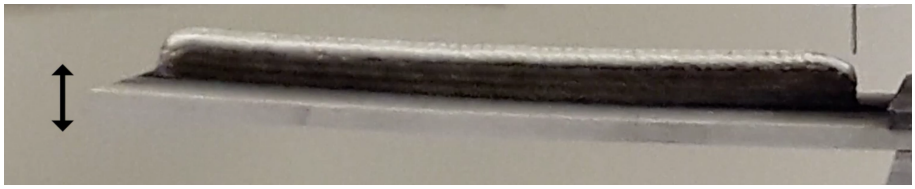

Figure 5.22 – *Experimental test (courtesy of J.Y. Hascoet at GeM Institute – Ecole Centrale de Nantes)*

new parameters were introduced, the first controlling the shrinkage intensity and the second the process progression, that is, the number of deposited layers.

The parametric solution was introduced into a GUI application able to evaluate the effect of any parameter in almost real-time. Moreover, parametric solutions open an appealing route for geometry compensation. That parametric solution was also successfully used with other three different purposes: (i) evaluating the parameters leading to the minimal part distortion; (ii) evaluating the solution sensitivity to the different parameters, and in particular to the ones related to the deposition trajectory; and (iii) propagating the uncertainty related to the intensity of the thermal shrinkage.

The numerical examples illustrate the effect of the different parameters and even if at present a quantitative validation requires additional efforts (it constitutes a work in progress), the first qualitative validation seems very promising.

Chapter 6

The Hybrid Twin concept

Contents

Introduction In this chapter a new concept for the simulation of mechanical processes is proposed, a Cyber Physical System called Hybrid Twin, which is then applied to an RTM process for the manufacturing of composite parts and to a dismantling process of a nuclear central. The Hybrid Twin allows to introduce in the simulation of the process unexpected events and evolutions induced by the real process and to use on line data collection for predictive maintenance.

In the first section of the chapter the concept of Hybrid Twin is presented and in particular its two main components: the parametric physically-based model (whose parameters will be updated on the fly from measurements) and the correction model. The next section deals with the application of the Hybrid Twin to the two mentioned processes.

This chapter and some of the results presented in it correspond to the following conference proceedings paper:

- G. Quaranta, E. Abisset-Chavanne, F. Chinesta, J.L. Duval, *A cyber physical system approach for composite part: From smart manufacturing to predictive maintenance*, ESAFORM2018 Conference, AIP Conference Proceedings, **1960**(1), 020025, 2018.

6.1 The Hybrid Twin system

A given physical system state can be characterized by a number of discrete (or discretized continuous) variables $\mathbf{X}$. Depending on the physics, $\mathbf{X}$ can contain temperature, velocities, stresses, viscosity, etc. The system evolution is then described by the evolution of $\mathbf{X}$ from the initial state $\mathbf{X}_0$ at time t_0 to the current state $\mathbf{X}(t)$ at time t. In the numerical simulation, this current state is predicted by integrating the rate of change $\dot{\mathbf{X}}(\tau)$, $\tau \in (0, t]$.

When the physics governing the physical system state evolution is well known and established, the rate of change $\dot{\mathbf{X}}(\tau)$ can be expressed as

$$\dot{\mathbf{X}}(t, \boldsymbol{\mu}) = \mathbf{A}(\mathbf{X}, t; \boldsymbol{\mu}), \tag{6.1}$$

where μ represents the set of parameters involved in the model and that have to be identified offline or online by enforcing that the prediction fits as much as possible to the experimental measurements. Thus by integrating $\mathbf{A}(\mathbf{X}, t; \boldsymbol{\mu})$ predictions can be made. This

integration can be performed by using standard numerical techniques (finite elements, finite differences, finite volumes, spectral methods, meshless or meshfree techniques, ...). However, as discussed in the previous chapters, these methods can not accommodate real-time constraints required in many applications; in that cases model order reduction techniques, in particular the Proper Generalized Decomposition, are used in order to provide real-time feedbacks and solve issues related to the parametric nature of the model [Chinesta & Ladeveze 2014, Chinesta *et al.* 2015].

Moreover, in the context of process or system control, external actions are applied for driving the model solution towards the given target. Thus, the state rate of change (when ignoring noise) can be decomposed into two contributions:

$$\dot{\mathbf{X}}(t,\boldsymbol{\mu}) = \mathbf{A}(\mathbf{X},t;\boldsymbol{\mu}) + \mathbf{C}(t), \tag{6.2}$$

where the term $\mathbf{C}(t)$ represents the control action.

$\mathbf{A}$ and $\mathbf{C}$ constitute the usual contributions of the numerical models used nowadays to predict and control process and system evolution.

However, a non-negligible deviation is often noticed between the simulation predictions and the real evolution acquired from collected data. The unbiased deviation contribution is associated to modeling or measurement noise and is easily addressed by using adequate filters [González *et al.* 2017]. However, biased deviations express hidden physics and required a particular treatment. It is then proposed to introduce in the system evolution a data-based deviation model, built on-the-fly directly from the deviation between the model prediction $\mathbf{X}(t,\boldsymbol{\mu})$ (with the optimal choice of the model parameters $\boldsymbol{\mu}$) and the collected data. That allows then to write the fundamental system of an Hybrid Twin:

$$\begin{cases} \dot{\mathbf{X}}(t,\boldsymbol{\mu}) = \mathbf{A}(\mathbf{X},t,\boldsymbol{\mu}) + \mathbf{B}(\mathbf{X},t) + \mathbf{C}(\mathbf{X}) + \mathbf{R} \\ \mathbf{Y} = \mathbf{D}(\mathbf{X}) + \mathbf{R}' \\ \mathbf{Z} = \mathbf{G}(\mathbf{X}) + \mathbf{R}'' \end{cases} \tag{6.3}$$

expressing that the rate of change of the system state at time t contains the following main contributions, that we sum up here:

1. A linear or nonlinear contribution, the so-called Parametric Reduced Model where it is emphasized its parametric dependence on the set of parameters grouped in vector $\boldsymbol{\mu}$, whose values result of the assimilated data $\mathbf{Y}$. This contribution comes from the almost known physical mechanisms, described in a classical way (parametric partial differential equations) or in a data-driven framework [Kirchdoerfer & Ortiz 2016, Ibáñez Pinillo *et al.* 2017]. In order to proceed fast (even under real-time constraints) $\mathbf{A}(\mathbf{X},t,\boldsymbol{\mu})$ can be expressed by a reduced model (within the Proper Orthogonal Decomposition or Reduced Basis framework) or replaced by a parametric solution within the PGD framework. In the last case the inclusion of model parameters as extra-coordinates facilitates data-assimilation (i.e. online determination of the model parameters from collected data) as well as data completion (field reconstruction). This first-order contribution concerns an almost deterministic model where eventually parameters could be stochastic. However, as soon as the parametric solution is available, uncertainty can be efficiently quantified and propagated.

2. A correction term $\mathbf{B}(\mathbf{X},t)$, that we called Data-Based Deviation Model, fully unknown at the beginning, modeling the noticed gaps between prediction and measurement. This term must be constructed on the fly from the collected data (mea-

surements $\mathbf{Z}$), by using for example machine learning techniques (data-mining, deep-learning, manifold learning, ... for citing few) [Brunton *et al.* 2016, Kutz 2013] or within a parametric form within the PGD framework by using the sparse-PGD method [Ibáñez Pinillo *et al.* 2018].

3. Control actions are integrated in vector $\mathbf{C}(\mathbf{X})$ that mimics forcing inputs, depending on the state $\mathbf{X}$.

4. Finally, $\mathbf{R}$ represents a Brownian term that accounts for the remaining error in the models or identified parameters and that is usually described by Gaussian distribution within the (linear or nonlinear) Kalman framework or a Bayesian/Fokker-Planck framework.

As said, the first set of measures $\mathbf{Y}$ are useful to assess the validity of the first order term and also to adapt dynamically the parameters that it involves, while the second set of measures $\mathbf{Z}$ are needed to dynamically identify the adaptive term $\mathbf{B}$ (continuous learning). Both measures should be collected at optimal locations (magic points when using the terminology employed in the reduced basis community). Both measures are assumed to be containing noise (usually Gaussian) contained in vectors $\mathbf{R}'$ and $\mathbf{R}''$.

In the previous expression (6.3), the data-based contribution $\mathbf{B}(\mathbf{X}, t)$ makes the difference between digital twins (whose main characteristic is assimilating measurements provided by sensors), and hybrid twins, the last combining a (well established and validated) physical model and a data based model to represent the real system all along its life, adapting it to any noticed deviation and keeping all its predictive capacity, necessary for control purposes and real-time decision making.

6.2 Applications

In this section we present the construction and functioning of two simple hybrid twins: the first one focuses on a Resin Transfer Moulding – RTM – process, the second one a dismantling process of a a nuclear central. For the sake of simplicity, realistic complexity has been sacrificed in favour of description simplicity.

6.2.1 Hybrid Twin for an RTM process

The problem consists in filling a square mold from its central point; an impermeable square insert is placed in the right-upper zone in order to break the solution symmetry. The experimental device is depicted in Fig. 6.1. The construction and the use of the two first contributions of the hybrid twin - the physical ($\mathbf{A}$) and the data-based ($\mathbf{B}$) models - is now described.

- First, the parametric solution of the flow problem, related to the mold filling process, is computed offline. The chosen parameter is the preform permeability κ, that, without loss of generality, is assumed constant and isotropic in the whole preform. The parametric solution is constructed by coupling PAM-RTM (ESI Group, France) and a non-intrusive formulation of the PGD constructor based on the Sparse Subspace Learning (SSL) method [Borzacchiello *et al.* 2017] (some details on the method are given in Appendix A). Then, as soon as this parametric solution has been computed offline, it can be particularized online almost in real-time, that is, all the fields

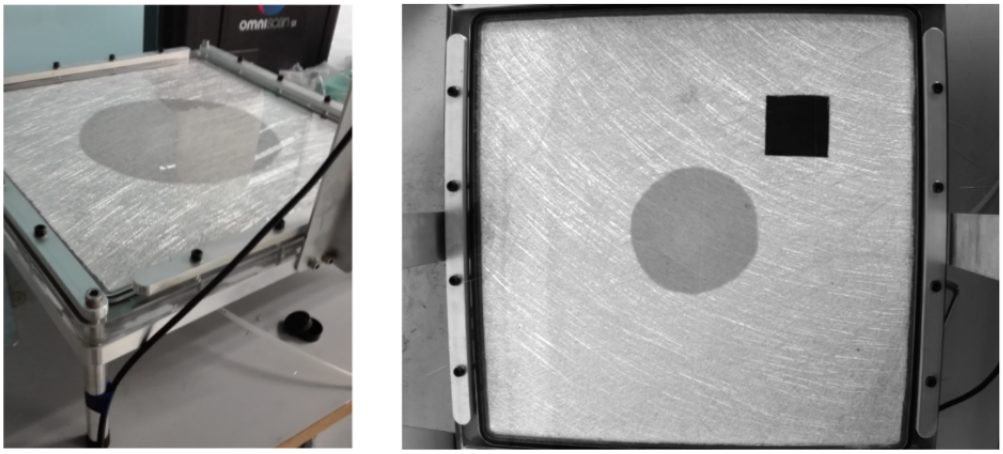

Figure 6.1 – *Experimental set up. The square mold is filled with an isotropic fibrous reinforcement and an impermeable square insert (black small square) is placed in the right-upper corner.*

(pressure, velocity, filling factor, ...) are accessible for any possible value of the permeability. Fig. 6.2 depicts the flow front at different instants and for three different permeabilities.

- Then, by comparing the real flow front (recorded with a camera) with the just computed parametric solution, the effective permeability of the fibrous preform can be identified. A classical inverse method, the Levenberg-Marquardt method [Pujol 2007], has been used to compute the permeability that, inserted into the parametric model, allows the best fit between the predicted flow front position and the recorded one at different filling times. As soon as the permeability has been properly identified, and in absence of any perturbation, the simulated filling process agrees in minute to the one experimentally observed, as shown in Fig. 6.3.
- In the previous process stage, the permeability has been successfully identified by using the first images recorded by the camera. However, the simulations used to build the parametric contribution assumes an homogeneous permeability, while, in fact, a variation of permeability appears in the neighborhood of the mold boundary due to the clamping system. Thus the simulation performed with $\mathbf{A}$ and the just identified permeability significantly deviates from the measurement when flow reaches the regions where the permeability is reduced. Fig. 6.4(a) compares the predicted solution with the one associated to the perturbed case. It can be noticed that, at the beginning, predictions are in perfect agreement with measurements, but, when the flow reaches the region with lower permeability, significant deviations occur.
- To tackle this issue, the data-based model $\mathbf{B}$ is introduced and constructed using, in this example, dictionary learning (alternatively a PGD form of the correction could be constructed by using the sparse-PGD method). To do so, a rich handbook of snapshots is produced, called the dictionary. Then the identified deviation, namely the difference between the real flow front position and the one predicted by $\mathbf{A}$, is projected on this dictionary. As soon as the dictionary contains elements able to described the noticed flow behavior, the deviation can be perfectly represented by

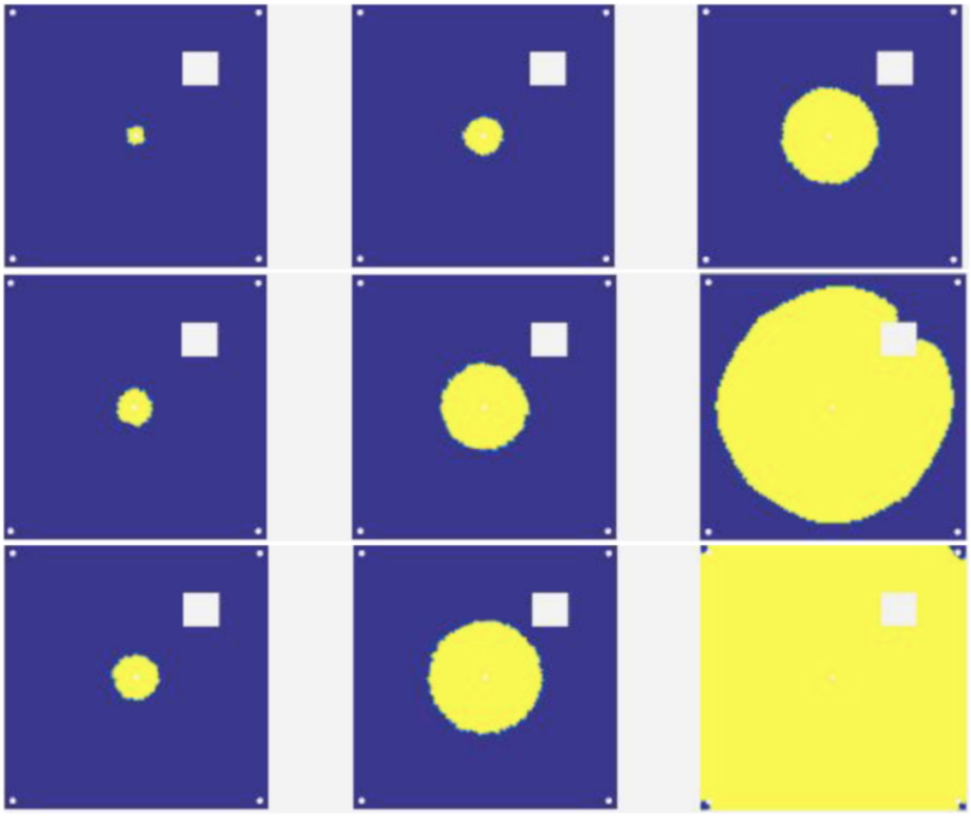

Figure 6.2 – *Particularizing the PGD-based mold filling solution for three different permeabilities (low at the left, intermediate a the center and high at the right) at three different time steps (from top to bottom).*

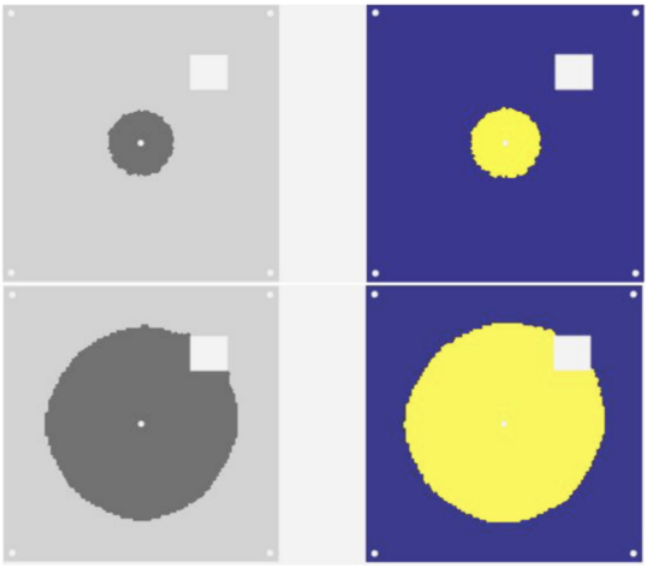

Figure 6.3 – *Identifying the fibrous reinforcement permeability and comparing measured (left) and predicted (right) flow front position at two time instants.*

the data-based contribution **B**, as illustrated in Fig. 6.4(b), ensuring the model predictability all along the filling process.

6.2.2 Dismantling Hybrid Twin

The problem consists in the dismantling process of a nuclear central. An operator must move in a room containing seven sources of emission (working points) located in different places, in order to reach one of the seven working points (target) by choosing the safest trajectory (i.e. the trajectory in which he accumulates the least quantity of emissions), Fig. 6.5. The steps of the problem are now described.

- First, the parametric solution of the problem is computed offline. The solution is composed of two parts: (i) any trajectory from the departure point (gate and 7 working points) to the destination (target) point, again the gate and the 7 working points; (ii) any combination of intensities related to the 7 sources of emission. In total a parametric solution (trajectories and the scalar field given by the sum of all the emissions) involving 9 parameters is computed, Fig. 6.6. The trajectories are computed as the streamlines of the scalar field solution $\phi(x, y)$ of the Poisson equation defined in the domain Ω

$$\Delta\phi(x, y) = s(x, y), \tag{6.4}$$

with the condition

$$\int_{\Omega} \phi(x, y) = 0, \tag{6.5}$$

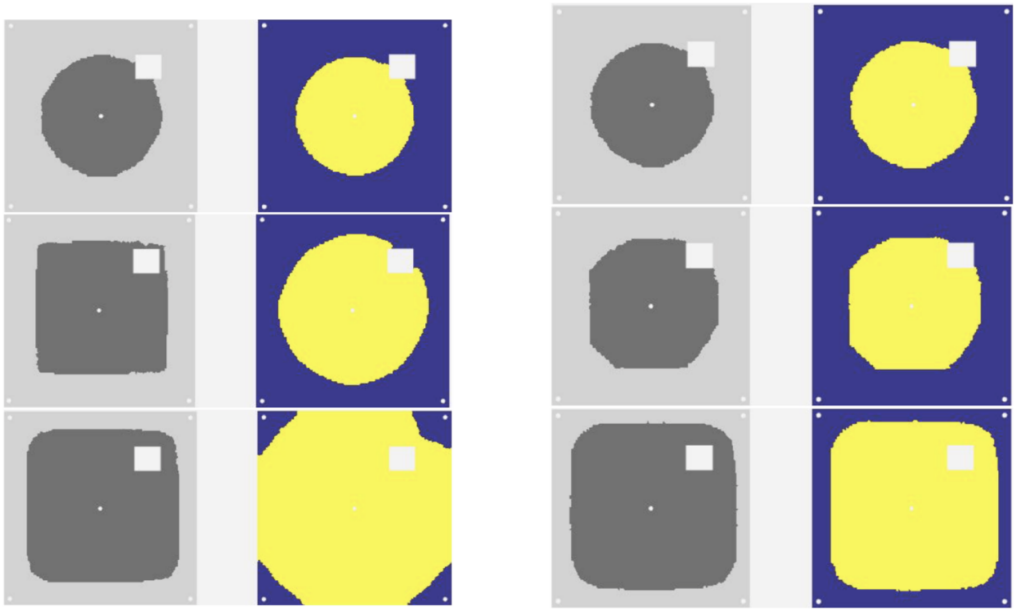

(a) (b)

Figure 6.4 – *Introducing a permeability reduction in the neighborhood of the mold boundary and comparing measured (left) and predicted (right) flow front position at three time instants (top to bottom): (a) without introducing the data-based model contribution and (b) introducing the data-based model contribution.*

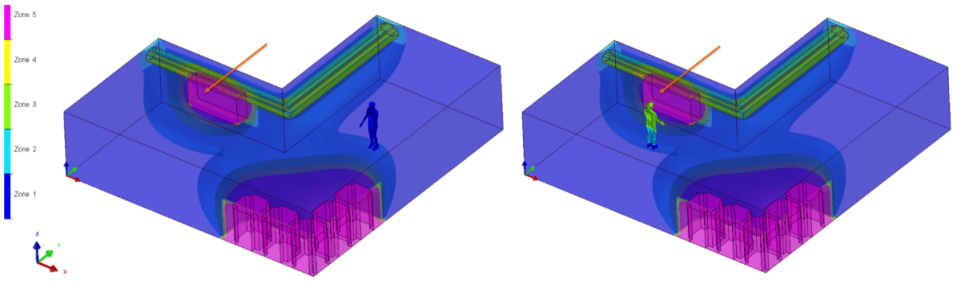

Figure 6.5 – *The dismantling problem.*

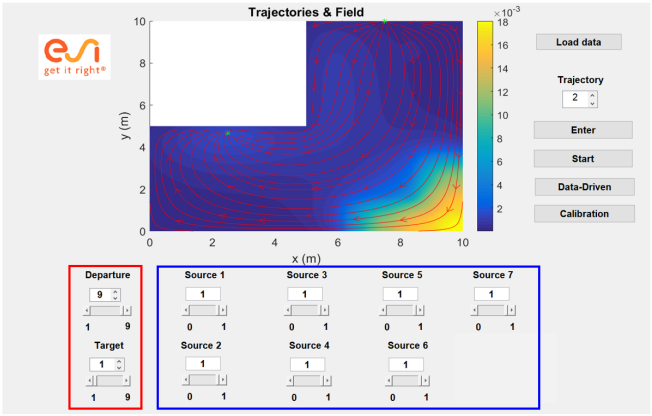

Figure 6.6 – *The parametric solution (trajectories and scalar field) involving 9 parameters: (i) any trajectory from the departure to the destination point, i.e. gate and 7 working points (red box) (ii) any combination of intensities related to the 7 sources of emission (blue box).*

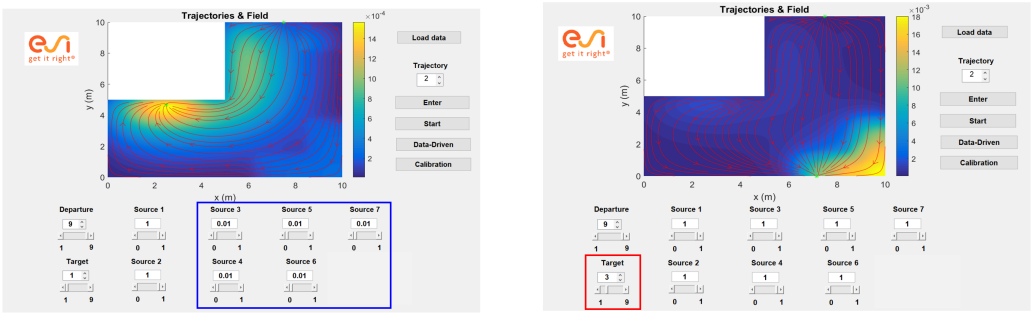

(a) (b)

Figure 6.7 – *Real-time particularization of the parametric solution: (a) change of intensities of the sources of emission, (b) change of trajectories by changing the destination point.*

and where

$$s(x,y) = \begin{cases} 1, & \text{if } (x,y) = (x_{in}, y_{in}), \\ -1, & \text{if } (x,y) = (x_{out}, y_{out}), \\ 0, & \textit{otherwise}. \end{cases} \tag{6.6}$$

The solution streamlines are expected representing trajectories from the starting point (x_{in}, y_{in}) to the destination point (x_{out}, y_{out}). The parametric scalar field is constructed by coupling SYSTUS (ESI Group, France) and the SSL. Once this parametric solution has been computed offline, it can be particularized online almost in real-time, as shown in Fig. 6.7.

- As depicted in Fig. 6.8, the process starts when the operator (the green circle in the figure), who is equipped with sensors, enters into the room and from the expected emissions (nominal data) he chooses the safest trajectory.

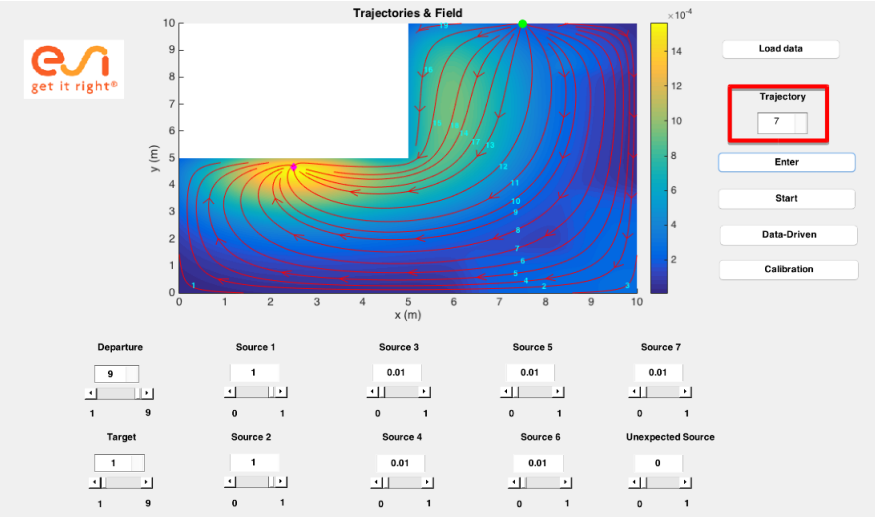

Figure 6.8 – *The Operator (greed circle) enters into the room, and from the nominal data (expected emissions) trajectory 7 is selected (he does not know there is an unexpected source, i.e. the value of the unexpected source is zero).*

- However, after a while, he detects an unexpected high emission and he identifies an unexpected source (e.g. a pool of polluted water), Fig. 6.9. Here is where the hybrid functionality comes out: the operator has to deal with a different configuration respect to the expected one but he is able to construct a new model based on the difference between the expected one and the measurements (data-driven model). Thus he selects a safer trajectory, and he continues by moving along it, Fig. 6.10.
- However by collecting new data he discovers that the nominal data of the sources of emission are not correct so that he updates the scalar field from the collected data, Fig. 6.11. Here we can note the functionality of the parametric model which allows to assimilate data and to update the parameters of the model from them (calibration). Once the parameters have been updated the operators decides again to move to a safer trajectory and he moves along it until reaching the destination point, Fig. 6.12. The total accumulated dose is given by integrating the accumulate dose all along the process.

6.3 Conclusions

In this work, a CPS called Hybrid Twin has been proposed and applied to composite manufacturing and to a dismantling process. It is composed of these fundamental elements: (i) a physically based model compressed as parametric solutions in order to achieve real time parameters identification, (ii) a dynamical correction constituted of a data-based model built on the fly from the collected data, that allows to fill the gap between the simulations and the observations, (iii) measurements to calibrate the physically-based model and to construct the data-driven model update, (iv) a control term able to lead the solution toward the final target and (v) noise filters.

The two applications show the efficient of such a concept in order to detect discrepancies between the measurements and the physical model based simulations and to correct them on the fly.

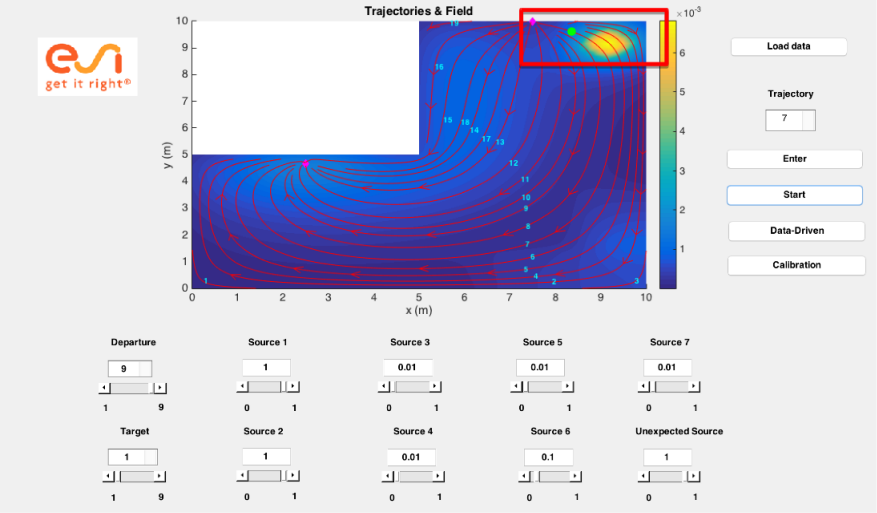

Figure 6.9 – *An unexpected high emission is detected by the operator and an unexpected source (e.g. a pool of polluted water) identified : Hybrid functionality (data-based inverse identification and construction of the model based on the data).*

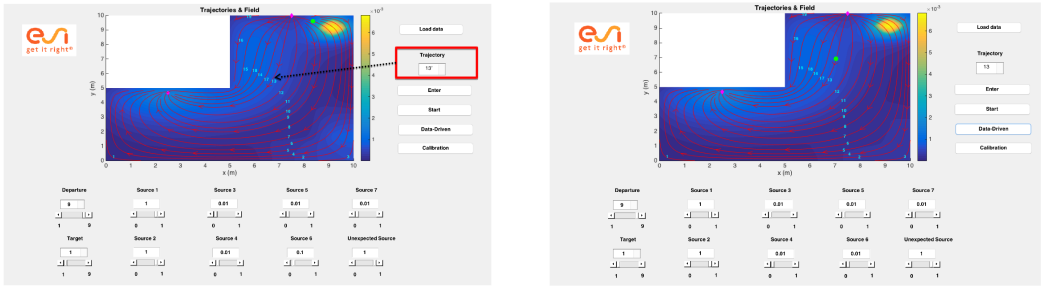

(a) (b)

Figure 6.10 – *(a) A safer trajectory, trajectory 13, is selected by the operator. (b) The operator moves along the new trajectory.*

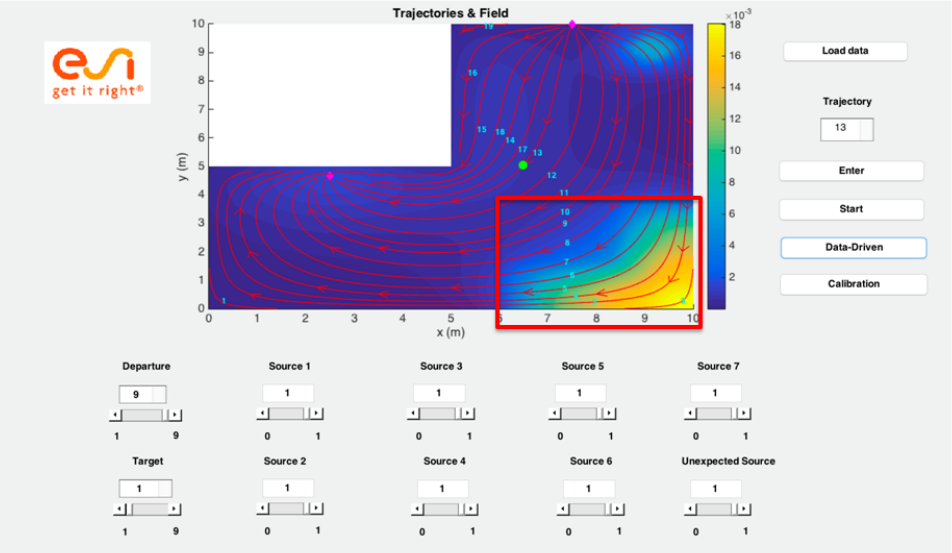

Figure 6.11 – *The collected data (the operator is equipped with sensors) allow calibrating the sources and the scalar field is updated from the collected data.*

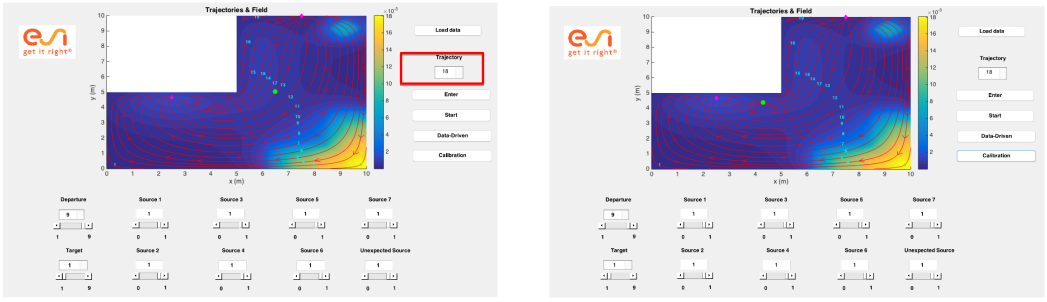

(a) (b)

Figure 6.12 – *(a) By using the collected data the operator moves to a safer trajectory, trajectory 18, further away from the hot region. (b) The operator moves along this trajectory until reaching the destination point (pink circle).*

Conclusions and perspectives

This thesis was devoted to the development of new techniques and simulation tools for real-time monitoring and control by using model order reduction and data-driven techniques with a twofold purpose.

First, model order reduction techniques, needed to manage with real-time constraints compulsory in many applications, were used in order to improve existing digital twins. The proposed simulation tools were developed at two different scales: (i) the one of the *mechanical component*, where, because of the importance the dynamical response has in structural health monitoring, for which a new method was also presented in this thesis, different techniques to get parametric linear and nonlinear dynamical responses of metal and composite plates were proposed; (ii) the one of the *mechanical process*, where the main goal was to develop a simulation tool allowing real time calculation (and re-calculation) of the predictions, optimization, parameters identification, control and inverse analysis during the process, which was then applied to an additive manufacturing process.

Second, we developed and applied the Hybrid-Twin concept at the scale of the mechanical processes, where, by using data-driven modeling, we were able to fill the gap between the parametric deterministic solution, computed by using the digital twins, and the measurements.

In Chapter 2 we proposed an efficient technique for real-time evaluation of damage in structures based on the combination of model order reduction with data-mining techniques. Moreover, in order to avoid data collection on the whole structure, the methodology was combined with a data-completion strategy based on the use of dictionary learning, allowing for an accurate damage location. The numerical test performed proved the validity and potential of the proposed approach that should be now validated experimentally.

In order to efficiently compute the dynamical response of a system in Chapter 3 we presented numerical techniques based on separated representation. First, we proposed a new time discretization scheme for solving 3D dynamical problems defined in in plate-like domains. The hybrid explicit/implicit in-plane-out-of-plane separated representation computed efficiently fully 3D solution without any kinematic hypothesis and where the stability constraints were exclusively dictated by the coarser in-plane mesh size. Second, we proposed an extension of the hybrid methodology combining harmonic and modal analyses for treating nonlinear parametric dynamics. A parametric solution in the frequency domain was derived which took into account different model parameters. Preliminary numerical results evidenced the potentialities of the proposed technique, while proving its computational efficiency. The inclusion of progressive damage models combined with dynamical effects constitutes a work in progress, where the separated representations seems an appealing option to better represent damage effects along the laminate thickness, and where explicit time integrations are usually employed in industrial applications.

However, fully 3D solution computed employing the in-plane-out-of-plane separated representation was revealed to be too intrusive for being introduced into existing commercial software. For this reason in Chapter 4 we presented minimally-intrusive methods which

allows integrating 3D descriptions in plate or shell models implemented in any software, preserving the direct minimally-invasive coupling and without affecting its computational 2D complexity. First, an enrichment procedure able to address 3D local behaviors and then a more general method able to deal with fully 3D descriptions were proposed. The methods were firstly developed in linear elastic settings and then successfully extended to structures exhibiting inelastic behaviors and dynamics. Again the inclusion of damage effects by using these non-intrusive methods constitutes a work in progress.

In Chapter 5 we proposed a simulation tool based on a simplified parametric modeling for evaluating parametrically distortions occurring in parts manufactured by additive manufacturing. The computed parametric solution, which involves as parameters the ones parametrizing the process trajectories, the thermal shrinkage intensity and anisotropy and the deposited layers, was introduced into a GUI application able to evaluate the effect of any parameter in almost real-time. Moreover the simulation tools also allowed to proceed to the required geometry compensation and to perform optimization, sensitivity analysis and uncertainty propagation. The first qualitative validation were very promising and the works in progress consider a quantitative validation too.

Finally in Chapter 6 we introduced the new Hybrid Twin concept. By employing data-driven modeling the gap between parametric deterministic solutions and the measured fields was filled, opening new possibilities in the field of dynamic data-driven application systems. The Hybrid Twin concept was successfully applied first to composite parts manufactured from RTM process and second to a dismantling process of a nuclear central. Different methods for the construction of the data-driven model as well as for the data assimilation can be employed and the exploration of these methods and the development of new ones constitute an ongoing work as well as the application of the hybrid twin concept to structural dynamics and additive manufacturing processes.

Appendix A

The Sparse Subspace Learning (SSL) method

When addressing a transient model involving the unknown field $u(\mathbf{x}, t)$ and a series of parameters $(p_1, \cdots, p_{\mathtt{p}})$, its separated representation reads

$$u(\mathbf{x}, t, p_1, \cdots, p_{\mathtt{p}}) \approx \sum_{i=1}^{N} X_i(\mathbf{x}) \cdot T_i(t) \cdot \prod_{k=1}^{\mathtt{p}} P_i^k(p_k). \tag{A.1}$$

If we are only interested on the parametrical aspect of the unknown field the separated representation can be written as

$$u(\mathbf{x}, t, p_1, \cdots, p_{\mathtt{p}}) \approx \sum_{i=1}^{N} X_i(\mathbf{x}, t) \cdot \prod_{k=1}^{\mathtt{p}} P_i^k(p_k). \tag{A.2}$$

The Sparse Subspace Learning (SSL) method [Borzacchiello *et al.* 2017] constructs the parametric solution in the separated form A.2 in a non-intrusive way by using commercial simulation softwares, circumventing the intrusivity of the standard PGD method [Chinesta *et al.* 2014a]. We will suppose, for the sake of simplicity, that in the model there is only one parameter $\mu \in [\mu_{min}, \mu_{max}]$ so that A.2 reduces to

$$u(\mathbf{x}, t, \mu) \approx \sum_{i=1}^{N} X_i(\mathbf{x}, t) \cdot M_i(\mu). \tag{A.3}$$

In the SSL method a hierarchical basis, providing nested collocation points and built-in error estimators, is chosen for the parametric domain. In this work the Gauss-Chebychev-Lobato points μ_i^j and the corresponding hierarchical Lagrangian interpolation polynomials $\psi_i^j(\mu)$ are used where i and j indexes refer to the i-point and the j-hierarchical level. At the first level, $j = 0$ the solution is computed, using for instance a commercial software, at the two collocation points $\mu_1^0 = \mu_{min}$ and $\mu_2^0 = \mu_{max}$, providing

$$u_1^0(\mathbf{x}, t) = u(\mathbf{x}, t, \mu = \mu_1^0), \tag{A.4}$$

and

$$u_2^0(\mathbf{x}, t) = u(\mathbf{x}, t, \mu = \mu_2^0). \tag{A.5}$$

The solution at level $j = 0$ is then approximated by using the two linear interpolation functions

$$\psi_1^0(\mu) = \frac{\mu - \mu_2^0}{\mu_1^0 - \mu_2^0} \tag{A.6}$$

and

$$\psi_2^0(\mu) = \frac{\mu - \mu_1^0}{\mu_2^0 - \mu_1^0}, \tag{A.7}$$

and it reads

$$u^0(\mathbf{x},t,\mu) = u_1^0(\mathbf{x},t)\psi_1^0(\mu) + u_2^0(\mathbf{x},t)\psi_2^0(\mu). \tag{A.8}$$

At the next level, $j=1$, the solution is computed at the collocation point $\mu_1^1 = 0.5(\mu_{min} + \mu_{max})$ and it writes

$$u_1^1(\mathbf{x},t) = u(\mathbf{x},t,\mu=\mu_1^1). \tag{A.9}$$

As the approximation at level $j=0$ (A.8) computed in $\mu=\mu_1^1$ already explained part of the solution, we can defined the so-called *surplus* as

$$\bar{u}_1^1(\mathbf{x},t) = u_1^1(\mathbf{x},t) - u^0(\mathbf{x},t,\mu_1^1). \tag{A.10}$$

The surplus is the part of the solution for $\mu=\mu_1^1$ not explained by the previous approximation, thus its norm is used as a local error indicator. Now defining the quadratic interpolation function

$$\psi_1^1(\mu) = \frac{(\mu-\mu_1^0)(\mu-\mu_2^0)}{(\mu_1^1-\mu_1^0)(\mu_1^1-\mu_2^0)}, \tag{A.11}$$

the approximation at level $j=1$ reads

$$u^1(\mathbf{x},t,\mu) = u^0(\mathbf{x},t,\mu) + \bar{u}_1^1(\mathbf{x},t)\psi_1^1(\mu). \tag{A.12}$$

The process continues with the following hierarchical approximation levels by adding surpluses until the norm of the surplus is small enough; this means that adding a new hierarchical level would not contribute sufficiently to improve the solution and the process is stopped. As it is possible to notice in (A.12) the solution computed using this method is in the separated form (A.3), however it could contain too many terms. For this reason at the end of the hierarchical process a post-compression is performed by applying the PGD algorithm to the computed solution [Chinesta *et al.* 2014a]. So, if the SSL solution is given by

$$u(\mathbf{x},t,\mu) \approx \sum_{i=1}^{N} X_i(\mathbf{x},t)\cdot M_i(\mu), \tag{A.13}$$

the post-compression step computes a solution

$$\tilde{u}(\mathbf{x},t,\mu) \approx \sum_{i=1}^{\tilde{N}} \tilde{X}_i(\mathbf{x},t)\cdot \tilde{M}_i(\mu), \tag{A.14}$$

with $\tilde{N} < N$ by solving the following equation with the PGD

$$\int_{\Omega_\mathbf{x}\times\Omega_t}\int_{\Omega_\mu} u^*(\tilde{u}(\mathbf{x},t,\mu) - u(\mathbf{x},t,\mu))\, d\mu\, dt\, d\mathbf{x}. \tag{A.15}$$

When more than one parameter is involved in the model, e.g. μ and θ, the j-level collocation points and the corresponding hierarchical basis are given respectively by (μ_i^k, θ_e^l) and $\psi_i^k(\mu)\xi_e^l(\theta)$, with $k+l=j$ (Smolyak's rule). Here $(\mu_i^k, \psi_i^k(\mu))$ (respectively $(\theta_e^l, \xi_e^l(\theta))$) correspond to the i (respectively e)-point of the k (respectively l)-hierarchical level for the 1D domain $[\mu_{min}, \mu_{max}]$ (respectively $[\theta_{min}, \theta_{max}]$).

Appendix B

Calculation of the plastic strain increment

When a structure is loaded, elastic strains, $\boldsymbol{\varepsilon}$, first appear and the relationship between them and the stresses, $\boldsymbol{\sigma}$, is given by the Hooke's law

$$\boldsymbol{\sigma} = \mathbb{C}\,\boldsymbol{\varepsilon}, \tag{B.1}$$

where $\mathbb{C}$ is the Hooke's fourth order tensor, or nonlinear elastic stress-strain relations. Increasing the loading the material begins to yield and plastic strains develop. In plasticity it is convenient to consider plastic strain infinitesimal incremental $d\boldsymbol{\varepsilon}^{\boldsymbol{p}}$, so that the total strain increment $d\boldsymbol{\varepsilon}$ is assumed to be the sum of the elastic strains increment $d\boldsymbol{\varepsilon}^{\boldsymbol{e}}$ and the plastic strain increment $d\boldsymbol{\varepsilon}^{\boldsymbol{p}}$

$$d\boldsymbol{\varepsilon} = d\boldsymbol{\varepsilon}^{\boldsymbol{e}} + d\boldsymbol{\varepsilon}^{\boldsymbol{p}}. \tag{B.2}$$

The plastic strain increment can be derived from a plastic potential g as

$$d\boldsymbol{\varepsilon}^{\boldsymbol{p}} = d\lambda \frac{\partial g}{\partial \boldsymbol{\sigma}}. \tag{B.3}$$

In the associated flow rule, g is taken as the scalar yield function, that is defined as

$$f(\boldsymbol{\sigma}, \boldsymbol{\alpha}) = 0, \tag{B.4}$$

where $\boldsymbol{\sigma}$ contains the six independent stress components and $\boldsymbol{\alpha}$ defines specific material parameters. The yield function defines a surface in the stress space, so that when $f < 0$ the behavior is elastic and $f = 0$ defines the elastic limit. Thus, the state of stress is given by a point either inside (elastic behavior) or on the yield surface (plastic behavior). In the case of the Von Mises criterion and perfect plasticity we have

$$f(\boldsymbol{\sigma}) = \sigma_e - \sigma_0, \tag{B.5}$$

where

$$\sigma_e = \left[\frac{1}{2}(\sigma_x - \sigma_y)^2 + \frac{1}{2}(\sigma_y - \sigma_z)^2 + \frac{1}{2}(\sigma_z - \sigma_x)^2 + 3\tau_{xy}^2 + 3\tau_{yz}^2 + 3\tau_{xz}^2\right]^{\frac{1}{2}} \tag{B.6}$$

and σ_0 is the uniaxial stress at yield. Equation (B.3) can then be rewritten as

$$d\boldsymbol{\varepsilon}^{\boldsymbol{p}} = d\lambda \frac{\partial f}{\partial \boldsymbol{\sigma}} = d\lambda \nabla f \tag{B.7}$$

where

$$\nabla f = \left[\frac{\partial f}{\partial \sigma_x}, \ldots, \frac{\partial f}{\partial \tau_{xz}}\right]^T \tag{B.8}$$

is the normal to the yield surface. As we said before, the yield surface defines the set of maximal permissible stresses and the conditions for which plastic deformations can continue to occur, that is as long as the stress point is located on the yield surface. These conditions can be written as

$$f(\boldsymbol{\sigma} + d\boldsymbol{\sigma}) = f(\boldsymbol{\sigma}) + \nabla f^T d\boldsymbol{\sigma} = 0, \tag{B.9}$$

and as $f(\boldsymbol{\sigma}) = 0$

$$df = \nabla f^T d\boldsymbol{\sigma} = 0. \tag{B.10}$$

This is the so-called consistency condition.

Now, from Hooke's law we have

$$d\boldsymbol{\sigma} = \mathbf{C} d\boldsymbol{\varepsilon}^{\boldsymbol{e}} = \mathbf{C}(d\boldsymbol{\varepsilon} - d\boldsymbol{\varepsilon}^{\boldsymbol{p}}) \tag{B.11}$$

and by using (B.7)

$$d\boldsymbol{\sigma} = \mathbf{C} d\boldsymbol{\varepsilon} - d\lambda \mathbf{C} \nabla f. \tag{B.12}$$

Substituting (B.12) into the consistency condition (B.10) we get

$$\nabla f^T \Big(\mathbf{C} d\boldsymbol{\varepsilon} - d\lambda \mathbf{C} \nabla f) = 0, \tag{B.13}$$

and solving for the scalar $d\lambda$ one obtains

$$d\lambda = \frac{\nabla f^T \mathbf{C} d\boldsymbol{\varepsilon}}{\nabla f^T \mathbf{C} \nabla f}. \tag{B.14}$$

In the case that isotropic hardening appears, the yield stress σ_0 is a function of an equivalent plastic strain ε^p_{eq} and (B.14) reads as

$$d\lambda = \frac{\nabla f^T \mathbf{C} d\boldsymbol{\varepsilon}}{H + \nabla f^T \mathbf{C} \nabla f}, \tag{B.15}$$

where H is defined as

$$H = \frac{d\sigma_0}{d\varepsilon^p_{eq}}. \tag{B.16}$$

In the case of the Von Misses criterion we have that

$$d\varepsilon^p_{eq} = d\lambda. \tag{B.17}$$

The plastic strain infinitesimal increment (B.7) is then computed as

$$d\boldsymbol{\varepsilon}^{\boldsymbol{p}} = \frac{\nabla f^T \mathbf{C} d\boldsymbol{\varepsilon}}{\nabla f^T \mathbf{C} \nabla f} \nabla f. \tag{B.18}$$

and plastic strain finite increment as

$$\Delta\boldsymbol{\varepsilon}^{\boldsymbol{p}} = \frac{\nabla f^T \mathbf{C} \Delta\boldsymbol{\varepsilon}}{\nabla f^T \mathbf{C} \nabla f} \nabla f. \tag{B.19}$$

More details about the plastic strain finite increment computation can be found for example in [Owen & Hinton 1980].

Appendix C

Calculation of the out-of plane functions in a minimally-intrusive manner

We write the virtual work principle

$$\begin{aligned}
&\boldsymbol{\varepsilon}^{*T}\boldsymbol{\sigma} = \boldsymbol{\varepsilon}^{*T}\mathbf{C}\boldsymbol{\varepsilon} \\
&= \{\boldsymbol{\Theta}^1(x,y)\circ\mathbf{F}^{1*}(z) + \boldsymbol{\Theta}^2(x,y)\circ\mathbf{F}^{2*}(z)\}^T\{\mathbf{C}_{xy}(x,y)\circ\mathbf{C}_z(z)\} \\
&\{\boldsymbol{\Theta}^1(x,y)\circ\mathbf{F}^1(z) + \boldsymbol{\Theta}^2(x,y)\circ\mathbf{F}^2(z)\} \\
&= \mathbf{F}^{1*T}(x,y)\{\hat{\mathbf{C}}^{11}_{xy}(x,y)\circ\mathbf{C}_z(z)\}\mathbf{F}^1(x,y) + \mathbf{F}^{1*T}(x,y)\ \{\hat{\mathbf{C}}^{12}_{xy}(x,y)\circ\mathbf{C}_z(z)\} \\
&\mathbf{F}^2(x,y) + \mathbf{F}^{2*T}(x,y)\{\hat{\mathbf{C}}^{21}_{xy}(x,y)\circ\mathbf{C}_z(z)\}\mathbf{F}^1(x,y) + \mathbf{F}^{2*T}(x,y) \\
&\{\hat{\mathbf{C}}^{22}_{xy}(x,y)\circ\mathbf{C}_z(z)\}\mathbf{F}^2(x,y).
\end{aligned} \tag{C.1}$$

In the previous expression matrices $\hat{\mathbf{C}}^{ij}_{xy}(x,y)$ results

$$\hat{\mathbf{C}}^{ij}_{xy_{kl}}(x,y) = \mathbf{C}_{xy_{kl}}(x,y)\boldsymbol{\Theta}^i_k(x,y)\boldsymbol{\Theta}^j_l(x,y), \quad i,j\in[1,2]\ \&\ \ k,l\in[1,\cdots,6]. \tag{C.2}$$

Now, the virtual work integral reads

$$\int_{\Omega_{xy}\times\Omega_z}\sum_{i=1}^{2}\sum_{j=1}^{2}\mathbf{F}^{i*T}(z)\{\hat{\mathbf{C}}^{ij}_{xy}(x,y)\circ\mathbf{C}_z(z)\}\mathbf{F}^j(z)\ dz\ dx\ dy$$

$$= \int_{\Omega_z}\sum_{i=1}^{2}\sum_{j=1}^{2}\mathbf{F}^{i*T}(z)\mathbf{P}^{ij}(z)\mathbf{F}^j(z)\ dz, \tag{C.3}$$

where

$$\mathbf{P}^{ij}(z) = \mathbf{C}_z(z)\circ\int_{\Omega_{xy}}\hat{\mathbf{C}}^{ij}_{xy}(x,y)\ dx\ dy. \tag{C.4}$$

Now, if we assume for instance an approximation based on piecewise linear interpolations on the 1D finite element mesh of $\Omega_z = \cup_{q=1}^{\mathtt{Q}}\Omega_z^q$, with the shape functions defined by $N_i^q(z),\ i=1,2;\ q=1,\cdots,\mathtt{Q}$; it results

$$\begin{cases} f^{x,q}(z) = N_1^q(z)f_1^{x,q} + N_2^q(z)f_2^{x,q} \\ f^{y,q}(z) = N_1^q(z)f_1^{y,q} + N_2^q(z)f_2^{y,q} \\ f^{z,q}(z) = N_1^q(z)f_1^{z,q} + N_2^q(z)f_2^{z,q} \end{cases} \tag{C.5}$$

Using that approximation we can express vectors $\mathbf{F}^i(z)$ in each element Ω_z^q from

$$\mathbf{L}^{qT} = (f_1^{x,q}, f_1^{y,q}, f_1^{z,q}, f_2^{x,q}, f_2^{y,q}, f_2^{z,q}), \tag{C.6}$$

and

$$\mathbf{F}^i(z \in \Omega_z^q) = \mathbf{T}^{i,q}(z)\mathbf{L}^q, \tag{C.7}$$

where $\mathbf{T}^{i,q}(z)$ contains the shape functions and theirs derivatives, according to the expressions involved in the components of $\mathbf{F}^i(z)$, $i = 1, 2$. Thus, integral (C.3) reads

$$\sum_{q=1}^{\mathtt{Q}} \mathbf{L}^{q*T} \left\{ \int_{\Omega_z^q} \sum_{i=1}^{2}\sum_{j=1}^{2} \mathbf{T}^{i,qT}(z)\mathbf{P}^{ij}(z)\mathbf{T}^{j,q}(z)\ dz \right\} \mathbf{L}^q$$

$$= \sum_{q=1}^{\mathtt{Q}} \mathbf{L}^{q*T}\mathbf{K}_z^q\mathbf{L}^q = \mathbf{L}^{*T}\mathbf{K}_z\mathbf{L}. \tag{C.8}$$

The virtual work (4.71) of the body forces can be expressed as

$$\mathbf{u}^{*T}\mathbf{g}(\mathbf{x}) = \mathbf{W}^{*T}(z)\hat{\mathbf{O}}(x,y)\mathbf{H}(z), \tag{C.9}$$

where matrix $\hat{\mathbf{O}}$ reads

$$\hat{\mathbf{O}}_{kl}(x,y) = \mathbf{I}_{kl}\mathbf{V}_k(x,y)\mathbf{G}_l(x,y), \tag{C.10}$$

with $\mathbf{I}$ the identity matrix. Now, the integral results

$$\int_{\Omega_{xy}\times\Omega_z} \mathbf{u}^{*T}\mathbf{g}(\mathbf{x})\ dz\ dx\ dy = \int_{\Omega_z} \mathbf{W}^{*T}(z)\mathbf{O}\mathbf{H}(z)\ dz, \tag{C.11}$$

with

$$\mathbf{O} = \int_{\Omega_{xy}} \hat{\mathbf{O}}(x,y)\ dx\ dy, \tag{C.12}$$

Integrating in the mesh $\Omega_z = \cup_{q=1}^{\mathtt{Q}}\Omega_z^q$,

$$\int_{\Omega_z} \mathbf{W}^{*T}(z)\mathbf{O}\mathbf{H}(z)\ dz = \sum_{q=1}^{\mathtt{Q}} \int_{\Omega_z^q} \mathbf{W}^{q*T}(z)\mathbf{O}\mathbf{H}^q(z)\ dz, \tag{C.13}$$

where $\mathbf{W}^q(z)$ and $\mathbf{H}^q(z)$ are approximated respectively from

$$\mathbf{W}^q(z) = \mathbf{S}(z)\mathbf{L}^q, \tag{C.14}$$

and

$$\mathbf{H}^q(z) = \mathbf{S}(z)\mathbf{M}^q, \tag{C.15}$$

with $\mathbf{M}^q$ containing the nodal values of $\mathbf{H}(z)$ and $\mathbf{S}(z) = [\mathbf{N}_1(z)\ \mathbf{N}_2(z)]$, and

$$\mathbf{N}_i = \begin{pmatrix} N_i^q(z) & 0 \\ 0 & N_i^q(z) \end{pmatrix}. \tag{C.16}$$

Thus, it results

$$\sum_{q=1}^{\mathtt{Q}} \int_{\Omega^q} \mathbf{W}^{q*T}(z)\mathbf{O}\mathbf{H}^q(z)\ dz = \sum_{q=1}^{\mathtt{Q}} \mathbf{L}^{q*T} \left\{ \int_{\Omega_z^q} \mathbf{S}^T\mathbf{O}\mathbf{S}\ dz \right\} \mathbf{M}^q$$

$$= \sum_{q=1}^{\mathtt{Q}} \mathbf{L}^{q*T}\mathbf{A}_z^q\mathbf{M}^q = \sum_{q=1}^{\mathtt{Q}} \mathbf{L}^{q*T}\mathbf{B}_z^q = \mathbf{L}^{*T}\mathbf{B}_z, \tag{C.17}$$

from which, the principle of virtual works reads

$$\mathbf{L}^{*T}\mathbf{K}_z\mathbf{L} = \mathbf{L}^{*T}\mathbf{B}_z. \tag{C.18}$$

Thus, the out-of-plane functions determining the kinematics can be obtained from a standard 1D software by using the elementary rigidity and forces given respectively by $\mathbf{K}_z^q$ and $\mathbf{B}_z^q$ considered in expression (C.8) and (C.17).

Bibliography

[Aguado *et al.* 2014] J.V. Aguado, A. Huerta, F. Chinesta and E. Cueto. Real-time monitoring of thermal processes by reduced-order modeling, volume 102. 2014.

[Aguado *et al.* 2017a] J.V. Aguado, B. Bognet, D. Canales, O. Desmaison, F. Boitout and F. Chinesta. *A reduced order modeling approach for fast thermo-mechanics simulation of additive layer manufacturing.* ECCOMAS Conference on Simulation for Additive Manufacturing, Munich, Germany., 2017.

[Aguado *et al.* 2017b] J.V. Aguado, D. Borzacchiello, C. Ghnatios, F. Lebel, R. Upadhyay, C. Binetruy and F. Chinesta. A simulation app based on reduced order modeling for manufacturing optimization of composite outlet guide vanes, volume 4. 2017.

[Ahmad *et al.* 1970] S. Ahmad, B. M. Irons and O.C. Zienkiewicz. Analysis of thick and thin shell structures by curved element, volume 2. 1970.

[Alfaro *et al.* 2014] I. Alfaro, D. González, F. Bordeu, A. Leygue, A. Ammar, E. Cueto and F. Chinesta. Real-time in silico experiments on gene regulatory networks and surgery simulation on handheld devices, volume 1. 2014.

[Ammar *et al.* 2006] A. Ammar, B. Mokdad, F. Chinesta and R. Keunings. *A new family of solvers for some classes of multidimensional partial differential equations encountered in kinetic theory modeling of complex fluids.* Journal of Non-Newtonian Fluid Mechanics, **139**, 153–176, 2006.

[Ammar *et al.* 2007] A. Ammar, B. Mokdad, F. Chinesta and R. Keunings. *A new family of solvers for some classes of multidimensional partial differential equations encountered in kinetic theory modelling of complex fluids: Part II: Transient simulation using space-time separated representations.* Journal of Non-Newtonian Fluid Mechanics, **144**, 98–121, 2007.

[Ammar *et al.* 2008] A. Ammar, F. Chinesta and P. Joyot. *The Nanometric and Micrometric Scales of the Structure and Mechanics of Materials Revisited : An Introduction to the Challenges of Fully Deterministic Numerical Descriptions.* 2008.

[Anandkumar *et al.* 2014] A. Anandkumar, R. Ge, D. Hsu, S.M. Kakade and M. Telgarsky. *Tensor Decompositions for Learning Latent Variable Models.* Journal of Machine Learning Research, **15**, 2773–2832, 2014.

[Argyris 1965] J.H. Argyris. *Elasto-plastic Matrix Displacement Analysis of Three-dimensional Continua.* The Journal of the Royal Aeronautical Society, **69**, 633–636, 1965.

[Barbarulo *et al.* 2015] A. Barbarulo, H. Riou, L. Kovalevsky and P. Ladeveze. Pgd-vtcr: A reduced order model technique to solve medium frequency broad band problems on complex acoustical systems, volume 60. 2015.

[Barrault *et al.* 2004] M. Barrault, Y. Maday, N.C. Nguyen and A.T. Patera. *An 'empirical interpolation' method: application to efficient reduced-basis discretization of partial differential equations.* Comptes Rendus Mathematique, **339**, 667–672, 2004.

[Bathe 2006] K.J. Bathe. Finite element procedures, volume 2. 2006.

[Bognet *et al.* 2012] B. Bognet, F. Bordeu, F. Chinesta, A. Leygue and A. Poitou. Advanced simulation of models defined in plate geometries : 3d solutions with 2d computational complexity, volume s 201-204. 2012.

[Bognet *et al.* 2014] B. Bognet, A. Leygue and F. Chinesta. *Separated representations of 3D elastic solutions in shell geometries.* Advanced Modeling and Simulation in Engineering Sciences, **1**, 4–, 2014.

[Bordeu *et al.* 2015] F. Bordeu, C. Ghnatios, D. Boulze, B. Carles, D. Sireude, A. Leygue and F. Chinesta. Parametric 3d elastic solutions of beams involved in frame structures, volume 2. 2015.

[Borzacchiello *et al.* 2017] D. Borzacchiello, J.V. Aguado and F. Chinesta. *Non-intrusive Sparse Subspace Learning for Parametrized Problems.* Archives of Computational Methods in Engineering, 2017.

[Boucinha *et al.* 2014] L. Boucinha, A. Ammar, A. Gravouil and A. Nouy. *Ideal minimal residual-based proper generalized decomposition for non-symmetric multi-field models - Application to transient elastodynamics in space-time domain.* Computer Methods in Applied Mechanics and Engineering, **273**, 56–76, 2014.

[Branch *et al.* 1999] M.A. Branch, F.T. Coleman and Y. li. A subspace, interior, and conjugate gradient method for large-scale bound-constrained minimization problems, volume 21. SIAM Journal on Scientific Computing, 1999.

[Brincker *et al.* 2001] R. Brincker, L. Zhang and P. Andersen. *Modal identification of output-only systems using frequency domain decomposition.* Smart Materials and Structures, **10**, 441, 2001.

[Brunton *et al.* 2016] S.L. Brunton, J.L. Proctor and J.N. Kutz. *Discovering governing equations from data by sparse identification of nonlinear dynamical systems.* Proc Natl Acad Sci USA, **113**, 3932–, 2016.

[Bur *et al.* 2016] N. Bur, P. Joyot, C. Ghnatios, P. Villon, E. Cueto and F. Chinesta. On the use of model order reduction for simulating automated fibre placement processes, volume 3. 2016.

[Canales *et al.* 2009] G. Canales, L. Mevel and M. Basseville. *Transmissibility based damage detection.* In 27th International Modal Analysis Conference (IMAC-XXVII), Orlando, United States, 2009. SEM.

[Capellari *et al.* 2015] G. Capellari, S. Eftekhar Azam and S. Mariani. *Damage Detection in Flexible Plates through Reduced-Order Modeling and Hybrid Particle-Kalman Filtering.* Sensors (Basel, Switzerland), **16**, 2, 2015.

[Cattarius & Inman 1997] J. Cattarius and D.J. Inman. *Time domain analysis for damage detection in smart structures.* Mechanical Systems and Signal Processing, **11**, 409–423, 1997.

[Cawley & Adams 1979] P. Cawley and R.D. Adams. *The location of defects in structures from measurements of natural frequencies.* The Journal of Strain Analysis for Engineering Design, **14**, 49–57, 1979.

[Chang & Chen 2004] C.C. Chang and L.W. Chen. *Damage detection of a rectangular plate by spatial wavelet based approach.* Applied Acoustics, **65**, 819–832, 2004.

[Chaturantabut & C. Sorensen 2010] S. Chaturantabut and D. C. Sorensen. Nonlinear model reduction via discrete empirical interpolation, volume 32. 2010.

[Chen & Zhang 2004] T. Chen and Y. Zhang. *Numerical simulation of two-dimensional melting and resolidification of a two-component metal powder layer in selective laser sintering process.* Numerical Heat Transfer, Part A: Applications, **46**, 633–649, 2004.

[Chinesta & Ladeveze 2014] F. Chinesta and P. Ladeveze. Separated representations and pgd-based model reduction: Fundamentals and applications. 2014.

[Chinesta *et al.* 2011] F. Chinesta, P. Ladeveze and E. Cueto. A short review on model order reduction based on proper generalized decomposition, volume 18. 2011.

[Chinesta *et al.* 2013a] F. Chinesta, A. Leygue, M. Beringhier, L. Tuan Nguyen, J.C. Grandidier, B. Schrefler and F. Pesavento. Towards a framework for non-linear thermal models in shell domains, volume 23. 2013.

[Chinesta *et al.* 2013b] F. Chinesta, A. Leygue, F. Bordeu, J.V. Aguado, E. Cueto, D. Gonzalez, I Alfaro, A. Ammar and A. Huerta. Pgd-based computational vademecum for efficient design, optimization and control, volume 20. 2013.

[Chinesta *et al.* 2014a] F. Chinesta, R. Keunings and A. Leygue. The proper generalized decomposition for advanced numerical simulations. a primer. 2014.

[Chinesta *et al.* 2014b] F. Chinesta, A. Leygue, B. Bognet, C. Ghnatios, F. Poulhaon, F. Bordeu, A. Barasinski, A Poitou, S. Chatel and M. Serge. First steps towards an advanced simulation of composites manufacturing by automated tape placement, volume 7. 2014.

[Chinesta *et al.* 2015] F. Chinesta, A. Huerta, G. Rozza and K. Wilcox. Model order reduction. chapter in the encyclopedia of computational mechanics, second edition, erwin stein, rené de borst & tom hughes edt. John Wiley & Sons Ltd., 2015.

[Chinesta *et al.* 2018] F. Chinesta, E. Cueto, E. Abisset-Chavanne, J.L. Duval and F.E. Khaldi. *Virtual, Digital and Hybrid Twins: A New Paradigm in Data-Based Engineering and Engineered Data.* Archives of Computational Methods in Engineering, 2018.

[Chiumenti *et al.* 2010] M. Chiumenti, M. Cervera, A. Salmi, C. Agelet de Saracibar, N. Dialami and K. Matsui. *Finite element modeling of multi-pass welding and shaped metal deposition processes.* Computer Methods in Applied Mechanics and Engineering, **199**, 2343–2359, 2010.

[Chiumenti *et al.* 2017] M. Chiumenti, X. Lin, M. Cervera, W. Lei, Y. Zheng and W. Huang. *Numerical simulation and experimental calibration of additive manufacturing by blown powder technology. Part I: thermal analysis.* Rapid Prototyping Journal, **23**, 448–463, 2017.

[Crandall 1970] S.H. Crandall. *The role of damping in vibration theory.* Journal of Sound and Vibration, **11**, 3–IN1, 1970.

[Criminisi *et al.* 2011] A. Criminisi, J. Shotton and E. Konukoglu. *Decision forests for classification, regression, density estimation, manifold learning and semi-supervised learning.* Technical report, Microsoft report TR-2011-114, 2011.

[Criminisi *et al.* 2012] A Criminisi, J Shotton and Ender Konukoglu. Decision forests: A unified framework for classification, regression, density estimation, manifold learning and semi-supervised learning, volume 7. 2012.

[Cueto *et al.* 2016] E. Cueto, D. González and I. Alfaro. *Proper generalized decompositions: An introduction to computer implementation with Matlab.* 1–94. 2016.

[Dai & Gu 2014] D. Dai and D. Gu. *Thermal behavior and densification mechanism during selective laser melting of copper matrix composites: Simulation and experiments.* Materials & Design, **55**, 482–491, 2014.

[Darcy 1856] H. Darcy. Fontaines publiques de la ville de dijon. Librairie des Corps Impériaux des Ponts et Chaussées et des Mines, 1856.

[Darema 2015] F. Darema. *DDDAS, A Key Driver for Large-Scale-Big-Data and Large-Scale-Big-Computing.* Procedia Computer Science, **51**, 2463–, 2015.

[Ding *et al.* 2011] J. Ding, P. Colegrove, J. Mehnen, S. Ganguly, P.M. Sequeira Almeida, F. Wang and S. Williams. *Thermo-mechanical analysis of Wire and Arc Additive Layer Manufacturing process on large multi-layer parts.* Computational Materials Science, **50**, 3315–3322, 2011.

[Dong *et al.* 2009] L. Dong, A. Makradi, S. Ahzi and Y. Remond. *Three-dimensional transient finite element analysis of the selective laser sintering process.* Journal of Materials Processing Technology, **209**, 700–706, 2009.

[Fan & Qiao 2009] W. Fan and P. Qiao. *A 2-D continuous wavelet transform of mode shape data for damage detection of plate structures.* International Journal of Solids and Structures, **46**, 4379–4395, 2009.

[Fish & Belytschko 2007] J. Fish and T. Belytschko. A first course in finite elements. John Wiley & Sons, 2007.

[Foteinopoulos *et al.* 2018] P. Foteinopoulos, A. Papacharalampopoulos and P. Stavropoulos. *On thermal modeling of Additive Manufacturing processes.* CIRP Journal of Manufacturing Science and Technology, **20**, 66–83, 2018.

[Gallagher 1962] R.H. Gallagher. *Stress Analysis of Heated Complex Shapes.* ARS Journal, **32**, 700–707, 1962.

[Germoso *et al.* 2016] C. Germoso, J.V. Aguado, A. Fraile, E. Alarcon and F. Chinesta. *Efficient PGD-based dynamic calculation of non-linear soil behavior.* Comptes Rendus Mécanique, **344**, 24–41, 2016.

[Ghnatios *et al.* 2015] C. Ghnatios, F. Chinesta and C. Binetruy. *3D Modeling of squeeze flows occurring in composite laminates.* International Journal of Material Forming, **8**, 73–83, 2015.

[Ghnatios *et al.* 2016a] C. Ghnatios, E. Abisset-Chavanne, C. Binetruy, F. Chinesta and S. Advani. *3D modeling of squeeze flow of multiaxial laminates.* Journal of Non-Newtonian Fluid Mechanics, **234**, 188–200, 2016.

[Ghnatios *et al.* 2016b] C. Ghnatios, G. Xu, A. Leygue, M. Visonneau, F. Chinesta and A. Cimetiere. *On the space separated representation when addressing the solution of PDE in complex domains*, 2016.

[Giner *et al.* 2013] E. Giner, B. Bognet, J.J. Ródenas, A. Leygue, F.J. Fuenmayor and F. Chinesta. *The Proper Generalized Decomposition (PGD) as a numerical procedure to solve 3D cracked plates in linear elastic fracture mechanics.* International Journal of Solids and Structures, **50**, 1710–1720, 2013.

[González *et al.* 2010] D. González, A. Ammar, F. Chinesta and E. Cueto. *Recent advances on the use of separated representations.* Int. J. Numer. Meth. Engng., **81**, 637–659, 2010.

[González *et al.* 2014] D. González, E. Cueto and F. Chinesta. *Real-time direct integration of reduced solid dynamics equations.* Int. J. Numer. Meth. Engng, **99**, 633–653, 2014.

[González *et al.* 2017] D. González, A. Badías, I. Alfaro, F. Chinesta and E. Cueto. *Model order reduction for real-time data assimilation through Extended Kalman Filters.* Computer Methods in Applied Mechanics and Engineering, **326**, 679–693, 2017.

[Goodfellow *et al.* 2016] I. Goodfellow, Y. Bengio and A. Courville. Deep learning. MIT Press, 2016.

[Gordan *et al.* 2017] M. Gordan, H. Abdul, Z. Ismail and K. Ghaedi. *Recent Developments in Damage Identification of Structures Using Data Mining.* Latin American Journal of Solids ans Structures, 2017.

[Gravouil & Combescure 2001] A. Gravouil and A. Combescure. Multi-time-step explicit - implicit method for non-linear structural dynamics, volume 50. 2001.

[Gregori *et al.* 2017] S. Gregori, M. Tur, E. Nadal, J.V. Aguado, F.J. Fuenmayor and F. Chinesta. *Fast simulation of the pantograph-catenary dynamic interaction.* Finite Elements in Analysis and Design, **129**, 1–13, 2017.

[Gui *et al.* 2017] G. Gui, H. Pan, Z. Lin, Y. Li and Z. Yuan. *Data-driven support vector machine with optimization techniques for structural health monitoring and damage detection.* KSCE Journal of Civil Engineering, **21**, 523–534, 2017.

[Heigel *et al.* 2015] J.C. Heigel, P. Michaleris and E.W. Reutzel. *Thermo-mechanical model development and validation of directed energy deposition additive manufacturing of Ti-6Al-4V.* Additive Manufacturing, **5**, 9–19, 2015.

[Hey *et al.* 2009] T. Hey, S. Tansley and K. Tolle. The fourth paradigm: Data-intensive scientific discovery. Microsoft Research, 2009.

[Huang *et al.* 2009] Y. Huang, D. Meyer and S. Nemat-Nasser. *Damage detection with spatially distributed 2D Continuous Wavelet Transform.* Mechanics of Materials, **41**, 1096–1107, 2009.

[Hughes & Liu 1978] T.J.R. Hughes and W.K. Liu. *Implicit-Explicit Finite Elements in Transient Analysis: Stability Theory.* Journal of Applied Mechanics, **45**, 371–374, 1978.

[Ibáñez Pinillo *et al.* 2017] R. Ibáñez Pinillo, D. Borzacchiello, J.V. Aguado, E. Abisset-Chavanne, E. Cueto, P. Ladeveze and F. Chinesta. Data-driven non-linear elasticity: constitutive manifold construction and problem discretization, volume 60. 2017.

[Ibáñez Pinillo *et al.* 2018] R. Ibáñez Pinillo, E. Abisset-Chavanne, A. Ammar, D. González, E. Cueto, A. Huerta, J.L. Duval and F. Chinesta. A multi-dimensional data-driven sparse identification technique: The sparse proper generalized decomposition, volume 2018. 2018.

[Ibáñez *et al.* 2017] R. Ibáñez, E. Abisset-Chavanne, F. Chinesta and A. Huerta. *Simulating squeeze flows in multiaxial laminates: towards fully 3D mixed formulations.* International Journal of Material Forming, **10**, 653–669, 2017.

[Ibrahim & Mikulcik 1976] S.R. Ibrahim and E.C. Mikulcik. *The experimental determination of vibration parameters from time responses.* The Shock and Vibration Bulletin, **46**, 187–196, 1976.

[Ibrahim & Mikulcik 1977] S.R. Ibrahim and E.C. Mikulcik. *A Method for the Direct Identification of Vibration Parameters from the Free Response.* Shock Vib. Bull., **47**, 183–196, 1977.

[Ibrahim 1986] S.R. Ibrahim. *Double least squares approach for use in structural modal identification.* AIAA Journal, **24**, 499–503, 1986.

[James *et al.* 1992] G. James, T. Carne, J. Lauffer and A. R. Nord. Modal testing using natural excitation, volume 2. 1992.

[Juang & Pappa 1985] J.N. Juang and R.S. Pappa. *An eigensystem realization algorithm for modal parameter identification and model reduction.* Journal of Guidance, Control, and Dynamics, **8**, 620–627, 1985.

[Kambhatla & Leen 1997] N. Kambhatla and T. Leen. Dimension reduction by local principal component analysis, volume 9. 1997.

[Kendall *et al.* 1992] K.N. Kendall, C.D. Rudd, M.J. Owen and V. Middleton. *Characterization of the resin transfer moulding process.* Composites Manufacturing, **3**, 235–249, 1992.

[Khairallah *et al.* 2016] S.A. Khairallah, A.T. Anderson, A. Rubenchik and W.E. King. *Laser powder-bed fusion additive manufacturing: Physics of complex melt flow and formation mechanisms of pores, spatter, and denudation zones.* Acta Materialia, **108**, 36–45, 2016.

[Kim & Melhem 2004] H. Kim and H. Melhem. *Damage detection of structures by wavelet analysis.* Engineering Structures, **26**, 347–362, 2004.

[Kirchdoerfer & Ortiz 2016] T. Kirchdoerfer and M. Ortiz. *Data-driven computational mechanics.* Computer Methods in Applied Mechanics and Engineering, **304**, 81–101, 2016.

[Kirchhoff 1850] G. Kirchhoff. *Uber das Gleichqewicht und die Bewegung einer elastichen. Scheibe.* J. Reine und Angewandte Mathematik, **40**, 51–88, 1850.

[Kolossov *et al.* 2004] S. Kolossov, E. Boillat, R. Glardon, P. Fischer and M. Locher. *3D FE simulation for temperature evolution in the selective laser sintering process.* International Journal of Machine Tools and Manufacture, **44**, 117–123, 2004.

[Kovaleva *et al.* 2014] I. Kovaleva, O. Kovalev and I. Smurov. *Model of Heat and Mass Transfer in Random Packing Layer of Powder Particles in Selective Laser Melting.* Physics Procedia, **56**, 400–410, 2014.

[Körner *et al.* 2011] C. Körner, E. Attar and P. Heinl. *Mesoscopic simulation of selective beam melting processes.* Journal of Materials Processing Technology, **211**, 978–987, 2011.

[Körner *et al.* 2013] C. Körner, A. Bauereiß and E. Attar. *Fundamental consolidation mechanisms during selective beam melting of powders.* Modelling and Simulation in Materials Science and Engineering, **21**, 085011, 2013.

[Kutz 2013] J.N. Kutz. Data-driven modeling & scientific computation: Methods for complex systems & big data. Oxford University Press, Inc., New York, NY, USA, 2013.

[Labudovic *et al.* 2003] M. Labudovic, D. Hu and R. Kovacevic. A three dimensional model for direct laser metal powder deposition and rapid prototyping, volume 38. 2003.

[Ladeveze 1985] P. Ladeveze. *On a family of algorithms for structural mechanics (in french).* Comptes Rendus Académie des Sciences Paris, **300**, 41–44, 1985.

[Ladeveze 1989] P. Ladeveze. *The large time increment method for the analyze of structures with nonlinear constitutive relation described by internal variables.* Comptes Rendus Académie des Sciences Paris, **305**, 1095–1099, 1989.

[Ladeveze 1996] P. Ladeveze. *Mécanique non linéaire des structures.* Hermès, Paris, 1996.

[Ladeveze 1999] P. Ladeveze. Nonlinear computational structural mechanics. new approaches and non-incremental methods of calculation. Springer Verlag, 1999.

[Ladevèze & Chamoin 2011] P. Ladevèze and L. Chamoin. *On the verification of model reduction methods based on the proper generalized decomposition.* Computer Methods in Applied Mechanics and Engineering, **200**, 2032–2047, 2011.

[Laraia 2012] M. Laraia. Nuclear decommissioning: Planning, execution and international experience. 2012.

[Laurent *et al.* 2013] G. Laurent, P. Vidal and O. Polit. Coupling finite element and reliability analysis through proper generalized decomposition model reduction, volume 95. 2013.

[Law *et al.* 2005] S.S. Law, X.Y. Li, X.Q. Zhu and S.L. Chan. *Structural damage detection from wavelet packet sensitivity.* Engineering Structures, **27**, 1339–1348, 2005.

[Lee & Verleysen 2007] J.A. Lee and M. Verleysen. Nonlinear dimensionality reduction. Springer Verlag, 2007.

[Li & Gu 2014] Y. Li and D. Gu. *Parametric analysis of thermal behavior during selective laser melting additive manufacturing of aluminum alloy powder.* Materials & Design, **63**, 856–867, 2014.

[Lin 2012] N. Lin. Monitoring of a frame structure model for damage identification using artificial neural networks. 2012.

[Liu *et al.* 2009] X. Liu, N. Lieven and P.J. Escamilla-Ambrosio. Frequency response function shape based methods for structural damage localization, volume 23. 2009.

[Ljung 1999] L. Ljung, editor. System identification (2nd ed.): Theory for the user. Prentice Hall PTR, Upper Saddle River, NJ, USA, 1999.

[Loh *et al.* 2015] L.E. Loh, C.K. Chua, W.Y. Yeong, J. Song, M. Mapar, S.L. Sing, Z.H. Liu and D.Q. Zhang. *Numerical investigation and an effective modelling on the Selective Laser Melting (SLM) process with aluminium alloy 6061.* International Journal of Heat and Mass Transfer, **80**, 288–300, 2015.

[Loutridis *et al.* 2004] S. Loutridis, E. Douka and A. Trochidis. *Crack identification in double-cracked beams using wavelet analysis.* Journal of Sound and Vibration, **277**, 1025–1039, 2004.

[Loutridis *et al.* 2005] S. Loutridis, E. Douka, L.J. Hadjileontiadis and A. Trochidis. *A two-dimensional wavelet transform for detection of cracks in plates.* Engineering Structures, **27**, 1327–1338, 2005.

[Lu & Hsu 2002] C.J. Lu and Y.T. Hsu. *Vibration analysis of an inhomogeneous string for damage detection by wavelet transform.* International Journal of Mechanical Sciences, **44**, 745–754, 2002.

[Maia *et al.* 1997] M.M.N. Maia, J. Silva and R. Sampaio. Localization of damage using curvature of the frequency response functions, volume 1. 1997.

[Mainini & Willcox 2015] L. Mainini and K. Willcox. *Surrogate Modeling Approach to Support Real-Time Structural Assessment and Decision Making.* AIAA Journal, **53**, 1612–1626, 2015.

[Malik *et al.* 2018a] H. Malik, D. Borzacchiello, F. Chinesta and P. Díez. Inclusion of frequency-dependent parameters in power transmission lines simulation using harmonic analysis and proper generalized decomposition: Malik et al. 2018.

[Malik *et al.* 2018b] M.H. Malik, D. Borzacchiello, J.V. Aguado and F. Chinesta. *Advanced parametric space-frequency separated representations in structural dynamics: A harmonic-modal hybrid approach.* Comptes Rendus Mécanique, **346**, 590–602, 2018.

[Marcal & King 1967] P.V. Marcal and I.P. King. *Elastic-plastic analysis of two-dimensional stress systems by the finite element method.* International Journal of Mechanical Sciences, **9**, 143–155, 1967.

[Marimuthu *et al.* 2013] S. Marimuthu, D. Clark, J. Allen, A. M. Kamara, P. Mativenga, L. Li and R. Scudamore. *Finite element modelling of substrate thermal distortion in direct laser additive manufacture of an aero-engine component.* Proceedings of the Institution of Mechanical Engineers, Part C: Journal of Mechanical Engineering Science, **227**, 1987–1999, 2013.

[Metoui *et al.* 2014] S. Metoui, E. Pruliere, A. Ammar, F. Dau and I. Iordanoff. *The proper generalized decomposition for the simulation of delamination using cohesive zone model.* Int. J. Numer. Meth. Engng, **99**, 1000–1022, 2014.

[Mindlin 1951] R.D. Mindlin. *Influence of rotatory inertia and shear in flexural motions of isotropic elastic plates.* J. Appl. Mech., **18**, 31–38, 1951.

[Mises 1913] R.V. Mises. *Mechanik der festen Krper im plastisch- deformablen Zustand.* Nachrichten von der Gesellschaft der Wissenschaften zu Gottingen, Mathematisch-Physikalische Klasse, **1913**, 582–592, 1913.

[Mohan *et al.* 2013] S.C. Mohan, D.K. Maiti and D. Maity. *Structural damage assessment using FRF employing particle swarm optimization.* Applied Mathematics and Computation, **219**, 10387–10400, 2013.

[Moitra 2018] A. Moitra. Algorithmic aspects of machine learning. Cambridge University Press, Cambridge, 2018.

[Muthuraman *et al.* 2016] U. Muthuraman, M.M. Sai Hashita, N. Sakthieswaran, P. Suresh, M. Raj Kumar and P. Sivashanmugam. An approach for damage identification and optimal sensor placement in structural health monitoring by genetic algorithm technique, volume 07. 2016.

[Nazeer *et al.* 2014] S.M. Nazeer, F. Bordeu, A. Leygue and F. Chinesta. *Arlequin based PGD domain decomposition.* Computational Mechanics, **54**, 1175–1190, 2014.

[Newmark 1959] N.M. Newmark. *A method of computation for structural dynamics.* Journal of the Engineering Mechanics Division, **85**, 67–94, 1959.

[Oñate 2010] E. Oñate. Structural analysis with the finite element method. linear statics. volume 2: Beams, plates and shells. 2010.

[Owen & Hinton 1980] D.R.J. Owen and E. Hinton. Finite elements in plasticity : Theory and practice. Swansea, U.K. : Pineridge Press, 1980.

[Pandey *et al.* 1991] A.K. Pandey, M. Biswas and M.M. Samman. *Damage detection from changes in curvature mode shapes.* Journal of Sound and Vibration, **145**, 321–332, 1991.

[Park *et al.* 2008] S.K. Park, H.W. Park, S. Shin and H.S. Lee. *Detection of abrupt structural damage induced by an earthquake using a moving time window technique.* Computers & Structures, **86**, 1253–1265, 2008.

[Parsa *et al.* 2018] B. Parsa, K. Rajasekaran, F. Meier and A. Banerjee. A hierarchical bayesian linear regression model with local features for stochastic dynamics approximation. 2018.

[Peña *et al.* 1999] J.M. Peña, J.A. Lozano and P. Larrañaga. *An empirical comparison of four initialization methods for the K-Means algorithm.* Pattern Recognition Letters, **20**, 1027–1040, 1999.

[Peeters & De Roeck 2001] B. Peeters and G. De Roeck. *Stochastic System Identification for Operational Modal Analysis: A Review.* Journal of Dynamic Systems, Measurement, and Control, **123**, 659–667, 2001.

[Pinho *et al.* 2006] S. Pinho, L. Iannucci and P. Robinson. Formulation and implementation of decohesion elements in an explicit finite element code, volume 37. 2006.

[Pope 1966] G.G. Pope. *A Discrete Element Method for the Analysis of Plane Elasto-Plastic Stress Problems.* Aeronautical Quarterly, **17**, 83–104, 1966.

[Popov *et al.* 1967] E.P. Popov, M. Khojasteh-Bakht and S. Yaghmai. *Bending of circular plates of hardening material.* International Journal of Solids and Structures, **3**, 975–988, 1967.

[Prior 1994] A.M. Prior. *Applications of implicit and explicit finite element techniques to metal forming.* Journal of Materials Processing Technology, **45**, 649–656, 1994.

[Prulière 2014] E. Prulière. *3D simulation of laminated shell structures using the Proper Generalized Decomposition.* Composite Structures, **117**, 373–381, 2014.

[Pujol 2007] J. Pujol. *The solution of nonlinear inverse problems and the Levenberg-Marquardt method.* GEOPHYSICS, **72**, W1–W16, 2007.

[Raissi *et al.* 2017a] M. Raissi, P. Perdikaris and G. Karniadakis. Physics informed deep learning (part i): Data-driven solutions of nonlinear partial differential equations. 2017.

[Raissi *et al.* 2017b] M. Raissi, P. Perdikaris and G. Karniadakis. Physics informed deep learning (part ii): Data-driven discovery of nonlinear partial differential equations. 2017.

[Reissner 1945] E. Reissner. *The effect of transverse shear deformation on the bending of elastic plates.* J. Appl. Mech., **12**, 69–76, 1945.

[Reyes & Deere 1966] S. F. Reyes and D.U. Deere. *Elastic-plastic Analysis of Underground Openings By the Finite Element Method*, 1966.

[Reynders *et al.* 2010] E. Reynders, A. Teughels and G. De Roeck. *Finite element model updating and structural damage identification using OMAX data.* Mechanical Systems and Signal Processing, **24**, 1306–1323, 2010.

[Rucka & Wilde 2006] M. Rucka and K. Wilde. *Application of continuous wavelet transform in vibration based damage detection method for beams and plates.* Journal of Sound and Vibration, **297**, 536–550, 2006.

[Ruocci *et al.* 2011] G. Ruocci, A. Quattrone and A. De Stefano. Multi-domain feature selection aimed at the damage detection of historical bridges, volume 305. 2011.

[Salehi *et al.* 2010] M. Salehi, S. Ziaei-Rad, M. Ghayour, M. Ali Vaziri-Zanjani, M. Salehi, M. Ghayour and M. A Vaziri-Zanjani. A structural damage detection technique based on measured frequency response functions, volume 3. 2010.

[Schölkopf *et al.* 1998] B. Schölkopf, A. J. Smola and K.R. Müller. Nonlinear component analysis as a kernel eigenvalue problem, volume 10. 1998.

[Schölkopf *et al.* 1999] B. Schölkopf, A. J. Smola and K.R. Müller. *Kernel principal component analysis.* In Advances in Kernel Methods - Support Vector Learning, 327–352. MIT Press, 1999.

[Selva *et al.* 2013] P. Selva, O. Cherrier, V. Budinger, F. Lachaud and J. Morlier. *Smart monitoring of aeronautical composites plates based on electromechanical impedance measurements and artificial neural networks.* Engineering Structures, **56**, 794–804, 2013.

[Siser & Slota 2016] M. Siser and J. Slota. Material model of aw 5754 h11 al alloy for numerical simulation of deep drawing process, volume 20. 2016.

[Sun *et al.* 2000] J.S. Sun, K.H. Lee and H.P. Lee. *Comparison of implicit and explicit finite element methods for dynamic problems.* Journal of Materials Processing Technology, **105**, 110–118, 2000.

[Swedlow *et al.* 1965] J.L. Swedlow, M.L. Williams and W.H. Yang. Elasto-plastic stresses and strains in cracked plates. Firestone Flight Sciences Laboratory, California Institute of Technology, 1965.

[T. Roweis & K. Saul 2000] S. T. Roweis and L. K. Saul. Nonlinear dimensionality reduction by locally linear embedding, volume 290. 2000.

[Taddei *et al.* 2016] T. Taddei, J. D. Penn, M. Yano and A. T. Patera. Simulation-based classification; a model-order-reduction approach for structural health monitoring. 2016.

[Taylor *et al.* 1995] L. Taylor, J. Cao, A.P. Karafillis and M.C. Boyce. *Numerical simulations of sheet-metal forming.* Journal of Materials Processing Technology, **50**, 168–179, 1995.

[Todorovska & Rahmani 2013] M.I. Todorovska and M.T. Rahmani. *System identification of buildings by wave travel time analysis and layered shear beam models–Spatial resolution and accuracy.* Struct. Control Health Monit., **20**, 686–702, 2013.

[Todorovska & Trifunac 2010] M.I. Todorovska and M.D. Trifunac. *Earthquake damage detection in the Imperial County Services Building II: Analysis of novelties via wavelets.* Struct. Control Health Monit., **17**, 895–917, 2010.

[Vandiver *et al.* 1982] J.K. Vandiver, A.B. Dunwoody, R.B. Campbell and M.F. Cook. *A Mathematical Basis for the Random Decrement Vibration Signature Analysis Technique.* Journal of Mechanical Design, **104**, 307–313, 1982.

[Vidal *et al.* 2012] P. Vidal, L. Gallimard and O. Polit. *Composite beam finite element based on the Proper Generalized Decomposition.* Computers & Structures, **102-103**, 76–86, 2012.

[Vidal *et al.* 2013] P. Vidal, L. Gallimard and O. Polit. *Proper Generalized Decomposition and layer-wise approach for the modeling of composite plate structures.* International Journal of Solids and Structures, **50**, 2239–2250, 2013.

[Vidal *et al.* 2014a] P. Vidal, L. Gallimard and O. Polit. *Shell finite element based on the Proper Generalized Decomposition for the modeling of cylindrical composite structures.* Computers & Structures, **132**, 1–11, 2014.

[Vidal *et al.* 2014b] P. Vidal, G. Laurent and O. Polit. Explicit solutions for the modeling of laminated composite plates with arbitrary stacking sequences, volume 60. 2014.

[Vidal *et al.* 2015] P. Vidal, L. Gallimard and O. Polit. *Assessment of variable separation for finite element modeling of free edge effect for composite plates.* Composite Structures, **123**, 19–29, 2015.

[Vitola *et al.* 2016] J. Vitola, M.A. Vejar, D.A.T. Burgos and F. Pozo. *Data-Driven Methodologies for Structural Damage Detection Based on Machine Learning Applications.* In S. Ramakrishnan, editor, Pattern Recognition - Analysis and Applications, Ch. 06. InTech, Rijeka, 2016.

[Wang & Deng 1999] Q. Wang and X. Deng. *Damage detection with spatial wavelets.* International Journal of Solids and Structures, **36**, 3443–3468, 1999.

[Warburton 1995] G.B. Warburton. *Dynamics of structures, by Ray W. Clough and Joseph Penzien, 2nd edition, McGraw-Hill, New York, 1993. No. of pages: 738. ISBN 0-07-011394-7.* Earthquake Engng. Struct. Dyn., **24**, 457–462, 1995.

[West 1986] M.W. West. Illustration of the use of modal assurance criterion to detect structural changes in an orbiter test specimen. 1986.

[Wilkins *et al.* 1980] M.L. Wilkins, R.D. Streit and J.E. Reaugh. Cumulative-strain-damage model of ductile fracture: simulation and prediction of engineering fracture tests. 1980.

[Wilson 1974] L.E. Wilson. *The static condensation algorithm.* International Journal for Numerical Methods in Engineering, **8**, 198–203, 1974.

[Xu & Chen 2004] Y.L. Xu and J. Chen. Structural damage detection using empirical mode decomposition: Experimental investigation, volume 130. 2004.

[Xu *et al.* 2015] W. Xu, M. Cao, W. Ostachowicz, M. Radzieński and N. Xia. *Two-dimensional curvature mode shape method based on wavelets and Teager energy for damage detection in plates.* Journal of Sound and Vibration, **347**, 266–278, 2015.

[Yam *et al.* 1996] L.Y. Yam, T.P. Leung, D.B. Li and K.Z. Xue. Theoretical and experimental study of modal strain analysis, volume 191. 1996.

[Zekovic *et al.* 2005] S. Zekovic, R. Dwivedi and R. Kovacevic. Thermo-structural finite element analysis of direct laser metal deposited thin-walled structures. 2005.

[Zeng *et al.* 2013] K. Zeng, D. Pal, N. Patil and B. Stucker. A new dynamic mesh method applied to the simulation of selective laser melting. 2013.

[Zhang & Aktan 1995] Z. Zhang and A. Aktan. The damage indices for the constructed facilities, volume 2460. 1995.

[Zhang & Zha 2003] Z. Zhang and H. Zha. Principal manifolds and nonlinear dimension reduction via local tangent space alignment, volume 26. 2003.

[Zienkiewicz *et al.* 1969] C.O. Zienkiewicz, S. Valliappan and I. King. Elasto-plastic solutions of engineering problems 'initial stress', finite element approach, volume 1. 1969.